Title	Electromagnetic modelling and experimentation for the development of a novel microwave thermal ablation therapy for adrenal tumours
Author(s)	Bottiglieri, Anna
Publication Date	2021-11-29
Publisher	NUI Galway
Item record	http://hdl.handle.net/10379/17081

Electromagnetic Modelling and Experimentation for the Development of a Novel Microwave Thermal Ablation Therapy for Adrenal Tumours

Presented by:

Anna Bottiglieri

to:

Electrical and Electronic Engineering,
College of Engineering and Informatics,
National University of Ireland Galway,

In fulfillment of the requirement for the degree of
Doctor of Philosophy.

Supervised by
Martin O'Halloran and Laura Farina

Contents

Declaration of Originality

I, the Candidate **Anna Bottiglieri**, certify that the thesis entitled **"Electromagnetic Modelling and Experimentation for the Development of a Novel Microwave Thermal Ablation Therapy for Adrenal Tumours"** is:

- all my own work;

- has not been previously submitted for any degree or qualification at this University or any other institution;

- and where any work in this thesis was conducted in collaboration, appropriate reference to published work by my collaborators has been made and the nature and extent of my contribution has been clearly stated.

Name:

Anna Bottiglieri

Abstract

Primary Aldosteronism is the main cause of the secondary hypertension, due to the abnormal functioning of the adrenal glands. Adreno-cortical adenomas and bilateral hyperplasia are the most common causes of the abnormal release of the hormone regulating the blood pressure in the adrenal glands. Eradicating the tumours and restoring the normal activity of the adrenal gland is crucial to address this condition. To date, surgical removal of the gland and pharmacotherapy are the gold standard techniques adopted in the management of unilateral adenomas and bilateral hyperplasia, respectively. Both techniques present drawbacks linked to invasiveness and ineffectiveness.

Currently, alternative techniques to the standard therapies are under investigation for the treatment of adrenal neoplasms. Recent clinical studies showed promising results in adopting thermal ablation techniques to eradicate solitary and encapsulated adrenal adenomas, and restore normal values of blood pressure and blood-hormone concentrations. However, most of the functional adrenal anomalies arise from the external part of the adrenal cortex and are covered by a fat layer enveloping the adrenal gland. In all these cases, the conventional approach to pierce the tumour and induce extremely high or low temperatures may increase the risk to compound the entire gland and the surrounding structures, with detrimental effects on the outcomes of the procedure.

In this thesis, the use of microwave thermal ablation is studied for the selective removal of shallow adenomas. In particular, a 'side firing' approach is proposed. This new approach relies on the intrinsic anatomical and dielectric characteristics of the adrenal gland and its surrounding fat capsule. More specifically, this thesis explores the possibility of using the fat layer enveloping the adrenal gland as a tool to selectively direct the electromagnetic energy into the tumour and shield the surrounding tissues.

Firstly, an animal model is chosen to study the dielectric properties of the adrenal gland. Next, the dielectric properties of *ex vivo* human adrenal tissues, both healthy and diseased, are measured and compared with those of the animal model. The dielectric properties of the target tissues are characterised at the operational frequencies typically

adopted for microwave thermal ablation. The degree of dielectric contrast with fat tissue is assessed. This contrast supports the proposed 'side firing' approach.

Secondly, a proof-of-concept study is completed to investigate the effect of the fat layer on the distribution of the electromagnetic energy and temperature in a simplified scenario. A microwave applicator operating at 2.45 GHz is placed at the interface between a muscle and fat layer. The outcomes show that the fat acts as a natural shield, helping to focus the electromagnetic energy toward a preferential direction. The fat-muscle interface is adopted in this preliminary study due to the conservative degree of dielectric contrast existing between muscle and fat compared to the contrast between the adrenal tissues and fat. Also, the large availability both of muscle and fat has facilitated the experimental assessment of the numerical study.

Given the positive results of the proof-of-concept study, the same 'side firing' approach at the same operating frequency (2.45 GHz) is applied using planar and 3D adrenal models representing the adrenal gland and its fat capsule. The effect of different geometrical characteristics of the target and different orientations of the microwave applicator on the shielding effect of the fat layer is studied numerically. Two levels of energy are considered both for *ex vivo* and *in vivo* conditions. *Ex vivo* and *in vivo* experimental microwave ablation procedures validate the proposed 'side firing' approach. Histology analyses of the *ex vivo* and *in vivo* samples confirmed the capability of the fat layer to induce asymmetric ablations and protect the surrounding sensitive structures (i.e. blood vessel).

Lastly, a higher MWA operating frequency, 5.8 GHz, is investigated. The higher dielectric contrast observed at higher frequencies compared with 2.45 GHz, suggests that a more focused 'side firing' effect is achievable. The shielding effect of the fat layer is confirmed also at 5.8 GHz. Moreover, the increase of the contrast in the electrical conductivity between the fat layer and the adrenal tissue helps to improve the thermal coverage and the sphericity of the ablation zone in the tissue target.

In summary, this thesis provides a comprehensive understanding of the role of the fat enveloping the tissue target during microwave ablation procedures and the possibility of

using this anatomical characteristic to create directional ablation zones. The results included in this thesis may provide additional information to improve the clinical protocols for the treatment of adreno-cortical adenomas through microwave thermal ablation.

Acknowledgements

I would like to thank Martin for giving me the opportunity to work in his group, Laura, Adnan and all the people who contributed to this work. In particular, I would like to thank Alessandra for having been my 'oasis' throughout these years and Emily for the constant support, even across the Atlantic. I would also like to thank my wonderful companions with whom I had the pleasure to share these years: Hamza, Bilal, Nadia, Nuno, Niko, Barry, Adam, Ana.

I am very grateful to my wonderful mum and my dad, for trusting in me more than I usually do and for always finding a reason to smile. Many thanks to my precious friends Giulia and Eduardo for the inspiring discussions, the hints, and the unique laughing. Finally, thanks to Lorenzo for having helped me to turn on the light.

List of Figures

List of Tables

Acronyms

PA Primary Aldosteronism

IVC Inferior vena cava

EMF Electromagnetic field

MWA Microwave thermal ablation

MW Microwave

SAR Specific absorption rate

PAC Plasma aldosterone concentration

SBP Systolic blood pressure

DBP Diastolic blood pressure

EH Essential Hypertension

APA Aldosterone producing adenoma

BIH Bilateral idiopathic bilateral hyperplasia

LVH Left ventricular hypertrophy

bK Blood potassium concentration

ARR Aldosterone-to-renin ratio

PRA Plasma renin activity

CPT Captopril test

SIT Saline infusion test

FST Fludrocortisone suppression test

SLT Saline loading test

CT Computer tomography

AVS Adrenal venous sampling

PET Positron emission tomography

MRAs Mineralocorticoid receptor antagonists

LA Laparoscopic adrenalectomy

RFA Radiofrequency ablation

US Ultrasound

MRI Magnetic resonance imaging

RF Radiofrequency

MRT Magnetic resonance thermometry

HCC Hepatocellular carcinoma

Chapter 1
Introduction

1.1 Motivation

Primary aldosteronism (PA) is the main cause of secondary hypertension which is currently recognised in approximately 11% of the hypertensive population worldwide [1]. PA is caused by unilateral adenomas or bilateral hyperplasia arising from adrenal glands [1]–[3]. These abnormalities are responsible for the uncontrolled release of the aldosterone hormone. Besides hypertension, persistently high levels of aldosterone are the cause of comorbidities such as hypokalaemia, ventricular hypertrophy, cerebrovascular ischemic events [4]–[7].

Conventional techniques currently used to manage PA are adrenalectomy and pharmacotherapy. The complete resection of the gland through adrenalectomy is the gold standard procedure for patients affected by unilateral adenoma. Pharmacotherapy based on the administration of hormonal antagonists is adopted to manage PA in non-surgical candidates, such as subjects affected by bilateral hyperplasia. These approaches show the following limitations:

- Pharmacotherapy is a life-long therapy whose side-effects are poorly tolerated, such as gynecomastia, menstrual disorders, mastodynia, obesity-related insulin resistance [8], [9];

- Adrenalectomy is a challenging surgical procedure at high risk of haemorrhages and damages to the surrounding organs, e.g. renal artery, inferior vena cava (IVC), diaphragm, spleen, liver, nerves;

- Adrenalectomy requires the removal of the entire gland, including the healthy functional adrenal tissues. Most of the patients living only with the contralateral adrenal gland needs hormonal supplement. Moreover, pharmacotherapy is required in case of recurrence of the disease in the contralateral gland.

Ablation techniques have been recently investigated to address some of the above-mentioned limitations. This thesis focuses on the use of microwave thermal ablation (MWA). The potentiality of a new MWA approach is investigated to selectively treat the tumour, preserving the integrity of the healthy tissues of the gland and of the surrounding sensitive structures.

MWA is an electromagnetic-based thermal technique designed to work at selected ISM frequencies in the microwave frequency range (500 MHz – 10 GHz). The operating frequencies typically used are 915 MHz and 2.45 GHz [10]–[13]. MWA relies on the interaction between the electromagnetic field (EMF) and the biological tissues to induce cytotoxic temperatures (> 55 °C) in the target tissue. Coagulation necrosis results from such an increase of temperature. MWA has been demonstrated to be a potent tool to locally destroy cancerous cells. Over the last twenty years, significant results have been obtained in the treatment of a range of tumours, such as hepatocellular carcinomas, liver metastasis, renal carcinomas [14]–[16]. Historically, MWA has been used to treat tumours larger than 30 mm in diameter. The increase in the tissue impedance with the temperature does not impede microwaves to reach the periphery of the target tissue. Moreover, microwaves are poorly affected by the heat sink effect induced due to adjacent big vessels or arteries. Such a characteristic makes MWA less susceptible to suboptimal results and the risk of local recurrence of the tumour. Recently, MWA has been investigated to also treat small critical targets. Adrenal neoplasms (≤ 20 mm diameter) in patients who refuse surgical procedures or are not surgical candidates are an example of these critical targets [17]–[19]. In these cases, the possibility of obtaining focused temperature increases in short timeframes has been exploited [20], [21]. Compared to other ablation procedures explored for PA treatment (i.e. chemical ablation, cryoablation, radiofrequency ablation), MWA has shown:

- A reduced number of hypertensive crises during the procedure [22];

- The possibility to reach complete coverage of the adenoma after a single procedure [17], [19];

- The possibility of treating functional adrenal tumours without the use, or with a minimal use, of alpha adrenergic blockade drugs in patients with pre-existing cardiovascular diseases [23].

Although promising performances has been observed in the most recent studies, further investigations are required to have a comprehensive understanding of the feasibility of MWA for PA treatment. In particular, the risk of damages to organs surrounding the adrenal glands remain a concern. The available clinical studies have adopted the MWA technique based on the infusion of a saline solution to create artificial ascites between the tumour target and the surrounding structures [17], [19]. The main purpose of this technique is to use the properties of the saline solution to isolate the ablation zone from the surrounding structures. Successful results are observed only where a separation of at least 5 mm is ensured during the MWA procedure. In addition, this procedure involves the use of a further catheter for the injection of the liquid, which enhances the invasiveness of the treatment [17], [23], [24]. An alternative technique recently explored is based on the use of reflector-based antennas to create directional heating patterns [25]. However, translation into a clinical application remains a concern. First, the diameter of the applicator must be increased in order to accommodate the metallic cable working as reflector. Then, reflector-based antennas need an accurate orientation in order to achieve satisfying results. This requirement could be challenging in a clinical scenario.

A different solution to create asymmetrical ablation was preliminary investigated in [20]. This new solution relies on the anatomical characteristics of the gland have to refine the MWA procedure. In particular, the fat layer surrounding the adrenal gland was exploited to shape the asymmetrical ablation zones.

In this thesis, the role of the fat layer in shaping microwave ablation zones is investigated in depth.

The areas for improvement identified above have informed the objectives of this thesis, which are as follows:

- Defining and optimising suitable adrenal models for accurate numerical simulations and experimental tests. For instance, identifying animal models whose properties are

a good representation of the properties of the human adrenal glands. Designing and prototyping microwave (MW) applicators given the operating conditions, e.g. size and shape of the tissue, frequency. Evaluating the factors which may influence the ultimate dimensions of the ablation zone (e.g. temperature-dependent dielectric properties, water vaporisation, blood perfusion). Implementing the models accounting for these factors to refine the numerical simulations;

- Characterising the role of the fat layer surrounding the adrenal gland through numerical and experimental studies. For instance, analysing the distribution of the electromagnetic energy and temperature accounting for different tissues geometries, orientations of the MW applicator, levels of energy dose (i.e. power and time settings), type of background material, effect of the blood perfusion and operating frequency;

- Evaluating the thermal effects of the 'side firing' approach on the microscopic structure of the tissue. For instance, correlating the changes in the cellular structures of the functional tissue with the treatment protocol used. Studying the effect of the temperature increase on the adipose cells. Evaluating the ability of the fat to preserve the closest structures from the transmural thermal lesion.

The research contributions of the thesis are summarised in the following sections. These include the journal and conference publications which resulted from these contributions.

1.2 Thesis contributions

This thesis investigates a new MWA approach that aims to use the fat surrounding the target to focus the electromagnetic energy in the target, whilst sparing the surrounding anatomical structures. This new approach is formulated given the anatomical characteristics of the adrenal gland and the dielectric contrast between the adrenal tissues and the surrounding fat capsule. A further objective is to limit unintended ablation of healthy functional adrenal tissues. To this end, the new method prioritises a lateral approach, named in the thesis as 'side firing' approach, which does not involve piercing the target tissue. The lateral approach takes advantage of the natural envelope of the adrenal gland in the fat capsule. As a result, the outermost fat and the underlying adrenal

tissue create the dielectric contrast used in this thesis to shape the ablation zone during the MWA treatment.

The principal contributions of the thesis based on the objectives mentioned in the previous section are:

1 Characterisation of the dielectric properties of the adrenal gland within the microwave frequency range. Firstly, the dielectric properties are measured *ex vivo* on each functional tissue of ovine adrenal glands. Then, these values are compared with those measured *ex v*ivo on human adrenal tissues, both normal and diseased. The accuracy of the proposed animal model in representing human adrenal tissues is evaluated across a broadband frequency range including operating frequencies suitable for MWA procedure (i.e. 915 MHz, 2.45 GHz. 5.8 GHz).

2 Prototyping of the MW applicators and designing of the workflow for electromagnetic and thermal simulations. The characteristics and performances of three different MW applicators are compared. Each applicator is adopted based on the specific operating conditions (e.g. operating frequency, *ex vivo* or *in vivo* application). The main parameters of influence to consider in the numerical simulations are identified (based on the levels of energy dose and the operating frequency). Then, the workflow for electromagnetic and thermal simulations is defined.

3 Analysis of the effect induced by the fat tissue adjacent to the tissue target on the distribution of the electromagnetic energy and temperature using 2.45 GHz as operating frequency. First, the performances of the proposed 'side firing' approach are assessed in a proof-of-concept study, where an interface between fat and muscle is represented. The variation in the shape and size of the ablation patterns is evaluated in comparison with an homogeneous muscle scenario. Then, the same approach is adopted in two different models representing adrenal glands. A number of electromagnetic and thermal simulations was conducted. The 'side firing' approach is evaluated considering a range of factors in the numerical simulations. These factors include the orientation of the MW applicator, the geometry of the tissues, the level

of energy delivered in the tissue, the type of background material and the blood perfusion.

4   Analysis of the histological features of the tissue after *ex vivo* and *in vivo* MWA treatments conducted at 2.45 GHz using the 'side firing' approach. The histology analysis is used to evaluate the ability of the 'side firing' approach to confine the ablation zone in proximity to the applicator, whilst sparing the remaining part of the functional tissues. Finally, the ability of the fat layer to protect the structure of the abutting blood vessel is examined.

5   The analysis of the performances of the proposed MWA method using a higher operating frequency. Numerical simulations are conducted in adrenal tissues model to evaluate how the increase in the operating frequency affects the asymmetric ablation profiles. In addition, the potential advantages of the higher frequency versus 2.45 GHz are discussed in terms of the shape and the size of the ablation zones. To this end, numerical simulations were conducted at the designed frequency, accounting for the geometry of the tissue, level of energy dose and water vaporisation. The temperature values obtained experimentally were compared to the values obtained from the numerical simulations.

1.2.1   Publications

The publications resulting from this research are as follows:

Journal Publications

- **A. Bottiglieri,** G. Ruvio, M.O'Halloran, L. Farina, "Exploiting fat tissue boundaries to shape microwave thermal ablation zones", *Sensors*, vol. 20, no. 14, pp. 3960 – 3975, 2020.

- **A. Bottiglieri**, A. Shahzad, P. Donlon, M. C. Dennedy, A. Lowery, M. O'Halloran, L. Farina, "Dielectric Characterization of Ex Vivo Ovine and Human Adrenal Glands for Microwave Thermal Ablation Applications", *IEEE Journal of Electromagnetics, RF and Microwaves in Medicine and Biology*, vol. 5, n. 3, pp. 254 – 261, 2021.

Conference Publications

- **A. Bottiglieri**, A. M. Elahi, A. Shahzad, P. Donlon, M. Dennedy, M. O'Halloran, "Experimental evaluation of the effective ablation zone on ex-vivo bovine liver samples", EMF-Med 1st World Conference on Biomedical Applications of Electromagnetic Fields (EMF-Med), Split, Croatia, Sept. 10 – 13 , 2018.

- **A. Bottiglieri**, M. A. Elahi, G. Ruvio, J. Eaton-Evans, A. Shahzad, M.C. Dennedy, M. O'Halloran, L. Farina, "Microwave thermal ablation: focusing energy in target tissue using fat layer", *European Conference on Antennas and Propagation (EuCAP)*, Krakow, Poland, Mar. 31 – Apr. 5, 2019.

- L. Farina, A.J. de Marco, **A. Bottiglieri**, G. Ruvio, J. Eaton-Evans, M.C. Dennedy, A.M. Elahi, M. O'Halloran, "Microwave ablation antenna for functional adenomas in the adrenal gland", *Photonics in Electromagnetics Research Symposium (PIERS-Spring),* Rome, Italy, Jun. 17 – 20, 2019.

Other contributions

- G. Ruvio, L. Farina, **A. Bottiglieri**, J. Eaton-Evans, M. Elahi, M. O'Halloran, R. Pinto, V. Lopresto, M. Cavagnaro, "Comparison of the coaxial open-ended probe based dielectric properties measurements on *ex-vivo* thermally ablated liver tissue", *European Conference on Antennas and Propagation (EuCAP),* Krakow, Poland, Mar. 31 – Apr. 5, 2019.

- **A. Bottiglieri**, E. Dunne, B. McDermott, M. Cavagnaro, E. Porter, L. Farina, "Monitoring Microwave Thermal Ablation using Electrical Impedance Tomography: an experimental feasibility study", *European Conference on Antennas and Propagation (EuCAP),* Copenhagen, Denmark, Mar. 15 – 20, 2020.

- N.P. Silva, **A. Bottiglieri**, R. C. Conceicao, M. O'Halloran, L. Farina, "Thermal properties of *ex vivo* biological tissue at room and body temperature", *European Conference on Antennas and Propagation (EuCAP),* Copenhagen, Denmark, Mar. 15 – 20, 2020.

- N. Istuk, **A. Bottiglieri**, E. Porter, M. O'Haloran, L. Farina, "Changes in the dielectric properties of *ex vivo* ovine kidney before and after Microwave Thermal Ablation", XXXIII General Assembly and Scientific Symposium of the International Union of

Radio Science, Rome, Italy, Aug. 29 – Sept. 5 2020.

- N.P. Silva, **A. Bottiglieri**, R.C. Conceicao, M. O'Halloran, L. Farina, "Characterisation of ex-vivo liver thermal properties for electromagnetic-based therapies", *Sensors,* vol. 20, no. 10, pp. 3004 – 3018, 2020.

1.3 Thesis Outline

The remainder of this thesis describes the background, the numerical studies, the experimental tests and the results to address the primary research objectives.

Chapter 2 provides a review of the anatomy of the adrenal gland, the biological mechanism regulating the levels of aldosterone and blood pressure and the types of adrenal abnormalities responsible for PA. The gold standard techniques for PA treatment are described, along with the advantages and main limitations that each technique presents. Ablation techniques recently proposed to address these limitations are described and compared. The chapter focuses on the current understanding of the MWA and the potential advantages compared to the other techniques in the PA treatment.

Chapter 3 presents the experimental dielectric data measured *ex vivo* on ovine and human adrenal tissues. The motivation, experimental setup and protocol, and procedure for the analysis of the results are described. The dielectric properties of the ovine adrenal models are compared with those measured *ex vivo* on human adrenal glands to estimate the discrepancy between the animal model and human adrenal tissues. In addition, the variation in the dielectric properties of a range of different types of diseased adrenal glands was observed. The dielectric values are shown both in the frequency range from 500 MHz to 8.5 GHz and at single operating frequencies used for MWA procedures, 915 MHz, 2.45 GHz, 5.8 GHz. In particular, the values of ovine adrenal tissues at 2.45 GHz are used to define the dielectric properties in the numerical simulations described in Chapter 6 and Chapter 7. The values at 5.8 GHz are used for the numerical study described in Chapter 8.

Chapter 4 reviews the cause-effect mechanisms underlying the interactions between EMF and biological tissues. The chapter reviews the main parameters and related mathematical expressions that will be used to evaluate the performances of the MW

applicator and the MWA procedure (e.g. reflection coefficient, specific absorption rate (SAR), increment of temperature). Additionally, the electromagnetic and thermal problems are defined and the methodology for the numerical solutions is presented. Next, the performances of three different MWA applicators are compared in terms of reflection coefficient and distribution of SAR. These applicators are designed and prototyped taking into account the operating conditions (i.e. 2.45 GHz or 5.8 GHz operating frequency) and the experimental scenario (i.e. *in vivo* or *ex vivo* scenario). Finally, the workflow for EM and thermal simulations is defined and the main factors of influence are discussed in relation to the operating frequency, power and time settings adopted.

Chapter 5 presents a proof-of-concept study where a numerical simplified scenario is characterised by a dielectric contrast between fat and muscle at 2.45 GHz. The numerical distributions of temperature are compared in terms of different widths of the fat layer and alignments of the MW applicator. Then, the temperature values obtained in the interface scenario are compared and contrasted with the results obtained in a reference scenario composed of homogenous tissue. Finally, experimental tests are conducted to support the numerical simulation.

Chapter 6 evaluates the distribution of SAR and temperature both in a simplified and 3D model, representing the structure of adrenal glands at 2.45 GHz. The simplified multilayered model is designed, and the MW applicator is placed parallel to the interface between fat and target tissue (i.e. adrenal cortex). The different dielectric contrast between fat and the adjacent tissue is compared with the scenario presented in Chapter 5. These two scenarios are compared in terms of shape and size of the ablation zones for each power and time setting adopted. Then, the numerical results obtained in the simplified model are compared with those achieved in the 3D model. In particular, the SAR and temperature distributions are described in relation to the influence of the geometry of the tissue and orientation of the MW applicator. Experimental tests are conducted by translating the 'side firing' approach investigated numerically into an *ex vivo* animal scenario. The extent of the ablation zones in the tissue target and the increments of temperature are correlated with the numerical. Finally, the chapter describes the procedure to conduct a histology analysis after a MWA procedure and

describes the changes in the cellular structure of the functional adrenal tissues, fat and adjacent blood vessels.

Chapter 7 evaluates the influence on the distribution of temperature of the background material and tissue blood perfusion in the same 3D adrenal models described in Chapter 6. First, the background material of the geometrical model is changed from air (used in Chapter 6) to blood. The distribution of SAR, the temperature and the ultimate extent of the ablation zones are discussed in relation to the results presented in Chapter 6. Next, two numerical models for blood perfusion are added to fat and adrenal tissues. The results are compared with those obtained in the absence of blood perfusion. Finally, the numerical findings are supported by an experimental *in vivo* study and by the histological analysis of the tissues after the MWA procedure.

Chapter 8 evaluates the impact of the higher operating frequency (i.e. 5.8 GHz) on the distribution of SAR and temperature both in the fat layer and in the adrenal gland. Simplified and 3D adrenal models and orientations of the MW applicator are used, consistent with Chapter 6. Next, a similar experimental MWA procedure as described in Chapter 6 is adopted. Thus, the temperature values and the extent of the ablation zones in the target tissue are compared with the values obtained in the numerical study. Finally, the comparison between numerical and experimental results helps to evaluate the influence of the water vaporisation on the peak temperature values and extent of the ablation zone.

Chapter 9 summarises the main results and conclusions of the thesis. In addition, future work is identified to improve the assessment of the MWA procedure in PA treatment and the next steps required for the acceptance of the method proposed.

Chapter 2
Background

2.1 Introduction

In this chapter, the biological mechanism underlying Primary Aldosteronism (PA) and the resulting hypertension are reviewed. Then, the chapter discusses the clinical approaches to manage PA and identifies the needs which new strategies should meet.

The main goal of new treatment approaches is to manage PA condition in a less invasive way compared with the gold standard techniques. To this end, different ablation techniques have been reviewed in terms of fundamental physical principles, treatment protocol and current clinical applications. Within these relatively new approaches, microwave thermal ablation (MWA) has been identified as the optimal candidate. The work of this thesis is focused on this technique.

The chapter aims to:

- Describe the renin-angiotensin system and the key role in the regulation of blood pressure both in the normal conditions and in presence of PA;

- Provide an overview of PA incidence on the hypertensive population and the state-of-the art of the diagnostic criteria;

- Describe the treatment modalities typically adopted in the clinical practice to solve or contain PA along with the drawbacks that need to be addressed;

- Discuss the recent ablation techniques that may potentially overcome the limitations of the traditional procedures.

The reminder of the chapter is as follows: the biological principles of PA are presented in Section 2.1. The development in methods to diagnose PA in recent years and the consequent changes in the incidence rates of the PA are discussed in Section 2.2. The techniques currently adopted for the treatment of PA are described in Section 2.3. Finally,
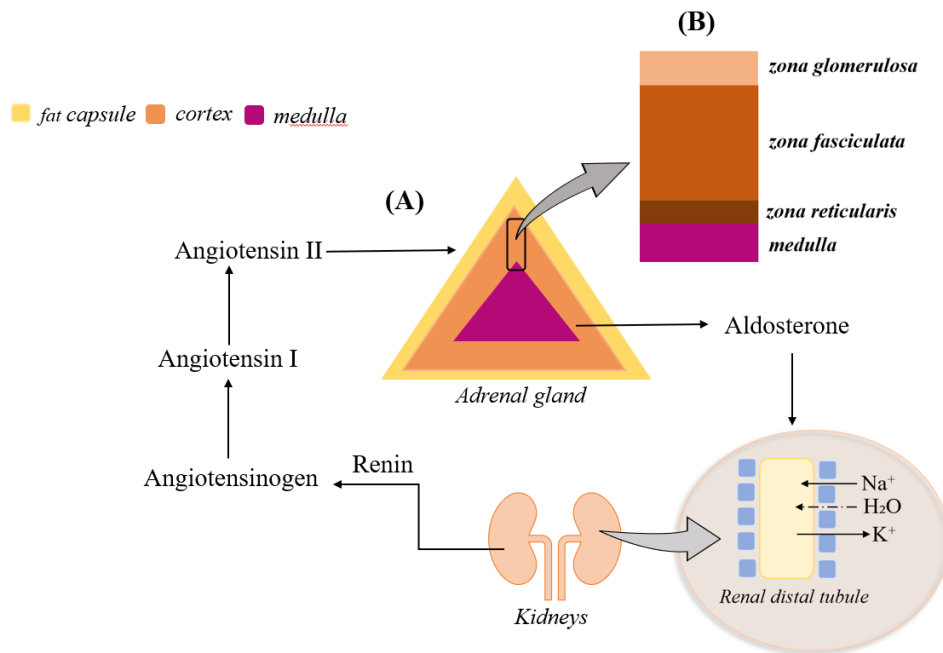
Figure 2.1: (A) Physiology of the renin-angiotensin system related to the synthesis, secretion and mechanism of action at the renal distal tubule of the aldosterone hormone. The synthesis of aldosterone is triggered from the renin protein contained in the renal proximal tubule. Then, the aldosterone is released from the zona glomerulosa of the adrenal cortex. The effect is the absorption of sodium (Na^+), the release of potassium (K^+) and the osmotic water (H_2O) reabsorption in the extracellular fluid; (B) three different regions composing the functional tissue of the adrenal cortex and responsible for the release of different types of hormones: zona glomerulosa, zona fasciculata and zona reticularis.

the available ablation techniques considered for the treatment of PA are reviewed in Section 2.4.

2.2 Primary Aldosteronism: biological principles

According to the data reported by World Health Organisation in September 2019, an estimated 1.13 billion people worldwide suffer from hypertension, with less than 1 in 5 hypertensive people having the problem under control.

The key mechanism regulating blood pressure is the renin-angiotensin-system, shown in Figure 2.1. In normal conditions, a decrease in the arterial blood pressure triggers the release of *renin* protein from the kidney. As a consequence, the renin concentration in the blood increases. Renin is a protein that catalyses the conversion from the protein *angiotensinogen* to the protein *angiotensin I*, which is converted in *angiotensin II*.

Angiotensin II is the most important stimulus activating the release of the *aldosterone* hormone from the adrenal glands [26]. Once the release of the aldosterone is activated, the concentration of sodium chloride (Na^+Cl^-) in the extracellular fluids increases as well as the excretion of the potassium (K^+) by the renal cells. The reabsorption of the sodium by the renal cells enables simultaneously the osmotic absorption of water. Vasoconstriction and increase of the blood pressure are the consequent effects.

In the cases of autonomous and persistent aldosterone secretion, the renin activity is suppressed. In turn, an excessive amount of both sodium and water are absorbed by extracellular fluids. In response to the high absorption of sodium, high level of potassium is excreted through the urine, in order to restore a balance between the intra- and extracellular concentration of sodium (Na^+) and potassium (K^+). The excessive decrease of potassium concentration is responsible for the hypokalaemia, whereas excessive levels of sodium and water in the extracellular fluids induce an uncontrolled increase of blood pressure responsible for hypertension. The parameter indicating the concentration of aldosterone in the blood is called plasma aldosterone concentration (PAC). When hypertension is developed, the levels of PAC can be up to ten times higher than the baseline value (i.e. PAC $\geq$ 16ng dl^{-1}). Systolic blood pressure (SBP) and diastolic blood pressure (DBP) can exceed 120 mm Hg and 80 mm Hg [27], [28].

2.2.1 Causes and Effects of Primary Aldosteronism

The condition known as essential hyperthension (EH) occurs when pathological levels of blood pressure are not correlated to a specific cause. Essential hypertension accounts for approximately 90% of all cases of hypertension and, generally different patients have different causal factors leading to high levels of blood pressure [29], [30]. In contrast to EH, the hypertension associated to Primary Aldosteronism (PA) is generally linked to abnormalities arising from the *zona glomerulosa* of the adrenal cortex. Abnormalities such as adenomas, clusters of nodules and hyperplasia are the principal cause for the secretion of large amount of aldosterone and for high levels of blood pressure.

The two major PA subtypes are:

- Aldosterone producing adenoma (APA);
- Bilateral idiopathic hyperplasia (BIH).

- APA is caused by an adenoma of approximately 20 mm in diameter arising from the outer surface of the adrenal cortex. In the case of BIH, the abnormal enlargements of both adrenal glands are induced by an excessive rate of cells proliferation [7], [31].

- Other less common causes for PA include:

- Congenital hyperplasia;

- Aldosterone-producing adrenocortical carcinoma;

- Familial hyperaldosteronism.

Congenital hyperplasia is caused by mutations of genes responsible for mineralocorticoids production, whereas the familial hyperaldosteronism is an inherited condition where the adrenal glands produce excessive amount of aldosterone. The aldosterone-producing adrenocortical carcinoma is an uncommon malignant disease (<1% of cases) affecting the adrenal cortex [31], [32].

The hypertension caused by PA could vary from moderate to severe levels and may be resistant to pharmacological treatments [32]. Patients affected by PA may also experience hypokalaemia which induces muscle spasms, weakness, palpitations, polyuria (i.e. abnormal production of urine), polydipsia (i.e. excessive thirst), nocturia (i.e. excessive urination at night). Moreover, the American Diabetes Association states hypokalaemia induced by APA as the second cause of type 2 diabetes mellitus [33].

Beside hypertension and hypokalaemia, further effects due to PA are cardiovascular, renal and metabolic disorders. In [7], a history of stroke was observed in 12.9% of PA patients against 3.4% of patients affected by EH. In the same study, atrial fibrillation was diagnosed in 7.3% of PA patients and only in 0.6% EH patients. In [4] cardiovascular complications were found in 34% of PA patients, within which strokes, cerebral infarctions and cerebral haemorrhages were found in 15.5%, 6.9% and 8.6% of the patients. A further medical condition associated with hypertension is the left ventricular hypertrophy (LVH) responsible for cardiac dysfunctions. In [34] LVH was observed in 53.3% PA patients and in 45.5% of EH patients. In [35] LVH was found in 57% PA patients whereas only 22% EH patients presented the same hypertrophy. In [36], metabolic abnormalities including high levels of triglycerides (>1.69 mmol·L^{-1}), low

levels of cholesterol ($<$1.1 mmol$\cdot$L^{-1}), fasting glucose ($>$6.1 mmol$\cdot$L^{-1}) were identified in 41.1 % PA patients and 29.6% EH patients. Finally, [37] observed diabetes mellitus and hyperglycaemia in 37.6% and 54.9% PA patients against 25.0% and 38.2% cases found within EH patients.

In summary, PA can have a significant impact on a range of serious medical conditions from stroke to metabolic complications. Each of these conditions may have considerable morbidity and mortality. By effectively treating PA, many of these conditions could be resolved or avoided, improving the quality of life of patients.

2.3 Epidemiology of Primary Aldosteronism

2.3.1 Initial diagnostic criteria

As discussed in the sections above, in patients affected by PA, a high amount of potassium is released to balance the excessive absorption of sodium and water due to the abnormal production of aldosterone. The release of large amount of potassium may give rise to hypokalaemia. Up to 15 years ago, the diagnosis of the PA was based on evidence of hypokalaemia within patients. Thus, the first studies considered the hypokalaemia as a unique parameter to determine PA condition. This measure underestimated the incidence of PA in the population affected by hypertension [8], [31]. For example, [38]–[40] showed an incidence of PA across the hypertensive population of approximately 1%, based on the blood potassium concentration test.

In [41] plasma aldosterone concentration (PAC) was for the first time investigated as an additional diagnostic method to be combined with the blood potassium concentration test. However, the combination of the two diagnostic criteria was adopted only for 22 of the 1036 patients included in the study. The remaining patients were tested by measuring the levels of potassium concentration in the blood (bK). As a result, PA diagnosis revealed only 2.2% positive cases in the patients showing levels of plasma aldosterone concentration higher than 8.0 ng$\cdot$dL^{-1}(baseline condition). The low evidence of PA cases (22/1036) [41] is likely due to the nature of the study, as the plasma aldosterone concentration was tested only on a small number of the patients involved in the study.

Table 2.1: Main clinical (SBP and DBP) and biochemical parameters (PAC, PRA, ARR and bK) evaluated during PA screening procedure. The listed baseline ranges in normal condition mention the Mayo Clinic reference values [44].

Baseline values					
Clinical Parameters		Biochemical Parameters			
SBP (mmHg)	DBP (mmHg)	PAC (ng·dL^{-1})	PRA (ng·mL^{-1}·h^{-1})	ARR (ng·dL^{-1}·mL·ng^{-1}·h)	bK (mmol·L^{-1})
$90 - 120$	$60 - 80$	1-15	$0.6 - 3.0$	1-20	$2.6 - 5.5$

In [42] Aldosterone-to-renin ratio (ARR) was proposed as a novel diagnosis parameter in an attempt to design a reliable screening protocol and to reduce the number of undiagnosed PA cases. The ARR parameter is the ratio between the plasma aldosterone concentration (ng·dL^{-1}) and the level of renin activity (ng·mL^{-1}· h^{-1}) (PRA). According to these new criteria, in [42] 9 over 348 hypertensive patients showed values of ARR higher than 60, which is three times the upper normal value. Scintigraphy test confirmed the presence of APA for the selected patients. For all the other patients, ARR was within the baseline values and the diagnosis of essential hypertension was confirmed. It is worth noting that the level of potassium was within the normal values range in six of the nine patients affected by APA. The diagnosis criteria used in [42] showed accurate results in the screening of APA subtypes, while the performances in the screening of BIH subtype were untested. However, the study presented in [42] was the precursor of screening protocols currently adopted for PA diagnosing.

2.3.2 Novel diagnostic criteria

In the last two decades, progress in diagnosis criteria changed the assumed rate of PA cases over the hypertensive population, denying hypokalaemia as a *condicio sine qua non* for PA. Both clinical and biochemical parameters are currently evaluated in the screening procedures [6]. The main clinical and biochemical parameters and their values in normal conditions (baseline values) are reported in Table 2.1 [43], [44]. Firstly, clinical parameters including systolic and diastolic blood pressure (SBP and DBP) must be measured to verify the existing of hypertension. Then, biochemical parameters (PAC, PRA, ARR, bK) measure the levels in the blood of aldosterone released by the adrenal cortex, the level of activity of the renin and the concentration of potassium in the blood.

It is worth noting that in the current clinical protocol, the blood potassium concentration is evaluated alongside the other biochemical parameters.

The combined use of multiple biochemical tests led to an increase in the number of PA diagnosis by 500 –1500% [3]. However, the above-mentioned tests must not be intended as definitive diagnostic tools. The abnormal secretions of aldosterone hormone need further investigation. Thus, all the positive cases resulting from the testing of clinical and biochemical parameters should be followed by at least one of the following confirmatory tests: captopril test (CPT), saline- or fluticortisone-based suppression tests (SIT or FST), oral saline loading test (SLT) [3]. These tests are described in detail below.

Captopril test (CPT)− ARR itself is a biochemical parameter that could not lead a conclusive PA diagnosis. A number of false positive, linked to ARR could be due to the high levels of renin activity not related to PA condition [45]. In more recent clinical protocols, ARR is measured after the administration of a single captopril dose [46], [47]. In non-PA patients, captopril causes the inhibition of the conversion mechanism from Angiotensin I to Angiotensin II, thus a decrease in the release of the aldosterone hormone. In the presence of PA, the autonomous aldosterone production is not affected by the effects of the captopril administration. Thus, in patients affected by PA, high levels of ARR are persistent. This method allows a more reliable screening of PA patients, avoiding the misinterpretation of high levels of ARR due to low activity of renin unrelated to PA.

Suppression test (SIT, FST)− Suppression tests are generally adopted to confirm that high levels of PAC are linked to PA condition. It is worth noting that the release of the aldosterone in the blood induces the absorption of the sodium and water and the release of potassium. Hence, the main goal of these suppression tests is to evaluate if the release of high amounts of the aldosterone hormone persists even after the administration of sodium and water. Both sodium and water are administrated through the intravenous saline (saline infusion test -SIT) or fludrocortisone acetate infusion (fludrocortisone suppression test – FST). The SIT is based on the administration of 2L of 0.9% NaCl over 4h, whereas FST generally implies the administration of 0.1 mg fludrocortisone every 6h

[3]. Then, aldosterone levels are measured. If values of aldosterone concentration are approximately above 6 ng dl^{-1}, PA diagnosis is confirmed [6], [48], [49].

Saline loading test (SLT)− A further method to confirm PA diagnosis involves the evaluation of the levels of urinary aldosterone and sodium after three days of a high sodium diet. The test relies on administrating 12.8g NaCl per day [3]. PA is confirmed in the case of levels of aldosterone higher than 12μg/day and levels of sodium lower than 200 mmol/day [3]. As this test is based on the increase of dietary sodium, it is not recommended in cases of patients affected by severe hypertension [6], [8], [46], [49].

Once PA diagnosis is confirmed, a computer tomography (CT) scan is required to identify the PA subtype and to exclude the presence of adrenal carcinomas. CT-scans show accurate results in identifying solitary, unilateral, hypodense adenomas with a diameter larger than 1 cm and up to 2 cm. However, CT-scans have difficulties distinguishing between small unilateral adenomas (< 1 cm diameter) and hyperplasia. Therefore, an additional test is required to accurately differentiate unilateral from bilateral PA subtype. This is achieved using adrenal venous sampling (AVS).

AVS is the reference standard test to identify PA subtype. During AVS test, adrenal veins are catheterised and blood samples are collected from adrenal veins and inferior vena cava (IVC). Then, the aldosterone-cortisol concentration ratio is calculated for each blood sample. In the cases of autonomous aldosterone release involving one of the adrenal glands, blood samples from the adrenal veins typically show aldosterone-cortisol ratios four-folds higher than those collected from IVC [3]. In patients with BIH, the mean aldosterone-cortisol ratios are approximately three-folds higher compared to the aldosterone-cortisol concentration ratios of the blood samples acquired from the IVC.

The above-described gold standard procedures for the lateralisation of PA disease are not without limitations. CT-scan shows low-performances for adenomas less than 1 cm diameter. AVS is an invasive diagnostic test and a technically demanding procedure due to the catheterisation of the adrenal veins and of IVC. The potential of PET-CT-scan is currently under investigation to overcome such limitations. In [50] ^{11}C-metomidate as a PET radiotracer was used to selectively identify unilateral or bilateral nodularity. The
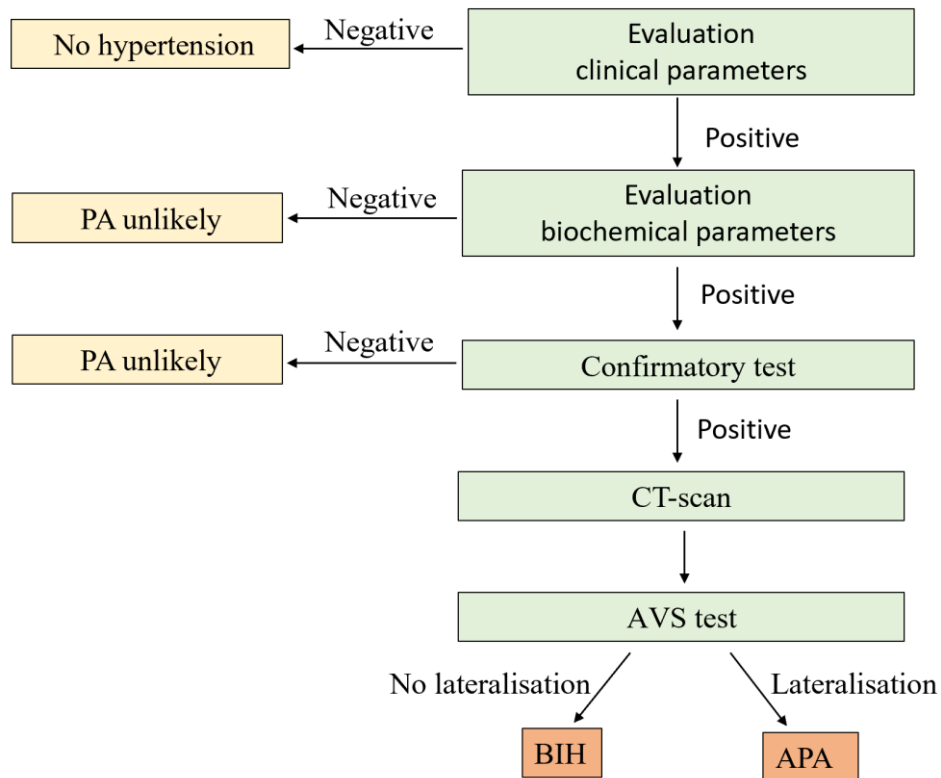
Figure 2 2: Main phases of the screening protocol for PA diagnosis: 1) Evaluation of the clinical parameters (SBP and DBP), 2) evaluation of the biochemical parameters (PAC, PRA, ARR, bK) in case of persistent hypertension, 3) test to confirm PA diagnosis (CPT, SIT, FST, SLT), 4) CT-scan to detect abnormalities in the adrenal glands, 5) Test to investigate the lateralisation (AVS test) of the abnormalities and reveal PA subtype.

procedure is based on the intravenous injection of ^{11}C-metomidate while the PET camera is centred to focus the adrenal mass via CT guidance. The main property of the ^{11}C-metomidate is to inhibit the enzymes (CYP11B2 and CYP11B1) responsible for the synthesis of aldosterone and cortisol in the adrenal cortex. Thus, an increase in the uptake of ^{11}C-metomidate from the adrenal glands can be observed during the PET-CT scan, in the presence of unilateral or bilateral functional nodularity. The ^{11}C-metomidate PET-CT showed promising results in the lateralisation of PA [51]–[53], however further investigations must be conducted in order to determine the specificity and sensitivity of the test and to evaluate the radioactivity concentrations in other organs.

To summarise, the clinical protocol for PA diagnosis recommended by the Endocrine Society [47] is schematised in Figure 2.2.

To complete the discussion about diagnosis strategies, data across 14 studies published in the last two decades were summarised in Table 2.2. In order to highlight the impact of the new strategies of screening on the rate of PA diagnosis, studies reporting at least one biochemical parameter, one confirmatory and the lateralisation test (AVS and/or CT-scan) were selected. Table 2.2 includes the name of the author and the country where the study was conducted, the type of study (i.e. retrospective or prospective) and the size of the sample. The same table lists the biochemical parameters examined in each study and the confirmatory test adopted. Ultimately, the percentage incidences of PA and of the subtype (i.e. APA or BIH) are reported. According to the results of the reported survey, the range of PA incidence ranges from 4.6% to 34.8%, with a median of 11.2%. The CT-scan and the AVS tests confirmed a prevalence of the APA and BIH subtypes ranging from 9.1 % to 50 % and from 22.2 % to 88.9 %, respectively.

The outcome of the review highlights the controversial consensus around the protocol adopted for PA diagnosis. The data gathered in Table 2.2 show non-uniform cut-off values for the biochemical parameters. In the case of ARR parameter, the threshold value to establish the positive patients ranges from 50 $ng \cdot dL^{-1} \cdot ng^{-1} \cdot mL \cdot h$ reported in [54] to 20 $ng \cdot dL^{-1} \cdot ng^{-1} \cdot mL \cdot h$ reported in [55]–[58]. For the PAC parameter, the cut-off values vary between 6 $ng \cdot dL^{-1}$ indicated in [57] and 16 $ng \cdot dL^{-1}$ reported in [59]. With reference to PRA, the upper limit value ranges between 0.3 $ng \cdot mL^{-1} \cdot h^{-1}$ reported in [56] [55] and 2 $ng \cdot mL^{-1} \cdot h^{-1}$ assumed by [57], [58]. An additional discrepancy includes the type and number of confirmatory tests adopted. According to the data reported in Table 2.2, SIT and SLT are the confirmatory tests widely used. A combination of two confirmatory tests is adopted in [28], [57], [58], while most of the studies use one confirmatory test for PA diagnosis. Absence of agreement is also visible around the procedures for PA lateralisation. The protocol (Figure 2.2) suggests an AVS test following the CT-scan to determine the PA subtype. However only one of the two procedures was adopted in four out of 14 studies reported in Table 2.2. Specifically, in [57] and [58] only AVS was conducted to establish the lateralisation. In [59] and [55] only CT-scan was executed.

This review of the progresses in the diagnostic criteria highlights the change over the last two decades in the prevalence of PA cases within the hypertensive population. The lack

of appropriate screening parameters leaves PA to be considered as a "needle in a haystack", thus PA remained considerably underdiagnosed [28], [60]. Progress in the clinical protocol led to an increase of approximately ten-fold the number of PA patients. However, further efforts are still required to overcome the existing inconsistency in the clinical protocols and diagnosis criteria adopted by different clinical centres (Table 2.2). A prompt diagnosis of PA followed by an identification of the subtype would help to identify a suitable cure and to avoid harmful effects, such as cardiometabolic injuries [28], [47], [61] [62]

Table 2.2:Summary of the main characteristics of the 14 studies included in the survey for the assessment of PA prevalence. Name and type of the studies (R: retrospective, P: prospective), size of the cohorts of hypertensive patients, values of the biochemical parameters measured, type of confirmatory test, percentage of PA cases and incidence of the PA subtypes (APA and BIH) are listed.

#	Study	Study type	# Hypertensive patients	Diagnosis approach				Confirmatory test	Subtype distinguishing test	PA prevalence (%)	PA subtype	
				Biochemical parameters cut-off values							APA (%)	BIH (%)
				PAC ($ng \cdot dL^{-1}$)	PRA ($ng \cdot mL^{-1} \cdot h^{-1}$)	ARR ($ng \cdot dL^{-1} \cdot ng^{-1} \cdot mL \cdot h$)	bK ($mmol \cdot L^{-1}$)					
1	[56] (Singapore)	R	350	> 15	< 0.3	> 20	< 3.5	SIT	CT-scan + AVS	28.6	50.0	NA
2	[59] (Chile)	P	609	> 16	< 1	> 25	< 3.5	FST	CT-scan	6.1	5.4	18.9
3	[54] (Czech Republic)	P	402	> 15	≤ 0.7	≥ 50	< 3.5	SIT	CT-scan + AVS	19.0	36.0	42.0
4	[55] (Minnesota, USA)	R	1112	> 15	NA	> 20	NA	SLT	CT-scan + AVS	10.8	28.0	72.0
5	[55] (Italy)	R	7343	> 15	≤ 0.1	≥ 40	NA	SIT	CT-scan + AVS	8.0	30.0	70.0
6	[55] (Singapore)	R	3850	> 15	< 0.7	≥ 20	NA	SLT	CT-scan + AVS	4.6	50.0	50.0
7	[55] (Chile)	R	914	> 10	< 0.3	> 25	NA	FST	CT-scan	7.2	9.1	88.9

8	[46] (Italy)	P	1125	NA	≤ 0.2	> 40	< 2.2	SIT+CPT	CT-scan + AVS	11.2	42.8	57.2
9	[63] (Georgia, USA)	P	100	> 15	< 0.1	> 30	< 3.5	SLT	NA	14.0	NA	NA
10	[64] (Italy)	P	254	> 15	< 0.2	> 40	< 4	SIT	CT-scan or AVS	7.1	27.8	72.2
11	[57] (Japan)	R	155	> 6	≤ 2	> 20	NA	SIT+CPT	AVS	29.1	31.1	68.9
12	[58] (Australia)	P	66	> 10	< 2	> 20	< 4	SIT + FST	AVS	34.8	34.8	47.8
13	[65] (Italy)	P	100	≥10	< 1	> 30	< 3.6	SIT	CT-scan + AVS	25.0	20.0	60.0
14	[48] (China)	P	531	> 10	NA	> 30	< 3.8	SIT	CT-scan + AVS	25.2	48.1	22.2

2.4 Established Treatments for Primary Aldosteronism

A range of existing treatments will be described in the following of the section. Based on the Endocrine Society guidelines, APA is generally treated via unilateral laparoscopic adrenalectomy, whereas the BIH is managed through pharmacotherapy based on the administration of mineralcorticoids receptors antagonists (MRAs) [47].

2.4.1 Laparoscopic Adrenalectomy

Laparoscopic adrenalectomy (LA) is the treatment method generally adopted for APA or unilateral hyperplasia [47],[66],[67]. The technique requires resection of the entire gland to ensure the complete removal of the adenoma.

Retroperitoneal access is the preferred surgical approach both for the right and left adrenalectomy. In order to finalise the resection of the gland, several small branches of the adrenal artery are removed [68]. Although the rate of mortality due to LA is less than 1%, post- and peri-operative complications are reported in different studies [69]–[72]. Firstly, the complete resection of the gland can induce adrenal insufficiencies and a consequent risk of developing a adrenal crisis. In these cases, a supplement therapy of steroid hormone is required [73]. Bleeding accounts for up to 40% of total complications, because of the extensive blood vessels network supplying the adrenal glands [69]. Further common complications include possible injuries to the surrounding vasculature, bowel, liver, spleen, pancreas and pleura [74], [75].

2.4.2 Mineralocorticoid receptor antagonists

The biological mechanism of the mineralocorticoids receptor antagonists (MRAs) is to block the abnormal activity of the aldosterone. The most commonly available options are the spironolactone and the eplerenone [76]–[78]. Spironolactone is a pharmacological treatment typically adopted in the presence of bilateral hyperplasia (BIH). Side-effects are observed following the administration of the spironolactone, such as gynecomastia in men and menstrual dysfunctions in women. Eplerenone is a relatively new pharmacotherapy. It was observed that eplerenone improved the patient's tolerability because of the reduced number of endocrine side-effects compared with spironolactone. However, different studies showed better results in the management of the hypertension

by the administration of spironolactone compared with eplerenone [77], [79]. As a result, the Endocrine Society recommends spironolactone as primary treatment for BIH [47].

2.5 Emerging treatment modalities for Primary Aldosteronism

The limitations observed for both adrenalectomy and MRAs pharmacotherapy suggest that new therapeutic strategies should be investigated for the treatment of PA. Alternative therapeutic techniques are required in the following cases:

- Unsatisfying results from the adrenalectomy and impossibility of administrating a life-long pharmacotherapy;

- Patients affected by bilateral PA condition showing poor tolerance to the effects induced by the administration of MRAs;

- Refusal of a surgical procedure;

- Both the surgical approach and the pharmacotherapy show no substantial improvements;

- Existing multiple comorbidities such as cardiovascular diseases, renal failure, or cerebral infarctions.

Ablation techniques could be a promising alternative to the traditional therapeutic solutions for PA and could enable the treatment of a larger number of patients. To date, ablation techniques including chemical ablation, cryoablation, radiofrequency ablation (RFA) and microwave ablation (MWA) are routinely adopted in the clinical practice for the treatments of different types of tumours, such as liver lesions, renal carcinoma and gastro-intestinal tumours [10], [80], [81]. Currently, ablation techniques are under investigation in order to extend their applications to other target such as lung and breast lesions, adrenal metastasis, adrenal adenomas and thyroids tumours [19], [82]–[85].

In this section, the abovementioned ablation techniques are introduced. The state of the art of each technique is briefly discussed, together with the potential application for the treatment of Primary Aldosteronism.

2.5.1 Chemical Ablation

Chemical ablation is performed through the direct injection of ethanol or acetic acid into the tumour. The biological mechanism inducing cell death involves the dehydration of the cytoplasm and the consequent necrosis of tumour cells [86]. The chemical agents induce the necrosis of endothelial cells and the consequent thrombosis of the vasculature system surrounding the tumour tissue [22], [87]. The equipment includes a syringe typically containing a solution of 95% ethanol or 50% acetic acid. The chemical agent flows through the connecting tubing from the syringe to the tip of a needle used for the direct injection into the tissue target. In clinical practice, the treatment is performed under ultrasound (US) guidance [80].

In the cases of lesions characterised by a high degree of vascularisation (such as hepatic malignancies), the de-vascularisation of the tumour through chemoembolisation represents an effective option to induce the ischemic necrosis of tumours [84], [87]. The embolisation is performed by injecting chemotherapeutic drugs and embolic agents directly into the main artery feeding the tumour. Chemical ablation is mainly used in the treatment of masses localised in the gastrointestinal tract, such as hepatocellular carcinomas [88], [89].

Nowadays, chemical ablation and chemoembolisation are mostly adopted as adjuvant of the thermal ablation techniques [90]–[94]. In recent years, chemoembolisation followed by thermal ablation has been widely applied to increase the necrotic effect of the thermal procedure by lessening the blood flow of the vasculature system surrounding the tumour [94].

Concerning the application of chemical ablation to the treatment of adrenal neoplasms, the first application of the ethanol-injection procedure in a patient affected by APA was presented in [34]. After one month follow up, the levels of the aldosterone (PAC) and the renin activity (PRA) in the blood were normalised, however the patient remained hypertensive. The normalisation of the biochemical parameters was obtained also in [95], where a single patient affected by unilateral adrenal adenoma (APA) was treated by CT-guided acetic acid-injection. The same procedure was performed in [96] in a cohort of ten patients affected by unilateral adrenal tumours; normalisation of the blood pressure

was found in seven of the ten patients. In [97], normal levels of blood pressure, potassium and aldosterone-to-renin ratio (ARR) were achieved after a second ethanol-injection procedure performed four years after the first one. In [98], normal levels of aldosterone and blood potassium were achieved one week after the acetic acid injection, whereas the blood pressure values decreased gradually up to the normal levels one month after the chemical ablation.

The performances of chemoembolisation for the treatment of PA were investigated only in two studies. In [99], ten patients affected by unilateral PA (APA) were treated through the injection of absolute ethanol to embolise the adrenal artery feeding the adrenocortical adenomas. A further clinical study on thirty-three patients was performed in [100] to treat unilateral adreno-cortical adenomas through the chemoembolisation of the adrenal artery. Both [99] and [100] showed normalisation of biochemical parameters and blood pressure levels after the procedure and during the follow-up period. In conclusion, the successful response ranged from a minimum of 30% in [99] to a maximum of 82% in [100].

Although the above-mentioned studies showed promising results, some concerns remain related to the use of the chemical ablation or chemoembolisation procedures in the cases of adrenocortical adenomas. In the cases where more than one injection is required to completely cover the target through the fluid, the risk to damage surrounding sensitive structures should be considered [95], [96]. Then, as the procedure is stopped, the injected fluid could leak outside the tumour and the downward diffusion of the acetic acid or ethanol could damage the kidneys [98]. Finally, the penetration of the tumour through the needle could increase the risk of pneumothorax when the lower edge of the lungs extends to the adrenal glands [95], [96].

2.5.2 Cryoablation

Cryoablation is an ablation method which uses subfreezing temperatures to induce the death of tumour cells. Those temperatures are delivered through the circulation of a cryogen gas within a cryoprobe that is then inserted in the tissue target. Irreversible tissue damage occurs at temperatures below -20°C. Current cryoablation systems use the combination of the compression and expansion of a specific gas (Joule-Thomson effect)

to reach temperature in the range of -20 − -40°C [80]. Nitrous oxide or argon gases are the cryoagents commonly used.

The freezing phase is the first phase of the procedure and it is followed by a thaw phase. Depending on the tumour size, one or multiple probes are placed in the middle of the lesion, with the tip touching the distal edge of the tumour. During the freezing phase, pressurised argon is pumped in the chamber placed at the distal end of the probe. Because of the gas expansion, the local temperature drops to -160 °C. An ice ball is created around the tip of the probe during the freeze phase of the treatment (generally 5-15 min duration) that causes the decrease of temperature in the surrounding tissue. In the following phase, the flow of the cryogen gas (e.g. argon) is interrupted and the frozen mass is allowed to thaw passively [80], [87], [101]. When the procedure is completed, the cryoprobe is heated and removed.

Cryoablation is used in the treatment of thoracic and abdominal masses such as lung tumours, endobronchial neoplasms, liver and kidney tumours. Contrary to hyperthermic thermal ablation techniques (described below), cryoablation can prevent irreversible damages to the pleura and the perforation of the organ [102], [103]. Few studies reported cryoablation as a potentially effective method for the treatments of adrenal functional neoplasms [104], [105]. In [104] a retrospective study was conducted on eleven patients to evaluate the clinical effectiveness of CT-guided cryoablation in the treatment of adreno-cortical adenomas. The complete normalisation of the biochemical parameters and blood pressure levels were achieved in all the patients treated. However, the study presented in [104] is the only study available where the performances of cryoablation were clinically explored. Because of the retrospective nature of the study and the lack of further available data, the feasibility of cryoablation for the treatment of adrenal adenomas cannot be confirmed. The main limitation of the technique relates to the thermal gradient between the cryoprobe surface and the distal zone of the freeze temperature. Commonly two freeze-thaw cycles are applied to mitigate the inhomogeneities in the temperature distribution in the target tissue. Thus, the procedure could cause excessive thermal stress in the cases of functional tissues such as in adrenal

glands. A further concern linked to cryoablation is the risk of "cryoshock" responsible for intravascular coagulation [106], [107].

2.5.3 Hyperthermic ablation techniques

The main goal of hyperthermic ablation techniques is to destroy the tumour cells by inducing a high temperature in the tumour [80]. The heating of the tissue target causes cell death by thermal coagulation necrosis [10], [80], [108]. The volume of the heating induced by hyperthermic ablation techniques depends on the distribution of temperature within the tissue. When the temperature is increased up to 46°C for approximately 60 minutes, irreversible damages of the cells occur. A further increase in temperature, even by a small degree, can shortens the time for cell death from 60 minutes to $4 - 5$ minutes. Between $50 - 100$°C, instantaneous coagulation necrosis occurs, which involves irreversible denaturation of the proteins and of cytoplasmatic and mitochondrial enzymes that are crucial for the DNA duplication [10], [80], [81]. Temperatures above approximately 110°C result in tissue carbonisation. A tumour is successfully treated when the entire lesion uniformly achieves cytotoxic temperatures (i.e. above 50°C).

The increase in temperature of the tissue is obtained through the interaction of an external source with the biological tissue. Electromagnetic (radiofrequency and microwave ablation), optic (laser ablation) and acoustic (ultrasound ablation) sources are typically adopted [109].

Electromagnetic based hyperthermic ablation techniques induce the temperature increase in the tissue. Specifically, the ionic conduction in the radiofrequency range $(100 - 500$ kHz) is the biophysical mechanism underlying the radiofrequency ablation (RFA). The polarisation and/or vibration of molecular dipoles in the microwave frequency range $(500$ MHz $- 10$ GHz) is the biophysical mechanism of the microwave ablation (MWA).

Radiofrequency ablation. During radiofrequency ablation (RFA), a needle-shaped electrode is placed into the tumour via CT, US or MRI-guidance. The RF electrode is a metal shaft completely insulated (with the exception of the exposed tip). In a monopolar system, an active electrode is placed directly inside the tumour and a ground pad is placed on the patient's skin. In a bipolar system, a passive electrode is generally placed in proximity of the active one. A RF generator is used to supply RF power to the active

electrode inserted in the tissue. The RF generator provides an alternating differential voltage between the two electrodes. A fixed frequency is selected in a range of 450 kHz − 500 kHz [110]. When the generator is switched on, the electric charge is transferred from the electrons inside the electrodes to the ions in the biological tissues. Thus, electric current flows from the active electrode to the passive electrode or to the ground pad through the tissue [80].

Essentially, the heating is produced by Joule effect caused by the resistive energy loss associated to ionic current into the biological tissues [10], [108]. Most of the heating occurs in the area of the tissues with the highest current density, while the peripheral part of the thermal lesion is caused by heat conduction [111]. The size and the shape of the ablation zone achievable by RFA depend on the characteristics of the tissue such as electrical conductivity, thermal conductivity, heat specific capacity and the degree of blood perfusion of the tissue [110]–[112]. In particular, the RFA procedure is highly affected by the impedance of the tissue. Indeed, the impedance of the tissue increases with a rise of temperature, inducing the risk of incomplete thermal coverage [112]–[114]. In addition, RFA is sensitive to the blood perfusion and the related risk of heat sink effect which also may contribute to suboptimal thermal coverage [115]. Strategies including the optimisation of the electrode design were developed to improve the energy deposition in the target tissue. Concerning the electrode design, multiprobe arrays were developed to increase the area of the coagulation zone in the case of larger tumours (up to 5 cm) [80]. Internally cooled electrodes also were designed to minimise the tissue charring around the electrode [116], [117] and bipolar systems were adopted in order to create more focal ablation zones in the tissue target. Combined with the optimisation of the electrode design, the optimisation of the clinical protocol helps to overcome the dehydration of the tissue and extend the coagulation area. One of the most used clinical protocol for RFA procedures is the impedance-controlled pulsing protocol. This protocol prevents the excessive increase in the electrical impedance by alternating periods of low current to periods of peak currents. Generally, the RF generator is switched off when the impedance exceeds 20 – 30 Ω [110], [114], [118].

Nowadays, RFA is adopted in clinical practice primarily for the treatment of cardiac arrhythmias, liver malignancies such as hepatocellular carcinoma (HCC) and hepatic metastases that cannot be treated surgically [119]–[122]. Other RFA applications include the treatment of gastrointestinal carcinomas, colorectal metastases, osteoid osteomas, metastatic bony lesions, and renal tumours [123]–[125].

Recently, RFA is under investigation for the treatment of adrenocortical neoplasms responsible for PA. In the case of patients not eligible both for pharmacotherapy and adrenalectomy, different studies suggested RFA as alternative therapeutic technique. The treatment is generally performed under CT- or laparoscopic US-guidance, after the evaluation of the clinical and the chemical parameters and the confirming test to evaluate the lateralisation of the disease. Based on the results reported in [126]–[131], RFA supports the successful treatment of functional APAs. In these studies, the outcomes of the procedure were evaluated through the investigation of the blood pressure levels, the biochemical parameters and the CT-scan of the adrenal gland, during each follow-up. In the most recent study [127], a long-term follow-up (6 ± 2 years) confirmed hypertension improvements in more than 50% patients. However, the studies reporting the success of the RFA application are limited to unilateral PA. The performances of RFA for the treatment of bilateral PA subtype are unclear, as no study about the application of RFA on bilateral functional adrenal masses has been performed so far.

Microwave ablation. Microwave thermal ablation (MWA) exploits the electromagnetic field radiated from an antenna to induce high (above 50˚C) and localised temperature increases in diseased tissues [10], [80], [81]. Because of the applied alternating electric field, the dipolar water molecules attempt to align with the electric field. The continuous rotations of the dipoles and the collisions between adjacent molecules cause the loss of energy that is converted in heat. The ability of the electromagnetic field to propagate in low water-content tissues (e.g. bone, lung) as well as in high water-content tissues (e.g. liver, kidney) allows for ablation zones up to 50 mm in diameter. As a result, MWA is less susceptible to the characteristics of the tissue compared with RFA. MWA procedures show better performances in tissues characterised by a high degree of vascularisation in comparison with RFA. In particular, microwaves are able to overcome the convective

cooling effect due to blood flow which counters with the heat generation due to the ablation procedure [132]. The energy from the MW generator is delivered to the antenna through coaxial cables. Overheating of the cable and a risk of unintended injuries to the tissue is minimised by adding a cooling jacket around the applicator [80], [133].

A clinical MWA setup typically includes a power generator, a coaxial cable terminated by a MW antenna and a cooling system. Omnidirectional antennas such as dipoles or monopoles are widely adopted for MWA procedures. These antennas can be miniaturised by using thin coaxial cables which are easily introduced in the targeted area through biopsy needles. The diameter of the feeding coaxial cables typically ranges from 11 gauge (2.5 mm) to 17 gauge (1.2 mm).

The MWA devices currently available include antennas optimised to operate at 2.45 GHz or 915 MHz. Such devices include HS Medical Amica^{TM} (HS Hospital Service, Rome, Italy), Emprint^{TM} (Medtronic, MN, USA), Ethicon NeuWave^{TM} (Johnson & Johnson, WI, USA), Acculis (AngioDynamics, NY, USA) and the Solero (AngioDynamics, NY, USA), the MicrothermX^{TM} (Varian Medical Systems Inc., CA, USA), MedWaves AveCure^{TM} (San Diego, CA, USA) [81]. MW applicators operating at higher frequencies (e.g. 5.8 GHz) are currently being researched. Recent studies showed that frequencies as high as 5.8 GHz are able to create more spherical ablation zones in a shorter time compared with the operating frequencies traditionally adopted [134], [135].

One of the parameters to be considered for the design of the MW applicators is the reflection coefficient. The reflection coefficient indicates the amount of power transmitted in the tissue target by the antenna with respect to the power delivered by the MW generator. The mismatch between the characteristic impedance of the coaxial cable and the impedance of the antenna causes the electromagnetic field to be partially reflected along the feeding coaxial cable. Thus, the length of the radiating element of the antenna should be optimised in order to have the minimum value (i.e. lower than 10 dB) of the reflected power at the operating frequency. The length of the radiating element also influences the length of the ablation zone and the sphericity index of the coagulation area. Further parameters that should be optimised when treatment planning include the position of the applicator inside the tumour, the power to be radiated by the antenna and

the time of irradiation. Power and time settings greatly influence the performances of the MWA procedure. Generally, the largest ablation zones are reached when delivering into the tissue high levels of input power (> 80 W) for relatively short time (< 3 min). These settings are able to overcome the heat-sink effect more effectively due to the blood perfusion. When high levels of power are maintained for longer time, the sphericity of the ablation zone degrades, because of the rapid increase of the ablation zone along the longitudinal dimension [109], [136], [137]. In addition, the boiling and carbonisation of the tissue may affect the operating conditions of the procedure. For example, the excessive dehydration of the tissue could induce the detuning of the antenna, which is a potential risk for the integrity of the MW applicator. On the other hand, excessively low input power levels (< 30 W) are unable to generate heating fast enough to overcome the effect of the blood perfusion [138]–[140].

The clinical practice currently used consists of positioning the MW applicator in the centre of the tumour, through image-guided procedures. The imaging guidance techniques include computer tomography (CT), ultrasound (US) or magnetic resonance imaging (MRI). One or more of the aforementioned imaging techniques are adopted at the different stages of the procedure. The stages of the clinical procedure include:

- Visualisation of the size and the position of the tumour;

- Proper placement of the MW applicator into the target tissue, avoiding surrounding sensitive structures;

- Real-time monitoring of the growth of the ablation zone during the treatment;

- Evaluation of the result of the procedure immediately after the procedure and during the follow-up periods.

US is generally used to introduce the ablation applicator in the target region, while it shows low performances for the real-time evaluation of the ablation areas. The hyper-echogenicity of the microbubbles arising during the ablation procedure impedes a clear visualisation of the applicator and the treated area. MRI is the most accurate technique to localise the position of the tumour and to visualise the coagulation effects after the procedure. The main limitations of MRI are the high cost and the low compatibility with

most commonly available MW applicators. Thus, CT is generally adopted for the real-time monitoring of the growth of the ablation zone during the procedure.

The real-time monitoring of the temperature is a further aspect of the microwave thermal ablation treatment that must be taken into account. The continuous measurement of the temperature during the procedure is crucial to ensure the thermal coverage of the tumour areas and to minimise the risk of thermal damage to critical structures such as blood vessels. To date, the temperature during MWA procedures can be monitored through single or multi-sensor probes including thermocouples or fiber optic sensors. The major limitations of these measurement techniques are the necessity of penetrating the tissue, and the ability to provide temperature readings only in a single point. Magnetic resonance thermometry (MRT) is a non-invasive temperature monitoring technique which provides 3D temperature maps. However, the main source of errors in temperature measurements through MRT is linked to the magnetic susceptibility of the applicator and the background noise.

All the factors of influence described so far must be considered in the treatment planning. MWA treatment planning workflow generally consists of:

- Development of the numerical models reproducing the target anatomical region to evaluate the distributions of the specific absorption rate (SAR) and the temperature;

- Numerical simulations aiming to optimise of the antenna design according to the operating frequency, the power to be delivered into the tissue and the duration of the treatment;

- Monitoring of the of the MW ablation procedure to ensure the quality of the treatment and the appropriate delivery of the thermal dose.

The distributions of SAR and temperature are influenced by the geometry and characteristics of the tissue target, such as thermal and dielectric properties [141]–[145]. Accurate knowledge of the tissue properties is required for reliable predictions of SAR and temperature distributions. Moreover, the changes in the blood perfusion occurring during the MW heating is a further component which should be characterised, since it influences the extent of the ablation areas especially for targets with an high degree of

vascularisation or in proximity to blood vessels (e.g. hepatic artery, inferior vena cava, portal vein) [146]–[148].

MWA is in routine clinical use for a number of tumours such as hepatocellular (HCC) carcinoma, lung tumours, renal cell carcinoma, liver and adrenal metastases. In the clinical practice, MWA showed effectiveness ($> 90\%$), safety ($> 95\%$) and survival rate ($> 60\%$) for the treatment of HCC, hepatic metastatic diseases and liver metastasis of gastric cancer [122], [149]–[151]. Technical success ($> 90\%$) and high survival rates ($> 80\%$) have also been demonstrated in the treatment of renal cell carcinoma [16], [152]. MWA also reported promising results in the treatment of lung tumours and in the local tumour control of colorectal lung metastases [82], [153]. Recently, MWA is being investigated for the treatment of osteoid osteomas [154], [155], pancreatic tumours [156], [157], parathyroid glands [158], [159] and adrenal metastases [84], [160].

Successful performances for the MWA treatment of adreno-cortical neoplasms were observed in a single-centre experience reported in [19]. However, no further investigations have been conducted to prove the effectiveness of MWA for other adreno-cortical pathologies, included PA.
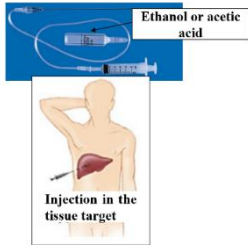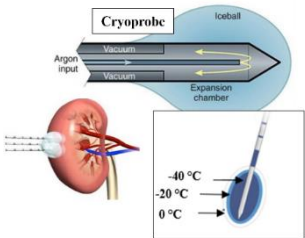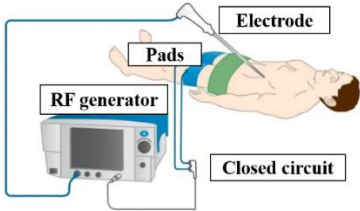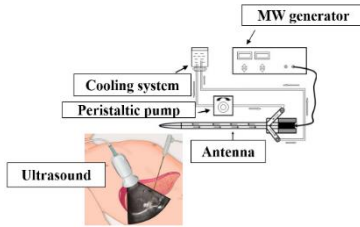
Table 2.3 provides a schematic summary of the relatively new therapeutic techniques for tumour treatment that are reviewed in this chapter, and evaluated in the context of treatment of PA. The main characteristics of the experimental setup are schematised for each ablation technique. The fundamental cause-effect mechanism of each technique, as well as the main application pitfalls are highlighted. In addition, the table includes the number of available studies showing the performances of one of the emerging techniques employed for PA treatment. Only the studies reporting the results of biochemical and/or clinical parameters before and after the treatment were included in the table.

A detailed analysis of the results across the available studies is provided in Appendix A. This review provides a better understanding of the performances of ablation techniques in the management of PA [19], [99], [104], [126]–[131] compared to the established treatment approaches [72], [129], [131], [161]–[168]

35

Following the comparative evaluation of the ablation techniques reviewed in this study (see Appendix A), MWA is selected for an in-depth analysis conducted in the thesis. The evaluation was based on key factors arising from the review:

- The therapeutic effect of MWA is based on the interaction between the electromagnetic field and dielectric properties of the tissue. Thus, the dielectric characteristic of the target area may offer an alternative tool to locally shape the profile of the ablation zone;

- Compared with other ablation techniques (e.g. RFA), the time required to achieve the therapeutic effect in the tissue target is lower with MWA. Lower treatment time helps to minimise the treatment-related distress of the patient;

- MWA is able to overcome the 'heat-sink' effect more effectively than RFA. This characteristic is particularly important for tissues highly vascularised, as for adrenal glands;

- Risks such as "cryoshock" responsible for multiorgan failure and disseminated intravascular coagulation observed in the cryoablation or intoxications due to acetic acid or ethanol used in chemical ablation are absent in the case of MWA;

- Laser ablation and ultrasound ablation have not been included in the comparative study due to lack of technical success reported in literature [169], [170].

Table 2.3: Summary of the emerging therapeutic technique for tumours treatment in terms of cause-effect mechanism, tissue targets generally treated, challenges in the application of each technique, number of available studies showing the performances regarding PA treatment.

	Chemical Ablation	Cryoablation	Radiofrequency ablation	Microwave ablation
Cause-effect mechanism	Acid or ethanol injection – dehydration of the cytoplasm and coagulation necrosis.	Gas expansion or compression – lethal subfreezing temperatures (-40 − -20°C).	Electric current – heating (above 50 °C) due to ionic conduction in the tissue target.	Electromagnetic field – heating (above 50°C) due to rotations, vibrations and collisions of water dipoles of the tissue.
Main targets	Hepatocellular carcinoma.	Hepatic tumours, colorectal metastases, lung tumours and renal cancers.	Hepatic tumours, gastrointestinal carcinomas, colorectal metastases, and renal tumours.	Hepatic tumours, lung tumours, renal cell carcinomas, thyroid tumours, breast lesions; pancreatic tumours.
Application challenges	Poor and uneven diffusion of injected drugs over the tumour; Intoxication due to diffusion of the acetic acid or ethanol through the surrounding tissues.	Inhomogeneous temperature distribution. Cryoshock causing multiorgan failure and disseminated intravascular coagulation.	Increase of circuit impedance with the increase of temperature; Difficulty to cover large tumour volume; Susceptibility to heat sink due to perfusion.	Higher risks of unintended injuries to surrounding tissues; Antennas prone to heating when higher levels of power are carried; Cumbersome applicator designs (especially compared to the simple electrodes used in RFA).
No. of available studies for PA management	1	1	6	1

2.6 Conclusions

In this chapter, the biological principles of Primary Aldosteronism (PA) responsible for secondary hypertension are presented with a focus on the two most common PA subtypes: aldosterone-producing adenoma (APA) and bilateral idiopathic hyperplasia (BIH). The chapter also discusses the state-of-the-art for the treatment of unilateral and bilateral PA, and the most recent developments in the minimally invasive treatment.

The review conducted in the chapter highlights:

- PA is the prevalent cause of secondary hypertension. Beside hypertension, PA is responsible for further medical conditions such as hypokalaemia, ventricular hypertrophy and cerebrovascular ischemia. Some of these conditions may represent life-threatening conditions. Existing treatment approaches (including surgical resections and medication treatments) show limitations that need to be addressed. Surgical resection is suitable only in the case of unilateral PA and only in patients not affected by other diseases. Treatments based on mineralocorticoid antagonists are generally administrated in the cases of bilateral PA. Pharmacotherapy helps to better manage the disease but does not solve the original condition. Thus, alternative and minimally invasive approaches should be investigated for PA treatment;

- Ablation techniques may represent a good alternative to the traditional techniques currently adopted for the management of PA. In particular, these new clinical approaches may help to overcome the limitations that adrenalectomy or the pharmacotherapy involve. Among the ablation techniques reviewed, MWA has the potential to address the limitations observed in standard techniques. For example, MWA may be applied both in the case of unilateral and bilateral PA. In addition, MWA is a valuable treatment strategy in the case of patients who poorly tolerate pharmacotherapy and/or are not candidate for surgical procedure. Compared with other ablation techniques, MWA is minimally invasive, relatively fast and effective also in the case of highly vascularised tissues. Ultimately, the effect induced by MWA relies on the dielectric characteristics of the tissue. It is worth noting that the structure of the adrenal gland is composed of two functional tissues (cortex and medulla) surrounded by a fat capsule. Different tissues present different behaviours to the microwaves depending on their dielectric properties. Thus, the dielectric

38

characteristics of the adrenal tissues and the fat capsule will be explored in the context of MWA in order to improve the effectiveness and reduce the invasiveness of the procedure.
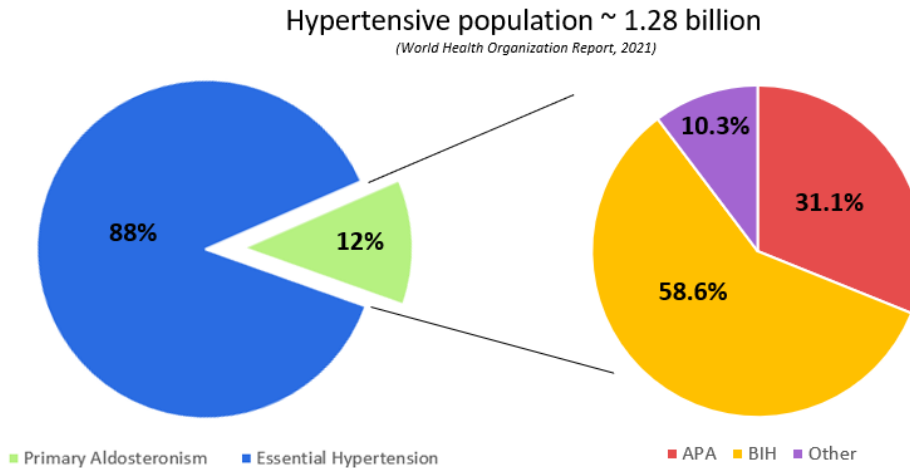
Figure 2.3: PA prevalence of 12% of the total population; within this, 31.1% has APA diagnosis, 58.6% has BIH diagnosis and 10.3% has an undetermined diagnosis.

Figure 2.3 highlights the size of PA population and the prevalence of PA subtypes, according to the data reported by World Health Organisation in 2021 and the results of the research studies gathered in Table 2.2. To summarise, approximately 48 million patients who are diagnosed with APA may benefit from ablation therapies. It should be mentioned that refining the ablation approach, as proposed in this thesis, the size of target population may increase to approximately 130 million patients.

The review presented in this chapter informs the remainder of this thesis. The next chapters will evaluate the effect of the dielectric contrast between the adrenal glands and their surrounding fat capsule on the shaping of the ablation patterns. The purpose is to investigate whether the dielectric contrast can maximise the therapeutic ablation effect into the tissue target, minimising the heating of the surrounding tissues. To help address the main research objective of this thesis, the dielectric properties of *ex vivo* adrenal glands were measured over the frequency range of microwave ablation applications. The dielectric characterisation of the adrenal gland and the rationale for choosing adrenal models are presented in Chapter 3. The chapter also describes the dielectric properties measured *ex vivo* on human adrenal glands affected by different types of diseases, including unilateral PA.

Chapter 3
Dielectric properties of the adrenal gland

3.1 Introduction

Chapter 2 described the key role of the aldosterone hormone in the regulation of blood pressure both where adrenal glands are in a normal condition and in the case of PA disease. The gold standard techniques (LA and MRAs) for the management of PA were described in relation to the PA subtype. The limitations observed for each technique opened a discussion for new strategies in PA treatment, especially in the cases of patients who are not surgical candidates. The state-of-the art in emerging ablation technique was reviewed in order to propose a potential solution to treat PA and the related hypertension using a minimally invasive approach suitable for a large cohort of PA patients. A particular focus was given to MWA, because of some theoretical advantages compared to the other technologies, such as the relatively short procedure and the minimal susceptibility to the heat sink effect due to blood vessels.

In this thesis, MWA is investigated with the aim of exploiting the dielectric composition of the tissues to selectively treat the target region while sparing adjacent structures. Thus, accurate knowledge of the dielectric properties of the tissues is essential in the design and optimisation of microwave hyperthermic techniques. Numerical models based on the dielectric properties of the anatomical target area are required during the planning phase. Numerical simulations are adopted to predict the distribution of the absorbed electromagnetic power and the consequent increase of temperature.

Animal models are widely adopted to conduct preclinical studies aiming to validate the numerical investigations. Therefore, numerical studies should be conducted using models with accurate dielectric properties of tissue which are able to represent an experimental scenario. With reference to the adrenal glands, multiple studies showed similar biological mechanisms in the release of hormones such as steroids and mineralocorticoids between human and ovine adrenal glands [171]–[173]. Ovine adrenal gland models are also adopted in endocrinology to study the disorders in the biosynthesis of hormones such as aldosterone, or the effects of endocrine diseases on the aldosterone

41

hormone levels [174]–[179]. Finally, ovine adrenal glands represent better the anatomical dimensions of human adrenal glands compared to other species such as bovine [180], [181].

Nevertheless, a comprehensive understanding of the dielectric properties of adrenal glands is still lacking. Only two studies described the dielectric properties of porcine and bovine adrenal glands, with no available data about the ovine adrenal glands.

This chapter describes:

- The dielectric characteristics of the adrenal cortex and medulla of the *ex vivo* ovine adrenal gland and the variability in the dielectric properties between ovine and bovine adrenal tissues;

- *Ex vivo* human adrenal glands affected by different types of diseases including unilateral PA. These data are then compared with the dielectric data acquired from ovine tissues;

- The values of the dielectric properties in relation to the operating frequencies typically adopted in microwave ablation devices.

The structure of this chapter is as follows: the physical basics of the dielectric properties and the link with the microwave thermal ablation are reviewed in Section 3.1. The measurement technique and the experimental protocol adopted are described in Section 3.2. The results relating to the dielectric properties of *ex vivo* animal adrenal glands and *ex vivo* human adrenal glands are described in Section 3.3, both in wideband (0.5−8.5 GHz) and at MWA operating frequencies (915 MHz, 2.45 GHz, 5.8 GHz). Section 3.4 concludes the chapter.

3.2 Dielectric properties of biological tissues

The interaction between the tissue and the external electric field is described by the complex relative permittivity $\varepsilon(\omega)^*$, defined as:

$$\varepsilon(\omega)^* = \varepsilon'(\omega) - j\varepsilon''(\omega) = \varepsilon'(\omega) - j\frac{\sigma(\omega)}{\omega\varepsilon_0} \tag{3.1}$$

where ω (rad s^{-1}) is the angular frequency. The real part of the complex permittivity describes the ability of the tissue to store the electromagnetic energy, whereas the imaginary part describes the dissipative nature of the tissue. Equation (3.1) shows also that the imaginary part is linked to the effective conductivity $\sigma(\omega)$ of the material: $\sigma(\omega) = \omega\varepsilon_0\varepsilon''$. The effective conductivity describes the ability of the tissue to absorb the electromagnetic energy and dissipate part of the energy as heat.

The mechanism of interaction between the biological material and the applied electric field depends on the frequency. Thus, dielectric properties vary with the frequency of the applied electric field. In the frequency range of the microwave ablation applications (500 MHz – 20 GHz), the main interaction is between the electric field and the water dipoles of the tissue. Due to the intrinsic dipole moment, each dipole rotates in the attempt to align along the same direction as the applied electric field. Vibrations and collisions also occur between adjacent dipoles. All of these interactions are responsible for the dissipation of energy in the material and the consequent conversion in heat [81], [182]–[184].

Several studies have been conducted to characterise the dielectric properties of different biological tissues [185]–[187]. The most comprehensive spectroscopic investigation of *ex vivo* animal tissues was conducted in [183]. Knowledge of the dielectric properties has improved due to several studies conducted not only on *ex vivo* animal tissues, but also on *ex vivo* human tissues in the last twenty years. In particular, differences between diseased and normal human tissues were dielectrically characterised for a selection of tissues, including liver and breast tissues [188], [189]. In addition, studies were conducted to evaluate the impact of the variability in dielectric properties on the MWA treatment [190]. Finally, the influence of temperature on the values of relative permittivity and effective conductivity was studied during and immediately after MWA treatment [143], [144], [191].

Despite progress in the knowledge of the dielectric properties of biological tissues, there is still a lack of investigation into the adrenal functional tissues. Only two studies were conducted on *ex vivo* animal adrenal glands [192], [193]. In [192] the relative permittivity and effective conductivity of the adrenal cortex tissue were measured *in vivo* on porcine
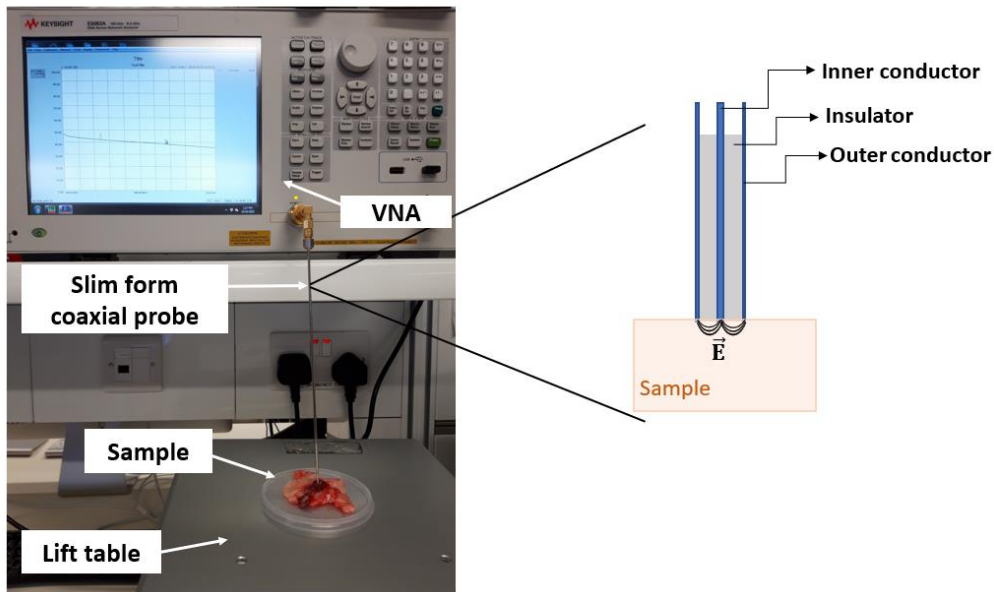
Figure 3.1: (left) Experimental set-up of the open-ended coaxial probe technique including the Vector Network Analyser, the slim form coaxial probe in contact with the sample under measurement and the lift table where the sample is placed; (right) section of the slim form probe composed by the inner conductor, the insulator (i.e. Teflon) and the outer conductor. The electric field propagate into the coaxial cable and it is partially reflected at the end of the probe, because of the impedance mismatch between the transmission line and the sample under test.

adrenal glands in the frequency range between 500 MHz − 20 GHz. Because of the anatomical structure of the gland, only the external functional tissue of the adrenal gland (cortex) was accessible. In [193] the relative permittivity and effective conductivity were measured *ex vivo* both for the cortex and medulla bovine adrenal glands.

To date, the dielectric characterisation of both adrenal functional tissues relies only on the data measured *ex vivo* on bovine adrenal glands [193]. A lack of knowledge in the dielectric properties of ovine adrenal models exists. Ovine adrenal models are used to understand the mechanism underlying the synthesis of the hormones, such as aldosterone [171], [194]. Thus, ovine adrenal gland is a suitable model for a comprehensive investigation of novel ablative approaches. To aid this goal, it is first required the characterise the relative permittivity and effective conductivity of ovine adrenal gland within the MWA frequency range, 0.5 – 8.5 GHz.

In this study, dielectric properties were measured *ex vivo* on freshly excised ovine samples, distinguishing between outer adrenal layer (cortex) and the inner adrenal layer (medulla). The study also provides new insights into the knowledge of the dielectric composition of human adrenal glands affected by different diseases (i.e. pheochromocytoma, paraganglioma, non-functional nodule and adreno-cortical adenoma). Where available, the dielectric properties were also acquired on the rim of normal tissue surrounding the diseased tissue.

3.3   Measurement methodology

In the section below, the dielectric properties of ovine adrenal glands will be presented and discussed along with the experimental data acquired on human adrenal glands after their surgical removal.

The dielectric properties of *ex vivo* ovine adrenal glands were measured on eight samples (N_O = 8). The excised samples were collected from a local slaughterhouse and transported in sealed bags to the laboratory of National University of Ireland Galway.

The protocol for measuring dielectric properties on human adrenal glands after excision was approved by the Galway University Hospitals Research Ethics Committee. The study included six patients (N_H = 6) with diagnosed adrenal abnormalities who were scheduled to undergo unilateral adrenalectomy. The sample was excluded from the study in cases where the pathologist did not provide either the histology analysis or the gross description of the removed gland.

3.3.1   Dielectric measurement system

Open-ended coaxial method. Measurements of complex permittivity were performed using the open-ended coaxial probe technique [182], [185], [188], [189]. Currently, the open-ended coaxial technique is the technique most commonly used to measure dielectric properties [182]. The open-ended coaxial probe allows a good fit between the sample and the measurement, reducing the preparation time and the risk of destructive handling of the sample [195]. Also, the open-ended coaxial technique enables reliable measurements across a broad frequency range both *in vivo* and *ex vivo* tissues [182], [196].

Experimental setup. Figure 3.1 depicts the measurement setup. The open-ended coaxial probe includes a section of transmission line which is connected to a vector network analyser (VNA) (Keysight VNA E5063A). A VNA consists of a signal source, a receiver and a display. The signal source transmits the input signal at a single frequency. The signal propagates through the transmission line up to the material under test where it is reflected due to the mismatch between the characteristic impedance of the transmission line and the impedance of the material under test. The reflected signal measured by the receiver differs from the input signal in terms of phase and magnitude. The process is repeated, stepping to the next frequency. Finally, the response of the material under test based on the reflected signal is shown as a function of the frequency [182], [195]. In this study, a frequency range equal to 0.5 – 8.5 GHz was selected in order to include 915 MHz and 2.45 GHz, i.e. the operating frequencies commonly used in microwave ablation applications [80], [81], [197], and 5.8 GHz, i.e. a further operating frequency currently under investigation for microwave thermal ablation therapies [135]. A total of 101 linearly spaced frequency points were considered within the selected frequency band (0.5 – 8.5 GHz). Such choice provided a good trade-off between the accuracy of measurements and the speed of data collection. The reflection coefficient acquired at each frequency point within the selected frequency band was then converted into complex permittivity values. Finally, the software (Keysight N1500A, Santa Rosa, CA, US) included in the VNA automatically converted the reflected signals to the complex permittivity.

The slim form open-ended coaxial probe was adopted both for animal and human studies. The probe was connected to the output port of the VNA without using an additional cable. The slim form probe is a common choice for measurements of biological tissues due to its small diameter, i.e. 2.2 mm [182], [188], [189] and the sensing radius comparable to the probe tip. Several studies showed that a distance of about 1 mm from the sample edge is sufficient to avoid reflections which may affect the measurements [198]. Additionally, [199] demonstrated that within a bulk heterogeneous tissue, approximately the first 1 mm material close to the tip of the probe significantly influences the dielectric properties. As

a result, this probe is appropriate for samples of small size, both liquids and semi-solid materials [195].

During each measurement, a lift table was used to guarantee firm contact between the probe and the sample. A right-angle connector was used for a tight connection between the input of the probe and the VNA, in order to minimise the effect of the cable movement in the dielectric data.

Confounders. Several factors could impact on the reliability of the measurements, such as a the change in the environmental parameters, the contamination of the probe, and the poor electrical connection in the experimental setup [182], [200]. To account for these confounders, a calibration process was required before the *ex vivo* measurement of the dielectric properties, both in animal and human samples. The accuracy of the calibration and potential anomalies which could occur during the measurement process were monitored through a validation process [182], [200].

Calibration. Firstly, the room temperature was monitored as changes in the environmental conditions could affect the measurements. All the connections were checked, and the tip of the probe was cleaned with alcohol wipes before each measurement. Then, the setup was calibrated through a standard procedure at the reference plane of the probe, with the probe connected to the VNA [182]. Three loads characterised by well-known dielectric properties were used for the calibration process: open circuit, short circuit and a broadband load. Regarding the broadband load, deionised water (DW) was used. The cleanliness of the probe (in the case of the open circuit) and the good contact (in the case of the short circuit) were monitored through the Smith Chart. Smith Chart is a graphical representation of the normalised complex impedance, which depends on the reflection coefficient between the load and the VNA. In the case of the open circuit load, the impedance marker indicates ohm $\rightarrow \infty$. In the case of short circuit, the impedance marker is around zero ohm [195]. When, the probe is immersed in deionised water, the jar containing the liquid is inspected before the measurement to eliminate air bubbles between the tip of the probe and the liquid. Air bubbles have the potential to introduce up to 20% deviations from the dielectric measurements [182],

[201]. The temperature of the liquid was also monitored, since the dielectric properties are temperature dependent [202], [203].

Measurements on a further material of well-known dielectric properties were performed, in order to validate the accuracy of the calibration.

Validation and measurement uncertainty. Validation was conducted immediately after the calibration and at the end of each measurement session. The validation procedure allows for accounting of systematic errors such as the error linked to the VNA drift over time. To this end, the dielectric properties of a reference material different from the material used during the calibration were measured at room temperature [182], [200], [204]. In this study, 0.1 M NaCl was chosen for the following reasons:

- The relative permittivity and effective conductivity of different concentrations of NaCl are well-characterised in the microwave frequency range [204]–[206];

- Among all of the different saline solutions, the dielectric properties of 0.1M NaCl are comparable to those of most biological tissues [186], [200], [204];

- The solution is relatively easy to obtain, without requiring particular handling [182].

Uncertainty was also reported along with the mean dielectric values, according to the National Institute of Standards and Technologies (NIST) guidelines [207]. The repeatability and accuracy associated with the measurements were determined over multiple measurements (at least three) acquired on the known material. According to the definition of uncertainty reported in [207], repeatability is expressed as the standard deviation across the measurements repeatedly acquired under the same measurement conditions. Accuracy is the averaged percentage difference between the acquired data and the reference model. In this study, the reference study adopted is [204]. The uncertainties related to accuracy and repeatability both contribute to the combined uncertainty. The combined uncertainty was calculated as the root sum squared of each uncertainty component. To calculate the uncertainty component, each standard deviation was divided by a factor to differentiate between Type A and Type B uncertainties, as reported in [204]. Type A uncertainty is expressed through the standard deviation calculated across the measurements. As a result, Type A uncertainty is linked to the

number of measurements acquired. In the case of Type B uncertainty, the evaluation is based on other information such as prior measurement experiences, instrument datasheets, calibration specifications. Thus, the distribution of probability for Type B uncertainty is assumed to be rectangular, as the true value might equally be between the upper and the lower of uncertainty distribution. These uncertainties were determined using 0.1M NaCl as reference material. However, further uncertainties mainly related to the complexity of the biological structure of the tissue under investigation may affect the dielectric measurements. According to NIST guidelines, the averaged value of the measurements should be reported alongside the 95% confidence interval (CI). Thus, the expanded uncertainty (k = 2) was calculated both for the relative permittivity and the effective conductivity.
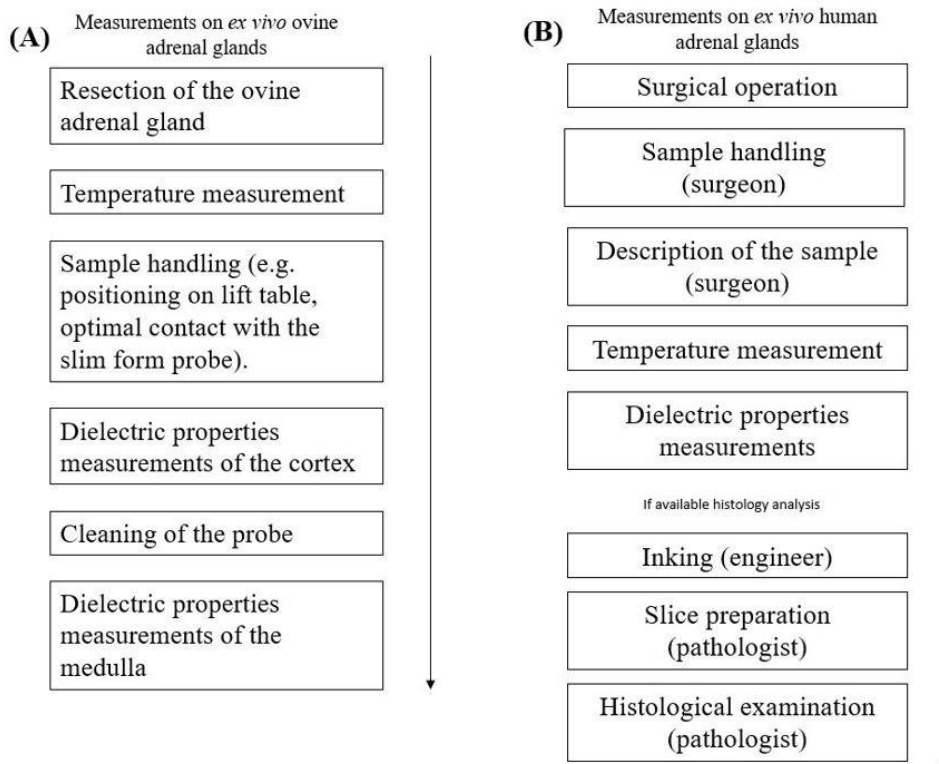
Figure 3.2:Protocol for measurement of dielectric properties of: (A) functional tissues identified on *ex vivo* ovine adrenal glands; (B) diseased adrenal glands of N_H = 6 patients scheduled for surgical operations and affected by different types of adrenal diseases. Histology analysis was also conducted after the excision for each *ex vivo* human adrenal gland.

3.3.2   Experimental protocols and data analysis

Ex vivo ovine adrenal glands. Eight ovine adrenal glands ($N_O = 8$) were excised and transported in sealed containers to the laboratory where the measurement process was conducted. The dielectric data was collected following the experimental protocol reported in Figure 3.2 (A). The average measured dimensions the adrenal glands are 16.0 $\pm$ 1.0 mm (length), 8.0 $\pm$ 1.0 mm (width), 6.0 $\pm$ 1.0 mm (thickness), with medulla sizes ranging between 3 – 4 mm in width and 8 – 9 mm in length. Each adrenal gland was preserved by the surrounding fat layer, in order to avoid the excessive dehydration of the sample. The temperature of each sample was repeatedly measured using an infrared thermometer in order to monitor the integrity of the tissue. The ovine samples were sectioned to provide access to both cortex and medulla layers and one measurement location was identified for each layer. Three measurements were subsequently repeated on each selected measurement point for a total of 48 measurements and 16 measurement points (8 for the cortex and 8 for the medulla). All the measurements were completed within 2h after the excision. On average, the temperature of the *ex vivo* ovine samples was 22.2 $\pm$ 1.5 °C.

Ex vivo human adrenal glands. Six patients ($N_H = 6$) with diagnosed adrenal abnormalities and scheduled to undergo adrenalectomy were included in this study. Figure 3.2 (B) depicts the experimental protocol adopted to measure the dielectric properties *ex vivo* on human adrenal glands. After the resection, each sample was

Table 3.1:Summary of the number of dielectric measurements for six patients, including the locations measurement points (i.e. normal tissue, diseased tissue), the type of analysis performed after the surgical excision (i.e. gross description, histology analysis), the type of adrenal disease (i.e. paraganglioma, pheochromocytoma, aldosterone-producing adenoma (APA) encapsulated non-functioning nodule).

Patient (#)	Measurement points		Post-excision analysis	Disease type
	Normal tissue	**Diseased tissue**		
1	0	3	GD + H	Paraganglioma
2	0	2	GD + H	Pheochromocytoma
3	0	1	GD + H	Aldosterone-producing adenoma
4	0	3	GD + H	Pheochromocytoma
5	1	1	GD + H	Encapsulated nodule
6	1	1	GD + H	Pheochromocytoma

GD: gross description; H: histology analysis; APA: aldosterone-producing adenoma

transported in a sealed container to the pathology suite at University Hospital Galway (UHG). Measurements were performed within approximately 30 minutes of the excision on different diseased tissue and, if available, on the surrounding healthy tissue. Before each measurement, the slim form probe was cleaned with alcohol wipes. The temperature of the samples varied between 20°C and 23°C. For each sample included in the study, three measurements were subsequently repeated on the selected measurement points of the tissue sample following the indication of the pathologist. The measurement locations were inked and preserved for histological identification in order to confirm the gross examination. The type of tissue at the designed measurement location was then univocally identified by the histology analysis. Where the histological identification was not possible, the measurement location was discarded. Table 3.1 summarises the number of measurements points acquired for each tissue type (i.e. normal or diseased tissue) and for each patient. The same also table reports the type of analysis conducted after excision (gross description and histology analysis) and the type of adrenal disease. For patients 5 and 6, the dielectric properties were measured, both on the diseased tissue and the region surrounding the tumour identified as normal tissue.

Analytical models. The data was analysed with MATLAB (R2017a, The MathWorks, Inc., Natick, MA, US). The mean and standard deviation values both for the relative permittivity and the conductivity over the frequency band of interest were calculated. Debye and Cole-Cole models were used in this study to describe analytically the frequency-dependent dielectric spectrum. Both models are represented collectively by Equation 3.2:

$$\varepsilon^*(\omega) = \varepsilon_\infty + \sum_n \frac{\Delta\varepsilon_n}{1 + (j\omega\tau_n)^{(1-\alpha_n)}} + \frac{\sigma_i}{j\omega\varepsilon_0} \tag{3.2}$$

Here ω (rad s^{-1}) is the angular frequency, ε_∞ is the permittivity at infinite frequencies (i.e. terahertz frequency range) related to the electronic polarisation, n indicates the number of poles, $\Delta\varepsilon_n$ is the drop in permittivity in the frequency range, σ_i (S·m^{-1}) is the ionic conductivity, ε_0 is the permittivity of the vacuum, α is the empirical variable that accounts for the distribution of the relaxation time and τ is the relaxation time characterising each dispersion region of the tissue [182], [183]. The relaxation time is

51

the time necessary for the molecules of the material under test to return to the low energy state (relaxation state) after the perturbation due to the applied electric field. Equation (3.2) indicates the link between the Debye model and the Cole-Cole model through the parameter α. When $\alpha = 0$, Equation (3.2) corresponds to the Debye model; in the case of $0 < \alpha < 1$, Equation (3.2) results in the Cole-Cole model. Both for Debye and Cole-Cole model, the parameters are optimised to find the best fit to the measured dielectric data [208], [209].

In this work, the non-linear weighted least square method was used to fit the dielectric data according to [208]. The algorithm was developed in MATLAB (R2017a, The MathWorks, Inc., Natick, MA, US). The minimum squared weighted error was calculated as described by Equation (3.3), considering a total of 5,000 iterations and a maximum error value of 0.1%.

$$E^2 = \sum_{i}^{N_f} \left[\frac{(c_{Re}(\omega_i) - d_{Re}(\omega_i))^2}{(e_{Re}(\omega_i))^2} + \frac{(c_{Im}(\omega_i) - d_{Im}(\omega_i))^2}{(e_{Im}(\omega_i))^2} \right] \tag{3.3}$$

N_f is the number of frequency points which was set equal to 101 for this study, ω_i (rad·s^{-1}) is the angular frequency, c_{Re} and c_{Im} are the real and the imaginary parts of the calculated complex permittivity, d_{Re} and d_{Im} are the real and imaginary parts of the experimental data, e_{Re} and e_{Im} are the real and imaginary parts of the allowable error which was chosen dependent on the complex permittivity as $e_i^*(\omega_i) = (\varepsilon^*(\omega_i))^\xi$. In accordance with [208], the power factor ξ was set equal to 0.75 in order to put more weighting on lower frequency data, where higher values of relative permittivity are obtained. In this study, Cole-Cole model was used for a reliable comparison with the experimental data related to the adrenal glands reported in [193]. The same fitting method was used to optimise the parameters also for the two poles Debye model. Thus, the performances of the two models were compared in terms of quality of fitting of the experimental data.

The mean values of relative permittivity and effective conductivity were highlighted at 915 MHz, 2.45 GHz, 5.8 GHz both for the cortex and medulla tissues and both for ovine and human samples. Such frequencies are included in the Industrial Scientific Medical

Table 3.2: Calculation of uncertainty components (u_i), combined uncertainty (u_c) and expanded uncertainty (u_e) for measured permittivity and conductivity of 0.1M NaCl, in the frequency range 0.5 – 8.5 GHz.
N = normal distribution, R = rectangular distribution

Relative permittivity

	Uncertainty component (%) a		Probability distribution	Divisor b	Standard Uncertainty (%) $u_i = \dfrac{a}{b}$	
	Ex vivo ovine study	*Ex vivo human study*			*Ex vivo ovine study*	*Ex vivo human study*
Repeatability	1.6	0.5	N	1	1.6	0.5
Accuracy	2.4	0.7	R	$\sqrt{3}$	1.4	0.4
Drift	0.05	0.04	R	$\sqrt{3}$	0.03	0.02
Combined Uncertainty (u_c)	2.2	0.7	$u_c = \sqrt{\sum u_i^2}$			
Expanded Uncertainty (u_e, $k = 2$)	4.4	1.4	$u_e = k u_c$			

Effective conductivity

	Uncertainty component (%) a		Probability distribution	Divisor b	Standard Uncertainty (%) $u_i = \dfrac{a}{b}$	
	Ex vivo ovine study	*Ex vivo human study*			*Ex vivo ovine study*	*Ex vivo human study*
Repeatability	0.9	0.7	N	1	0.9	1.1
Accuracy	2.2	3.1	R	$\sqrt{3}$	1.3	1.8
Drift	0.06	0.05	R	$\sqrt{3}$	0.06	0.03
Combined Uncertainty (u_c)	1.6	2.0	$u_c = \sqrt{\sum u_i^2}$			
Expanded Uncertainty (u_e, $k = 2$)	3.2	4.0	$u_e = k u_c$			

(ISM) frequency band and are three frequencies of interest to MWA devices. In particular, 915 MHz and 2.45 GHz are the operating frequencies commonly used in clinical applications of MWA and 5.8 GHz is a further operating frequency recently

under investigation. In the context of MWA, the increase in the operating frequencies is linked to the increase of the effective conductivity of the tissue. As a result, the rate of electromagnetic power absorbed by the tissue is influenced by the frequency at which the MWA applicator operates. More details about the relation between the rate of the absorbed electromagnetic power and the operating frequency will be provided in Chapter 4.

3.4 Results

3.4.1 Measurement uncertainty

Table 3.2 reports the main steps to calculate the expanded uncertainty associated with the relative permittivity and effective conductivity of 0.1M NaCl. The same calculation protocol was adopted both for animal and human studies. The uncertainty component related to the random errors (repeatability) can be assumed as normally (N) distributed, according to the guidelines defined by the National Institute of Standard and Technology (NIST). The uncertainty components related to the systematic errors (accuracy and drift error) can be modelled by a rectangular (R) distribution [207]. The values of the expanded uncertainty related to the *ex vivo* ovine study are 4.4% for the relative permittivity and 3.2% for the effective conductivity. The values of the expanded
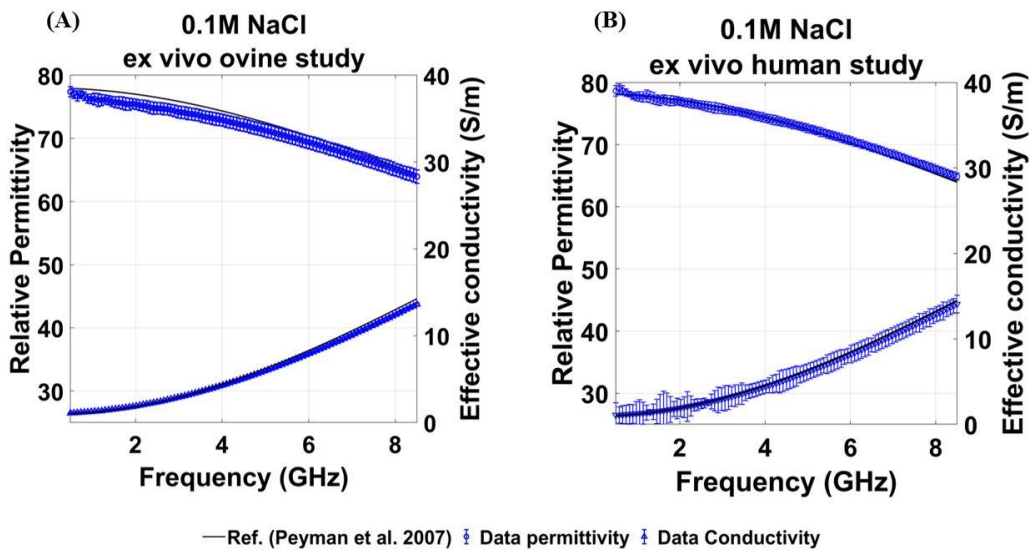
Figure 3.3: Relative permittivity and effective conductivity values across the frequency range of 0.5 – 8.5 GHz obtained during the validation procedures performed before the studies concerning the dielectric characterisation of *ex vivo* ovine adrenal glands (A) and *ex vivo* human adrenal glands (B).

uncertainty related to the *ex vivo* human study are 1.4% for the relative permittivity and 4.0% for the effective conductivity. This data is affected by the different number of measurements when compared with animal data, and by the different environmental parameters of the pathology room.

Figure 3.3 shows a direct comparison between the dielectric properties acquired on 0.1M NaCl and the reference data reported in [204], to support the validity and the reliability of the dielectric data.
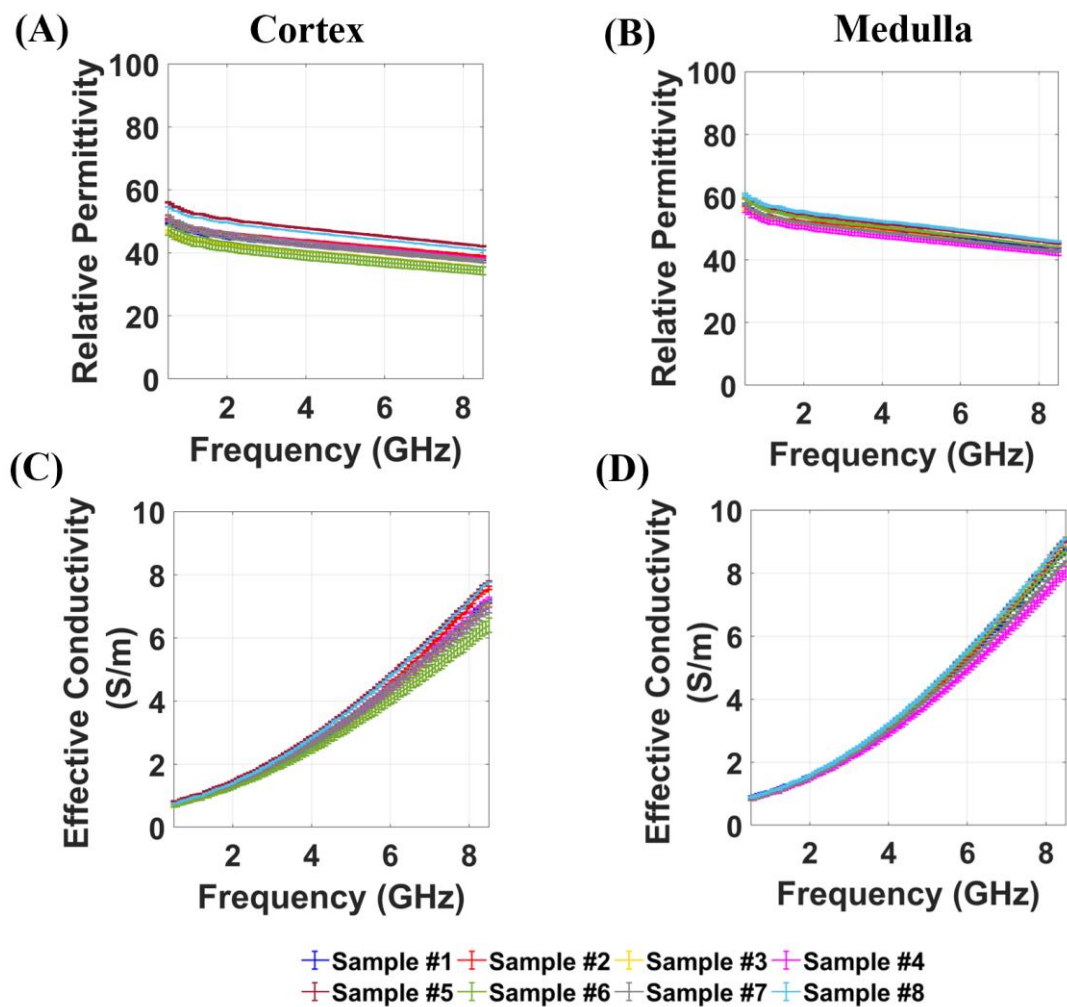
Figure 3.4: Values of relative permittivity (A–B) and effective conductivity (C–D) obtained from the measurements performed on *ex vivo* ovine adrenal glands ($N_O = 8$) within 0.5 – 8.5 GHz. The curves represent the average value calculated over three consecutive measurements performed on each functional tissue: cortex (A–C) and medulla (B–D).

Overall, the values of relative permittivity and effective conductivity of 0.1M NaCl are comparable to the reference values across 0.5 – 8.5 GHz frequency range both for the *ex vivo* animal study (Figure 3.3 (A)) and *ex vivo* human study (Figure 3.3 (B)).

3.4.2 Dielectric properties of *ex vivo* ovine adrenal glands

Analysis in 0.5 – 8.5 GHz frequency band. Figure 3.4 shows the relative permittivity (A-B) and the effective conductivity (C-D) within the 0.5 – 8.5 GHz frequency range. The values of the dielectric properties refer to each *ex vivo* ovine adrenal gland used in the study. Each curve represents the mean and the standard deviation calculated over three consecutive measurements acquired on a single location in the cortex (Figure 3.4 (A-C)) and medulla (Figure 3.4 (B-D)). A good agreement can be observed in the values of relative permittivity and effective conductivity across all the samples.

Figure 3.5 shows the dielectric data for each functional tissue (cortex and medulla) along with the data acquired *ex vivo* on bovine adrenal glands reported in [193]. Each curve represents the mean values of relative permittivity and conductivity for all the given samples. In addition, Figure 3.5 shows two pole Cole-Cole and Debye models fitted to the *ex vivo* ovine adrenal tissues from 0.5 to 8.5 GHz. The fitting error is less than 3% for both models. However, the two pole Cole-Cole model shows an excellent fit to the
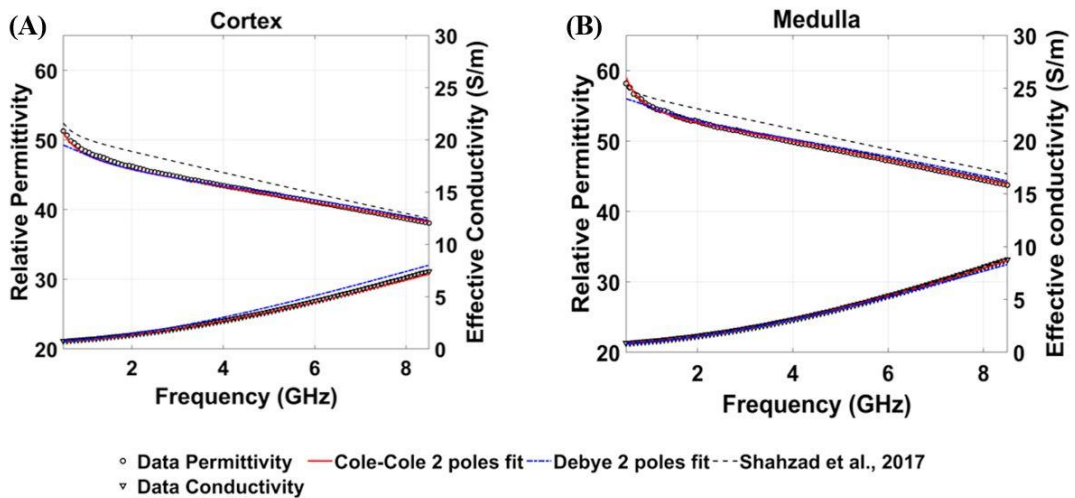
Figure 3.5: Average values of relative permittivity and effective conductivity calculated across all the measurements performed on *ex vivo* ovine cortex tissue (A) and medulla tissue (B) and reported along with the two poles Cole-Cole fitting model, the two pole Debye fitting model and the reference data [193].

experimental data, in agreement with the findings observed in [193]. Table 3.3 lists the optimised parameters both of the Debye and Cole-Cole models. The table also includes the parameters for the Cole-Cole models used in [193] to fit the related experimental data. A good agreement can be observed between the Cole-Cole parameters calculated in this study for the *ex vivo* ovine adrenal gland and the literature data of [193]. Debye and Cole-Cole models also show similar values in the two relaxation times (τ_1 and τ_2). An higher difference between the two models can be observed in the values of permittivity delta associated with the polarisation of cellular membrane ($\Delta\varepsilon_2$). This phenomenon occurs from 500 kHz up to about 1 GHz, as observed in Figure 3.5. The superior performances of the Cole-Cole model compared to the Debye model are visible mainly at these lower frequencies (i.e. between 500 MHz and 1 GHz). The end of the tail of the dispersion region linked to the polarisation of the cell membrane (region *β*) may overlap with the dispersion region linked to the polarisation of the water molecules (region *γ*) [183], [210]. The overlapping between the two dispersion regions is better modelled by the Cole-Cole model compared with the Debye model. This is because of the parameter alpha (α) in the Cole-Cole model (Equation 3.2) which accounts for multiple polarisations. Comparing the Cole-Cole model related to the data of ovine

Table 3.3: Parameters of the two poles Debye model and the two poles Cole-Cole model fitted (5,000 iterations) to the measured adrenal data related to the cortex and medulla in the frequency ranges of 0.5 – 8.5 GHz. For comparison, the reference parameters of the two poles Cole-Cole model fitted to the *ex vivo* bovine adrenal tissues [193] are also reported.

| Parameters | Two poles Debye model | | Two poles Cole-Cole model | | | |
| | This study | | This study | | Reference [193] | |
	Cortex	Medulla	Cortex	Medulla	Cortex	Medulla
ε_∞	10.0	8.8	1.0	1.8	3.57	3.88
$\Delta\varepsilon_1$	34.5	42.6	45.3	51.1	47.08	52.95
τ_1	8.7 ps	8.5 ps	6.4 ps	7.1 ps	8.33 ps	7.01 ps
α_1	-	-	0.1	0.1	0.16	0.17
$\Delta\varepsilon_2$	5.5	5.1	54.6	60.5	52.31	62.05
τ_2	0.1 ns	0.1 ns	1.7 ns	1.3 ns	1.69 ns	4.28 ns
α_2	-	-	0.1	0.1	0.03	0.14
σ_s	0.6	0.8	0.4	0.4	0.46	0.62

adrenal tissues presented in this study, and the Cole-Cole model presented in [193] related to the data acquired from bovine glands, similar dispersion trends are visible, considering the same frequency range. For relative permittivity, the curves describing the Cole-Cole fit to the data of ovine medulla and cortex tissues are approximately 5%

Table 3.4: Average (calculated over three consecutive measurements) and standard deviation values of relative permittivity and effective conductivity for the cortex tissue of *ex vivo* adrenal samples (N_O=8) at 915 MHz, 2.45 GHz and 5.8 GHz.

Tissue type	*Ex vivo* ovine adrenal cortex					
	915 MHz		2.45 GHz		5.8 GHz	
	ε_r	σ (S m^{-1})	ε_r	σ (S m^{-1})	ε_r	σ (S m^{-1})
1	47.1 ± 0.3	0.9 ± 0.01	44.2 ± 0.3	1.5 ± 0.01	40.7 ± 0.3	4.1 ± 0.1
2	48.5 ± 0.2	0.8 ± 0.01	45.8 ± 0.2	1.5 ± 0.01	42.0 ± 0.2	4.3 ± 0.1
3	44.4 ± 0.4	0.8 ± 0.01	42.1 ± 0.3	1.4 ± 0.01	38.7 ± 0.1	4.0 ± 0.1
4	48.4 ± 0.9	0.9 ± 0.1	44.9 ± 0.9	1.6 ± 0.1	40.9 ± 0.8	4.2 ± 0.1
5	53.5 ± 0.2	1.0 ± 0.1	49.8 ± 0.2	1.7 ± 0.1	45.5 ± 0.2	4.6 ± 0.1
6	44.7 ± 1.6	0.8 ± 0.1	41.2 ± 1.5	1.5 ± 0.1	37.2 ± 1.3	3.8 ± 0.2
7	48.3 ± 0.9	0.9 ± 0.1	44.7 ± 0.9	1.6 ± 0.1	40.6 ± 0.7	4.2 ± 0.2
8	52.2 ± 0.1	0.9 ± 0.01	48.7 ± 0.1	1.6 ± 0.01	44.3 ± 0.1	4.5 ± 0.1
Mean	48.4 ± 0.6	0.9 ± 0.1	45.2 ± 3.0	1.6 ± 0.1	41.2 ± 2.8	4.2 ± 0.2

Table 3.5: Average (calculated over three consecutive measurements) and standard deviation values of relative permittivity and effective conductivity for the medulla tissue of *ex vivo* adrenal samples (N=8) at 915 MHz, 2.45 GHz and 5.8 GHz.

Tissue type	*Ex vivo* ovine adrenal medulla					
	915 MHz		2.45 GHz		5.8 GHz	
	ε_r	σ (S m^{-1})	ε_r	σ (S m^{-1})	ε_r	σ (S m^{-1})
1	54.7 ± 0.2	1.1 ± 0.01	51.5 ± 0.2	1.9 ± 0.01	47.0 ± 0.2	5.1 ± 0.1
2	54.6 ± 0.1	1.0 ± 0.01	51.7 ± 0.1	1.8 ± 0.01	47.7 ± 0.1	5.0 ± 0.1
3	53.7 ± 0.3	1.0 ± 0.01	51.0 ± 0.3	1.8 ± 0.01	46.5 ± 0.2	5.2 ± 0.1
4	53.5 ± 1.1	0.9 ± 0.1	49.9 ± 1.0	1.7 ± 0.1	45.7 ± 0.9	4.7 ± 0.1
5	57.1 ± 0.3	1.0 ± 0.01	53.6 ± 0.2	1.8 ± 0.01	49.3 ± 0.2	5.2 ± 0.1
6	56.5 ± 0.2	1.0 ± 0.01	52.6 ± 0.3	1.9 ± 0.01	48.0 ± 0.2	5.1 ± 0.1
7	54.8 ± 0.3	0.9 ± 0.01	51.0 ± 0.3	1.7 ± 0.01	46.4 ± 0.2	4.9 ± 0.1
8	58.0 ± 0.4	1.0 ± 0.1	54.4 ± 0.3	1.9 ± 0.1	49.9 ± 0.3	5.2 ± 0.1
Mean	55.4 ± 0.4	1.0 ± 0.1	52.0 ± 0.4	1.8 ± 0.1	47.6 ± 0.3	5.1 ± 0.1

lower than the Cole-Cole fit to data of the ex vivo bovine adrenal gland presented in [193]. On the other hand, an excellent match in the Cole-Cole fitting between the two different species is visible for the effective conductivity.

Overall, the values in relative permittivity and effective conductivity investigated in this study are comparable with the reference data [193]. The slight difference (less than 5%) in the relative permittivity for lower frequency may be linked to the different mammalian species, performances of the fitting algorithm or the variability in the experimental measurements. A difference in the relative permittivity and effective conductivity is visible between cortex and medulla within 0.5 – 8.5 GHz frequency range, in agreement with what was already observed in [193]. In the context of MWA, this information indicates that the two functional tissues of the gland could have a different degree of interaction with the electromagnetic field. In particular, medulla would absorb more electromagnetic power because of the higher effective conductivity compared with cortex. Medulla is the tissue responsible for the release of hormones (*epinephrine* and *norepinephrine*) which excite the heart rate and allow for the contracting of the blood vessels during stress conditions (§ 2.1). Thus, the heating of the medulla should be carefully managed to avoid the risk of cardiac failures during the MWA procedure.

Comparison of single frequency dielectric data. Tables 3.4 and 3.5 summarise the dielectric properties of *ex vivo* ovine adrenal cortex and medulla at 915 MHz, 2.45 GHz and 5.8 GHz. The mean and standard deviation values both for the relative permittivity and effective conductivity were computed for each sample. At 5.8 GHz, the mean value of conductivity is 367% higher compared with the conductivity at 915 MHz and 163% higher compared with the value at 2.45 GHz. A less evident difference was observed in the relative permittivity values. At 5.8 GHz, the value of relative permittivity is 15% and 9% lower than the values observed at 915 MHz and 2.45 GHz, respectively. Examining the medulla, at 5.8 GHz the mean value of the effective conductivity is 410% higher compared with 915 MHz and 183% higher compared with 2.45 GHz. The relative permittivity is 14% and 8% lower compared with the values at 915 MHz and 2.45 GHz, respectively.
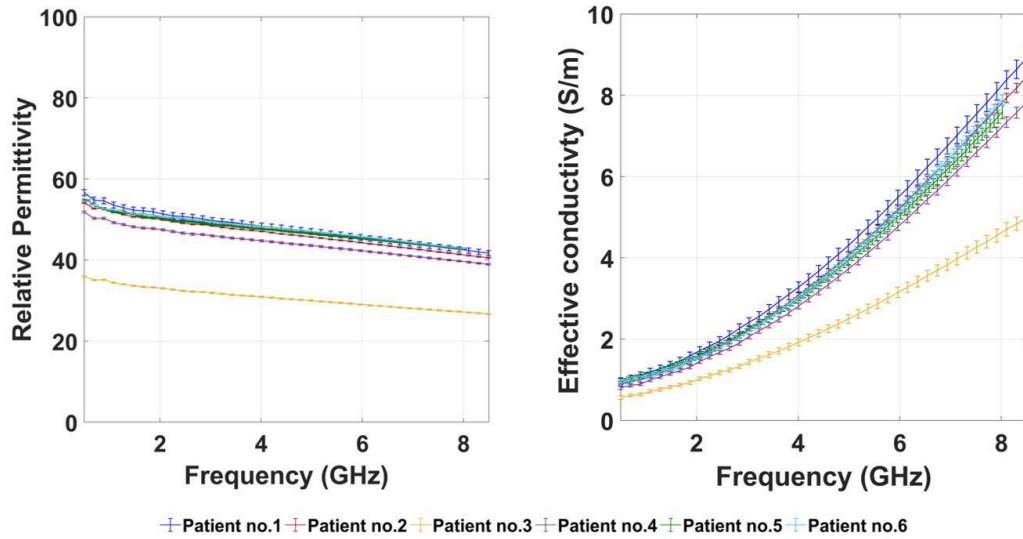
Figure 3.6: Relative permittivity and effective conductivity related to paraganglioma (Patient 1), pheochromocytoma (Patient 2, Patient 4, Patient 6), aldosterone-producing adenoma (Patient 3) and encapsulated nodule (Patient 5).
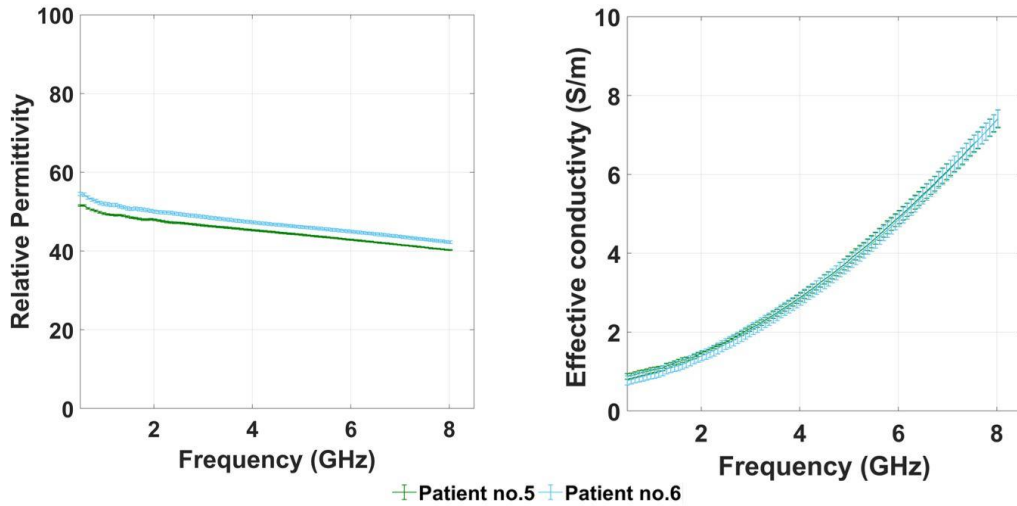
Figure 3.7: Relative permittivity and effective conductivity measured on the available healthy tissue identified by the pathologist in two samples (Patient 5 and Patient 6) in the frequency range of 0.5 – 8.5 GHz.

Previous studies showed that the performances of the MWA devices change with the operating frequency. The study conducted in [197] showed that the higher value of effective conductivity of liver at 2.45 GHz compared with 915 MHz results in a higher deposition of the electromagnetic power in the tissue. The result is linked to the proportional relationship between the effective conductivity and the electromagnetic power absorbed by the tissue. In light of the results included [197], this study suggests
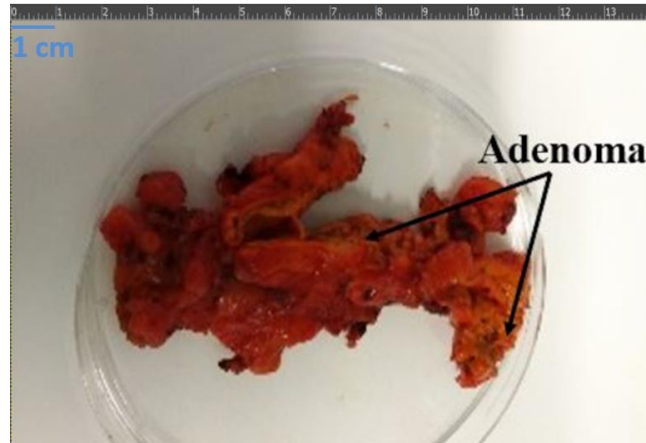
Figure 3.8: Excised hyperfunctioning adrenal adenoma responsible for primary aldosteronism clearly visible due to the yellow colour typically characterising lipid-rich masses, like adreno-cortical adenomas.

that the higher effective conductivity at 5.8 GHz compared with the other frequencies results in a greater absorption of the electromagnetic power in the tissue. The performances of the MWA applicator at 5.8 GHz compared to 2.45 GHz will be discussed in Chapter 4, while Chapter 8 will be dedicated to the effects of the higher frequency on the ultimate ablation zone.

3.4.3   Dielectric properties of *ex vivo* human adrenal glands

Analysis in 0.5 – 8.5 GHz frequency band. Figure 3.6 shows the relative permittivity and effective conductivity as a function of frequency for six diseased adrenal glands excised from six different patients. The dielectric data refer to:

- Paraganglioma for Patient 1;
- Pheochromocytoma for Patient 2, Patient 4 and Patient 6;
- Adreno-cortical adenoma for Patient 3;
- Benign nodule for Patient 5.

The histology analysis supports the gross description provided by the pathologist following the excision of the tissue. Figure 3.7 shows the values of the dielectric properties related to the available normal tissue of the *ex vivo* human sample (Patient 5 and Patient 6). Comparable results are obtained between the normal *ex vivo* human adrenal cortex (Figure 3.7) and the ovine adrenal cortex (Figure 3.5). The average values

of relative permittivity and effective conductivity are both 6% higher in healthy cortical human tissue compared with the ovine adrenal cortex within 0.5 – 8.5 GHz.

Hereafter, the relative permittivity and effective conductivity measured on diseased adrenal tissues will be compared with the normal adrenal tissue. The condition of the tissue, normal or diseased, was indicated by the pathologist according to the histopathological findings.

For the non-functioning nodule, arising from the cortex, data were collected only from one sample. When compared to the normal human cortical tissue, the non-functioning nodule appears to differ less than 3% in relative permittivity and less than 6% in effective conductivity values. With respect to the normal *ex vivo* human dielectric values, paraganglioma appears noticeably more conductive than normal cortical tissue. Data collected from only one sample showed relative permittivity and effective conductivity were 4% and 13% higher than normal human adrenal cortex. Looking at the pheochromocytoma data (collected from 3 different samples), a difference of less than 1% in relative permittivity and less than 4% in effective conductivity can be observed in comparison with the normal human adrenal cortex data. Adreno-cortical adenoma is approximately 33% lower both in relative permittivity and effective conductivity values, compared with the normal *ex vivo* human dielectric values.

It can be observed that human adenoma presents dielectric properties visibly different from the other diseased tissues. These substantial differences may be attributed to the abundant lipid composition of the adreno-cortical adenoma due to the infiltration of the tumour into the adipose tissue of the external capsule. In addition, the histology analysis also revealed the infiltration of collagen fibres into the adenoma. The collagen may further contribute to the lower dielectric values of the adreno-cortical adenoma, as collagen is typically characterised by low dielectric properties (ε_r=13.0, $\sigma = 0.08$ S m^{-1} at 1GHz) [183], [211]. Figure 3.8 shows a picture of the sample of functioning adenoma excised from the patient affected by unilateral PA (Patient 3). The surface (yellow in colour) is typical for cortical adenomas infiltrating the adjacent layer of fat tissue.

Given the small number of samples, the results presented above should be considered

with caution. In particular, only one sample of adrenocortical adenoma was included in the study. This sample is characterised by adipose and collagen infiltration, which contributed to lower the dielectric properties of such diseased tissue. However, the percentage of adipose tissue can vary depending on the degree of infiltration of the adenoma in the fat capsule. Further investigations are needed to include a broader number of adenomas characterised by different content of adipose tissue.

Comparison of single-frequency dielectric data. Tables 3.6 and 3.7 summarise the dielectric properties of *ex vivo* diseased and normal human adrenal glands, respectively, at 915 MHz, 2.45 GHz and 5.8 GHz.

Echoing the results of the *ex vivo* ovine adrenal tissue tests, an increase in the effective conductivity is observed with an increase in frequency (i.e. 915 MHz, 2.45 GHz and 5.8

Table 3.6: Averaged and standard deviation values for relative permittivity and effective conductivity of diseased adrenal glands excised from six patients at 915 MHz, 2.45 GHz and 5.8 GHz.

Patient #	Diseased adrenal tissue					
	915 MHz		2.45 GHz		5.8 GHz	
	ε_r	σ (S m^{-1})	ε_r	σ (S m^{-1})	ε_r	σ (S m^{-1})
1	54.1 ± 0.8	1.1 ± 0.1	50.7 ± 0.8	1.9 ± 0.1	45.9 ± 0.7	5.2 ± 0.2
2	52.3 ± 0.2	1.1 ± 0.1	49.1 ± 0.2	1.8 ± 0.1	44.6 ± 0.2	4.9 ± 0.1
3	34.8 ± 0.2	0.7 ± 0.1	32.4 ± 0.2	1.2 ± 0.1	29.2 ± 0.2	3.0 ± 0.2
4	49.8 ± 0.3	1.0 ± 0.1	46.6 ± 0.3	1.7 ± 0.1	42.6 ± 0.3	4.5 ± 0.1
5	52.5 ± 0.2	1.1 ± 0.1	49.6 ± 0.2	1.8 ± 0.1	45.6 ± 0.2	4.8 ± 0.1
6	52.7 ± 0.1	1.0 ± 0.1	50.2 ± 0.1	1.8 ± 0.1	46.0 ± 0.1	4.9 ± 0.1
Mean	49.4 ± 0.3	1.0 ± 0.1	46.4 ± 0.3	1.7 ± 0.1	42.3 ± 0.3	4.6 ± 0.2

Table 3.7: Averaged and standard deviation values for relative permittivity and effective conductivity of normal tissue of adrenal glands measured in two over six patients at 915 MHz, 2.45 GHz and 5.8 GHz.

Patient #	Normal adrenal tissue					
	915 MHz		2.45 GHz		5.8 GHz	
	ε_r	σ (S m^{-1})	ε_r	σ (S m^{-1})	ε_r	σ (S m^{-1})
5	49.8 ± 0.3	1.0 ± 0.1	47.2 ± 0.2	1.7 ± 0.1	43.1 ± 0.2	4.6 ± 0.2
6	52.2 ± 0.5	0.9 ± 0.2	49.5 ± 0.4	1.6 ± 0.2	45.2 ± 0.4	4.6 ± 0.2
Mean	51.0 ± 0.4	1.0 ± 0.2	48.4 ± 0.3	1.7 ± 0.2	44.2 ± 0.3	4.6 ± 0.2

GHz) in *ex vivo* human tissues both for normal and diseased tissues. Regarding the relative permittivity, a decrease can be noticed with the increase in frequency, both for normal and diseased tissues. At 5.8 GHz, the effective conductivity is 360% and 171% higher than the values at 915 MHz and 2.45 GHz in normal tissues. Considering relative permittivity in normal tissue, the values in relative permittivity at 5.8 GHz are 9% and 13% lower compared with 915 MHz and 2.45 GHz. Similar exchange rates were obtained in effective conductivity and relative permittivity for the *ex vivo* human diseased adrenal tissues.

It is worth noting that a considerable increase in effective conductivity also involves the adreno-cortical adenoma. For this type of diseased tissue, the effective conductivity at 5.8 GHz is 329% and 150% higher than the values reported at 915 MHz and at 2.45 GHz. Considering the relative permittivity, a decrease of 16% and 10% is observed in the adreno-cortical adenoma with the increase of frequency from 915 MHz to 5.8 GHz and from 2.45 GHz to 5.8, respectively. As discussed above, the infiltration of fat in the adenoma is responsible for the lower values in dielectric properties compared with the normal tissue, and also compared with other types of diseased tissues. However, the increase in effective conductivity at 5.8 GHz remains considerably high compared with
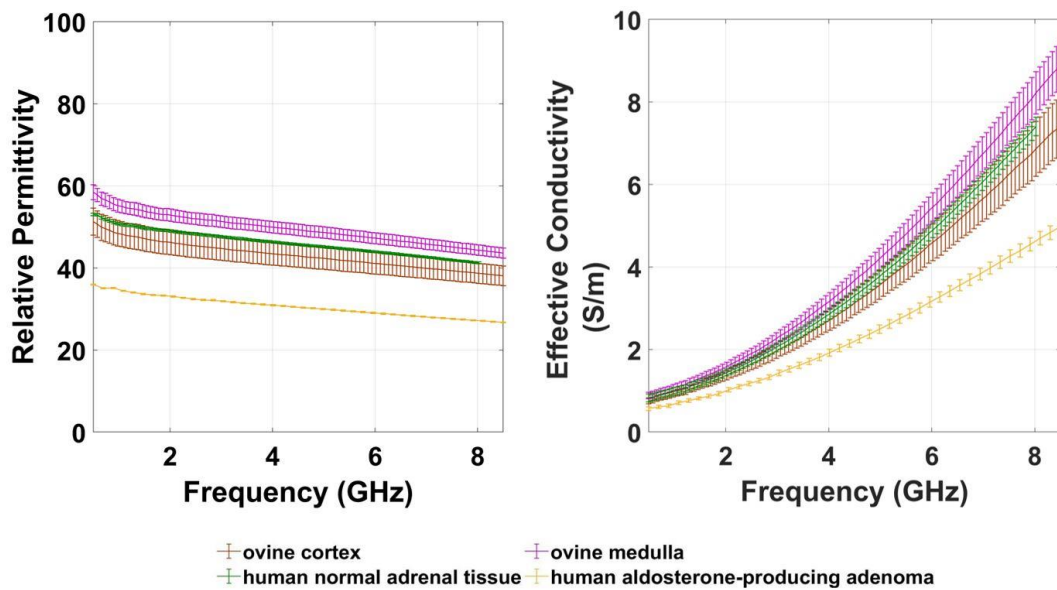
Figure 3.9: Mean and standard deviation values of relative permittivity and effective conductivity reported for *ex vivo* ovine adrenal cortex, *ex vivo* ovine adrenal medulla, *ex vivo* human normal tissue and *ex vivo* human aldosterone-producing adenoma responsible for PA.

915 MHz and 2.45 GHz. As already observed for the values regarding *ex vivo* ovine adrenal glands, the higher values in effective conductivity at 5.8 GHz compared to other frequencies would suggest that higher rates of deposition of electromagnetic power are achievable at this frequency.

Figure 3.9 summarises the key findings of the broadband dielectric analysis of *ex vivo* ovine adrenal glands and *ex vivo* human adrenal glands. The figure shows the mean values both for cortex and medulla tissues of *ex vivo* ovine models, *ex vivo* human normal adrenal tissue and *ex vivo* human adreno-cortical adenoma. In addition, the dielectric properties related to the functioning adenoma responsible for PA are shown, since this tissue is the ablation target of interest for this project.

Similar values in relative permittivity and effective conductivity between the *ex vivo* ovine cortex tissue and the normal human tissue suggests that ovine adrenal glands can be exploited as models for the human adrenal glands. Thus, in the modeling of MWA systems the dielectric properties derived for ovine adrenal samples can be used as good approximation for the dielectric properties of human adrenal glands. Most of the *ex vivo* human diseased adrenal tissues examined in this study shows relative permittivity and effective conductivity close to the values in normal conditions (Figure 3.6 – Figure 3.7). The highest difference between normal and diseased tissue was observed for the adreno-cortical adenoma in the values of effective conductivity. As already discussed, lower values in relative permittivity and effective conductivity are observed for the functioning adenoma compared to normal adrenal tissues. This result is in agreement with the features observed in a range of adreno-cortical adenomas [212], [213]. Adreno-cortical adenomas contain intracytoplasmic fat in different percentage. This feature is likely responsible for the lower values of dielectric properties compared with the other adrenal tissues observed in this study (Figures 3.6 – Figure 3.9). The presence of intracytoplasmic fat is a parameter used to differentiate between benign adenomas and malignant adrenal masses in the imaging scanning tests, e.g. CT. Lipid content is rarely present in malignant adrenal lesions. Approximately 60 – 70% of adrenal adenomas are lipid-rich, thus they are easily to detect through CT or MRI [214]–[217]. However, about 30-40% of adrenal adenomas are lipid-poor as well as other types of adrenal tumours [212], [218], [219].

Further features of adrenal adenomas may include cystic foci, hemorrhagic areas, calcification, degeneration in macroscopic fat (myelolipoma) [215], [220]. The relatively wide range of histological features of the adreno-cortical adenomas suggests that further measurements of the dielectric properties are required.

3.5 Conclusions

In this chapter, a dielectric study of adrenal glands is conducted over the frequency range used in microwave thermal ablation applications. The primary research objective of this chapter was to develop accurate knowledge of the relative permittivity and effective conductivity of the adrenal gland. This knowledge could then be exploited to numerically predict the rate of the electromagnetic power absorbed by the tissue (SAR), and ultimately the size and shape of the ablation zone.

A literature survey concerning dielectric studies of adrenal glands revealed two significant gaps: (1) a lack of studies considering the dielectric properties of ovine adrenal tissues, the animal model widely used to study endocrine disorders; (2) no available studies on the dielectric properties of healthy and diseased human adrenal tissues.

This chapter presents some important findings, including:

- No substantial differences are observed in the dielectric properties of *ex vivo* ovine adrenal glands reported in this study and the *ex vivo* bovine adrenal glands reported in the reference study [193]. However, ovine adrenal glands provide a better representation of the human adrenal glands because of the similar anatomical dimensions;

- The dielectric properties of *ex vivo* ovine adrenal functional tissues represent a good approximation of the *ex vivo* human adrenal tissues in normal conditions. Thus, the relative permittivity and the effective conductivity of *ex vivo* ovine adrenal tissues will be exploited for the numerical simulations. The accurate dielectric values of the animal model adopted will enable a more reliable comparison between the numerical results and the data obtained from the experimental assessment;

- Relative permittivity and effective conductivity in the case of the adreno-cortical adenoma are lower compared to the dielectric properties of pheochromocytomas, paraganglioma and non-functioning adrenal nodules. The low dielectric values of the adenoma between 0.5 – 8.5 GHz are most likely attributable to the higher lipid content characterising some types of adreno-cortical adenoma;

Since the effective conductivity determines the SAR distribution over the tissue, the values of conductivity are highlighted at the frequencies of interest for MWA devices. It is worth noting that the conductivity at 5.8 GHz is 150% higher than the value at 2.45 GHz. This result would suggest that 5.8 GHz is worth investigating as a potential tool to obtain high and localised levels of SAR in adrenal tumours.

Chapter 4

Design of applicators and computational models for MWA

4.1 Introduction

Chapter 3 reported the relative permittivity and effective conductivity of ovine adrenal glands, as well as those of normal and diseased human adrenal tissues measured through the open-ended coaxial method. The study showed comparable dielectric properties between *ex vivo* human and ovine adrenal tissues within the frequency range from 0.5 GHz to 8.5 GHz. The results support the use of ovine adrenal models for pre-clinical assessing of MWA procedures on adrenal glands.

The dielectric properties of the target tissue are a key factor in assessing a MWA procedure. Other factors influencing the outcome of the MWA procedures include the design of the MWA applicator and the operating frequency. The influence of these factors is typically assessed through numerical methods aimed at modelling the distributions of the electromagnetic power and the increase of temperature over the region of interest [21], [144], [221], [222].

This chapter aims to illustrate the theoretical aspects of the electromagnetic modelling and the workflow adopted to design and prototype the MWA applicators used throughout this thesis. This chapter reviews:

- The cause-effect mechanisms underlying the interaction between biological tissues and electromagnetic fields. In addition, the numerical approaches to solve the electromagnetic and thermal problems are described;
- The performances of the applicators in terms of antenna reflection coefficient (S_{11}) and distribution of specific absorption ratio (SAR) over the tissue model. At this stage, liver is used as a testing model to evaluate the performances of each applicator in a homogeneous and well-characterised scenario [144], [223];
- The main parameters of influence on the temperature increase during MWA procedures. To this end, electromagnetic and thermal simulations were completed at

- 60 W for 60 s in the homogeneous tissue model, considered as a reference scenario. In this chapter, Section 4.1 reviews the principles of interaction between electromagnetic fields and biological tissues. The section also describes the numerical approaches to obtain the distribution of the electric field and the temperature over the region of interest. Section 4.2 presents the workflow adopted to model and prototype the MW applicators. The section also details the methodology used to set electromagnetic and thermal simulations aiming to reproduce *ex vivo* and *in vivo* experimental scenarios. Section 4.3 describes the performances of the proposed MW applicators and the relevant parameters of influence during MWA. In particular, the models for water vaporisation and for changes in the dielectric properties with temperature are discussed in relation to the designed frequency and to the power and time settings adopted in the thesis.

4.2 Biophysical mechanisms underlying MWA and mathematical expressions for the EM and thermal problem

4.2.1 Interactions between EM field and biological tissues

The therapeutic effect of MWA relies on the temperature increment induced by the electromagnetic (EM) field interacting with the biological tissues in the microwave
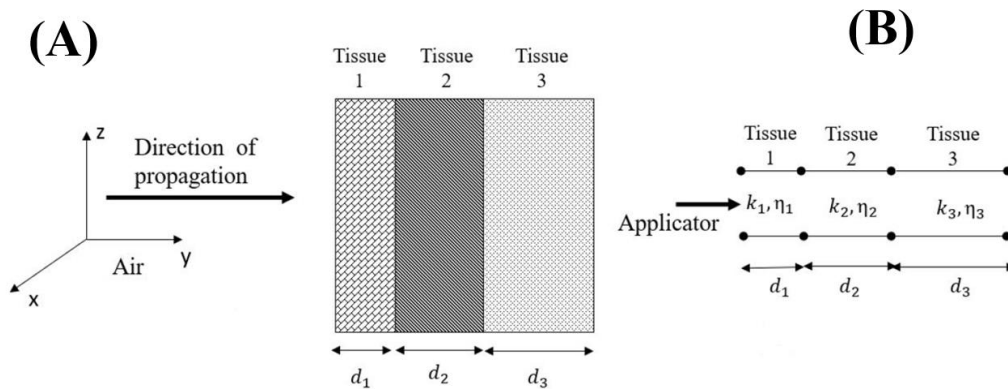
Figure 4.1: Electric field impinging perpendicularly on a multilayer structure where multiple tissues of different dimensions (d) are schematised as a succession of two-dimensional layers (A); representation of the equivalent transmission line where each tissue layer is identified by the specific propagation constant k and intrinsic impedance η (B).

frequency range. The increment of tissue temperature results from the absorption of the electromagnetic power. The amount of the electromagnetic power deposited in the biological tissue is evaluated numerically solving the Maxwell's equations. The actual configuration of the energy source in contact with the biological tissue should be accounted in the solution of the Maxwell's equations [224]–[226]. The antenna and the surrounding biological tissues are generally complex structures, which make the electromagnetic problem difficult to solve. A method used to simplify the study of the interactions between the EM field and the tissues is the assumption of a plane wave incident on a one-dimensional multi-layered structure, as represented in Figure 4.1 (A). The multi-layered structure can be studied using the equivalence with transmission line [227]. Each section of the transmission line represents a tissue layer, as depicted in Figure 4.1 (B). The propagation constant (k) and the intrinsic impedance (η) identifying each layer depend on the properties of the biological tissue. The direct wave impinging on the layer will split in a reflected wave and a wave which continues to propagate through the structure. Equations (4.1) and (4.2) express the reflected and directed waves.

$$V_i = V_i^+ e^{-jk_i r} + V_i^- e^{jk_i r} \tag{4.1}$$

$$I_i = \frac{V_i^+}{\eta_i} e^{-jk_i r} - \frac{V_i^-}{\eta_i} e^{jk_i r} \tag{4.2}$$

V_i^+ and V_i^- represent the amplitudes of the direct and reflected waves at the boundary between two adjacent layers; k_i and η_i are the propagation constant and the characteristic impedance described by equations (4.3) and (4.4).

$$k_i = \sqrt{\omega^2 \mu_i \varepsilon_i^*} \tag{4.3}$$

$$\eta_i = \frac{\mu_i}{\varepsilon_i^*} \tag{4.4}$$

μ_i and ε_i^* are the magnetic permeability and the complex permittivity (Equation (3.1)) of the specific tissue, ω (rad s^{-1}) is the angular frequency. As the biological tissues are lossy materials, while the waves propagate through a layer, the magnitude of the wave

decreases exponentially. The propagation constant k in a lossy material is indicated as a complex quantity $k = \beta - j\alpha$. Thus, equations (4.3) and (4.4) turn to equations (4.5) and (4.6).

$$V_i = V_i^+ e^{-\alpha_i r} e^{-j\beta_i r} + V_i^- e^{-\alpha_i r} e^{j\beta_i r} \tag{4.5}$$

$$I_i = \frac{1}{\eta_i} (V_i^+ e^{-\alpha_i r} e^{-j\beta_i r} - V_i^- e^{-\alpha_i r} e^{j\beta_i r}), \tag{4.6}$$

where α is the attenuation undergone by the wave while propagating in the tissue and β is the term indicating the phase of the electromagnetic wave. Equations (4.7) and (4.8) provide the mathematical expressions for the attenuation coefficient (α) and the propagation coefficient (β).

$$\alpha = \omega \sqrt{\frac{\mu_r \varepsilon_r}{2} \left(\sqrt{1 + \left(\frac{\sigma}{\omega \varepsilon_r} \right)^2} - 1 \right)}, \tag{4.7}$$

$$\beta = \omega \sqrt{\frac{\mu_r \varepsilon_r}{2} \left(\sqrt{1 + \left(\frac{\sigma}{\omega \varepsilon_r} \right)^2} + 1 \right)} \tag{4.8}$$

ε_r is the relative permittivity, i.e. the real part of the complex permittivity (ε^*), and (σ) is the effective conductivity (§ 3.1). Both attenuation coefficient (Equation 4.7) and propagation coefficient (Equation 4.8) depend on the dielectric properties of the tissue (ε_r, σ) and the frequency ($\omega = 2\pi f$) of the applied alternating electric field. In particular, the attenuation of the electromagnetic field and the phase shift undergone by the wave increase with the effective conductivity and the frequency (f). This is due to the dissipative nature of the tissue (§3.1).

When the electromagnetic wave propagates between two adjacent tissues with different dielectric properties, part of the electric field is reflected at the interface between the two layers. Equation (4.9) defines the reflection coefficient, which provides a measure of the wave reflected at the boundary between two tissue layers with respect to the incident wave.

$$S_{11} = \frac{V_i^-(r)}{V_i^+(r)} \tag{4.9}$$

For an electromagnetic wave propagating from a medium of intrinsic impedance η_1 to a medium of intrinsic impedance η_2, the reflection coefficient can be expressed as indicated in Equation (4.10):

$$S_{11} = \frac{\eta_{i+1} - \eta_i}{\eta_{i+1} + \eta_i} \tag{4.10}$$

In the case of two adjacent tissues characterised by similar dielectric properties (i.e. η_i is approximately close to η_{i+1}), the reflection of the electric wave is minimum.

In MWA procedures, a therapeutic applicator is inserted in the anatomical region of interest. The electromagnetic field is excited from the antenna at the designed operating conditions (i.e. frequency, power and time). Thus, part of the electric field is deposited in the tissues [224], [226]. The amount of EM energy absorbed by each tissue, and the consequent temperature increment are of particular relevance in thermal-based therapies such as MWA, as detailed below.

4.3 Definition of the EM and thermal problem

The distribution of the electric field over the region of interest derives from the solution of the Helmholtz's equation, expressed in homogeneous form by Equation (4.11). The equation considers the electric field vector ($\boldsymbol{E}$).

$$\nabla^2 \boldsymbol{E} - k_0^2 \left(\varepsilon_r - \frac{j\sigma}{\omega \varepsilon_0} \right) \boldsymbol{E} = 0 \tag{4.11}$$

k_0 (m^{-1}) is the propagation constant in the free space, ω (rad s^{-1}) is the angular frequency, μ_0 is the permeability of free space, ε_0 is the relative permittivity in free space, ε_r and σ (S m^{-1}) are the relative permittivity and the effective conductivity of the tissue.

The parameter commonly used to quantify the amount of electromagnetic energy deposited in the tissue is the specific absorption rate – SAR (W kg^{-1}) [224], [228]. SAR defines the power transferred in an infinitesimal volume of tissue divided by the mass of the object. Equation (4.12) provides the mathematical expression for SAR.

$$SAR = \frac{\sigma \, |\boldsymbol{E}|^2}{2\rho} \qquad (4.12)$$

σ (S m^{-1}) is the effective conductivity, $|\boldsymbol{E}|^2$ is the intensity of the electric field (V m^{-1}) and ρ (kg m^{-3}) is the density of the tissue. According to the Equation (4.12), SAR varies with the effective conductivity (σ). Therefore, tissues with higher water content (such as liver) are able to absorb a higher amount of electromagnetic energy when compared with tissues characterised by lower values of σ (such as fat).

Once SAR is known, the increase of temperature can be determined. The bioheat equation (BHE) described through Equation (4.13) links the rate of temperature increment to the heat accumulated per unit volume in each point of the tissue.

$$\rho c \frac{\partial T}{\partial t} = \nabla \cdot (k \nabla T) + \rho SAR + \rho Q - m_b \rho \rho_b c_b (T - T_b), \qquad (4.13)$$

T ($^\circ$C) is the temperature, t (s) is the time, k (W $^\circ$C^{-1} m^{-1}) is the thermal conductivity of the biological tissue, Q (W kg^{-1}) indicates the metabolic heat generation rate, SAR (W kg^{-1}) is the rate of absorption of the electromagnetic power by the biological tissues, m_b (m^3 kg^{-1} s^{-1}) is the blood mass perfusion rate, c_b (J kg^{-1} $^\circ$C^{-1}) heat capacity of the blood, ρ_b (kg m^{-3}) and ρ (kg m^{-3}) are the densities of blood and tissue respectively, T_b ($^\circ$C) is the temperature of the blood. Equation (4.13) shows the multiple factors that determine the increment of temperature other than the heat induced by the external source (SAR). Those factors include: the heat transfer via thermal conduction through the tissues ($\nabla \cdot (k \nabla T)$), the heat developed by the metabolic processes (ρQ), and the heat dissipated because of the blood flow through the tissues ($m_b \rho \rho_b c_b (T - T_b)$) [226], [229], [230].

For short durations ($\leq$30 s), the contribution of thermal conduction ($\nabla \cdot (k \nabla T)$) in Equation (4.13) is negligible. Thus, the initial increment of temperature over the time (slope) can be correlated to the rate of the absorbed electromagnetic power in the tissue. Under this condition, SAR can be derived according to Equation (4.14) [222], [231].

$$SAR = \frac{c \Delta T}{\Delta t} \qquad (4.14)$$

ΔT ($°C$) is the temperature increment, c (J kg^{-1} $°C^{-1}$) is the specific heat capacity of the tissue and Δt (s) is the time interval within which the increment of temperature ΔT is measured. With a longer time of exposure, the heat transfer associated with the thermal conduction of the tissue becomes dominant, and the temperature increases non-linearly.

4.3.1 Numerical solution of the EM and thermal problem

As observed so far, the solution of the EM and thermal problem is provided from the Maxwell's equations and the BHE equation respectively. Several numerical techniques were developed to solve the EM and thermal problem. Within them, the Finite Difference (FD) decomposition is the method widely adopted to approach the EM problem expressed in time domain and the thermal problem [225]. Equation (4.15) describes finite-difference (FD) decomposition along *x* direction in a general form (F represents the function of interest, i.e. electric field, temperature). The same expression is used to discretise the space also along *y* and *z* dimensions.

$$\frac{\partial F(x,y,z,t)}{\partial x} = \frac{F\left(x + \frac{\Delta x}{2}, y, z, t\right) - F\left(x - \frac{\Delta x}{2}, y, z, t\right)}{\partial x} \tag{4.15}$$

For the EM problem, the FD method requires the expression of the electric and magnetic field of Maxwell's equations in time domain (TD). Thus, each component of the electric and magnetic field at a specific time point is calculated as a function of the adjacent component obtained in the previous time point. The calculation domain is divided in a finite number of cuboid cells, and the EM field is considered uniform within each cell. Therefore, a single meshing cell can be filled by a unique material. The solution of the thermal problem is found using the explicit FD method, as expressed by Equation (4.15). Another method used to calculate the solutions of the electromagnetic and thermal problem is the Finite Integration technique (FIT). For the EM problem, FIT calculates the electric field and magnetic field by solving the Maxwell's equation in time domain, as observed also for finite-difference time-domain (FDTD). However, in the case of FIT, the Maxwell's equations are solved in the integral form rather than the differential form. The electric and magnetic fields are calculated through the integral over each cell discretising the model [232]. As a result, FIT provides a better approximation of curved

and complex geometries (i.e. characterised by multiple materials), overcoming the 'staircase' effect resulting from the simplification of the geometry occurring with FDTD.

Once the distribution of the electric field over the region of interest is obtained, the distribution of SAR can be calculated according to Equation (4.12). Then, the solution of the EM problem is coupled to the BHE as described by Equation (4.13), which provides the distribution of temperature.

In this thesis, a three dimensional (3D) full-wave electromagnetic software (CST MWS Suite 2018, Darmstadt, Germany) based on FIT algorithm is used. The tissue model is discretised accounting for at least ten cells per wavelength considering the shortest wavelength. This standard was adopted in order to achieve a sufficient level of accuracy in the results [233]. As the wavelength depends on the relative permittivity of the material, it is worth noticing the importance of the dielectric properties of the material under test as input parameters for the electromagnetic simulations. In addition, the smallest size of the mesh cells is determined by the least relevant geometrical detail of the geometry that needs to be discretised for the simulation [222]. In MWA application, the smallest relevant features are related to the components of the MW applicator. To limit the computational domain, absorption boundary conditions (ABCs) need to be specified at the edges of the model. Perfectly matched layer (or 'open' condition) is the boundary condition adopted to minimise the reflection of the electromagnetic waves while propagating within the geometrical domain.

The EM simulation will stop when the energy decayed to the user-defined level (generally lower than -40dB), described as the convergence level. The faster the time-domain signal propagates through the model, the faster the simulation will provide the numerical solution. However, the maximum time-step should satisfy the stability condition expressed by Equation (4.16).

$$\Delta t_{max} \leq \frac{1}{u_{max}} \frac{1}{\sqrt{\frac{1}{\Delta x^2} + \frac{1}{\Delta y^2} + \frac{1}{\Delta z^2}}} \tag{4.16}$$

u_{max} is the propagation velocity of the wave through the model, which is determined by the material properties; $\Delta x, \Delta y, \Delta z$ are the size of the meshing cells. According to
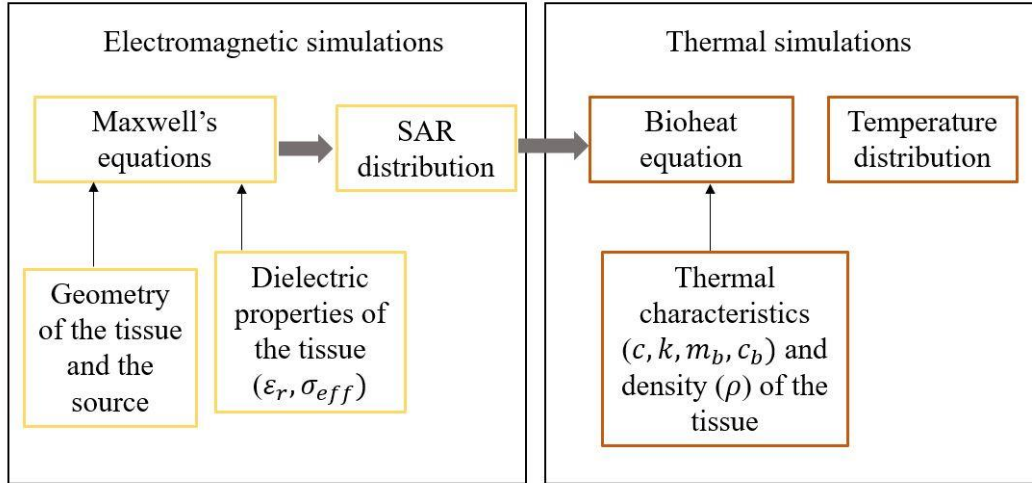
Figure 4.2: Workflow of the numerical electromagnetic and thermal simulations: the calculation of SAR is performed through the electromagnetic simulations considering the model of the tissue and of the antenna other than the dielectric properties of the tissue as input parameters; then SAR distribution is the input parameter for the bioheat equation other than the thermal properties and the density of the tissue model, to calculate the distribution of temperature.

Equation (4.16), the maximum time-step is determined by the size of the meshing cells: the smaller the meshing cell, the smaller the time-step must be. In the case of geometries discretised by cells varying in size, the time-step is determined by the mesh cell with the smallest dimension.

Convective boundary conditions expressing the continuity of the heat flow perpendicular to the external surface of the geometry should be settled for the solution of the thermal problem, according to Equation (4.17) [234].

$$-k \left.\frac{\partial T(r)}{\partial n}\right|_S = h \left(T(r) - T_e\right) \qquad (4.17)$$

n is the vector perpendicular to the boundary of the surface S, r is the vector indicating the position in the space domain, h (W m^{-2} °C^{-1}) is the convection coefficient and T_e (°C) is the temperature of the surrounding environment. Figure 4.2 summarises the workflow for the electromagnetic and thermal numerical simulations used for this study.

4.4 Applicators for MWA

In MWA, the EM field is applied by interstitial applicators that generally consist of feeding transmission lines terminated by a radiating element, i.e. an antenna. Dipoles and
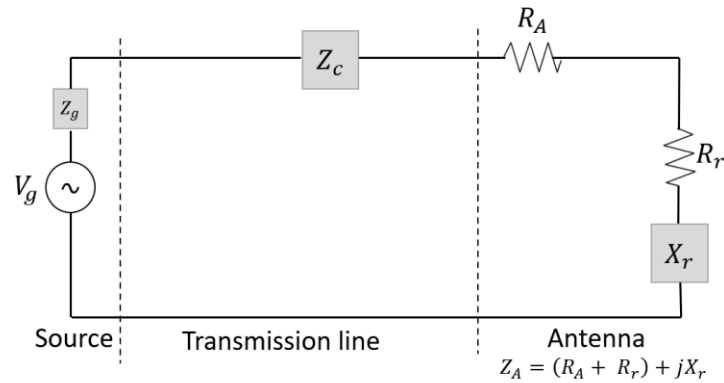
Figure 4.3: Equivalent circuit representing the transmitting system of the electric field to be radiated by the antenna. The circuit is composed by the voltage of the generator, the intrinsic impedance of the transmission line and the impedance of the antenna. The impedance of the antenna accounts for the losses due to conductive materials of the antenna and the impedance associated to the radiation of the antenna.

monopoles are the types of antenna mostly used for MWA [225]. The dipole antenna is important for theoretical reasons because any other linear antenna, such as monopole, can be derived from a dipole structure. Thus, the basic radiation concepts of a dipole antenna can be also extended to the monopole.

Both for dipole and monopole antennas, the feed point is connected to a transmission line, which guides the electromagnetic energy from the MW generator to the antenna. Figure 4.3 shows the equivalent circuit representing the source of energy, the transmission line and the radiating element. The source is represented by an ideal generator and the related impedance (Z_g), Z_c indicates the characteristic impedance of the transmission line and Z_A is the impedance of the antenna, i.e. the load of the transmission line. The impedance of the antenna accounts for the resistive losses (R_A) due to the antenna structure and the radiation impedance $(R_r + jX_r)$. The voltage applied across the two conductors of the transmission line creates a travelling wave current. Because the two conductors are parallel, the field radiated by the first wire is essentially cancelled out by the field radiated by the second wire, thus no net radiation occurs. When the terminating part is approached, the radiation begins, as the electromagnetic field generated is not cancelled by the second wire. Under ideal circumstances, the energy provided by the generator should be transferred to the antenna. However, several losses

77

are generated by the mismatch between the transmission line and the antenna. The amount of the reflected wave generated at the load is quantified through the reflection coefficient, according to Equation (4.9).

The antenna radiation pattern is defined as the representation of the radiation properties of the antenna as a function of the space coordinates. Both dipoles and monopoles provide omnidirectional radiation pattern. Omnidirectionality consists of an infinite number of principal planes for the electric field and the single plane for the magnetic field. Thus, along the direction of the antenna there is no radiation, while the maximum radiation lies along the orthogonal planes where symmetric radiation patterns are observed [225]. A graphical representation of the omnidirectional pattern is provided in Figure 4.4. In this figure, the plane related to the electric field (E) is *xz-plane*, while the reference plane for the magnetic field (H) is *xy-plane*. In the space surrounding the antenna, three different regions can be identified: the reactive near-field, the radiated near field and the far-field regions. The reactive near field region is the portion of space immediately surrounding the antenna, where the magnitude of the electric field varies with the spatial coordinates. The radiating near field is the intermediate region between the reaction near field and the far field. Far field is the region where the angular field distribution is essentially independent of the distance from the antenna. Generally, this region exists at distances greater than $\frac{2D^2}{\lambda}$, where D is the maximum dimension of the antenna. In the case of MWA, the distribution of the electromagnetic energy within the tissue is highly dependent of the antenna-tissue interactions, falling within the near field conditions [197], [227], [235]. The performances of the antennas used for MWA must be evaluated considering the matching characteristics of the target tissue, and the behaviour of the antenna when the physical properties of the surrounding tissue change. Further factors to be evaluated include the shape and dimension of the tissue, and the orientation of the antenna with respect to the target.

For MWA applications, dipoles or monopoles are generally fabricated from coaxial cables. Dipole antennas are created by connecting the inner conductor of a coaxial cable with the outer conductor of another cable with a known length. Thus, one arm of the dipole antenna is the feeding line [236], [237]. Monopole antennas are commonly made

by removing the outer conductor of a semirigid coaxial cable and exposing the length of the central conductor at a designed length [225]. In both dipole and monopole antennas, the insertion depth of the applicator into the biological tissue influences the reflection coefficient and deposition of SAR. This is caused by an unsuitable match of the antenna with the surrounding material, which results in reflected currents along the coaxial cable. Strategies to limit these problems include the use of a third metallic axis [238], [239] or a choke [237], [240]. In the case of the third axis, the residual currents flowing along the external surface of the coaxial cable are shielded by the third axis. In the case of the choke, a metallic cable of $\frac{\lambda}{4}$ length is soldered on the surface of the coaxial line, such that an open-end impedance is seen from the antenna to the feed line. Thus, the insertion depth has no influence on the input impedance of the applicator.

In this thesis, a monopole antenna is used. The relatively simple design of the monopole allows for easier miniaturisation, manufacturing and optimisation of the cooling path. Finally, monopole antennas exhibit lower sensitivity in the reflection coefficient with
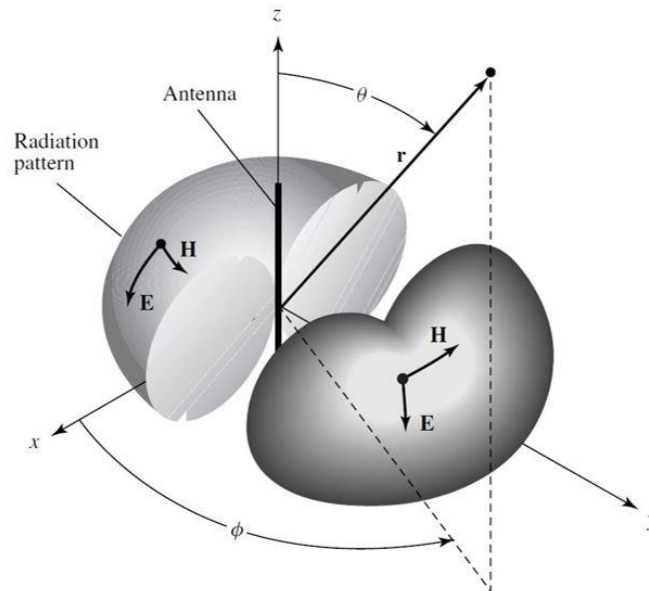
Figure 4.4: Graphical representation of the omnidirectional pattern provided by a dipole antenna, where *xz*-planes refer to the electric field (E) and *xy*-plane refers to the magnetic field (H). The omnidirectional patterns are characterised by infinite reference planes of the electric field and one reference plane for the magnetic field, while along the direction of the antenna no radiation is provided. The figure is obtained from [225].

respect to the dielectric properties of the surrounding medium when compared with dipoles [241].

4.5 Methodology

4.5.1 Antenna models

Three different antennas are now described, which will be employed in the following chapters: a coaxial monopole antenna operating at 2.45 GHz, a triaxial monopole antenna operating at 2.45 GHz and a triaxial monopole antenna operating at 5.8 GHz.

Numerical modelling. In this work, MW applicators were modelled within CST MWS software. The first objective was to establish the suitable length of the radiating element. To this end, a parametric simulation was used within the appropriate frequency range. Frequency ranges from 0.5 to 3 GHz and from 4 GHz to 6.5 GHz were considered to include 2.45 GHz and 5.8 GHz operating frequencies, respectively. The length (l_r) of the radiating element was optimised in order to obtain 1) the minimum value in amplitude of the reflection coefficient (S_{11}) at the operating frequency; 2) values of the S_{11} lower than -10dB within the largest possible bandwidth. The resonance of the reflection coefficient over the selected frequency band was evaluated for different lengths of the radiating element: from 1 mm to 10 mm at 0.5 mm step. The analysis was conducted considering the model of the applicator inserted in a 60 mm cube of water (ε_r =83.0; σ = 1.4 S m^{-1} at 2.45 GHz, ε_r =78.0; σ = 7.1 S m^{-1} at 5.8 GHz). Each applicator was placed in water with an insertion depth of 30 mm; such length was measured between the insertion point and the feed of the applicator. Then, the insertion depth was reduced from 30 mm to 15 mm to evaluate the effect of the insertion depth on the reflection coefficient for each applicator. The maximum threshold for the reflection coefficient amplitude was set at -10 dB, which corresponds to 10% in reflected power. In the case of triaxial applicators, a stainless-steel cable was added to the coaxial monopole structure to limit electrical currents flowing along the outer conductor of the coaxial cable. Those backwards electrical currents resulted from the impedance mismatch between the transmission line and the radiating element. Because of resistive losses occurring in the metallic cable, the backward electrical currents can induce overheating of the cable and the surrounding tissue. A further parametric study was conducted to evaluate the optimal

distance (d) of the third metallic cable from the feed of the antenna. To this end, the amplitude of the reflection coefficient and the resonance shape were evaluated considering seven different positions (0:0.5:3 mm) for the triaxial cable with reference to the feed point. Two concentric polyamide tubes embedded in the coaxial structure were also modelled, to account for the cooling system. For each antenna design, a fully cooled applicator was used to limit the increase of the temperature within the cables. The water acts as a matching medium, preventing detuning between the antenna and tissue during the procedure. The temperature of the water circulating in the cooling system was set equal to 18°C, to provide a suitable refrigeration. Convective boundary conditions represented by Equation (4.17) were applied between the external surface of the applicator and the tissue. The convection coefficient h was set equal to 1000 (W m^{-2} °C^{-1}) to account for the forced convection induced by the cooling system [234]. Figure 4.5 shows the fully cooled monopole coaxial applicator (A) and monopole triaxial applicator (B) both in the longitudinal and cross sections.

Experimental setup. The designed applicators were then fabricated by exposing the suitable length for the radiating element (l_r) from the inner conductor of a semirigid
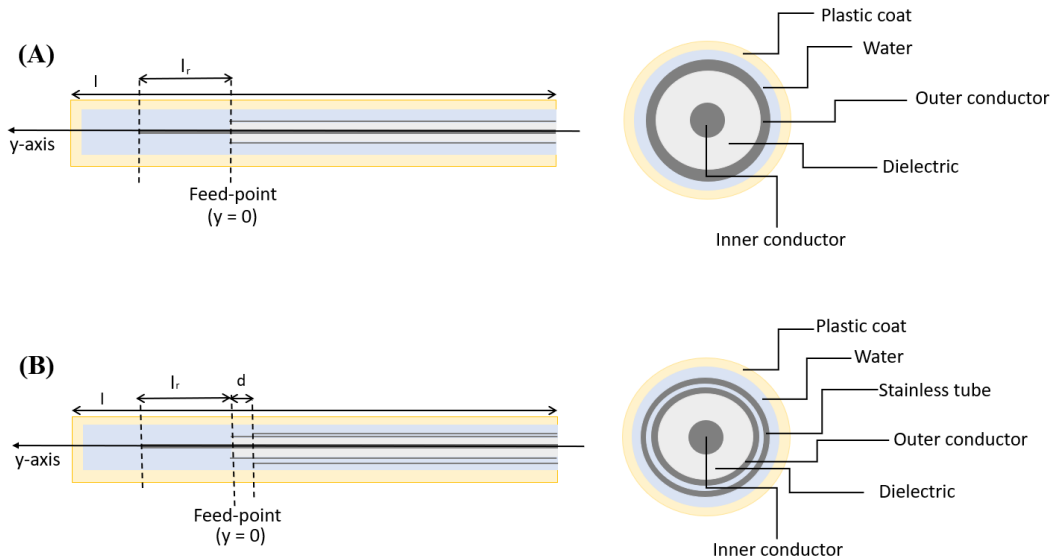
Figure 4.5: Schematisation of a coaxial monopole applicator (A) and a triaxial monopole applicator (B) provided in longitudinal (left) and transversal (right) sections. The length of the radiating element (l_r) and the overall length (l) are highlighted for the two applicators. In the case of the triaxial structure, the distance (d) of the third metallic cable from the feed-point is indicated. For both applicators, an integrated water refrigerating system was modelled.

coaxial cable. A SMA connector was connected to the input of the coaxial transmission line, to power the antenna by the MW generator (Sairem, SAS, France). The SMA connector of the antenna was connected to the MW generator through a low loss coaxial cable. The impedance matching of the fabricated antennas was evaluated in terms of reflection coefficient (S_{11}), by connecting the antenna to an antenna analyzer (Rohde & Schwarz® ZVH8 100 kHz – 8 GHz). A full one-port calibration of the analyser was performed, considering three different calibration standards: open circuit, short circuit and 50 Ω load. Five measurements were conducted loading the test device (ablation antenna) with water at room temperature. The values of reflection coefficient were recorded at 201 linearly spaced frequency points over 0.5 – 3 GHz or 4 – 6.5 GHz, depending on the operating frequency. The design of the applicator was completed with the cooling system. In the case of a monopole applicator, two polyimide tubes were used to provide the inward and outward path for the cooling water. In the case of triaxial design, the stainless tube was used to provide the inward path, while an external polymide casing was used for the outward water flow.

Table 4.1 summarises the geometrical characteristics of each applicator. The table includes the length of the radiating element and the distance of the third cable from the feed-point, which were optimised during the numerical modelling. The table also reports the overall length of each applicator and the type of coaxial cable used.

Cable losses and passive heating. A further numerical analysis was conducted to evaluate the power losses occurring along the length of the cable in the real scenario. Losses, named also as attenuation, are defined in manufacturer datasheets of the coaxial cable as decibel (dB) per unit length expressed at given frequencies [242]. The resistive losses due to the electrical current flowing in the conductive materials vary depending on the operating frequency and on the diameter of the metallic cables. In this study, the losses of each coaxial cable were calculated based on the specifications included in the datasheet. For each applicator, the power losses were provided at the corresponding operating frequency. The calculation of the power losses along the cable enables to set the appropriate power at the MW generator in order to obtain the suitable power at the tip of the antenna, according to the experimental protocol.

Table 4.1: Characteristics of a monopole coaxial applicator operating at 2.45 GHz (first line), monopole triaxial applicator operating at 2.45 GHz (second line), monopole triaxial applicator operating at 5.8 GHz (third line). For each applicator, the descriptive information reported include: the type of coaxial cable (third column), the length of the radiating element (fourth column), the distance of the third cable from the feed-point (fifth column), the length of the entire applicator (sixth column).

Applicator	Operating frequency	Type of coaxial cable	Length radiating element (l_r)	Feed - triaxial base distance (d)	Overall length (l)
Monopole coaxial applicator	2.45 GHz	*UT-047 [242]	6 mm	-	190 mm
Monopole triaxial applicator	2.45 GHz	**UT-020 [242]	6 mm	0.5 mm	220 mm
Monopole triaxial applicator	5.8 GHz	‡UT-034 [242]	3 mm	0.5 mm	165 mm

*cable outer diameter = 1.194 mm; **cable outer diameter = 0.584 mm; ‡cable outer diameter = 0.864 mm

4.5.2 Framework for EM and thermal simulations

After the optimisation procedure, each modelled applicator was immersed in a 60 mm cube of material mimicking liver. Liver represents a control scenario for MWA, thanks to its homogeneity and well-known dielectric and thermal characteristics [136], [221], [243], [244]. Table 4.2 lists thermal and dielectric properties of the tissue model used for the numerical simulations, as reported in [245].

The initial temperature of the tissue model was set at 25°C. The convection coefficient in the boundary conditions expressed by Equation (4.17) was set equal to 20 (W m^{-2} °C^{-1}), to account for the air-free convection between the tissue model and the surrounding medium [141], [234].

The models were meshed in order to have a finer mesh in the regions characterised by the smallest size, (i.e. within the antenna) and a coarser mesh in the homogeneous tissue. First a minimum meshing size was considered (i.e. ten cells per wavelength in the tissue model). The number of cells per wavelength was then increased until two consecutive simulations showed a discrepancy in the amplitude of the reflection coefficient lower than 0.1% between (Cauchy convergence test) [222].

Table 4.2: Dielectric and thermal properties at room temperature of liver employed in the numerical simulations. Relative permittivity and effective conductivity are provided at the two operating frequencies adopted, 2.45 GHz and 5.8 GHz.

Parameter	Liver	
Frequency (GHz)	2.45	5.8
Relative permittivity, ε_r	43.0	38.0
Effective conductivity, σ_{eff} (S/m)	1.7	4.6
Heat capacity, c (J kg^{-1} °C^{-1})	3540	3540
Thermal conductivity, k (Wm^{-1}K^{-1})	0.39	0.39
Density, ρ (kg m^{-3})	1079	1079

Electromagnetic and thermal-transient simulations were executed as schematised in Figure 4.2. The distribution of SAR was calculated as expressed by Equation (4.12) considering 60 W delivered for 60 s. Then the temperature in the tissue model was obtained by solving the BHE (4.13).

Tissue-descriptive parameters. The increase of temperature in proximity to the applicator may induce changes in the characteristics of the tissue during the MWA procedure. These changes should be accounted for in the numerical simulations, as they may affect the distribution of the electromagnetic energy and the increase of temperature. In [143], [144] relative permittivity and effective conductivity were measured in liver during a MWA procedure performed at 2.45 GHz. In both studies the experimental values of relative permittivity and effective conductivity were fitted over the temperature. As a result, both [143], [144] developed mathematical functions describing the changes in dielectric properties with the increase of tissue temperature. It is noteworthy that the above-mentioned models were developed following MWA procedures only at 2.45 GHz. The same models may be not suitable to reproduce the changes in the dielectric properties occurring during MWA procedures conducted at 5.8 GHz. Water loss due to vaporisation is another effect resulting from the increase of tissue temperature. In [145] the losses in water content over the temperature were considered for a MWA procedure conducted at 2.45 GHz in a bovine liver tissue. The water losses due to phase change from liquid to vapour, and the release of water through condensation, were modelled in BHE as a change in specific heat of the tissue.

In this work, the above-mentioned temperature-dependent models for relative permittivity and effective conductivity [143], [144] were neglected in the numerical simulations. Firstly, the lack of available data at 5.8 GHz makes the temperature-dependent models unsuitable for operating frequencies different from 2.45 GHz. Secondly, the studies [142], [143] show a relatively small influence of those models on the increase in temperature within 60 s (Appendix B). Based on those evaluations, first standard BHE (Equation 4.13) was implemented neglecting the terms for blood perfusion and metabolic heat to reproduce the *ex vivo* conditions.

Then, a modified BHE was used to account for the vaporisation phenomena when temperatures approached 100°C. BHE was modified to incorporate a model for changes in specific heat of the tissue linked to the water vaporisation. This study adopted the model reported in [142] to describe the changes in water content (W) over the temperature. The expression (4.18) also represented in Figure 4.6 described the changes in the tissue's water content over the temperature.
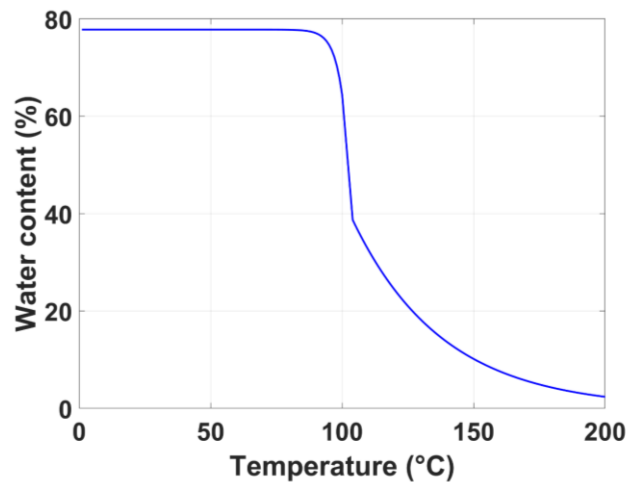
Figure 4.6: Percentage of the water content in the tissue modelled over the temperature according to the model expressed in [142]. A starting water content of 80% was considered as baseline condition. Then, this content drops when temperature approaches 100°C, due to water vaporisation. Ultimately, a decrease in water loss with a slower rate is modelled after 104°C in order to account for the release of water through the tissue due to condensation.

$$\begin{cases} 0.778 \cdot \left(1 - e^{\frac{T-106}{3.42}}\right) & 70°C \leq T < 100°C \\ 7.053 - 0.064096 \cdot T & 100°C \leq T < 104°C \\ 0.778 \cdot e^{-\frac{T-80}{34.37}} & T \geq 104°C \end{cases} \tag{4.18}$$

The above model defined the modified specific heat in agreement with [145]:

$$c' = c - \frac{\alpha}{\rho} \frac{\partial W}{\partial T} \tag{4.19}$$

Where c is the specific heat of tissue at room temperature, α indicates the water latent heat constant which is equal to 2260 (kJ kg^{-1}), T (°C) is the temperature and W is the percentage of water content (Figure 4.6). The derivative of water content (W) over the temperature was implemented in the thermal simulations to solve the BHE. The numerical study was conducted considering 60 W, radiated by the antenna for 120 s. A longer time window was set in order to observe the mechanism of influence of the vaporisation including the temperatures (100°C $\leq$ T > 104°C) at which the drop in the water content of the tissue occurs. The temperature was evaluated at three different radial distances from the feed-point: 2 mm, 4 mm, 7 mm. The temperature values obtained by the standard BHE equation were then compared with those achieved using the vaporisation model in BHE.

In BHE, the blood flow rate through the tissue was considered to better represent the *in vivo* scenario. Chapter 7 is devoted to discussing the influence of blood perfusion on the increase of temperature, in the scenario of interest (adrenal gland).

4.6 Results

4.6.1 Antenna performances

Reflection coefficient. Figure 4.7 shows the amplitude of the antenna reflection coefficient obtained for the monopole coaxial applicator operating at 2.45 GHz (A), for the monopole triaxial applicator operating at 2.45 GHz (B), and for the monopole triaxial applicator operating at 5.8 GHz (C) inserted in water. The antenna reflection coefficients are reported within the frequency range suitable to include the MWA operating frequencies discussed in this thesis, i.e. 2.45 GHz (A) – (B) or 5.8 GHz (C). The

numerical results refer to two different insertion depths of each applicator inserted in water: 30 mm and 15 mm. Ablation antennas are inserted in biological tissues which vary depending on the composition, thus it is important to acknowledge the impact of the antenna insertion depth. A broad bandwidth of the antenna is desirable; this requirement is to ensure a good match between the antenna and the tissue regardless of any variation in the characteristics of the tissue. All the applicators show values of reflection coefficient lower than -10 dB at the frequencies of interest. Values of the refection coefficient lower than -10 dB expand from 1.5 GHz to 3 GHz, for the monopole coaxial applicator. In the case of the triaxial applicators, reflection coefficients are lower than -10 dB from 2.2 GHz to 3 GHz (B) and from 4.5 GHz to 6.2 GHz (C). It can be observed that for the two applicators operating at 2.45 GHz, numerical results show a narrower bandwidth in the case of the triaxial structure. But in the coaxial applicator, the insertion depth influences the amplitude of the reflection coefficient and the resonance shape (Figure 4.7 (A)). Changing the insertion depth from 30 mm to 15 mm, the amplitude in reflection coefficient increases from -23 dB to -17 dB at 2.45 GHz and spurious peaks appear in the shape of resonance around 2.45 GHz. However, the reflection coefficient is lower than the threshold fixed at -10 dB both at 30 mm and 15 mm of insertion depth. In the triaxial structure, the amplitude of the reflection coefficient and the resonance shape is independent from the insertion depth. Triaxial applicators guarantee a better
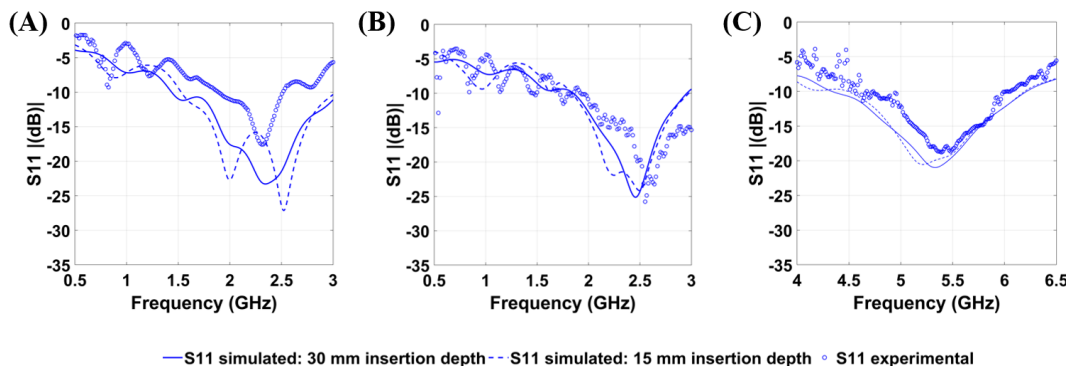
Figure 4.7: Comparison in terms of reflection coefficients between a monopole coaxial applicator operating at 2.45 GHz (A), a monopole triaxial applicator operating at 2.45 GHz (B) and a monopole triaxial applicator operating at 5.8 GHz (C). The amplitude of the reflection coefficients (dB) is provided over the 0.5 – 3 GHz in order to include 2.45 GHz (A) – (B) and over 4 – 6.5 GHz (C) in order to include 5.8 GHz.
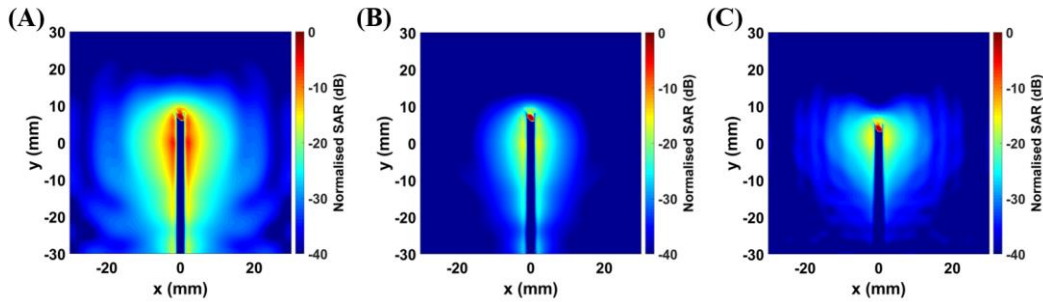
Figure 4.8: Comparison in terms of SAR obtained in a homogenous tissue model between a monopole coaxial applicator operating at 2.45 GHz (A), a monopole triaxial applicator operating at 2.45 GHz (B) and a monopole triaxial applicator operating at 5.8 GHz (C). Values of SAR are normalised and expressed in decibel (dB). The results are presented on the frontal plane (xy-plane) with reference to the longitudinal axis (y-axis) of the applicator.

match between the feed line and the antenna, independent of the insertion depth of the applicator in the tissue. Thus, higher energy can be deposited in the tissue, allowing the focusing of most of the SAR around the tip of the radiating element. The reflection coefficients of the antennas described in the chapter were validated experimentally as reported in Figure 4.7.

SAR. Figure 4.8 illustrates numerical SAR distributions obtained over a homogeneous material (liver) by the monopole coaxial applicator at 2.45 GHz (A), the monopole triaxial applicator at 2.45 GHz (B) and the monopole triaxial applicator at 5.8 GHz (C). The distributions of SAR provide information regarding the ability of each applicator to deposit the electromagnetic field in the tissue surrounding the radiating element. All SAR values are normalised with respect to the maximum values in the *xy*-plane. The monopole coaxial applicator (Figure 4.8(A)) shows SAR values along the feed line higher than those observed in the triaxial applicator (Figure 4.8(B)) operating at the same frequency, i.e. 2.45 GHz. For the monopole coaxial applicator, SAR higher than -20 dB are visible along the overall length of the applicator. In the triaxial applicator, values of SAR higher than -20 dB are confined within 15 mm below the feed point. Figure 4.8 (C) shows values of SAR higher than -20 dB extend no further than 8 mm along the longitudinal distance from the feed point, when the operating frequency is 5.8 GHz.

These results highlight the ability of the third metallic axis to reduce the backward currents arising at the feed-point because of the impedance mismatch between the

transmission line and the radiating element. As a result, most of the SAR is focused around the tip of the antenna in the case of triaxial applicator. The sphericity in the SAR profile is enhanced, increasing the operating frequency from 2.45 GHz to 5.8 GHz. The short length of the radiating element (3 mm) compared with the length used at 2.45 GHz (6 mm) contributes to the spherical pattern of SAR. In addition, a higher operating frequency provides a faster deposition of the electromagnetic power in the tissue, because of the higher effective conductivity of the tissue at higher frequencies (Table 4.2).

On the other hand at 5.8 GHz, an higher attenuation in power is achievable along the coaxial cable compared with 2.45 GHz. The diameter of the coaxial cable is another factor that can contribute to the increase in power attenuation. The following section discusses the influence of the operating frequency and geometry of the feeding cable on the power losses.
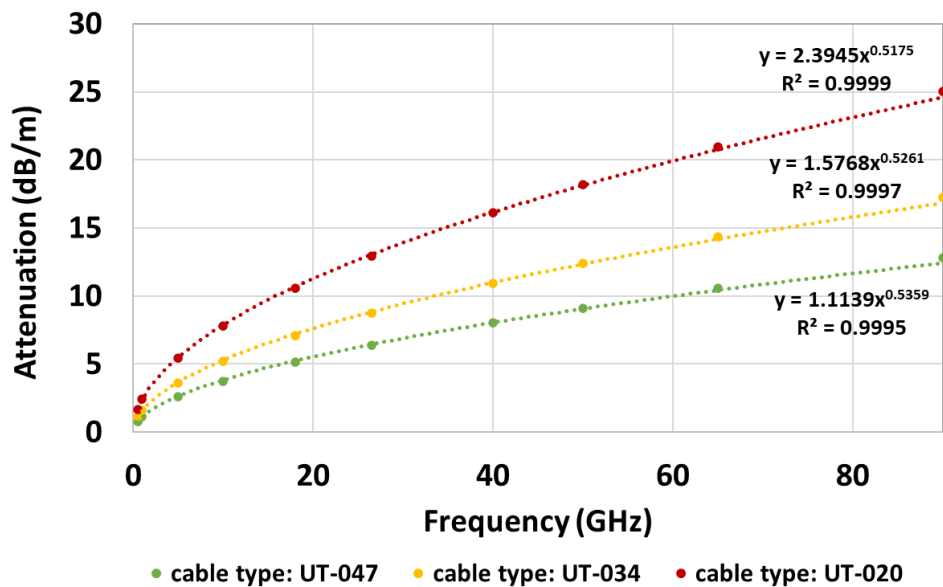
Figure 4.9: Representation of the power attenuation (dB/m) provided by the manufacturer datasheet of each coaxial cable at different frequencies (marker). Then, the values of power attenuation were interpolated over the frequencies. The equations describing the trend and the related squared error are indicated for each cable. The coaxial cables reported are: UT-047 (green) used to fabricate the monopole coaxial applicator operating at 2.45 GHz; UT-020 (red line) used to fabricate the monopole triaxial applicator operating at 2.45 GHz; UT-034 (yellow line) used to fabricate the monopole triaxial applicator operating at 5.8 GHz.

Cable losses. Figure 4.9 shows the power attenuation along each semi-rigid coaxial cable used to fabricate the above-mentioned MW applicators. The attenuation is expressed in decibels per unit of length (meter – m) over 0.5 – 90 GHz frequencies, as reported in the datasheet of each type of cable [242]. Losses in power depend on different factors. Resistive losses and resulting heating are caused by the dissipation of the current flowing into the conductor materials. Generally, the resistive losses rise with the increase in frequency and with the decrease of the area of the conductor cable [225]. The equations fitting the data reported in each manufacturer datasheet (Figure 4.9) show that resistive losses increase with respected to the root square of the frequency. Such equations are used to calculate the losses (attenuation) for each MW applicator described in this work, considering the type of coaxial cable and the operating frequency. Table 4.3 reports the losses along each realistic length of the applicator. Given the losses calculated for each cable, the power was set on MW generator in order to ensure the designed power at the tip of the antenna. Coaxial cable with the largest diameter, i.e. UT-047, shows a percentage in losses over the overall length below 8%. For UT-020, the increase in the percentage losses per unit length is correlated to the smaller diameter of the cable. Similar percentage losses per unit length are observed in the case of UT-034 cable. In the latter,

Table 4.3: Calculation of the power losses (%), for each type of applicator operating at the designed frequency. The percentage losses were calculated according to the datasheet of the coaxial cable used to fabricate each applicator. Depending on the power needed at the tip of the antenna, the power at the MW generator was set accounting for the attenuation occurring along the length of the coaxial cable. Specifically, two powers were accounted at the tip of the antenna: 30 W and 60 W.

Applicator	Frequency (GHz)	Coaxial cable	Outer Diameter (mm)	Losses unit length (%)	Overall length (mm)	Losses length (%)	Power generator (W)		Power antenna tip (W)	
Monopole coaxial applicator	2.45	UT-047 [242]	1.194	0.04	190	7.6	32	64	30	60
Monopole triaxial applicator	2.45	UT-020 [242]	0.584	0.08	220	17.8	35	71	30	60
Monopole triaxial applicator	5.8	UT-034 [242]	0.864	0.09	165	14.2	34	68	30	60

the resistive losses are mainly associated with an increase of the operating frequency instead of the diameter of the cable, which is comparable to the cable UT-047. Overall, coaxial cables with larger diameters ensure better operative conditions. This is due to the robustness of the applicator to the resistive losses. However, a reduced section of the cable is desirable for a less invasive applicator to be inserted in the target tissue. In the following chapters of the thesis, coaxial cable larger in diameters were adopted for *ex vivo* applications. The coaxial cable with a smaller diameter was preferred for the *in vivo* test. This was to reduce the invasiveness of the MWA procedure, especially in the presence of relatively small organs such as adrenal glands.

4.6.2 EM and thermal simulations: factors of influence

Figure 4.10 compares the temperature values achieved by the standard BHE and the BHE implementing the vaporisation model for two operating frequencies, 2.45 GHz and 5.8 GHz. At 2.45 GHz, the values of temperature reached considering the vaporisation model differ less than 0.5°C from those achieved through the standard BHE. Overall, the temperatures remain below 70°C within the considered time interval. Thus, vaporisation has a null impact at 2.45 GHz for the power and time set. Increasing the frequency from 2.45 GHz to 5.8 GHz, higher temperatures are observed. At 2 mm and 4 mm distance from the feed point, temperatures reach 101°C and 90°C after 120 s respectively, in the case of standard BHE. Such temperatures decrease to 87°C and 85°C, when water vaporisation model (Equation 4.24) is implemented in the numerical simulations. At further distances from the feed point, vaporisation has a poor impact because of the lower temperatures reached (< 70 °C). At 7 mm, the temperature achieved through the modified BHE differ less than 2°C from the value obtained through the standard BHE. Results show a considerable impact of the vaporisation model when severe temperature increases (above 70°C) are observed. In particular, when water vaporisation is considered in the numerical simulations, the results show a plateau when temperature approaches 100°C, as observed in [142]. When the vaporisation model is neglected in the numerical simulations, the temperature increases steadily beyond 100°C. The plateau in temperature is linked to the increase in the specific heat capacity of the tissue due to

water vaporisation (4.25). At approximately 100°C, the thermal energy supplied is partially spent for the transition phase of water from liquid to vapour.
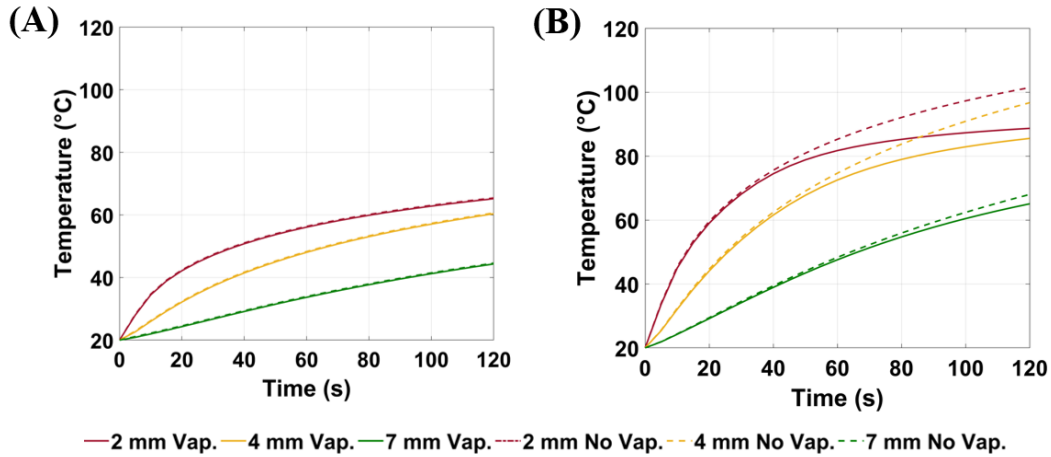
Figure 4.10: Comparison between temperatures achieved through standard BHE (dot line) and BHE implementing vaporisation model (solid line) at 2.45 GHz (A) and 5.8 GHz (B). Values of temperature are monitored up to 120 s at three radial distances from the feed point of the antenna: 2 mm (red line), 4 mm (yellow line), 7 mm (green line).

For the power and time setting adopted in the thesis, vaporisation plays a critical role in the increase of temperature only at 5.8 GHz. Thus, the vaporisation model is adopted for the studies conducted at 5.8 GHz for the development of more accurate numerical models (see Chapter 8); while vaporisation is absent for the studies conducted at 2.45 GHz (Chapter 5–7).

4.7 Conclusions

This chapter describes the numerical and practical approaches adopted to model and prototype the MW applicators used in the following chapters of this thesis. This chapter also discusses the criteria adopted to set electromagnetic and thermal simulations in order to adequately represent the realistic testing scenarios. In particular, primary contributing factors, such as tissue water vaporisation and modifications of the dielectric properties with the tissue temperature, are discussed in relation to the operating conditions adopted in the thesis.

The study shows:

- The methodology used to design and optimise the MW applicators adopted throughout the thesis. Depending on the operating frequency, parameters such as the length of the radiating element and of the third axis of the applicator were investigated. The reflection coefficient and SAR deposition were evaluated to assess the performances of three MW applicators. Two geometries (coaxial and triaxial) and operating frequencies (2.45 GHz and 5.8 GHz) were investigated. Results show good correlation in the values of the reflection coefficients between the numerical models and the prototyped applicators.

- The criteria adopted to create accurate electromagnetic and thermal simulations with the main purpose of representing the corresponding experimental scenario. Numerical simulations also aim to reduce time and cost linked with the experimental testing iterations, and to accomplish "The Three Rs" requirements (Replacement,

Table 4.4:Summary of the characteristics of each MW applicator (i.e. type of structure, length of the radiating element, operating frequency), assumptions adopted for the numerical simulations (i.e. standard BHE, blood perfusion, vaporisation model), description of the study and related chapter.

Type of MW applicator	Operating frequency	Numerical assumptions	Type of study	Chapter Number
Coaxial OD = 1.194 mm; l_r = 6 mm	2.45 GHz	Standard BHE	Proof-of-concept study in muscle – fat interface model *(Ex vivo)*	5
Coaxial OD = 1.194 mm; l_r = 6 mm	2.45 GHz	Standard BHE	Adrenal gland multilayered simplified and 3D models *(Ex vivo)*	6
Triaxial OD = 0.584 mm; l_r = 6 mm	2.45 GHz	Standard BHE + blood perfusion	Adrenal gland 3D model *(In vivo)*	7
Triaxial OD= 0.864 mm; l_r = 3 mm	5.8 GHz	Modified BHE + Vaporisation model	Adrenal gland multilayered model *(Ex vivo)*	8

OD: outer diameter feeding coaxial cable; l_r = length radiating element; Standard BHE (Equation 4.13) must be intended without the terms of blood perfusion ($m_b \rho \rho_b c_b (T - T_b)$) and metabolic heat ($\rho Q$); Modified BHE must be intended as standard BHE (Equation 4.13) modified to account to for the change in the heat specific capacity (Equation 4.19).

Reduction and Refinement) [246] for developing faster and better tools for scientific purposes. The loss in water content of the tissue due to vaporisation was included in the numerical simulations to better foresee temperatures exceeding 70 °C given the frequency, power and time setting chosen (i.e. at 5.8 GHz, 60 W, > 30 s). At 2.45 GHz, the standard bioheat equation was evaluated sufficiently to represent the *ex vivo* scenario, neglecting the blood perfusion and heat developed for metabolic processes. The variation in the baseline tissue temperature was considered when modelling *ex vivo* and *in vivo* scenarios. The impact of the background material and the blood perfusion are considered for the *in vivo* scenario; the standard bioheat equation was used accounting for the blood perfusion. Blood flow rate through the tissue was also considered, to better represent the high degree of vascularisation characterising the adrenal gland (more in details in Chapter 7).

Table 4.4 summarises the main results discussed in this chapter that will be used in the following chapters of the thesis. In particular, the table includes the models of each MW applicator and the numerical assumptions defined in relation to the operating conditions.

Chapter 5

Shaping the ablation zone through tissue dielectric properties

5.1 Introduction

Chapter 4 presented the numerical models and antenna prototypes used in this thesis. Then, the workflows adopted to solve the electromagnetic and thermal problems were examined. Chapters 2, 3 and 4 explored the technical and clinical background of this thesis. This exploration was fundamental to support and understand the investigations presented in the following chapters. As mentioned in Chapter 2, the main clinical objective in MWA procedures is to achieve ablative temperatures (at least 55°C) in the target tissue, while sparing the surrounding healthy tissues.

A piercing approach is traditionally adopted in MWA therapies. According to this approach, the needle-shaped MW applicator is placed approximately in the middle of the tissue target. However, this approach is undesirable in the case of small functional tissues in proximity to sensitive structures, e.g. large blood vessels such as renal artery, renal vein, inferior vena cava (IVC). A 'side firing' approach was recently proposed as an alternative to the traditional piercing methods in the above-mentioned critical scenarios. In [25], [247], the 'side firing' approach consists of placing directional antennas adjacent to the tissue target, avoiding piercing the organ. Such type of antennas are equipped by a metallic cable which works as shield for the electromagnetic field. When adequately orientated, the directional antennas focus most of the electromagnetic energy only into the tissue target. To reach satisfactory results, the tissue target must lie along the same direction as the focal point of the metallic shield.

The main objective of the thesis is to pursue the 'side firing' approach mentioned above. In particular, the thesis intends to provide an alternative to the directional antennas in achieving asymmetrical ablation patterns. The role of the fat layer surrounding the tissue target is investigated as natural 'shield' to the electromagnetic energy. The approach

proposed in the thesis aims to achieve effective MWA procedures and to minimise the risk of unintended damages to surrounding sensitive structures, as in the approach using directional antennas [25], [247]. However, the use of the dielectric contrast between the tissue to be treated and the surrounding fat may help to overcome some limitations linked to the directional antennas. Such limitations include the increase in the transversal dimension of the applicator due to the presence of the metallic 'shield' cable. Additionally, the directional antennas require accurate orientation to achieve the desired effect. Thus, the ultimate results of the MWA procedure through directional antennas depend on the ability of the surgeon to find the correct orientation with respect to the tissue to be treated.

In this chapter, a proof-of-concept study is conducted to explore the feasibility of exploiting the fat layer to purposely and effectively direct the ablation zone. To this end, fat and muscle tissues are selected in order to reproduce a simple geometry, characterised by a high dielectric contrast between the two tissues. For a comprehensive understanding of the deposition of the electromagnetic power and the consequent temperature increase in the presence of a dielectric contrast, this study explores:

- The temperature distribution obtained numerically in a two-layers scenario positioning the interstitial coaxial monopole antenna operating at 2.45 GHz (§4.2) parallel to the interface of the two tissues;

- The influence of the width of the fat layer on the growth of the ablation zone in both tissue layers;

- The influence of the antenna alignment along the layers' interface on the ablation zone asymmetry;

- The 'shielding effect' of the fat layer through *ex vivo* experiments which exploit the natural interface between fat and muscle of porcine tissue samples.

In Section 5.1, the methodology adopted for the numerical simulations and the experimental tests is described. In Section 5.2 the results are described comparing the numerical and experimental outcomes in terms of the temperature distributions. Section 5.3 concludes the chapter.

5.2 Methodology

5.2.1 Numerical study

Geometrical model. Two tissue models were considered in this study: a homogeneous muscle scenario and an interface scenario including two adjacent layers of muscle and fat. The dielectric and thermal properties of both muscle and fat are listed in Table 5.1. The dielectric properties were obtained experimentally and loaded into the material library of the CST MWS software. Measurements were conducted *ex vivo* on porcine tissue using the measurement protocol described in Chapter 3 (§ 3.2). The values related to heat capacity, thermal conductivity and density were obtained from the literature [245] and manually loaded into the material settings of the CST MWS software. The tissue geometries were created using the same software. A 60 mm cube was modelled for the homogeneous scenario. Two adjacent cuboids were modelled for the interface scenario, considering two different widths: 30 mm muscle and 10 mm fat. Then, the width of the fat layer was varied. Overall, three different widths for the fat layer were considered: 15 mm, 10 mm and 5 mm.

The coaxial monopole applicator operating at 2.45 GHz and described in Chapter 4 (§ 4.2) was positioned in the middle of the geometry both for the homogeneous and interface scenario. In the case of the interface scenario, the applicator was aligned along the margin between fat and muscle. The influence of the antenna positioning was also explored, by shifting the antenna by 1.5 mm in the fat layer and 1.5 mm in the muscle layer with reference to the initial position.

Table 5.1: Tissue dielectric properties, i.e. relative permittivity and effective conductivity, density and thermal properties, i.e. specific heat capacity and thermal conductivity, employed in the numerical simulations.

Parameter	Fat	Muscle
Relative permittivity, ε_r	8.7 ± 0.5	41.0 ± 2.1
Effective conductivity, σ (Sm^{-1})	0.1 ± 0.1	0.7 ± 0.1
Specific heat capacity, c ($Jkg^{-1}K^{-1}$)	2065 ± 0.2	3322 ± 0.3
Density, ρ ($kg\,m^{-3}$)	909 ± 0.1	1103 ± 0.1
Thermal conductivity, k ($Wm^{-1}K^{-1}$)	0.2 ± 0.2	0.5 ± 0.1
Frequency (GHz)	2.45	

Electromagnetic and thermal simulations. The entire geometry was discretised by a finite number of tetrahedral elements. This was done in order to numerically calculate the distribution of the electromagnetic field in the tissue, hence of the SAR. The models were meshed in order to have denser mesh in the regions charcaterised by the smallest details, i.e. MW applicator (§ 4.2). Overall, the geometry was discretised with tetrahedral cells ranging between 0.1 mm and 3.3 mm. Boundary conditions according to Equation (4.17) were applied between the surface of the applicator and the tissue model to account for

Table 5.2: Summary of the numerical simulations performed considering, for each input power (30 W, 60 W), different scenarios including the homogeneous muscle scenario and the interface scenario consisting of muscle and fat. For the interface scenario, there different widths for the fat layers were considered for each input power: 5 mm, 10 mm, 15 mm. For two different interface scenarios (5 mm and 10 mm width of the fat layer), two cases of misalignment of the antenna were considered: 1.5 mm shift in the fat and 1.5 mm shift in muscle with reference to the middle position.

#	Tissue scenario	Thickness Fat	Antenna position	Input Power (W)	Duration (s)
1	Homogeneous	-	Aligned	30	60
2	Homogenous	-	Aligned	60	60
3	Interface	15	Aligned	30	60
4	Interface	10	Aligned	30	60
5	Interface	5	Aligned	30	60
6	Interface	15	Aligned	60	60
7	Interface	10	Aligned	60	60
8	Interface	5	Aligned	60	60
9	Interface	10	Shifted in fat	30	60
10	Interface	5	Shifted in fat	30	60
11	Interface	10	Shifted in fat	60	60
12	Interface	5	Shifted in fat	60	60
13	Interface	10	Shifted in muscle	30	60
14	Interface	5	Shifted in muscle	30	60
15	Interface	10	Shifted in muscle	60	60
16	Interface	5	Shifted in muscle	60	60

the forced convection due to the cooling system ($h = 1000$ W m^{-2} °C^{-1}). They were also applied between the outer surface of the modelled region and surrounding background material ($h = 20$ W m^{-2} °C^{-1}) to represent free convection (§ 4.2).

For the tissue models, the starting temperature was set to 25 ˚C. The effect of two power levels commonly used were compared over 60 s: 30 W and 60 W. All the numerical simulations performed are summarised in Table 5.2 considering the input power level and the type of scenario (homogeneous or interface). In the case of the interface scenario, the width of the fat layer and the position of the antenna are detailed. In total, 16 numerical simulations were performed.

The values obtained from the numerical simulations were exported and analysed in MATLAB (R2017a, The MathWorks, Inc., Natick, MA, US); the error introduced for the representation of the ablation profiles is around 0.1%.

5.2.2   Experimental *ex vivo* study

Experiments were conducted *ex vivo* on porcine tissue to validate the results of the numerical study. The temperature of the material under test (porcine tissue) was measured using an infrared thermometer (Fluxe 62 Max IR Thermometer, -30˚C−500˚C
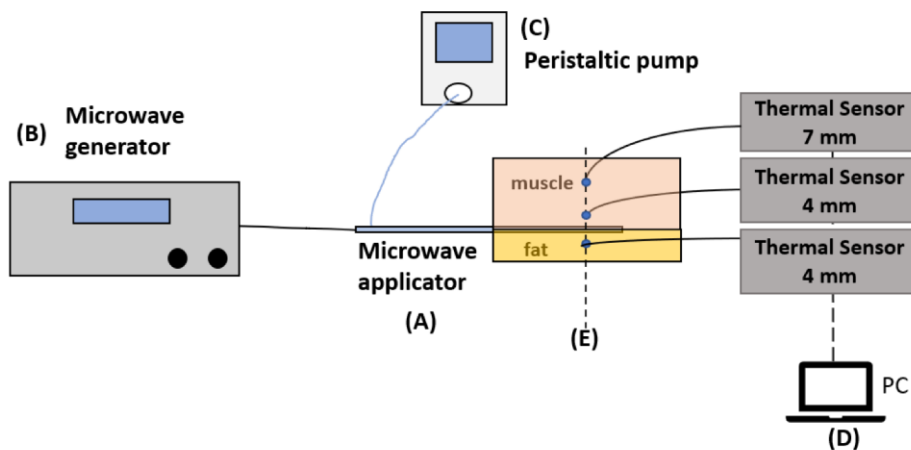
Figure 5.1: Experimental setup including: microwave applicator (A) powered at 2.45 GHz by a microwave generator (B). A peristaltic dispensing pump (C) connected to the inner tube of the applicator. Three fibre optic sensors connected to a laptop (D) for the monitoring of the temperature and inserted at three different radial distances from the antenna feed in the tissue (E) under treatment.

temperature range, accuracy of 1.5˚C of reading at temperature $\geq$ 0˚C). The applicator was placed along the interface between fat and muscle layers, and covered by another layer of tissue with the same pattern. Two power and time settings were experimentally considered: 30 W for 60 s and 60 W for 60 s. The output powers at the microwave generator (Sairem, SAS, France) were set at 32 W and 64 W (§ 4.3) in order to ensure the designed operating conditions (i.e. 30 W and 60 W respectively) at the feed of the antenna (§ 4.5.1). A peristaltic dispensing pump (DP2000, Thermo-Fisher Scientific Inc., Waltham, Massachusetts, US) was connected to the inflow channel of the ablation applicator, operating at 50 ml min^{-1}. For each experiment, the temperature was monitored using three fiber optic sensors (Neoptix Inc., Québec, CA) placed at three different distances from the antenna axis (reference axis) in correspondence with the antenna feed. Two fiber optic sensors were placed at a radial distance of 4 mm from the antenna feed in the muscle tissue and fat tissue. This was done in order to ascertain the increase of temperature caused by the direct heating in proximity to the antenna. One fiber optic sensor was placed at 7 mm from the antenna feed in the muscle. This was done in order to account for the heat transfer due to diffusion phenomena through the tissue (i.e. muscle) at a higher distance from the antenna feed. At t= 0 s the power supply from the MW generator was switched on, then the temperature was monitored over 60 s. The experimental setup adopted is schematized in Figure 5.1.

5.3 Results

5.3.1 Numerical study

The optimised monopole coaxial antenna described in Chapter 4 was adopted to conduct the numerical studies discussed in this section, accounting for different tissue models and antenna placements. In the following figures, the thermal distributions achieved after 60 s in each tissue model are mapped for both power settings considered, i.e. 30 W and 60 W. Two temperature profiles are highlighted. An isothermal contour at 55˚C marks the area where instantaneous coagulation occurs (i.e. ablation zone). An isothermal contour at 90°C indicates the area where phenomena linked to a high increase in temperature may occur, such as vaporisation of the tissue water content or tissue contraction [145], [248]
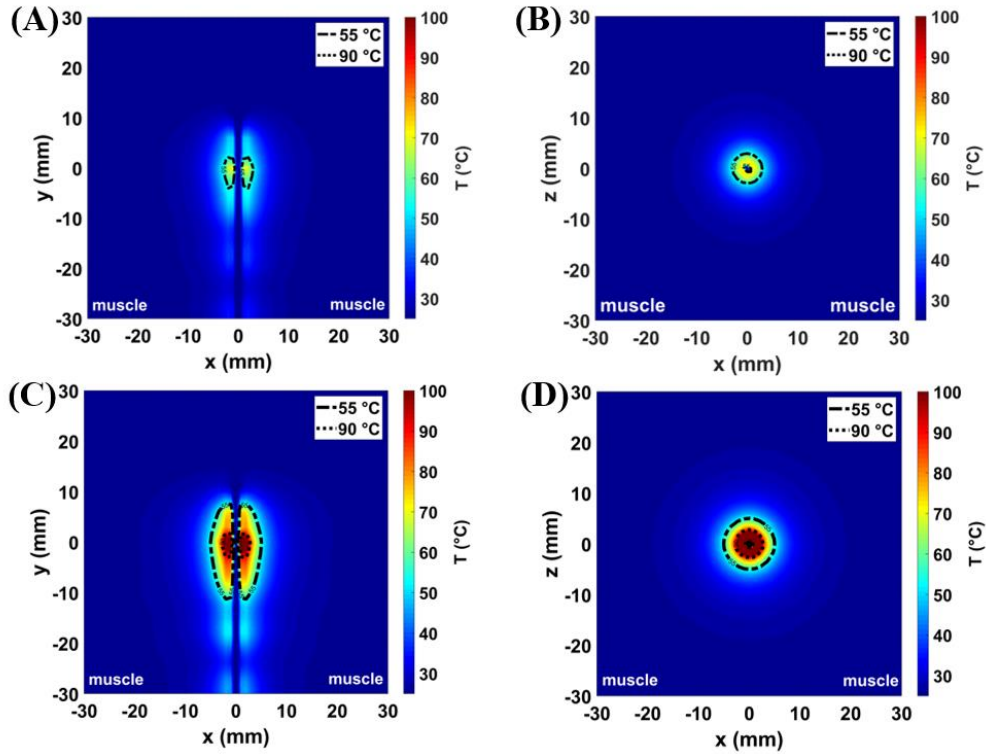
Figure 5.2: Simulated temperature patterns in the homogeneous muscle scenario shown both in a coronal plane (first column) and transverse plane (second column) with reference to the antenna feed. Two different power-time settings are reported: 30 W- 60s (A-B); 60W- 60s (C-D). The dash-and-dot lines represent 55°C boundary and the dot lines represent 90°C boundary.

Comparison between muscle and fat-muscle scenarios. Figure 5.2 and Figure 5.3 show the temperature profiles obtained in the homogeneous muscle model and in the muscle-fat interface model (fat layer: 10 mm wide), respectively. The temperature profiles refer to two different input power levels, both delivered in the tissue for 60 s: 30 W (A) – (B) and 60 W (C) – (D). Figure 5.3 shows the asymmetry in the ablation zone due to the dielectric contrast between the two different tissues (muscle and fat) with respect to the homogeneous muscle scenario (Figure 5.2).

For the low input power (30 W), the temperature in the tissue close to the antenna is below 90 °C both in the homogenous scenario (Figure 5.2 (A) – (B)) and in the interface scenario (Figure 5.3 (A) – (B)). The area enclosed in the 55°C contour is 10 mm^2 each side (20 mm^2 overall) in the case of homogeneous scenario. In the case of the interface scenario, the extent of the area exceeding 55°C is 3 mm^2 in fat and 41 mm^2 in muscle. Increasing the input power (60 W), the MW heating affects larger areas both in muscle
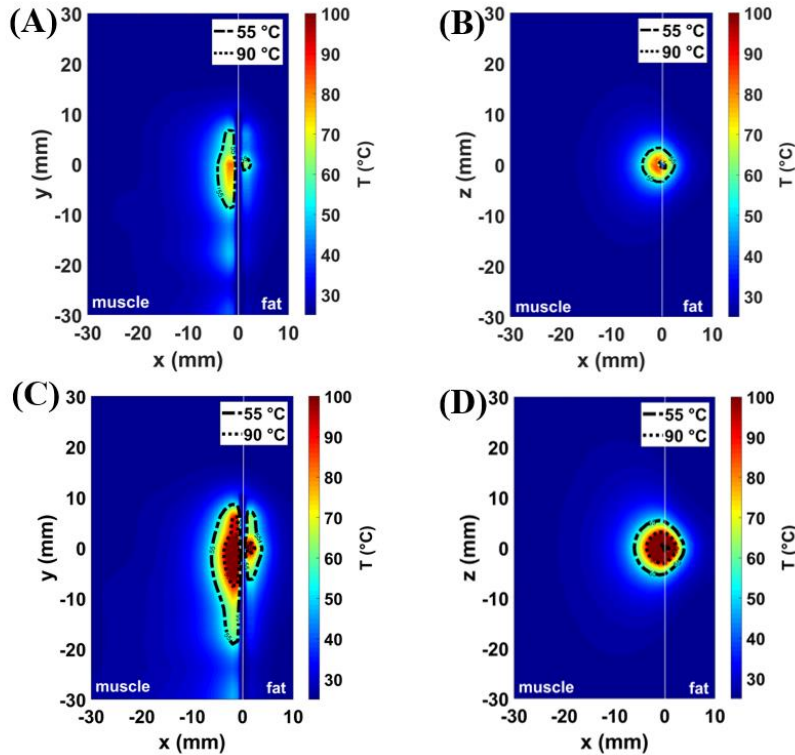
Figure 5.3: Simulated temperature patterns in muscle-fat (fat width = 10 mm) interface scenario shown both in a coronal plane (first column) and transverse plane (second column) with reference to the antenna feed. Two different power-time settings are reported: 30 W- 60s (A-B); 60W- 60s (C-D). The dash-and-dot lines represent 55°C boundary and the dot lines represent 90°C boundary.

homogeneous (Figure 5.2 (C) – (D)) and in muscle-fat interface scenario (Figure 5.3 (C) – (D)). In the case of 60 W setting, temperatures higher than 90°C are found in proximity to the antenna feed both in the homogeneous muscle and muscle-fat interface scenarios. However, temperature values exceeding 90 °C involve a smaller area in fat (< 3 mm^2) compared to the muscle (< 30 mm^2) in the case of muscle-fat interface model. The area where the temperature exceeds 55 °C is around 65 mm^2 each side (130 mm^2 overall) in the homogeneous muscle model. In the interface scenario this area is approximately 31 mm^2 in fat and 117 mm^2 in muscle.

Overall, at 30 W the interface scenario shows that the ablation area in muscle is about ten times bigger than the area in fat, and four times the area in muscle in the homogeneous scenario. At 60 W, the ablation area in muscle is about four times the area in fat considering the interface scenario, and two times the area in muscle in the homogeneous case.

Interface scenario with different fat widths. Figure 5.4 shows the impact of the fat layer width on the profiles of the ablation zone. Starting from the initial condition (Figure 5.3) where the width of the fat layer was set at 10 mm, here the width of the fat layer was in one case reduced to 5 mm (Figure 5.4 (A) – (B)) and in the other case increased to 15 mm (Figure 5.4 (C) – (D)). The temperature distributions are illustrated for the two different settings above mentioned: 30 W – 60 s in Figure 5.4 (A-B) and 60 W – 60 s in Figure 5.4 (C-D)).

It is notable that the changes in the width of the fat layer do not show noticeable variations in the extent of the ablation zone compared with the scenario of a 10 mm fat layer (Figure 5.3). In the case of 15 mm wide fat layer and at 30 W input power, the areas where the temperature exceeds 55 °C are 39 mm^2 in muscle and 3 mm^2 in fat. Increasing the input power to 60 W, the areas delineated by 55 °C isothermal contour are 112 mm^2 in muscle and 30 mm^2 in fat. In the case of smallest width of the fat layer (5 mm), at 30 W the areas
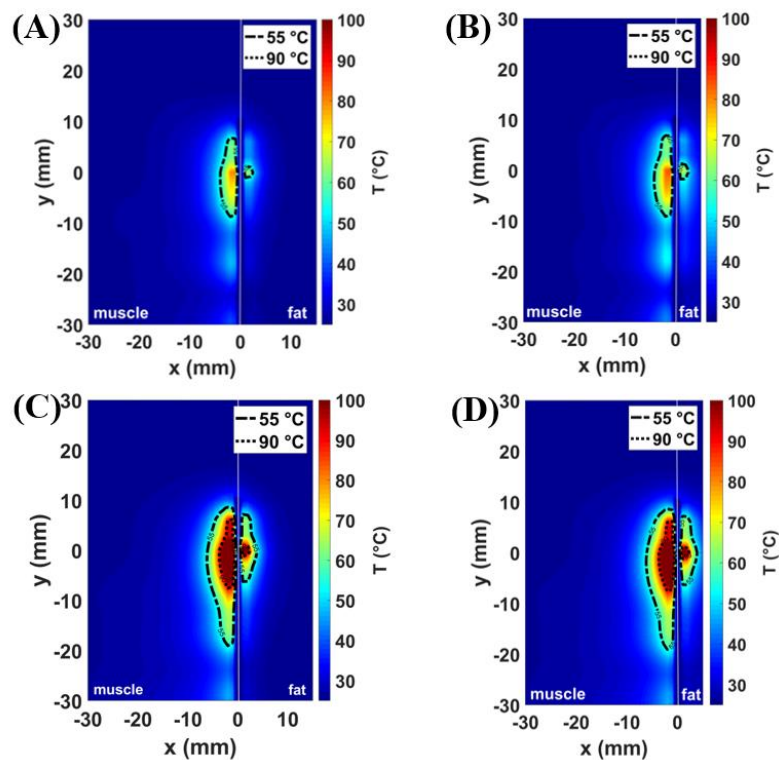
Figure 5.4: Simulated temperature patterns in muscle-fat interface scenario shown in a coronal plane with reference to the antenna feed for two different fat layer widths: 15 mm (A-C) and 5 mm (B-D). Two different power-time settings are reported: 30 W-60s (A-B); 60W-60s (C-D).

Table 5.3: Areas of ablation zones calculated at 30 W (first line) and at 60 W (second line) in muscle in the case of homogeneous scenario and both in muscle and in fat in the interface scenario considering 15 mm, 10 mm and 5 mm fat layer width.

Settings		Area enclosed in 55°C contour						
		Homogeneous		Interface Fat width: 15 mm		Interface Fat width: 10 mm		Interface Fat width: 5 mm
P (W)	t (s)	Muscle*	Fat	Muscle	Fat	Muscle	Fat	Muscle
30	60	10 mm^2	3 mm^2	39 mm^2	3 mm^2	41 mm^2	4 mm^2	43 mm^2
60	60	65 mm^2	30 mm^2	112 mm^2	31 mm^2	117 mm^2	31 mm^2	114 mm^2

delimited by 55 °C isothermal contour are 43 mm^2 in muscle and 4 mm^2 in fat. At 60 W, those areas are 114 mm^2 in muscle and 31 mm^2 in fat.

Table 5.3 lists the extent of the ablation areas calculated at 30 W and 60 W both for the homogeneous scenario and for muscle-fat interface scenario, considering the three different widths of the fat layer. The asymmetric patterns observed in Figure 5.3 and Figure 5.4 compared with Figure 5.2 respond to the different interaction mechanism with the EM field between fat and muscle. Because of the lower values in relative permittivity and effective conductivity, ablation zones in the fat layer are observed to be constantly smaller and more spherical compared to the muscle layer, independent of the width of the fat layer. Different ratios in the asymmetric ablation profiles were observed between muscle and fat for the two power settings investigated. The ablation zone in fat was at least ten times smaller than in muscle for the lower power (30 W) and about four times for the higher power (60 W).

The high contrast in effective conductivity between fat and muscle at the interface induces higher levels of electromagnetic energy (and consequently of heating) in the muscle layer compared to the homogeneous scenario. Thus, it is conceivable that the fat layer not only shields the electromagnetic radiation, but also reflects the electromagnetic power into the adjacent tissue characterised by higher values of relative permittivity and effective conductivity. Part of the electromagnetic field reflected in the muscle (at the interface with fat) is redistributed along the antenna axis inducing a noticeable, yet not desirable, elongation of the ablation zone in muscle. In the used applicator, back-heating
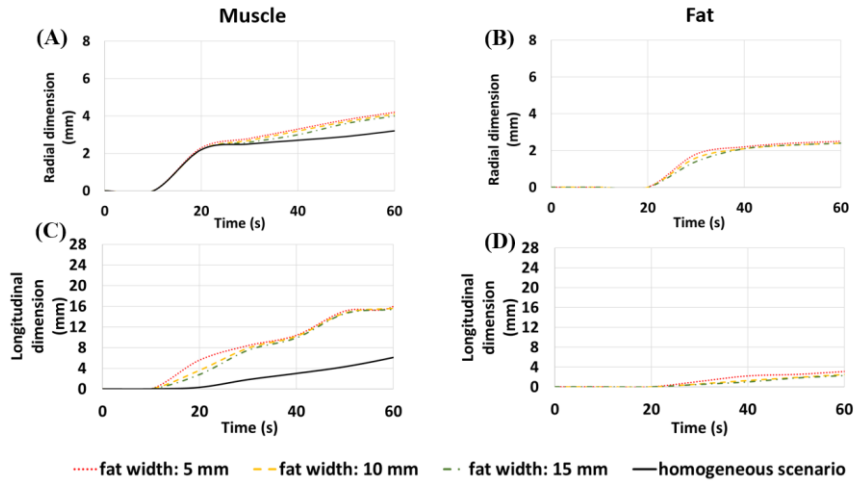
Figure 5.5: Variations of the radial (A-B) and longitudinal (C-D) dimensions of the ablation zone over time at 30 W in muscle (A-C) and in fat (B-D). Interface scenarios (red line: 5 mm wide fat case; yellow line: 10 mm wide fat case; green line: 15 mm wide fat case) and homogenous scenario (black line) are compared.
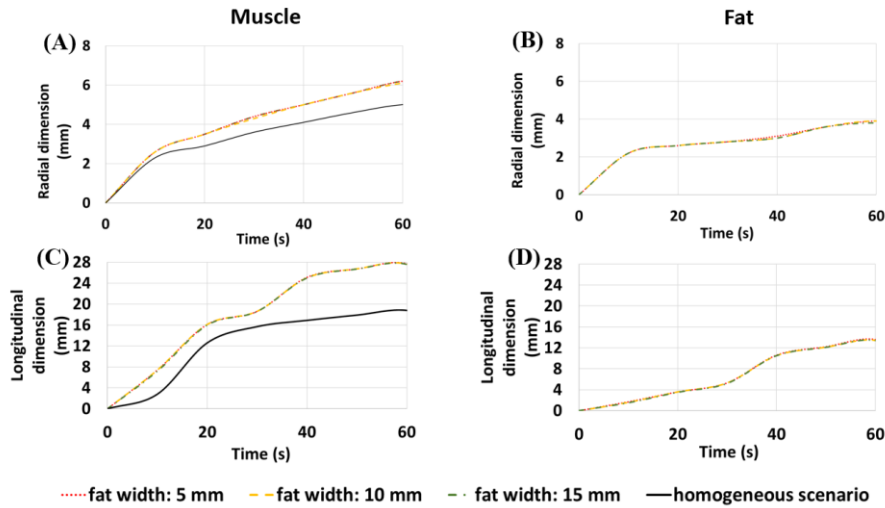
Figure 5.5: Variations of the radial (A-B) and longitudinal (C-D) dimensions of the ablation zone over time at 60 W in muscle (A-C) and in fat (B-D). Interface scenarios (red line: 5 mm wide fat case; yellow line: 10 mm wide fat case; green line: 15 mm wide fat case) and homogenous scenario (black line) are compared.

along the antenna axis is limited only by the active cooling that balances the temperatures increase. Thus, such increase in the longitudinal direction would be expected, but could be further minimised by adopting a different antenna design.

Figure 5.5 and Figure 5.6 show the variations in the radial and longitudinal dimensions of the ablation zone against the time of the ablation procedure (up to 60 s, at 10 s time

step). The changes in the radial and longitudinal dimensions are reported for the homogenous scenario and for the interface scenario, considering all the different widths of the fat layer (5, 10, 15 mm). It can be observed that the growth rate of the ablation zone in both tissues of the interface scenario is independent of the width of fat.

In the case of the 30 W setting (Figure 5.5), the ablation zone appears after 10 s in muscle and only after 20 s in fat. In the interface scenario, the radial dimension of the ablation zone in muscle starts increasing with respect to the homogeneous scenario after 20 s. This difference becomes sizeable after about 40 s. In fat, the radial dimension of the ablation zone reaches the steady state after 40 s. Longitudinally, the growth of the ablation zone in fat is limited during the whole procedure. A substantial increase of the ablation zone in muscle with respect to the homogeneous case is observed also along the longitudinal dimension. In particular, the longitudinal dimension in muscle grows of about 0.3 mm/s steadily from 10 s to 40 s. At 40 s, the rate of the increment in the longitudinal dimension decreases to approximately about 0.5 mm/s, before reaching a plateau.

In the case of the 60 W setting (Figure 5.6), higher values of the radial dimension of the ablation zone in muscle compared to the homogeneous scenario are visible already after 10 s. This difference remains constant over time. In fat, the radial dimension of the ablation zone reaches a plateau after 10 s, and slowly starts increasing again after 40 s. In contrast to the 30 W case, at 60 W the growth of the ablation zone along the longitudinal dimension is noticeable in fat. Longitudinally the ablation zone in fat is limited for the first 30 s. Then, at 30 s a change in the slope of the curves leads to a substantial increase in the ablation zone length over the following 30 s (up to the end of the procedure). A similar change of slope can be observed in muscle at the same time (at 30 s). A worsening of the capability of the fat to shield the ablation zone in the case of high power (i.e. 60 W) can be observed.

Both at 30 W and 60 W, the change in the slope of the curves related to the longitudinal dimension of the ablation zone occurs when the radial dimension of the ablation zone in muscle in the interface scenario becomes noticeably higher (at least 10%) than the equivalent dimension in the homogeneous scenario. At 40 s in the case of 30 W, and at 30 s in the case of 60 W, the ablation length in muscle increases faster than the

corresponding one in the homogenous scenario, inducing the elongation of the ablation zones. A similar behavior was observed for MWA in thin tissue samples [141]. These differences suggest that the success of this approach is highly dependent on the power and time settings of the procedure. Lower power and relatively short ablation time enable more controlled ablation zones and promising results.

Misalignment of the antenna along fat and muscle interface. The ability of the fat layer to create asymmetric ablation zones was also evaluated in the case of antenna misalignments. Figure 5.7 shows the results obtained for 30 W - 60 s (Figure 5.7 (A) – (B)) and 60 W - 60 s (Figure 5.7 (C) – (D)) settings. The influence of the antenna misalignment was investigated considering in one case the antenna shifted by 1.5 mm in fat (Figure 5.7 (A) – (C)), then in muscle (Figure 5.7 (B) – (D)), with respect to the initial condition (Figure 5.3).

In the case of 1.5 mm displacement of the antenna in fat, the longitudinal axis of the antenna is positioned inside the fat layer, thus the antenna is immersed in fat. In the case
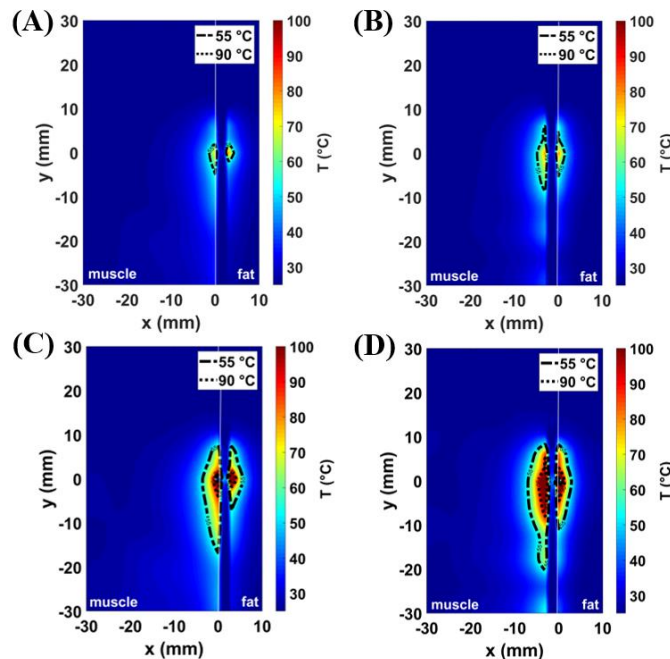
Figure 5.6: Simulated temperature patterns in muscle-fat interface scenario shown in a coronal plane with reference to the antenna feed for 1.5 mm displacement of the antenna along x-axis in fat (A-C) and in muscle (B-D). Two different power-time settings are reported: 30 W-60s (A-B); 60W-60s (C-D).

of 1.5 shift of the antenna in muscle, the longitudinal axis of the antenna is positioned inside the muscle region, thus the antenna is immersed in muscle. Considering 1.5 mm misalignment in fat and 30 W input power, the sizes of the ablation zones are 7 mm^2 in muscle and 4 mm^2 in fat. At the same power, the areas exceeding 55°C are 20 mm^2 in muscle and 10 mm^2 in fat in the case of antenna misalignment in muscle. At 60 W, the ablation zones become 67 mm^2 in muscle and 28 mm^2 in fat, when the antenna is in fat. For the antenna misalignment in muscle, such areas increase up to 89 mm^2 in muscle and 47 mm^2 in fat.

Compared to the scenario of perfect alignment of the antenna along the interface between fat and muscle (Figure 5.3), the asymmetric ablation profiles are less pronounced. The ablation areas in muscle are only two times the ablation areas in fat. For both the misalignment scenarios, the fat-muscle interface has less impact on the reflection of the electromagnetic energy in the target tissue. However, a two-fold asymmetry is still observed independently of the power applied. These findings suggest that the precise orientation of the antenna is not strictly required to create the shielding effect induced by the fat, but it should be considered to properly predict the resulting dimension of the ablated zone.
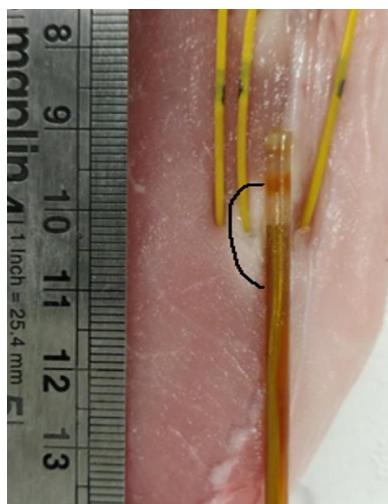
Figure 5.7: Section of a MWA obtained in ex vivo porcine sample: the applicator (MW antenna) and fibre optic sensors placement in the tissue is showed. The antenna is placed at the visible interface between the muscle and the fat, and the ablation zone obtained in the muscle is marked. The ablation zone is not visible in fat.

5.3.2   Experimental *ex vivo* assessment

Finally, the numerical results have been experimentally validated. Experimental MWAs (N=10, five at 30 W for 60 s and five at 60 W for 60 s) were obtained using the natural muscle-fat interface of *ex vivo* porcine tissue. The MW antenna was placed adjacent to the interface between muscle and fat. The increase in temperature at different radial distances from the antenna axis was monitored, with fiber optic sensors placed in fat at 4 ± 1 mm from the antenna axis and in muscle at 4 ± 1 mm and at 7 ± 1 mm from the antenna axis (Figure 5.8).

Figure 5.9 provides a comparison between the thermal profiles observed numerically and the experimental values obtained from the fiber optic sensors. The figure shows the temperature values at 30 s and 60 s during the MWA procedure conducted at 30 W (A) and 60 W (B). The increase in temperature is reported as a function of the radial distances from the feed of the antenna.

The experimental data well match the numerical trends. The impact of the differences in electrical and thermal characteristics between the two tissues is visible. A minimal discrepancy between the numerical and experimental data can be observed in muscle only in the case of 60 W input power setting. This mismatch is likely related to the transient deformations (i.e. shrinkage) occurring in the tissue in proximity to the antenna [249]–[251]. Moreover, the thermal lesions obtained from the numerical simulations are calculated considering 55 ˚C as the suitable temperature to obtain the coagulation effect.
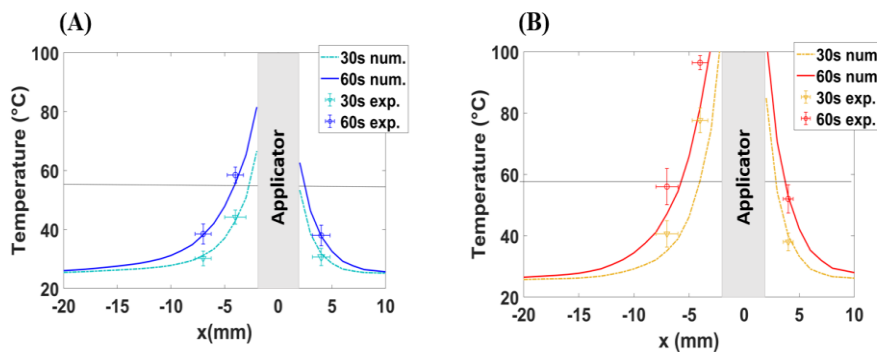
Figure 5.8: Numerical (num.) and experimental (exp.) values of temperature over the radial distance from the MW antenna axis (applicator) both in muscle (negative x axis) and fat (positive x axis) at 30 s and 60s for 30 W (A) and 60 W (B). The horizontal line highlights the temperature threshold at 55°C.

However, such a value can vary within 50 – 60 ˚C depending on the tissue types and the initial conditions of the tissue (e.g. initial temperature) [252].

5.4 Conclusions

This chapter explores the ability of the fat layer to reflect the electromagnetic power into the tissue target while reducing the heating in the opposite direction. Thus, this work aims to highlight the role of the fat layer at the interface with the tissue target to potentially act as a 'shield' for the electromagnetic energy in the context of MWA procedures. In the following chapters the presented strategy will be applied to the adrenal scenario, in order to achieve shallow ablation zones and to spare the surrounding healthy tissue.

The results of this study shows that when a MWA antenna is placed at the interface between a layer of fat tissue and a tissue characterised by higher dielectric properties (e.g. muscle):

- The area of the ablation zone in the latter tissue increases with respect to the scenario where such an interface is absent (i.e. homogeneous scenario). This increase is caused by the dielectric contrast between the two adjacent tissues. Because of this dielectric gap, the electromagnetic field is reflected into the tissue characterised by higher dielectric properties, while only a small portion of the field propagates through the "shielding" tissue (i.e. fat). It is conceivable that the fat layer not only shields from the electromagnetic energy, but also redirects the energy into the tissue characterised by higher values of relative permittivity and effective conductivity;

- The ablation zone achieved in the "higher-dielectric" tissue is larger than the ablation zone achieved in the fat layer, regardless of the width of the fat layer. The ratio in the asymmetric ablation area depends on the power settings used; the asymmetry ratio decreases when the power increases. In the interface scenario, ablation zones in muscle are larger when compared with the homogeneous muscle scenario of approximately ten times at 30 W and four times in the case of 60 W;

- Asymmetric ablation patterns are also achievable in the case of antenna misalignment. At least two-fold asymmetry ratio is guaranteed even when the antenna is slightly shifted (up to 1.5 mm) into one of the two tissues (misalignment).

This result suggests that precise orientation of the antenna is not strictly required to obtain asymmetric ablation zones. However, better alignment of the MWA applicator improves the asymmetry in the ablation zones.

- Ablative temperatures (i.e. above 55°C) are achieved only in close proximity to the applicator ($\leq$ 4mm), in the tissue characterised by lower dielectric and thermal properties (i.e. fat tissue).

Given the results presented in the chapter, it is conceivable that the presence of the periadrenal fat capsule surrounding adrenal glands, target of thesis, may be capable of preserving the surrounding healthy structures from damage caused by unintended heating (e.g. blood vessels shielded by at least 4-5 mm of fat). Thus, Chapter 6 is devoted to studying the effect of the fat layer in relation to the dielectric and geometrical characteristics of the adrenal glands.

Chapter 6

Numerical and experimental evaluation of asymmetric ablation zones in adrenal glands

6.1 Introduction

Chapter 5 showed that asymmetric ablation profiles can be created by exploiting the contrast in dielectric properties between a fat layer and an adjacent target tissue. The discrepancy in relative permittivity and effective conductivity between the two tissues redirects the electromagnetic field toward the tissue characterised by higher dielectric properties compared to fat. Therefore, the MW applicator should be positioned parallel to the interface between the target tissue and the fat layer. This interface was numerically modelled using two contiguous layers of muscle and fat. In this interface scenario it was observed that the ablation zones increased in muscle of approximately four times at 30 W – 60 s and two times at 60 W – 60 s compared with the homogeneous scenario (i.e. muscle-muscle). In the fat layer, ablation zones were approximately ten times (30 W – 60 s) and four times (60 s – 60 s) smaller than in muscle. The study showed comparable asymmetries in the ablation patterns while varying the width of the fat layer and shifting the position of the applicator with respect to the interface of the two tissues. The experimental validation conducted *ex vivo* on porcine muscle confirmed the ability of the fat layer to lag the increase of temperature during the MWA procedure.

This chapter investigates whether the above-described 'side firing' approach can be translated in the case of the adrenal gland encapsulated in the fat layer. In the adrenal tissues, both in the cortex and in the medulla, relative permittivity and effective conductivity are up to 27% and 157% higher, respectively, compared with muscle (§3.4.2). The higher dielectric properties of the adrenal tissues result in a higher dielectric contrast with the surrounding fat which may emphasise the 'side firing' effect observed (§5.3). The study investigates:

- The effect of the higher dielectric properties of the tissue target on the ablation profiles. The dimensions of the ablation zones were compared with those achieved in the previous study (i.e. fat-muscle) at the same settings: 30 W – 60 s and 60 W – 60 s. To this purpose, a simplified geometry similar to the model showed in the previous chapter was used to represent the adrenal tissues and the surrounding fat layer. The dielectric properties experimentally acquired *ex vivo* on ovine adrenal tissues (§3.3.2) were used to characterise each tissue layer representing the adrenal numerical model;

- The influence of the geometry of the tissue target on the deposition of the electromagnetic power in the region of interest and on the ablation profiles. The extent of the ablation zones was also evaluated in a three-dimensional (3D) geometry representing the adrenal gland structure. The numerical findings obtained from the 3D model were compared with the dimensions of the ablation zone obtained in the simplified model. The 3D model included a model of a kidney to observe the distribution of the electromagnetic field through non-targeted tissues;

- The changes in temperature on *ex vivo* ovine adrenal tissues and the surrounding fat over the radial distance from the axis of the MW applicator. The experimental results were compared with those obtained from the numerical simulations at two power levels (30 W and 60 W). Radial and longitudinal dimensions of the coagulation area in the tissue were evaluated by visual inspection. The extent of the tissue whitening induced by the MW heating was estimated;

- The features of the cellular microstructure of the tissue treated by MWA and the surrounding structures including the fat layer and the adjacent blood vessel.

Section 6.1 describes the numerical models specifying the orientation of the MW applicator in each model and the setup for the experimental assessment. Section 6.2 explores the ablation profiles for each numerical geometry, the temperature
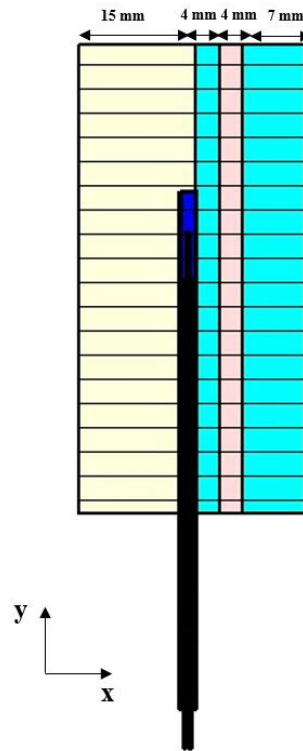
Figure 6.1: Simplified geometry for modelling each functional tissue composing the adrenal gland and the surrounding fat layer. The entire geometry is 60 mm in height, 60 mm in thickness and 30 mm in width. In detail: fat layer (yellow) is 15 mm wide, the outer part of the cortex adjacent to the fat layer (dark pink) and medulla layer (light pink) are both 4 mm wide and the inner layer of cortex (dark pink) is 7 mm width.

valuesvarying over the radial distance from the applicator and the changes in the cellular structure of the tissue. Section 6.3 concludes the chapter.

6.2 Methodology

6.2.1 Numerical study

Simplified model. Figure 6.1 depicts a multi-layer geometry drawn within the CST MW Studio software to model the adrenal tissues and the adjacent fat layer. The multilayer structure – four 3D geometries of 30 mm in height, 30 mm in thickness and varying widths – is a simplified representation of the adrenal gland. In the model, the medulla was enclosed within two layers named 'outer cortex' (adjacent to the fat layer) and 'inner cortex' (far from the fat layer) representing the adrenal cortex. Depending on the type of tissue, different widths were assigned to each layer: 15 mm for fat, 4 mm both for the

Table 6.1:Tissue dielectric and thermal properties employed in the numerical simulations

Parameter	Fat	Cortex	Medulla
Relative permittivity, ε_r	8.7 ± 0.5	45.2 ± 3.0	52.0 ± 0.4
Effective conductivity, σ_{eff} (Sm^{-1})	0.1 ± 0.1	1.6 ± 0.1	1.8 ± 0.1
Specific heat capacity, c ($Jkg^{-1}K^{-1}$)	2065 ± 0.2	3425 ± 0.1	3425 ± 0.1
Density, ρ ($kg\ m^{-3}$)	909 ± 0.1	1030 ± 0.1	1030 ± 0.1
Thermal conductivity, k ($Wm^{-1}K^{-1}$)	0.2 ± 0.2	0.4 ± 0.2	0.4 ± 0.2
Frequency (GHz)		2.45	

inner part of the cortex and the medulla, 7 mm for the outer layer of cortex. The width of the fat layer was set equal to 15 mm, as the previous study (§5.2.1) showed comparable asymmetric ablation profiles for different widths of the fat layer (15, 10, 5 mm). The width of the medulla and the inner layer of cortex represents a realistic margin between the two functional adrenal tissues [253]–[255]. The width of the outer layer of cortex was set at 7 mm to minimise the impact of the boundary effects between the geometry and the surrounding medium (air). Table 6.1 lists dielectric and thermal properties assigned to each layer. For cortex and medulla, the dielectric properties at the operating frequency of 2.45 GHz described in Chapter 3 (§3.3.2) were loaded into the material library of the CST MW Studio software. The dielectric properties of fat as well as the values related to heat capacity, thermal conductivity and density of each material were acquired from the literature [245] and manually loaded into the material settings of the simulation software. The fully refrigerated coaxial monopole applicator optimised to work at the operating frequency of 2.45 GHz (§ 4.2.1) was aligned at the margin between fat and the inner layer of the cortex, as shown in Figure 6.1. A total of 3,003,520 tetrahedral meshing cells ranging between 0.2 mm and 3.3 mm in size discretised the entire model. A denser mesh was created in the regions where geometrical details are of smaller size compared to the other elements of the geometry, i.e. the applicator and the tissue surrounding the applicator.

Three-dimensional model. Figure 6.2 shows a second model representing a pyramidal-shaped adrenal gland and the position of the gland on the top of the kidney [26]. First a
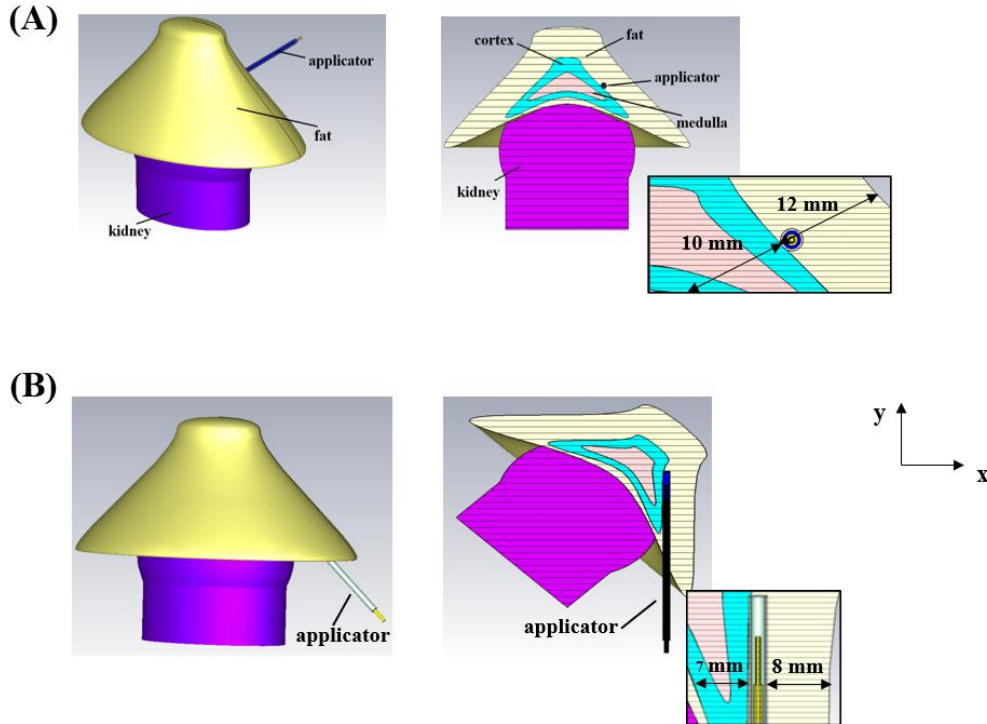
Figure 6.2: Three-dimensional geometry for modelling each functional tissue composing the adrenal gland and the surrounding fat layer. The entire geometry is 60 mm in height, 60 mm in thickness and 30 mm in width. In detail: fat layer (yellow) is 15 mm wide, the outer part of the cortex adjacent to the fat layer (dark pink) and medulla layer (light pink) are both 4 mm wide and the inner layer of cortex (dark pink) is 7 mm width.

pyramidal shell was designed within CST MW Studio software. The shell was scaled to reproduce the dimensions of medulla (inner shell) and the cortex (outer shell). The geometries representing medulla and cortex were 13 mm and 24 mm in height, 40 mm and 60 mm in width, 20 mm and 30 mm in thickness. A fat capsule enveloped the modelled adrenal tissues. The dimensions of the fat capsule were 45 mm in height, 108 mm in width and 30 mm in thickness. Finally, the model of the adrenal gland was arranged on the top of a kidney model (49 mm in height, 32 mm in width and 33 mm in thickness) in agreement with the first model presented in [20]. The same dielectric and thermal properties listed in Table 6.1 were used for the components of the adrenal geometry. The dielectric and thermal properties from the IT'IS database [245] were used to characterise the geometry representing the kidney. The same MW applicator used for the simplified model was positioned at the boundary between fat and cortex considering

two different orientations, Orientation #1 (Figure 6.2 (A)) and Orientation #2 (Figure 6.2 (B)). In the case of Orientation #1, the angle between the longitudinal axis of the applicator and the *y*-axis of the adrenal model approximates 90°. For Orientation #2, the longitudinal axis of the applicator is approximately parallel to the *y-axis*. A total of 11,856,00 tetrahedral cells ranging between 0.04 mm and 0.4 mm discretised the entire geometry. Because of the excessive computational load, only half of the three-dimensional model (right side in Figure 6.2) was used to compute the electromagnetic and thermal simulations. In this configuration, the number of meshing cells was reduced to 6,278,052 and the computational time decreased accordingly.

Electromagnetic and thermal simulations. The distribution of the electromagnetic power and temperature over the geometry were computed using CST MW Studio software as described in Chapter 4 (§ 4.2). Boundary conditions accounting for convection heat exchange between the tissue model and the surrounding environment completed the
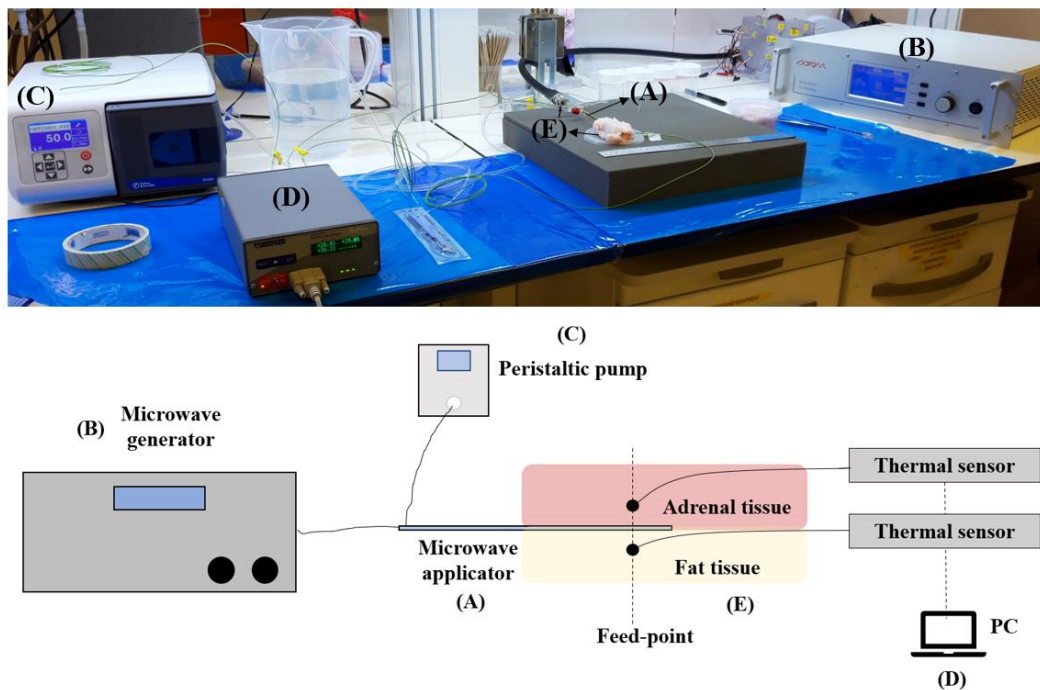
Figure 6.3: Setup adopted for the experimental validation of the computational results (top) and related schematisation (bottom). The setup includes the microwave applicator (A) powered for 60 s at the input power selected at the microwave generator (B); a peristaltic pump (C) connected to the inflow and outflow tubes of the refrigerating system integrated in the applicator; two fiber optic sensors connected to a laptop (D) to acquire values of temperature at 0.1 s time step.

bioheat equation (§ 4.2). The dielectric properties of the air ($\varepsilon_r = 1, \sigma = 0$) were set as the background material, which is representative of the *ex vivo* conditions of the experimental scenario. Two different input power levels were used in the electromagnetic-thermal simulations, i.e. 30 W and 60 W both for 60 s, for both the simplified and 3D models. The values obtained from each simulation were exported and analysed in MATLAB (R2017a, The MathWorks, Inc., Natick, MA, US).

6.2.2   Experimental *ex vivo* study

Microwave ablation experiments were conducted on a total of six *ex vivo* ovine adrenal glands with the objective of assessing the validity of the computational models. The glands were obtained from a local abattoir together with the corresponding kidneys and the surrounding fat. Each adrenal gland was then dissected in our laboratories, within one hour of excision. The procedure for the resection of the adrenal gland and the surrounding fat capsule was detailed in Chapter 3 (§3.3.2).

Figure 6.3 provides an overview of the experimental setup along with the related schematisation of each component included in the setup. The temperature of the material under test was measured by an infrared thermometer (Fluxe 62 Max IR Thermometer, -30°C− 500°C temperature range, 1.5°C accuracy at temperature $\geq$ 0°C). The fully refrigerated monopole applicator was placed between the surface of the gland and the periadrenal fat. In agreement with the numerical study, two different power settings were supplied for a duration of 60 s: 30 W and 60 W. A total of six ablations were performed on six different adrenal glands: three applying 60 W for 60 s and three applying 30 W for 60 s. The input power was supplied at 2.45 GHz from a microwave generator (Sairem, SAS, France) connected to the applicator through a low loss coaxial cable and an SMA connector attached to the distal end of the MW applicator. A peristaltic dispensing pump (DP2000, Thermo-Fisher Scientific Inc., Waltham, Massachusetts, US) was connected to the inner and outer tube of the applicator and a continuous water flow was ensured for the duration of the microwave heating at a flow rate of 50 ml/min. The temperature of the cooling water was maintained within 16 - 18.5 °C.

Table 6.2: Summary of the power and time settings and of the radial distances of fibre optic sensors from the antenna feed adopted for each MWA experimental procedure.

Sample #	Settings		Fibre optic positions	
	Power (W)	Time (s)	Fat	Adrenal gland
1	60	60	1 mm	2 mm
2	60	60	1 mm	5 mm
3	30	60	1 mm	2 mm
4	30	60	6 mm	3 mm
5	30	60	1 mm	4 mm
6	60	60	-	-

For five of the six experiments, two fibre optic sensors (Neoptix Inc., Québec, CA) were placed in the adrenal and fat tissues along the radial direction from the antenna feed of the applicator to continuously monitor the temperature of the tissue. For the Sample #6, drawbacks were encountered during the experimental procedure which hindered the reading of the temperature values. The thermal sensors system was connected to a laptop equipped with a dedicated MATLAB code for automatic temperature recording. Table 6.2 detailed each experiment, providing the levels of input power, duration of the MWA procedure and the positions of the fibre optic sensors.

6.2.3 Histology analysis

Histology analysis qualitatively assessed the degree of injury in the cellular structure of the ablated adrenal tissue and the adjacent fat layer. The histology analysis also helped to verify the integrity of the structures surrounding the ablation site, i.e. blood vessels. Sections of 9 ± 2 mm in length, 4 ± 1 mm in width and 2 ± 1 mm in thickness of each adrenal sample were cut and processed for histology analysis. Figure 6.4 details the
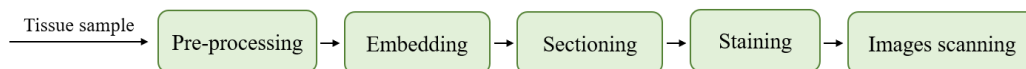
Figure 6.4: Schematisation of the main phases of the protocol adopted for the histology analysis of each tissue sample following the MWA procedure. The workflow includes pre-processing of the tissue to fix the cellular structure and to prevent the breakdown of the tissue, embedding of the tissue in the wax blocks then sectioned by a microtome at a thickness of 5 μm; staining of the tissue slices with haematoxylin and eosin (H&E) to visualise the microstructure of the tissue through the digital scanner, i.e. the cellular nuclei stained by haematoxylin (purple or dark blue) and the cytoplasm stained by eosin (pink).

workflow for the histology analysis consisting of straightforward consecutive phases [256], [257].

During the pre-processing, adrenal sections were placed into processing cassettes. Each cassette was labelled specifying the type of tissue, the progression number, the power and time settings of the MWA procedure and the date of the experiment (e.g. AG#P#t#_ddmmyy). Then, the cassettes were immersed in a fixative solution of 10% neutral buffered formalin (Sigma-Aldrich, Steinheim, DE) to prevent the degradation of the tissue. Within 48h after the MWA procedure, the cassettes containing the samples were transported to the pre-processing suite and placed in the tissue processor (Thermo Scientific^{TM} Excelsior AS Tissue Processor, Waltham, Massachusetts, US). Inside the processor, alcohols (i.e. 75% NaCl solution) and xylene were distributed into the tissue. This process removed water from the tissues (dehydration) replacing it with molten paraffin wax.

Once the pre-processing was completed (after about 12h), the histology cassettes were removed from the reaction chamber of the tissue processor. An embedding process was executed immediately after the pre-processing in order to fix each section of tissue in a block of supporting material. During the embedding process, each tissue was placed at the base of a mould and liquid paraffin was poured until entirely covering the tissue. Finally, the mould containing the tissue and the base of the histology cassette were placed on a cooling plate in order to solidify the paraffin. As a result, the tissue samples were surrounded and impregnated by paraffin in solid tissues blocks.

The paraffin embedded tissues were sectioned using a rotary microtome (Essential Microtome, Leica RM2125 RTS, Wetzlar, DE). First, each tissue block was clamped in a position parallel to the blade of the rotary microtome. Then the wheel of the machine was unlocked; slices of the tissue and the surrounding wax were trimmed at a thickness of 5 μm, starting from the tissue surface. Each slice was placed for a few seconds in a water bath at a temperature of 37°C (i.e. below the melting point of the wax ~ 40°C). Warm water smoothed possible wrinkles or creases occurring on the surfaces of the tissue slices. Each slice was picked up from the water bath and placed onto a glass slide. The

details of each tissue slice (i.e. AG#P#t#_ddmmyy) were written on the frosted edge of the slide. Then, the slices were placed on a drying rack at room temperature overnight.

A staining procedure was then performed to examine the cellular structure of the tissue sections under a digital scanner. The staining technique based on haematoxylin and eosin (H&E) was adopted. Haematoxylin binds on basophilic components of the cellular structure, i.e. DNA and RNA of the tissue, as a result cellular nucleus is dark blue or purple. Eosin binds with acidophilic components such as amino-acids contained in the cellular cytoplasm; as a result the cytoplasm is pink or orange. The staining process consists of three different phases: deparaffination/rehydration, dying and dehydration. First, the tissues were placed in xylene for 10 minutes, to remove paraffin from the tissues. Second, the tissues were rehydrated using different concentrations of ethanol solution for 30 minutes: 100% ethanol solution for 10 minutes, 95% ethanol solution of 10 minutes and 70% ethanol solution for the remaining 10 minutes. The tissues were rinsed in deionised water for 10 minutes. After the deparaffination and rehydration of the tissues, the tissues were placed in a jar containing haematoxylin (powder, 302.28 g/mol, Sigma-Aldrich, Steinheim, DE) for 20 – 30 seconds. The tissues were washed with tap water. For the second dyeing, i.e. with eosin, the tissues were immersed in a solution of 95% ethanol for 2 minutes and then into a container with eosin (90% dye content, 624.06 g/mol, Sigma-Aldrich, Steinheim, DE) for another 2 minutes. The tissue slices were immersed in three different concentrations of ethanol solution for 12 minutes for dehydration (70% ethanol for 4 minutes, 95% ethanol for 4 minutes, 100% ethanol for the last 4 minutes). To conclude the dehydration phase, the tissues were immersed in hystoclear (Histo-Clear^{TM} Tissue Clearing Agent, Thermo Scientific^{TM}, Waltham, Massachusetts, US) solution for 10 minutes. Compared to xylene, hystoclear is not toxic and leaves the tissues more flexible. At the end of the staining process, a synthetic resin mountant (DPX mountant, Sigma-Aldrich, Steinheim, DE) was applied on the glass where the slices of the tissues were placed in order to fix the cover glass.

Finally, the microstructure of each tissue section was visualised through a digital scanner (Olympus VS120-S5, Hamburg, DE) using the integrated software (Olympus VS-ASW-

S6). The name of each slide was specified consistently with the nomenclature used during the previous steps (i.e. AG#P#t#ddmmyy). For this study, the suitable magnification to clearly visualise the details of each slide was 20X, corresponding to 0.33μm/pixel. The number of focus points describing the space domain were adjusted manually in order to cover the entire area of interest. At the end of each scanning, the images were exported and then qualitatively analysed with a dedicated program (OlyVIA v3.2.1, 64bit Installer, Olympus, Tokyo, JP).

6.3 Results

6.3.1 Numerical study

Figure 6.5 depicts the geometrical assumptions adopted to charcaterise the radial and longitudinal dimensions of the ablation patterns in the simplified model and in the 3D model with reference to the local coordinates system (*u*-axis, *v*-axis and *w*-axis). The radial dimension (R) refers to the distance from the longitudinal axis of the applicator to

(1) Longitudinal dimension ablation zone in fat region
(2) Radial dimension ablation zone in fat region
(3) Longitudinal dimension ablation zone in adrenal layer
(4) Radial dimension ablation zone in adrenal region
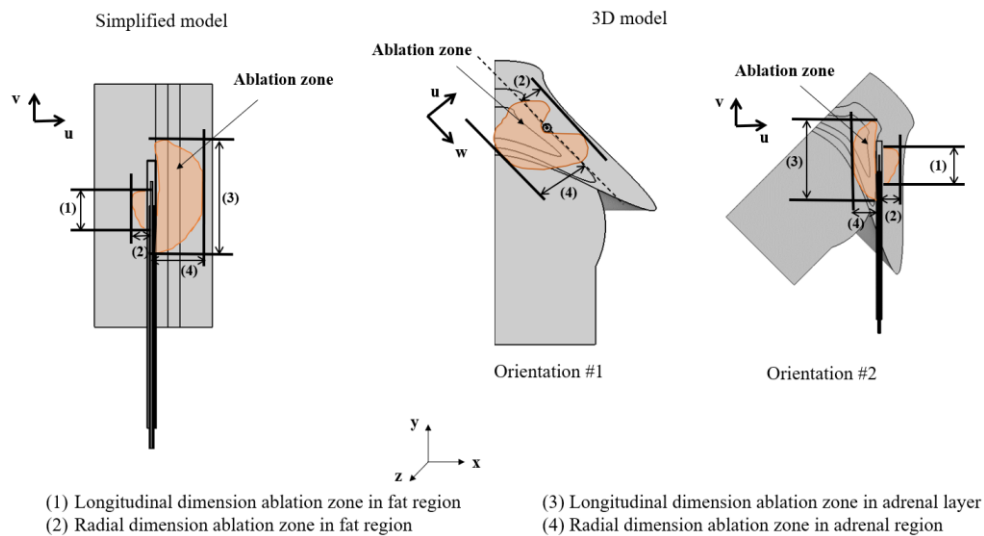
Figure 6.5: Definitions of radial and longitudinal dimensions of the ablation zones obtained in fat and in the adrenal layers both for the simplified model and the 3D model. For the 3D model both the orientations for the MW applicator are represented. With reference to the local coordinates system (u,v,w), the radial dimension is defined as the maximum extent of the ablation zone both in fat and in the adrenal tissue along the u-axis. The longitudinal dimension is defined as the maximum extent of the ablation zone both in fat and the adrenal tissues along the v-axis. In the 3D model the radial dimensions are visible for the Orientation #1 while the longitudinal dimensions are visible for Orientation #2, on the frontal plane of the global coordinates systems (x,y,z)
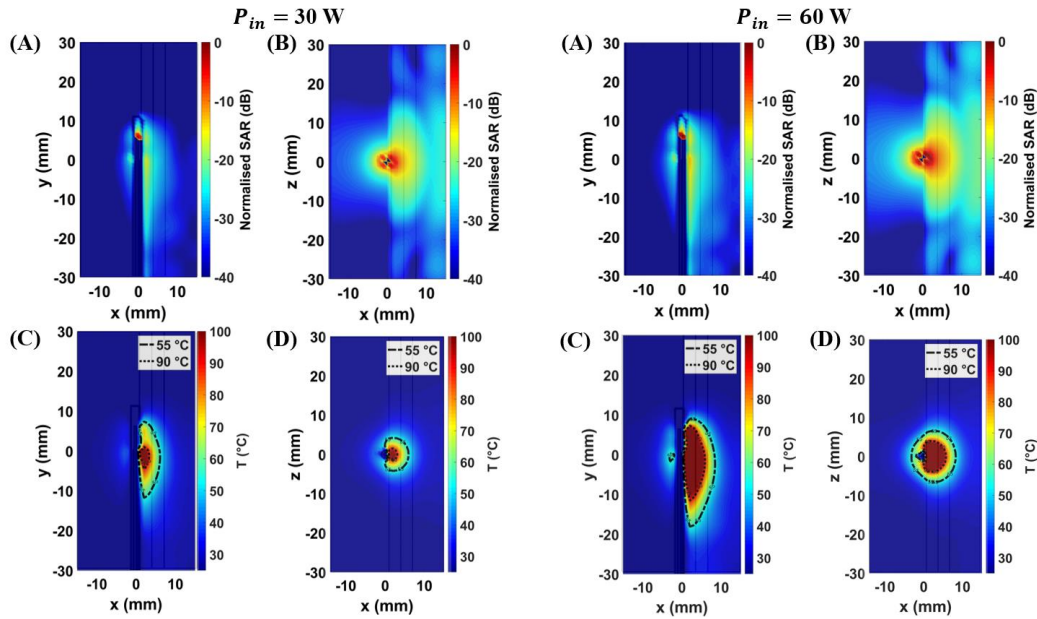
Figure 6.6: Maps of SAR (A) – (B) and of temperature (C) – (D) obtained numerically in the simplified model at 30 W and 60 W. Profiles of SAR and temperature are presented both in the frontal plane (xy-plane) and in the coronal plane (xz-plane) with reference to the feed of the antenna.

the maximum extent of ablation zone along the *u*-axis. The logitudinal dimension (L) refers to the distance between the maximum and the minimum points in the extent of the ablation zone along the *v*-axis.

Simplified model. Figure 6.6 maps the distributions of SAR (A) – (B) and temperature (C) – (D) in the simplified geometry of the adrenal gland at 30 W and 60 W input powers. SAR, normalised to the maximum and expressed in decibel (dB), and thermal profiles at 60 s are depicted in the frontal (A) – (C) and coronal (B) – (D) planes. The isothermal contour at 55°C indicates the temperature threshold suitable to achieve instantaneous coagulation (i.e. ablation zone). The isothermal contour at 90°C indicates the temperature at which vaporisation in the tissue may occur. Values of SAR higher than -20 dB extend up to 3 mm (at 30 W) and 5 mm (at 60 W) radially from the axis of the applicator in the adrenal tissue. In the fat tissue, values of SAR higher than -20 dB are absent in the case of 30 W and extend no farther than 2 mm from the longitudinal axis of the applicator at 60 W. As a result, the asymmetry in the thermal profile due to shielding effect of the fat layer is visible for both input power levels. In the case of low power (i.e. 30 W),

temperature values higher than 55°C are visibile only in the adrenal region. Increasing the input power up to 60 W, a larger ablation zone is achieved in the adrenal layer, while only a 'hot spot' in proximity to the applicator is visible in the fat layer.

Table 6.3 reports radial (R) and longitudinal (L) dimensions of the ablation zone. The table also shows the ratio between the radial and the longitudinal dimension indicating the sphericity of the ablation zone in the target tissue (i.e. the aspect ratio). For low input power, the radial and longitudinal dimensions of the ablation zone extend up to 7 mm and 19 mm in the adrenal layer, while the ablation zone is negligible in the fat layer. At 60 W, ablation zone reaches 9 mm and 27 mm along radial and longitudinal dimensions in the adrenal layer, while it slightly increases up to 2 mm along both directions in the fat layer. Table 6.3 also provides the dimensions of the ablation zones and the related aspect ratio achieved in muscle and fat. These values refer to the muscle - fat interface scenario presented in Chapter 5 at the same power and time settings, i.e. 30 W – 60 s and 60 W – 60 s. The differences in the extent of the ablation zones between the two simplified models show the impact of higher values in relative permittivity (one-fold) and effective conductivity (two-fold) of the adreno-cortical tissue adjacent to the fat layer, compared with the fat-muscle case. This contrast helps achieve larger ablation zones in the adrenal gland compared with muscle. The ablation zones in the adrenal layer increase in the radial direction up to 75% at 30 W and 50% at 60 W, compared to the fat-muscle scenario. In the adjacent fat layer the ablation zones are more than 50% smaller than the muscle-fat interface scenario, along both directions. Thus, the results indicate that the degree of contrast in dielectric properties between the two adjacent tissues

Table 6.3: Radial and longitudinal extents calculated at 30 W (first line) and at 60 W (second line) in the simplified geometry including fat and adrenal tissue reported along with the dimensions of the ablation zones previously calculated (Chapter 5) in the simplified interface model including fat and muscle. To compare the sphericity of the ablation between the two scenarios, the aspect ratio of the ablation zone achieved in target tissues, i.e. adrenal gland and muscle, are reported.

Settings		Simplified model Fat-adrenal					Simplified model Fat-muscle (Chapter 5, §5.3)				
		Fat		Adrenal gland			Fat		Muscle		
P (W)	t (s)	R	L	R	L	AR	R	L	R	L	AR
30	60	0	0	7	19	0.4	2	2	4	15	0.3
60	60	2	2	9	27	0.3	4	13	6	26	0.2
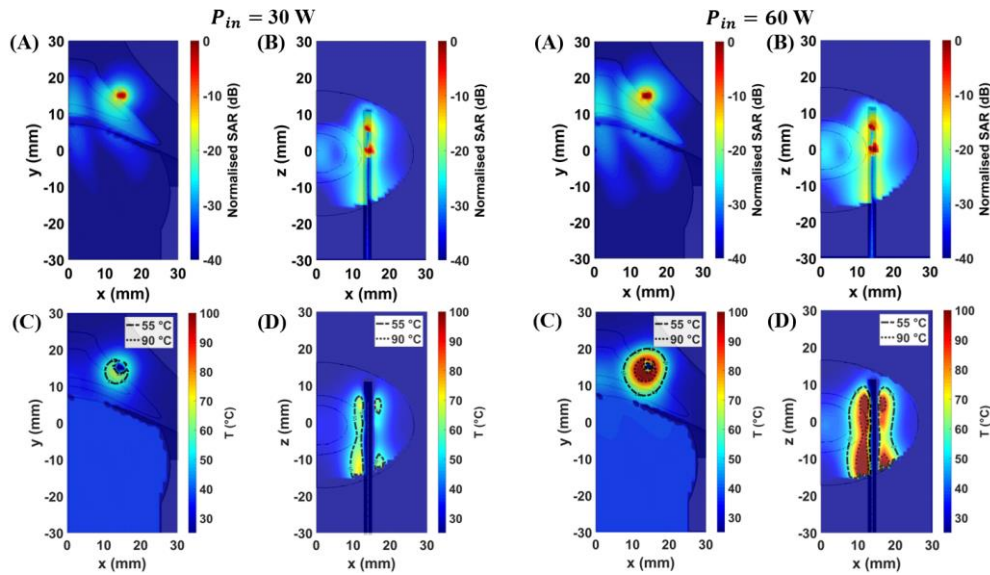
Figure 6.7: Maps of SAR (A) – (B) and of temperature (C) – (D) obtained in the 3D model at 30 W and 60 W considering the applicator aligned at the interface between fat and adrenal gland as depicted in Figure 6.6 (Orientation #1). Profiles of SAR and temperature are presented both in the frontal plane (xy-plane) and in the coronal plane (xz-plane) with reference to the feed of the antenna.

influences the asymmetry in the ablation zones. A higher dielectric contrast emphasises the asymmetric profile and the ability of the tissue characterised by lower dielectric properties (i.e. fat) to shield the electromagnetic field. Moreover, the higher dielectric contrast induces larger ablation zones and slightly improves the aspect ratio (AR) of the ablation zone in the target tissue, as observed comparing the two different planar interface scenarios (i.e. muscle – fat and adrenal gland – fat).

The impact of the variation in relative permittivty and effective conductivity on the length and diameter of the ablation was investigated in previous studies across the literature. Sensitivity analyses were conducted in [190] and [258] considering liver as reference tissue. The analysis conducted in [190] showed that a variability of ±25% in effective conductivity of the tissue results in discrepancies in the dimensions of the ablation zone up to 5.6% (length) and 7.5% (diameter). In [258] a variability of 38% upon the reference value of effective conductivity resulted in a size of the ablation zone fourteen times higher than the reference scenario.
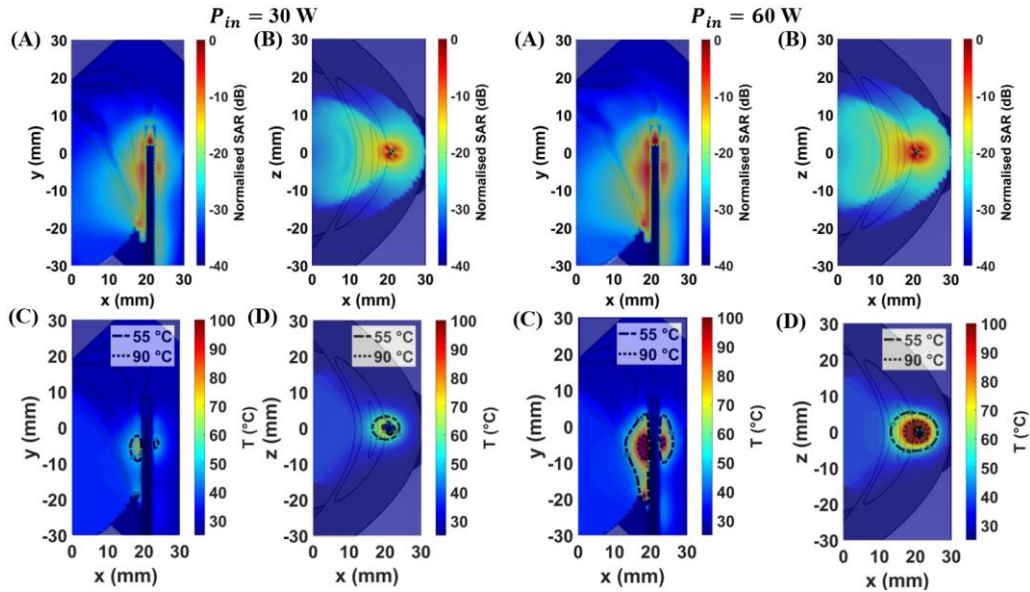
Figure 6.8: Maps of SAR (A) – (B) and of temperature (C) – (D) obtained in the 3D model at 30 W and 60 W considering the applicator aligned at the interface between fat and adrenal gland as depicted in Figure 6.6 (Orientation #2). Profiles of SAR and temperature are presented both in the frontal plane (xy-plane) and in the coronal plane (xz-plane) with reference to the feed of the antenna.

In the present study, the 'side firing' approach emphasises the influence of the higher values in relative permittivity and effective conductivity of the adrenal gland on the ablation zone. Because of the higher values in dielectric properties, the adrenal gland is characterised by a lower intrinsic impedance (Equation 4.4) than fat. Thus, part of the electric field emitted by the antenna is reflected from the fat layer into the tissue characterised by lower impedance, i.e. adrenal gland. The interface scenario between adrenal tissues and the fat layer contributes to achieving a larger ablation zone in the target tissue, i.e. adrenal tissue, while minimising the increase of temperature in the fat layer.

Three-dimensional model. Figures 6.7 and 6.8 map the distributions of SAR (A) – (B) and temperature (C) – (D) obtained in the 3D model at 30 W – 60 s and 60 W – 60 s. The maps refer to the two orientations, Orientation #1 and Orientation #2, of the MW applicator with respect to the boundary between fat and the adrenal cortex (Figure 6.2). The frontal view and coronal view provide two different planar perspectives for SAR and thermal profiles in the 3D model. For both orientations of the MW applicator, SAR

values higher than -20 dB expand through the adrenal layers while they remain confined in proximity to the applicator in the fat layer. This is consistent with the findings observed in the simplified model. The temperature profiles in the 3D geometry differ depending on the level of the input power. At 30 W, temperatures exceeding 55°C are confined within a few millimetres in the adrenal tissues while the fat tissue is entirely spared. Thus, at low power the shielding effect of the fat layer lessens the temperature below 55°C and drives the ablation zone toward the adrenal tissue (Figure 6.8(C)). At 60 W, ablation zones increase both in fat and in the adrenal gland, resulting in less asymmetric ablation profiles compared with the lower input power scenario.

Table 6.4 lists the radial and longitudinal dimensions of the ablation zone obtained in the simplified model and in the 3D model, for the two different orientations of the applicator. At 30 W, the ablation zone in the fat layer is visible in the 3D model. Comparable dimensions are reached for both orientations of the MW applicator. Results show that low input power induces a relatively small and spherical ablation zone in the fat layer. In the adrenal tissue, the ablation zone is bigger than in fat as expected. However, the radial and longitudinal dimensions in the adrenal gland vary depending on the orientation of the MW applicator. Radial and longitudinal dimensions are 29% and 21% smaller in the case of Orientation #1 and 29% and 63% smaller in the case of Orientation #2, compared with the simplified model.

At 60 W, the ablation zone in fat becomes visibly larger and more elongated compared with the low power case. This change in the ablation profile is linked to the curvature of

Table 6.4: Radial and longitudinal extents calculated at 30 W (first line) and at 60 W (second line) in the simplified geometry and in the 3D model. The radial and the longitudinal dimensions of ablation zones measured experimentally are reported in terms of mean and standard deviation for each power and time setting considered.

Settings		Simplified model				3D model Orientation # 1				3D model Orientation #2				Experimental	
		Fat		Adrenal gland		Fat		Adrenal gland		Fat		Adrenal gland		Adrenal gland	
P (W)	t (s)	R	L	R	L	R	L	R	L	R	L	R	L	R	L
30	60	0	0	7	19	2	4	5	15	3	3	5	7	4 ± 2	14 ± 2
60	60	2	2	9	27	5	21	7	17	5	13	8	20	8 ± 2	16 ± 2

the geometry in the 3D scenario, which weakens the ability of the fat to lag the temperature increase. As a result, a reduced amount of the electric field is reflected from the fat layer to the adrenal tissue, and the ablation zones in the adrenal tissue are smaller compared with the simplified model. In particular, radial dimensions decrease by 22% for Orientation #1 and by 11% for Orientation #2; the longitudinal dimensions decrease by 37% for Orientation #1 and by 26% for Orientation #2.

It is worth noting that the 3D model has an impact on the longitudinal dimension of the ablation zone more than on the radial dimension. The pronounced curvature of the surfaces of the 3D model shapes the space around the applicator forcing the ablation zone to grow toward the longitudinal direction in fat. This effect becomes noticeable in the case of high power for Orientation #1. A similar effect was observed in [221] and [141], after a microwave ablation procedure conducted in liver at 60 W for 10 min. These studies show the ablation zone progresses along the longitudinal dimension rather than the radial dimension in samples where the height is smaller than the achievable radial extent. In the thin samples, the ablation zone increases up to 13% [221] and 22% [141] in longitudinal dimension compared with unrestricted samples.

Compared with Orientation #1, Orientation #2 guarantees a better contact area between the applicator and the tissue and better alignment of the antenna at the interface between the fat and adrenal gland. Thus, an improvement in the shielding effect of the fat layer and the consequent asymmetric ablation zones can be observed both at low and high input powers.

Finally, it can be noted that kidney is unaffected by the increase in temperature for both antenna orientations and both input power settings adopted.

6.3.2   Experimental *ex vivo* assessment

The shielding effect caused by the presence of the fat layer at the interface with the adreno-cortical tissues was investigated experimentally on N = 6 *ex vivo* ovine adrenal glands surrounded by the adrenal fat capsule. A total of N = 6 MWAs were performed, N = 3 at 30 W and N = 3 at 60 W. Figure 6.9 shows an example of ablation zone achieved *ex vivo* in an ovine adrenal gland. A shallow coagulation area is visible through the
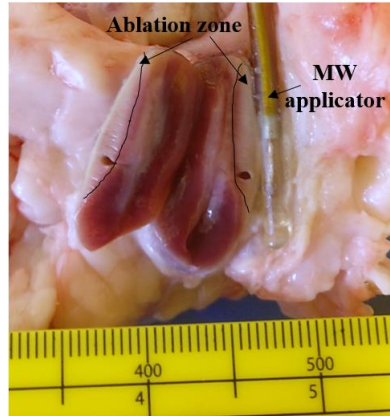
Figure 6.9: Section of a MWA zone obtained in ex vivo ovine adrenal gland: the applicator (MW antenna) is placed at the visible interface between the adrenal gland and the surrounding perinephric fat, and the ablation zone obtained in the adrenal gland is marked. The ablation zone is not visible in fat.

whitened tissue resulting from the MWA procedure. Also, it can be seen from Figure 6.9 that the applicator is placed at the interface between the adreno-cortical tissue and the surrounding fat.

Table 6.4 reports the experimental radial and longitudinal dimensions of the ablation zone measured in the adrenal gland. It can be observed that the highest discrepancy in the extent of the ablation zone is visible between the experimental scenario and the simplified model. The ablation dimensions achieved in the 3D numerical model agree with the experimental findings, at both 30 W and 60 W. It should be noted that the ovine samples appear rounded shaped [259]. Thus, the 3D model better represents the convexity of the external surfaces of the adrenal gland compared with the simplified model.

Figure 6.10 shows the temperature values acquired by the fibre optic sensors. The data refer to 30 W (A) and 60 W (B) input power and to two-time steps (30 s and 60 s). The experimental values are compared with the values achieved in the 3D model, considering the same settings. All the data is presented as a function of the radial distance from the longitudinal axis of the MW applicator. The comparison reported in Figure 6.10 also accounts for the two different orientations of the MW applicator with respect to the interface between fat and adrenal gland. In addition, a temperature threshold equal to

55°C is highlighted to assess the extension of the coagulation necrosis [80], [184], [260]. The two different orientations of the MW applicator highlight a discrepancy in the temperature results between a minimum of 0.2°C and a maximum of 11°C observed at high input power in the adrenal layer. The shape and the size of the fat and adrenal gland layers surrounding the applicator vary due to the curvature of the surfaces modelled in the 3D geometry. The radial dimensions of the adrenal and fat layers at the antenna feed are 7 mm and 8 mm for Orientation #2, and 10 mm and 12 mm for Orientation #1. The variability in the geometry together with the convex profile of the surfaces in the 3D model correlate with the variability observed in the simulated temperatures between the two orientations. Nevertheless, the experimental values lie within the values obtained from the numerical simulations, suggesting numerical results reasonably estimate the extent of the ablation zone.

The curves in Figure 6.10 show that a high power setting (i.e. 60W) allows for an improved ablation zone in the target adrenal tissue. However, a sizable undesired heating is observed in the fat layer within the first 30 seconds of ablation. Conversely, at a low power setting (i.e. 30 W) temperatures below 55°C are observed for most of the fat tissue even after 60 s; while sizable ablation zones in the target tissue are induced. Thus, the results suggest that a low power setting (i.e. 30 W) may allow a more cautious approach to be translated in the *in vivo* study (Chapter 7).
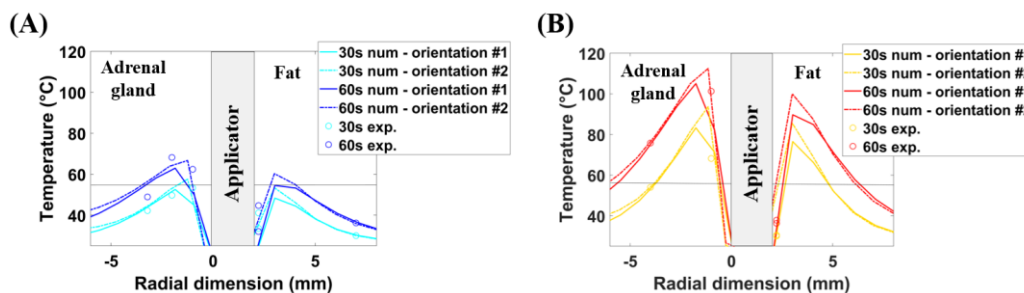
Figure 6.10: Numerical (num.) and experimental (exp.) values of temperature along the radial distance from the MW antenna axis (applicator) both in the fat and adrenal gland at 30 s and 60 s for 30 W (A) and 60 W (B). Temperature value obtained from the 3D model accounting for the orientation #1 (solid lines) and orientation #2 (dash-dot lines). Horizontal line highlights the temperature threshold at 55 °C.

6.3.3   Histology analysis

The thermal injury induced in the tissue by the MWA procedures was evaluated on two out of six available samples. Figures 6.11 and 6.12 show the histological results obtained in the adrenal sample after MWA procedures conducted at 30 W (Figure 6.11) and 60 W (Figure 6.12) for 60 s. Figures 6.13 and 6.14 show the histological findings related to the periadrenal fat (Figure 6.13) and the adjacent blood vessel (Figure 6.14) after a MWA procedure conducted at 60 W for 60 s.

The changes in the cellular structure due to the thermal effect are visible to a certain extent in the adrenal glands. Three different zones are defined with respect to distance from the applicator:

- Zone 1: proximal zone
- Zone 2: transition zone
- Zone 3: distal zone

Zone 1 is a more eosinophilic region of the adrenal sample, due to an absence of the cellular nuclei. This characteristic indicates that complete cell death occurred both at high
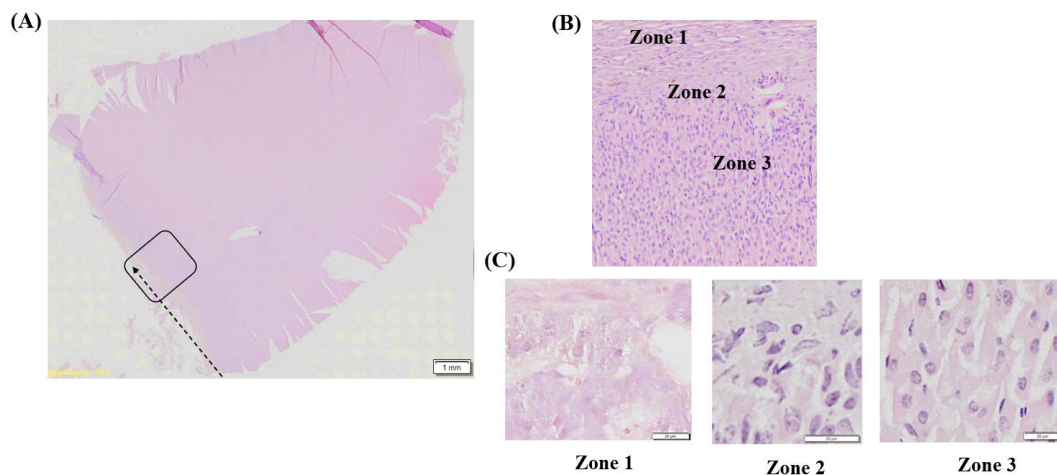
Figure 6.11: A histological section of the adrenal gland stained with H&E after an ablation procedure performed at 30 W for 60 s and the placement of the MW applicator (A). Three zones with different histological features are recognised at different distances from the placement of the applicator (B): coagulative necrosis characterised by a more eosinophilic region due to the damage of the cellular nuclei (Zone 1); a transition zone from the injury zone and the untreated region characterised by a mixture of 'ghost' cells and morphologically normal cells (Zone 2); non-targeted adrenal zone distal from the applicator position, which contains cells morphologically normal (Zone 3).
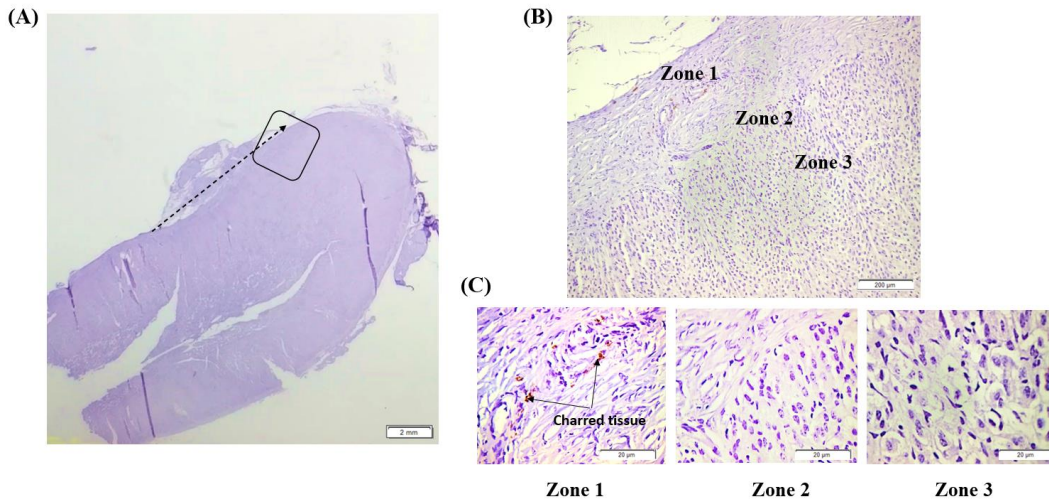
Figure 6.12: A histological section of the adrenal gland stained with H&E after an ablation procedure performed at 60 W for 60 s and the placement of the MW applicator (A). Three zones with different histological features are recognised at different distances from the placement of the applicator (B): coagulative necrosis characterised by spots of charred tissue in the zone adjacent to the applicator (Zone 1); a transition zone from the injury zone and the untreated region characterised by a mixture of 'ghost' cells and morphologically normal cells (Zone 2); non-targeted adrenal zone distal from the applicator position, which contains cells morphologically normal (Zone 3).

and low input powers. The main difference between the two power settings is determined by the presence of brown-coloured spots visible only at 60 W. These spots indicate charred areas in the tissue in contact with the applicator. Zone 2 and Zone 3 show similar histological features regardless of the input power at which the MWA procedure was conducted. Zone 2 presents a mixture between intact areas of tissue and areas injured by thermal insult. The cells of this transitional zone closer to Zone 1 show a cytological architecture compromised by the high temperatures. The cells far from the margin with Zone 1 show elongated cellular nuclei and/or partially damaged cellular membrane. In Zone 3, cells appear with rounded blue-coloured nuclei and well-defined cytological architecture. The rounded shapes of the cellular nuclei indicate that the tissue remained intact after the MWA procedure.

The histological findings suggest that low input power prevents the risk of charred spots in the tissue. In addition, the cautious approach provided by low input power helps to avoid extremely high temperature which can compromise the functionality of the gland. The 'zonation' observed in the adrenal gland (Figures 6.11 – 6.12) is in agreement with

the histological results provided by other studies. In [261] a histology analysis showed the changes occurring in ten porcine hepatic tissues. The samples were analysed after MWA procedures conducted *in vivo* at 60 – 70 W for 5 -10 min. In [261] irreversible impairments characterised by the absence of nuclei is observed solely in the centre of the ablation zone. In [148] a section of porcine renal tissue was examined after a MWA procedure conducted *in vivo* at 50 W for 10 min. The results showed a region of complete cell death characterised by interstitial haemorrhage only in the region surrounding the axis of the MW applicator. In a recent study, [262] evaluated the histological changes in porcine adrenal tissue immediately after MWA procedures conducted *in vivo* at 45 W and 70 W for 60 s. Regardless of the input power used, the histological findings demonstrated evidence of coagulation necrosis only in the area adjacent to the probe placement. All the aforementioned studies also reported consistency in the histology characteristics of the transition zone (between the distal and proximal zones). Essentially, in this zone the cellular membranes were partially deformed, and the images appeared faded ("ghost effect"), as observed in the present study. In addition, the present study offered a complete understanding of the effects of the MWA procedure not only on the microstructure of the adrenal gland, but also on the fat and adjacent blood vessel.

The effects of the heating on the microstructure of the periadrenal fat and the adjacent blood vessel were studied only in the case of the highest input power (i.e. 60 W). At 60 W, temperatures above 55 °C were observed numerically up to 5 mm from the axis of the applicator in fat (Figures 6.6 – 6.8, Figure 6.10). Thus, 60 W showed a higher potential to cause unintended damages to the structures surrounding the gland (e.g. blood vessels).

Two different zones are identified in the fat layer, by reference to distance from the applicator (Figure 6.13).

Zone 1 is the proximal region, thus more susceptible to the heating due to MWA. Vascular congestion is visible within adipocytes (i.e. fat cells) in this zone.

Zone 2 is the area far from the applicator and closer to the blood vessel reported in Figure 6.14. This region shows no inflammatory areas or changes in the microvasculature within

adipocytes. This result suggests that the area of fat abutting the blood vessel was not affected by the increase in temperature. The integrity of the vessel morphology (Figure 6.14) confirms the ability of the fat layer to spare the surrounding sensitive structures from the thermal injury. The blood vessel examined here is a large artery surrounded by the periadrenal fat. All the three main structures which typically compose the wall of the blood vessel are distinguishable and their histologic features are visibly intact [263]. These structures include:

- Tunica adventitia
- Tunica media
- Internal elastic lamina

The tunica adventitia is the external component of the vasculature wall. This layer consists mainly of connective tissue (Figure 6.14 (C)). The tunica media is the middle layer including smooth muscle cells, which appear as elastic lamellae. These cells appear in vessels of at least 2 mm in diameter and regulate the blood pressure through vasodilation and vasoconstriction. Finally, the internal elastic lamina consists of
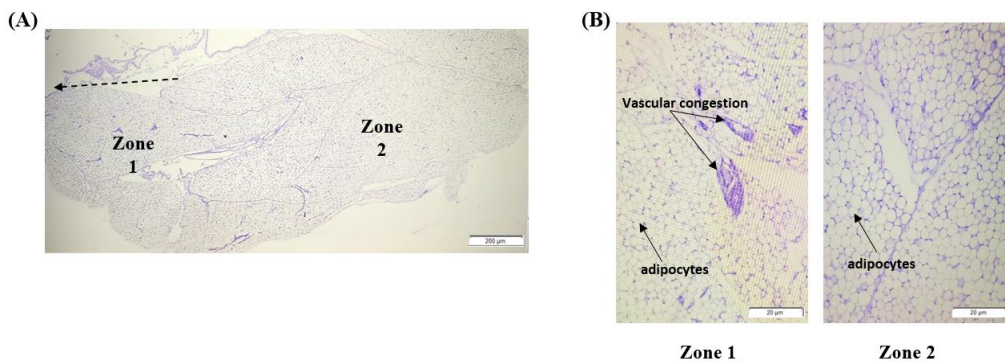
Figure 6.13: A histological section of the fat layer surrounding the adrenal gland stained with H&E after an ablation procedure performed at 60 W for 60 s. (A) Two different zones with different histological features are recognised at different distances from the applicator (B): an inflammatory zone denoted by the enlargement of the microvasculature within adipocytes (Zone 1); a distal zone where a normal microvasculature within adipocytes indicates that no increase in temperatures occurred (Zone 2).
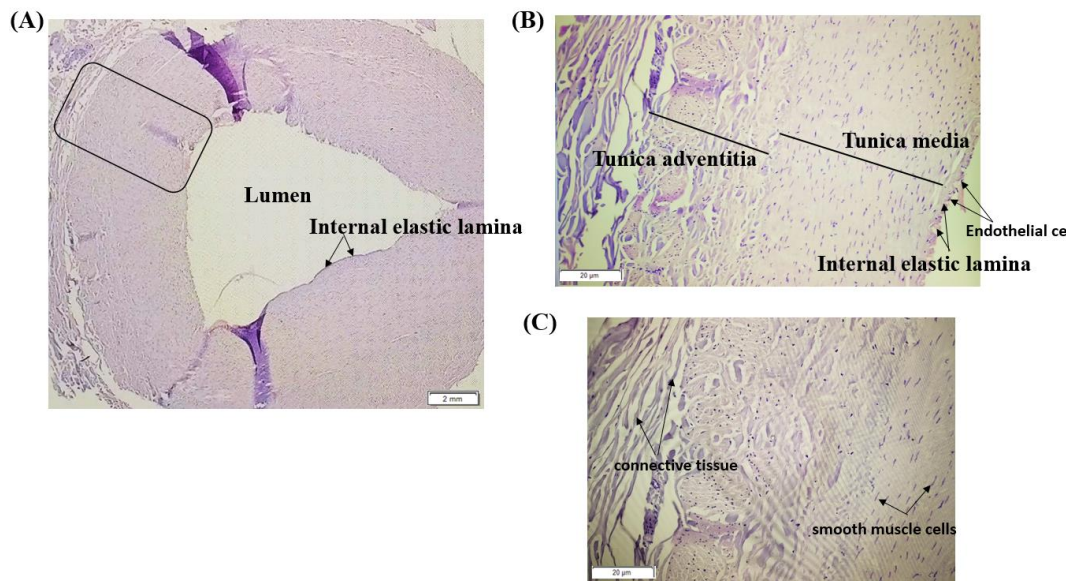
Figure 6.14: A histological section of a blood vessel after an ablation procedure performed at 60 W for 60 s. The blood vessel was adjacent to the fat layer which separated the vessel from the adrenal gland. (A) The integrity of the structure of the blood vessel is indicted by the presence the intact internal elastic lamina and the aperture of the lumen (in the case of damage the blood vessel collapses, and the lumen occludes). All the three main structures of the blood vessel (B) and their histological features (B) – (C) are intact: Tunica adventitia mainly characterised by connective tissues; Tunica media composed of smooth muscle cells; Internal elastic lamina characterised by endothelial cells.

squamous and elongated endothelial cells. The endothelium acts as an antithrombogenic barrier and ensures the tone of the vasculature wall [263]. When the barrier of endothelial cells is damaged, the entire structure of the blood vessel collapses and a cascade of platelets aggregations obstructs the normal blood flow. This phenomenon results in the formation of intravascular clots or thrombi, which are potentially life-threatening conditions [264]. Blood vessels abutting ablation targets are exposed to higher risks of thrombotic events induced by the coagulation necrosis.

In this study, the histology analysis revealed the microscopic features after MWA procedure not only in the tissue target (i.e. adrenal gland) but also in the surrounding fat layer and the adjacent blood vessel. This analysis helped to overcome drawbacks encountered during the experimental assessment. As described in the previous sections, visual inspection was adopted to estimate the extents of the ablation area in the adrenal gland (Figure 6.9). However, the whitening effect observed immediately after the MWA

procedure made it difficult to evaluate to what extent the ablation zone affected the fat layer. Thermal sensors (e.g. fiber optic sensors, thermocouples) were used only to monitor the local temperature increase in the tissue during the ablation procedure (Figure 6.10). Overall, the histological findings confirmed the ability of the fat layer to confine the thermal effects induced by the increase of temperature in the area proximate to the applicator. The presence of the fat layer helped to preserve the integrity of the blood vessel abutting the adrenal gland. As a result, the coagulation necrosis of the tissue was observed only in the adrenal gland and it was particularly visible in the case of the highest input power. The scattered brown-coloured areas identified in the case of 60 W suggest that the charring of tissue ensued from the very high temperatures reached in proximity to the applicator (Figure 6.10). It is worth noting that the time (60 s) at which MWA procedures were conducted helped to spare the medulla, even in the case of the highest power. Relatively short times may contribute to preserving the functionalities of the adrenal tissues, which are crucial to the release of hormones. In addition, short durations help to minimise the stress induced to the adrenal medulla. The heating of the gland during the MWA induces the medulla to release a higher amount of catecholamines which contribute to the increasing of the cardiac rate of the patient.

6.4 Conclusions

This chapter examines the influence of dielectric and geometrical characteristics of the adrenal tissues on shaping asymmetric ablation profiles. In the numerical study, the extent of the ablation zone both in the adrenal gland and in the adjacent fat layer was estimated at two levels of input power (30 W and 60 W). Two different numerical models were accounted for: a simplified multilayer structure and a 3D model. An experimental *ex vivo* study was conducted on ovine adrenal glands to support the numerical investigation. The same power settings (30 W and 60 W) supplied for 60 s were used for both the numerical and experimental investigations.

The results of the study show that:

- The electromagnetic field in the planar adrenal-fat scenario – facing an higher contrast in relative permittivity and effective conductivity – induces more

pronounced asymmetric ablation patterns when compared with the planar muscle-fat scenario (Chapter 5);

- The geometry of the tissues influences the shape and the size of the ablation zones. In the fat layer, the curvature of the 3D geometry reduces the radial space achievable by the ablation zone. Thus, the electromagnetic field redistributes along the longitudinal dimension, resulting in longer ablation zones compared with the simplified model. The final shape and size of the ablation zone also depend on the orientation of the antenna at the interface between the two tissues. Thus, in the 3D geometry, the alignment of the antenna has a higher impact on the ablation asymmetry than in the 2D multilayer scenario.

- The 3D model adopted in this study provides a reliable representation of the experimental *ex vivo* scenario. The experimental data are in good agreement with the numerical findings. Thus, the study suggests that potential pitfalls during the treatment planning can be avoided or reduced by considering the orientation of the applicator, the geometrical characteristics of the target and the surrounding tissue;

- The histological analysis conducted within 48h after the MWA procedures on *ex vivo* ovine adrenal tissues confirms the presence of coagulated tissue only in the target area. Critical structures in proximity to the applicator (such as blood vessels) are preserved thanks to the effect of the fat lagging the temperature increase. In the adrenal gland, the cell death is observed only in the area closer to the MW applicator. In the fat layer, the inflammation response is the only visible effect to the thermal insult. This response is limited to the zone of the tissue closer to the MW applicator. Thanks to the presence of fat, the abutting blood vessel showed an integer structure without any sign of the effect of the temperature increase.

Following the proof-of-concept study presented in Chapter 5, this study provides a broader description of the 'side firing' approach in the case of the adrenal gland and its surrounding fat layer. The entire investigation was conducted accounting for the *ex vivo* scenario. Thus, the effects of the blood surrounding the target and the blood perfusion

rate of each tissue were neglected. Chapter 7 is dedicated to evaluating the feasibility of the 'side firing' approach in the *in vivo* scenario.

Chapter 7

MWA on adrenal glands through 'side firing' approach: an *in vivo* study

7.1 Introduction

Chapter 6 described the influence of the dielectric and geometrical characteristics of the tissue target, i.e. adrenal cortex, on the ability of the fat layer to shield the EM field and to shape asymmetric ablation profiles. The ability to perform a side firing ablation exploiting the shielding effect of the fat layer was also validated experimentally and confirmed histologically.

First, a simplified model reproduced the dielectric contrast between fat and adrenal cortex. The contrast was 13% higher in terms of relative permittivity and 150% higher in terms of effective conductivity compared with the muscle-fat contrast. This contrast was shown to produce up to 75% larger ablation zones in the adrenal tissue and up to 50% smaller ablation zones in the fat layer compared with the muscle-fat scenario. The increased contrast in the adrenal-fat scenario enhanced the shielding effect of the fat tissue.

Next, a 3D geometry was used to investigate the influence of anatomically realistic shapes and sizes of the target tissues on the thermal patterns. Two different orientations of the MW applicator were considered to account for the cases of best and worst alignment with respect to the interface. Results also showed asymmetric ablation profiles in the 3D model. However, the extent of the ablation zones was affected by the curvature of the geometry and the alignment of the applicator at the interface.

The 'side firing' approach was tested on N = 6 *ex vivo* ovine adrenal glands. The resulting ablation zones were in agreement with the dimensions predicted by the 3D model, laying within the variability observed in the numerical findings. Finally, histology analysis was used to map the thermal damage in the target tissue, the surrounding fat layer and the adjacent blood vessel. The histological findings revealed an impairment in the cellular

structure only in the adrenal tissue in proximity to the applicator. No coagulation necrosis was observed in the fat layer surrounding the adrenal gland and in the adjacent blood vessel.

This chapter seeks to translate the investigation into an *in vivo* scenario. The 3D model presented in Chapter 6 (§ 6.1.1) was used as a test platform and modified to better represent the *in vivo* scenario. The background material was set to mimic blood properties and the starting temperature was set equal to 37°C. Blood perfusion rates were assigned to both the adrenal and fat layers to account for the effect of blood perfusion on the final extent of the ablation zones. Two different levels of volumetric blood flow rate were assigned to the layers representing cortex and medulla ($4 \cdot 10^{-5}$ $m^3kg^{-1}s^{-1}$) and the surrounding fat layer ($5 \cdot 10^{-7}$ $m^3kg^{-1}s^{-1}$) according to [265]. The study aims to:

- Compare the extent of the ablation zone achieved in the case of background material set as blood with the findings achieved in the *ex vivo* numerical scenario. The MW applicator was placed at the interface between fat and adrenal cortex according to the two orientations presented in Chapter 6, i.e. Orientation #1 and Orientation #2 (§ 6.1.1). The distributions of the EM power and of temperature in the model were computed considering two input powers, 30 W and 60 W, delivered for 60 s;

- Evaluate the extent of the ablation zone achieved for each orientation and setting combination with and without blood perfusion;

- Translate the 'side firing' approach *in vivo* using an adult sheep model. For the *in vivo* study, 30 W was supplied for 60 s and the MW applicator was placed on the surface of the adrenal gland at the interface with the periadrenal fat. The analysis includes both visual and histological inspection.

The structure of the chapter is as follows: section 7.1 describes the numerical models adopted to represent the *in vivo* scenario. The section also describes the protocol adopted for the acute animal study. Section 7.2 presents the ablation profiles obtained numerically for each orientation of the MW applicator and for each setting, along with the experimental results. Section 7.3 concludes the chapter.

7.2 Methodology

7.2.1 Numerical study

The 3D numerical model used in the previous study (§6.1.1) was adopted in the present study to represent the adrenal gland and the surrounding fat capsule. The same thermal and dielectric properties reported in Table 6.1 (§6.1.1) were used to characterise each tissue. The triaxial MW applicator described in Chapter 4 was positioned at the interface between fat and adrenal tissue according to the two different orientations already presented, i.e. Orientation #1 and Orientation #2 (§6.1.1).

First, blood was assigned as the background material instead of air (used in Chapter 6 to simulate the *ex vivo* scenario) to better represent the *in vivo* scenario. The values of the thermal and dielectric properties for blood were acquired from [245] and reported in Table 7.1. The blood surrounding the tissue model and the MW applicator placed at the interface between fat and adrenal cortex was modelled by a cuboid of 126 mm in height, 148 mm in width and 60 mm in the case of Orientation #1; the surrounding blood was modelled by a cuboid of 80 mm in height, 102 mm in width, 76 mm in thickness, in the case of Orientation #2. The entire geometry was discretised by a total number of tetrahedral meshing cells equal to 5,085,045 ranging from 0.1 mm to 6.1 mm in the case of Orientation #1. The total number of meshing cells was equal to 3,876,880 ranging from 0.1 mm to 6.4 mm, for Orientation #2. The convergence criteria adopted to establish the suitable number of meshing cells are the same as those presented in Chapter 4. A minimum of ten cells per wavelength (frequency = 2.45 GHz) was considered, then the

Table 7.1: Dielectric and thermal properties of blood employed in the numerical simulations

Parameter	Blood
Relative permittivity, ε_r	58.3 ± 3.0
Effective conductivity, σ_{eff} (Sm^{-1})	2.5 ± 0.2
Specific heat capacity, c ($Jkg^{-1}K^{-1}$)	3651 ± 0.1
Density, ρ ($kg\ m^{-3}$)	1046 ± 0.1
Thermal conductivity, k ($Wm^{-1}K^{-1}$)	0.5 ± 0.1
Frequency (GHz)	2.45
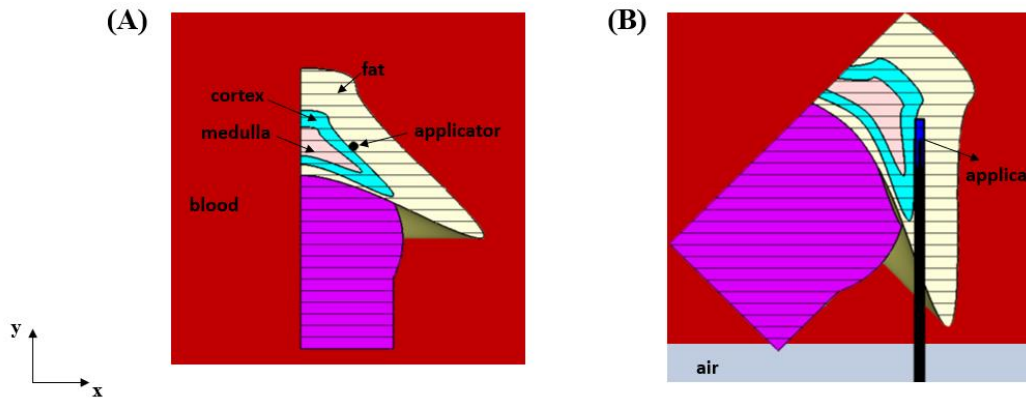
Figure 7.1:Three-dimensional model for the adrenal gland and the surrounding fat capsule. Each scenario accounts for a different orientation of the MW applicator with respect to the interface between fat and adrenal cortex. In both models, a block of blood surrounded the geometry of the tissues. The feeding of the coaxial cable (i.e. waveguide port) was kept outside the block of blood, as required to adequately excite the signal for the electromagnetic and thermal simulations.

number of the cells was increased until the mismatch in the magnitude values of the reflection coefficient between two consecutive simulations was less than 0.1%. Figure 7.1 depicts the two numerical scenarios investigated, including blood surrounding the geometry.

Electromagnetic and thermal simulations were performed using CST MW Studio to obtain the distributions of SAR and temperature. The boundary conditions between the applicator and the surrounding tissue were assigned as reported in Chapter 4 (§ 4.2), to account for the forced convection heat exchange. Boundary conditions were modelled as described in Chapter 4 (§ 4.2) to account for the free convection exchange between the tissue model and the surrounding blood. The initial temperature of the tissue model was set equal to 37°C to reproduce the initial body conditions of the *in vivo* scenario. As well as for the previous study, two different input power levels were supplied for 60 s for each orientation of the MW applicator (30 W and 60 W).

Next, the numerical model was further refined to represent the *in vivo* scenario accounting for the influence of the blood perfusion of the tissues on the ablation zone. Two different volumetric blood flow rates were assigned to the adrenal and fat tissues
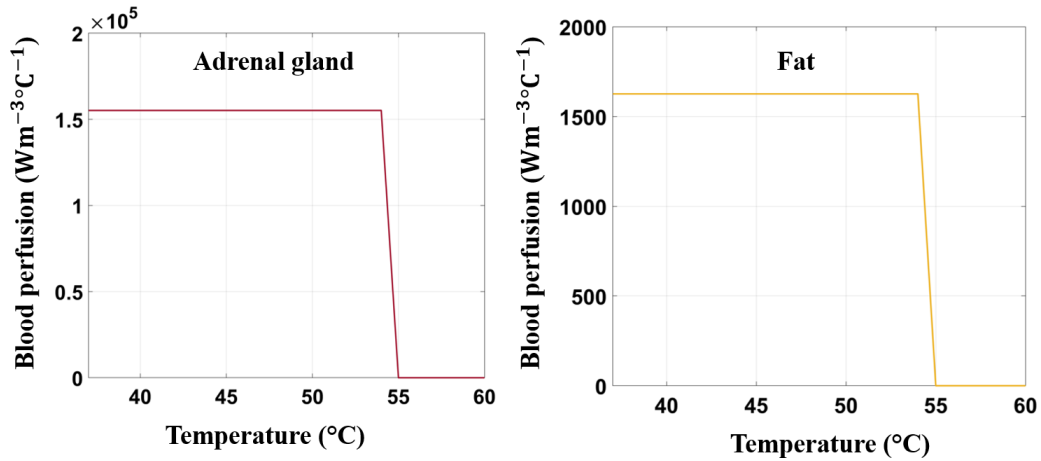
Figure 7.2: Models for blood perfusion as function of the temperature, both for adrenal gland and fat. The rectangular function accounts for the collapsing of the blood supply to the tissue due to the coagulation effect when ablative temperatures (above 55°C) are approached. The coefficients for blood perfusions were assigned according to the values reported in [265]: 1,626 Wm^{-3}°C^{-1} in fat and 155,163 Wm^{-3} °C^{-1} in adrenal tissues.

according to the values reported in [265]: 5·10^{-7} m^{3}kg^{-1}s^{-1} for fat and 4·10^{-5} m^{3}kg^{-1}s^{-1} for adrenal cortex and medulla. As a result, the terms of blood perfusion in Equation 4.13 become equal to 1,626 Wm^{-3}°C^{-1} for the fat tissue and to 155,163 Wm^{-3}°C^{-1} for adrenal tissues.

Figure 7.2 shows the curves for blood perfusion both in the adrenal gland and in the fat tissue against temperature. The rectangular function aims to account for the disruption of the microvasculature of the region of interest. When the temperature exceeds 55°C, the coagulation effect induces the collapse of the blood supply in the area of the tissue under treatment [266]–[268]. The functions were first modelled in MATLAB and then integrated in the simulations to enable the iterative calculation of the tissue temperature. In total, four simulations were performed accounting for the same set of input power and duration and the same two orientations of MW applicator as described above.

7.2.2 Experimental *in vivo* animal study

An acute animal study was conducted at the Hospital Virtual Valdecilla (HvV), Santander, Cantabria, Spain, according to an approved protocol (National Regulatory Body approval and HvV Ethical Committee authorisation). First, a bilateral sham test

was performed *ex vivo* on swine tissue to allow the surgeon to familiarise themselves with the experimental setup. The optimal strategy to access the adrenal gland and to position the antenna at the interface between fat and adrenal gland was identified. Next, an adult 20 kg sheep was used to test the directive ablation hypothesis *in vivo* on the left adrenal gland (note: generally, in ovine the second adrenal gland is too small to be representative of a human gland and it lies slightly distant from the apex of the correspondent kidney therefore it was not used).

The animal was positioned on dorsal recumbency and anesthetised by Ketamine (15-35 mg/kg) and xylazine (5 mg/kg). The anaesthesia was maintained by halothane or isofluorane for the duration of the procedure. To access the adrenal gland, a ventral midline celiotomy was executed and the triaxial MW applicator (Chapter 4) was placed in direct contact with the surface of the adrenal gland beneath the adrenal layer. The use
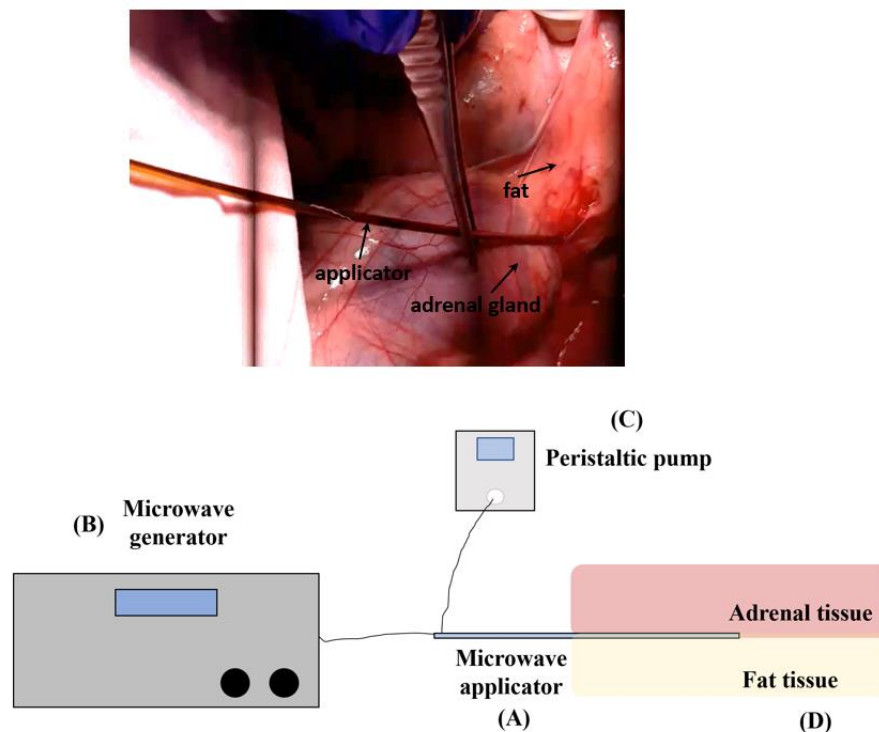
Figure 7.3: Positioning of the MW applicator at the interface between the ovine adrenal gland and the surrounding fat during the in vivo experimental study (top). Related schematisation of the experimental setup including the microwave applicator (A), connected to a microwave generator (B) through a low loss coaxial cable; a peristaltic dispensing pump (C) was connected to the inflow and outflow tubes of the refrigerating system integrated in the applicator.

of a triaxial antenna made the access to the adrenal gland easier and less invasive due to the smaller diameter compared with the monopole antenna used in the *ex vivo* study. In addition, the triaxial structure improves the impedance matching of the antenna and the surrounding tissue (Chapter 4). This feature of the triaxial structure helps to minimise the detuning issues due to tissue heterogeneity which are less controllable in the presented *in vivo* scenario. Thus, the triaxial applicator allows for a more efficient delivery of the EM power in the tissue, reducing the return of the current flow along the cable. The current could cause the applicator to overheat, resulting in cable failure. Figure 7.3 shows the positioning of the MW applicator adjacent to the adrenal gland and the surrounding fat; the figure shows also a schematisation of the experimental setup.

The adequate position of the MW applicator was assessed through visual inspection. The vital parameters of the animal were monitored to confirm the status of the animal prior to the procedure. Input power set at 30 W was supplied for 60 s from a microwave generator (Sairem, SAS, France). The generator was connected to the applicator through a low loss coaxial cable and an SMA connector. A refrigerating system including a peristaltic pump (DP2000, Thermo-Fisher Scientific Inc., Waltham, Massachusetts, US) was connected to the MW applicator and ensured continuous water at 16 – 18 °C via a flow rate of 50 ml/min. During the procedure, analgesics (fentanyl citrate 0.05 mg/kg or nalbuphine hydrochloride 2mg/kg) and tranquiliser (diazepam or midazolam at 2mg/kg) were administered.

The animal was euthanised after the procedure with intravenous pentobarbital (65-100 mg/kg), and the adrenal gland was removed to be visually inspected. A tissue section of 40 mm in length, 32 mm in width and 17 mm in thickness was histologically analysed within 48 h after the procedure. The protocol detailed in Chapter 6 was used for the H&E staining to enable the histology analysis through the light microscope (Zeiss Axio Observer, Oberkochen, DE).

7.3 Results

7.3.1 Numerical study

Figure 7.4 and Figure 7.5 map the distributions of SAR (A) – (B) and temperature (C) – (D) obtained at 30 W – 60 s and 60 W – 60 s considering two different orientations of the MW applicator (i.e. Orientation #1, Orientation #2) and the blood background at a temperature of 37°C. SAR and thermal profiles are provided both in the frontal (A) – (C) and coronal (B) – (D) planes.

At 30 W, values of SAR in the adrenal gland higher than -20 dB extend along the radial distance from the axis of the applicator up to 4 mm in the case of Orientation #1 and up to 6 mm in the case of Orientation #2. At 60 W, the radial extent of the area in the adrenal gland where SAR values exceed -20 dB are 6 mm for Orientation #1 and 8 mm for Orientation #2. In the fat tissue, values of SAR higher than -20 dB are seen extending radially no further than 4 mm for both input power levels. Asymmetric SAR profiles
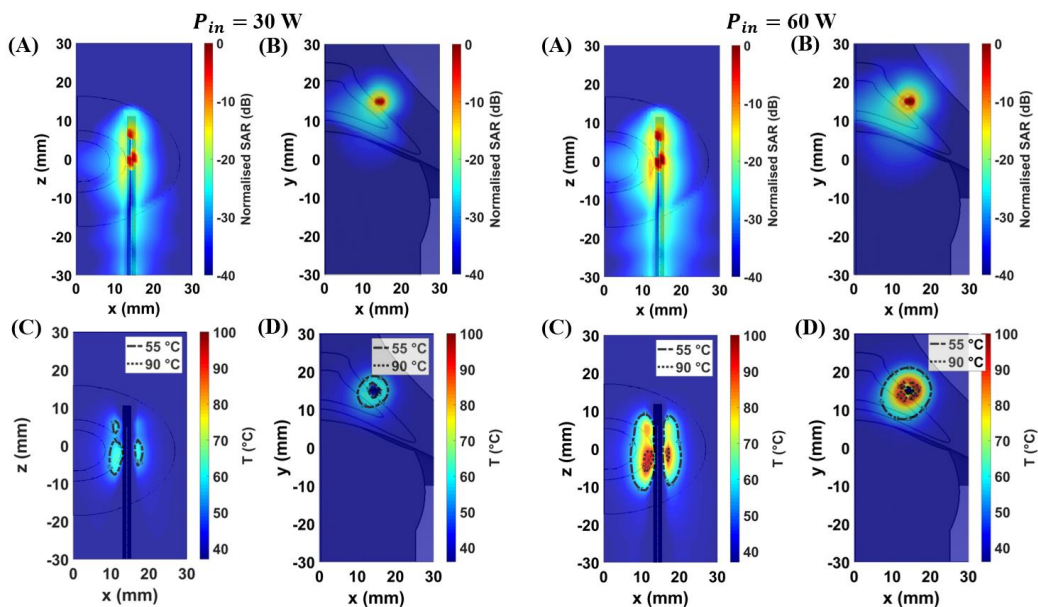
Figure 7.4: Maps of SAR (A) – (B) and of temperature (C) – (D) obtained in the 3D model considering the in vivo numerical scenario (i.e. blood surrounding the geometry and 37°C) at 30 W and 60 W. Consistent with the previous study (Chapter 6), the applicator was aligned at the interface between fat and adrenal gland as described for Orientation #1. Profiles of SAR and temperature are presented both in the frontal plane (xy-plane) and in the coronal plane (xz-plane) with reference to the feed of the antenna.
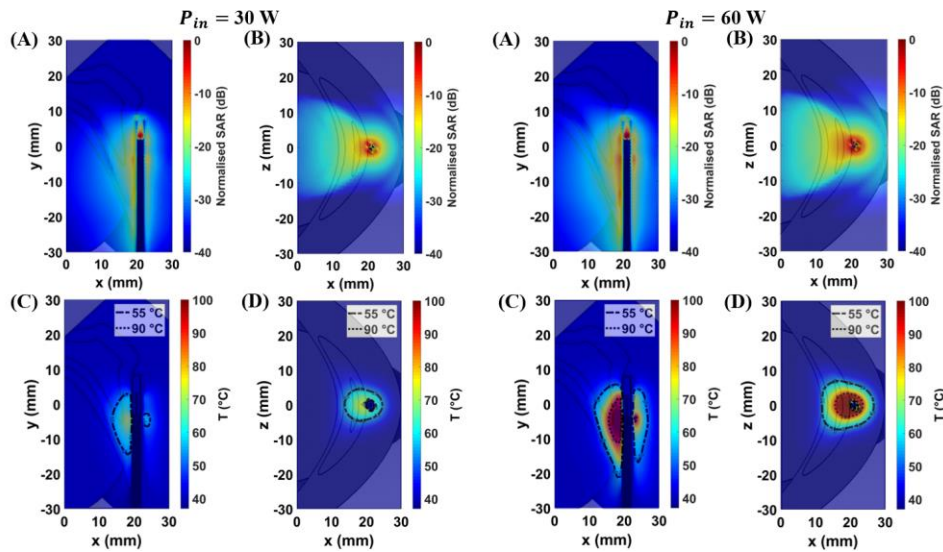
Figure 7.5: Maps of SAR (A) – (B) and of temperature (C) – (D) obtained in the 3D model considering the in vivo numerical scenario (i.e. blood surrounding the geometry and 37°C) at 30 W and 60 W. Consistent with the previous study (Chapter 6), the applicator was aligned at the interface between fat and adrenal gland as described for Orientation #2. Profiles of SAR and temperature are presented both in the frontal plane (xy-plane) and in the coronal plane (xz-plane) with reference to the feed of the antenna.

show the electromagnetic power confined in proximity to the applicator in the fat tissue; while the electromagnetic power is deposited throughout the adrenal layers.

Compared with the air background material (Figure 6.7(A)), the dispersive and dissipative characteristics of blood induce non-null values of SAR in the space surrounding the adrenal model. In particular, non-null values of SAR are visible along the feeding cable of the MW applicator (Figure 7.4 (A)), outside the adrenal gland. However, those values are lower than -60 dB, thus they have no substantial impact on the thermal distributions. The thermal maps reflect the asymmetric profiles obtained from the deposition of SAR in the tissues. At 30 W, the areas where the temperatures exceed 55°C are more confined in proximity to the applicator in fat, compared to the air background case. The area delineated by the isothermal contour at 55°C extend through the cortex and the medulla layers in the adrenal gland both for Orientation #1 and Orientation #2. Increasing the input power to 60 W, ablation zones become larger both in fat and in the adrenal gland, lessening the asymmetry in the thermal pattern compared with 30 W.

147

Table 7.2: Radial and longitudinal extents calculated at 30 W (first line) and at 60 W (second line) in the in vivo numerical study considering the 3D model presented in Chapter 6. The dimensions of the ablation zones previously calculated (Chapter 6) in the ex vivo numerical scenario including the same 3D geometry for the adrenal gland and the surrounding fat layer are also reported to allow a comparatively evaluation.

Settings		Background material: blood								Background material: air							
		Orientation # 1				Orientation # 2				Orientation #1				Orientation #2			
P (W)	t (s)	Fat		Adrenal gland		Fat		Adrenal gland		Fat		Adrenal gland		Fat		Adrenal gland	
		R	L	R	L	R	L	R	L	R	L	R	L	R	L	R	L
30	60	4	6	5	8	4	4	7	17	2	4	5	15	3	3	5	7
60	60	6	18	8	17	6	21	9	22	5	21	7	17	5	13	8	20

Table 7.2 lists the radial and longitudinal dimensions of the ablation zones achieved in the adrenal tissues and in the fat layer for the two different orientations of the MW applicator both at 30 W and 60 W. The dimensions correspond to the area identified by the isothermal contour at 55°C. In fat, the results show that the radial dimensions of the ablation zone remain unvaried with the change in the orientation of the MW applicator. Instead, the two orientations differ by approximately 30% at 30 W and by 14% at 60 W in the longitudinal dimension. Similarly, in the adrenal gland the higher differences between Orientation #1 and Orientation #2 are visible in the longitudinal dimension of the ablation zone. As a result, the ablation zones are 53% at 30 W and 23% at 60 W shorter in the case of Orientation #1 compared with Orientation #2.

At 30 W the radial dimension of the ablation zone in fat remains confined within 4 mm independent of the orientation of the applicator. It is worth mentioning that a radial extent of the ablation zone within 5 mm is desirable to preserve the surrounding sensitive structures, such as blood vessels. Considering 5 mm as a safe margin, at 60 W the radial extent of the ablation zone in fat is slightly beyond this limit, for both orientations of the MW applicator. In addition, at a lower input power the ablation zone in fat is more spherical than that observed at higher power level. In particular, longitudinal and radial dimensions of the ablation zone coincide in the case of Orientation #2. Increasing the input power from 30 W to 60 W, the ablation zone increases in the longitudinal dimension by three folds in the case of Orientation #1 and five folds for Orientation #2.

Overall, lower input power improves the asymmetric ablation profile and enhances the ability of the fat layer to lag the growth of the ablation zone compared to higher power.

Table 7.2 also reports the dimensions achieved in the numerical study reproducing *ex vivo* conditions (Table 6.4) for comparison. In the radial dimension, slightly larger ablation zones (not exceeding 2 mm) were observed both in the fat layer and in the adrenal gland in the case of blood background compared with the air background (i.e. *ex vivo* conditions). This difference is likely due to the higher initial temperature (37°C) that was considered for the blood background material compared with the *ex vivo* scenario (25°C). In the case of Orientation #1 and for both input powers, the ablation zones do not reach the margin of the geometry, resulting in shorter and more spherical profiles compared with the *ex vivo* scenario. Overall, the results confirm high variability in the numerical results depending on the orientation of the MW applicator in agreement with the results related to the *ex vivo* scenario (Table 6.4). As already discussed in Chapter 6, this variability particularly involves the longitudinal dimension of the ablation zone. Such an effect can be attributed to the redistribution of the electromagnetic power along the longitudinal direction when the radial space constraints, due to the curvature of the 3D geometry. Independent of the background material, better performances were observed in the case of Orientation #2 compared with Orientation #1 in terms of creating asymmetric ablation profiles. One of the reasons for this result is that Orientation #2 improves the alignment of the MW applicator at the interface between the adrenal cortex and the fat layer. It is also worth noting that the two orientations of the MW applicator are responsible for two different radiating conditions. In the case of Orientation #2, the force lines of the electric field are parallel to the interface between the fat and adrenal gland. In the case of Orientation #1 the force lines of the electric field approximate more the perpendicular condition with respect to the interface between the two tissues. The first condition (Orientation #2) likely induces a greater absorption of the electromagnetic power in the tissue characterised by higher electrical conductivity compared with the second condition [269]–[271].

Figure 7.6 shows the maps of temperature achieved by adding the effect of blood perfusion. The thermal profiles are shown in the case of Orientation #1 (A) – (B) and Orientation #2 (C) – (D) of the MW applicator both at 30 W and 60 W. The results show thermal profiles (55°C isothermal contour) for the perfused scenario comparable with the non-perfused numerical scenario (Figure 7.4, Figure 7.5). The blood perfusion shows no impairment in the ability of the fat to lag the increase of the temperature, for both orientations of the MW applicator. Overall, the presence of the blood perfusion appears to mitigate the increase in tissue temperature without dramatically affecting the dimension of the ablation zone for the power and time settings adopted.

A difference between the perfused and non-perfused scenarios is visible in the extent of the area delineated by the isothermal contour set at 90°C, in the case of high input power (i.e. 60 W). The peak temperature values in the presence of blood perfusion are lower than the peak temperature values achieved in the non-perfused model. As a result, the areas where the temperature is above 90°C in the non-perfused model are smaller than in
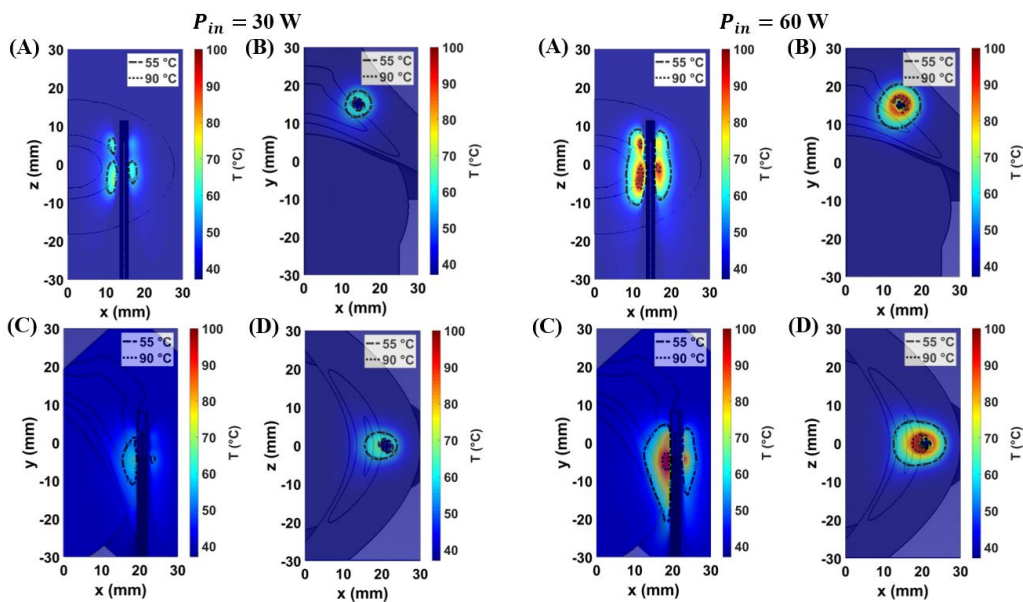
Figure 7.6: Maps of temperature obtained in the 3D model considering the blood perfusion both in fat and adrenal tissues to better represent numerically the in vivo scenario at 30 W and 60 W. Consistently with the previous numerical studies, the thermal maps refer to the two different orientations of the MW applicator: orientation #1 (A) – (B) and orientation #2 (C) – (D). Profiles of temperature are presented both in the frontal plane (xy-plane) and in the coronal plane (xz-plane) with reference to the feed of the antenna.

the perfused model. In the adrenal gland, the extent of the area where the temperature exceeds 90°C narrows by 3 mm in radial dimension and 1 mm in longitudinal dimension in the case of Orientation #1 (Figure 7.6 (A) – (B)), and 3 mm and 9 mm respectively in the case of Orientation #2 (Figure 7.6 (C) – (D)). The fat layer shows no temperature above 90°C when the perfusion model is included in the case of Orientation #1; while for Orientation #2 this area is reduced by 1 mm along both dimensions with respect to non-perfused model. According to Equation (4.13), the term indicating blood perfusion varies with the temperature gradient between tissue and blood. The higher such a gradient becomes, the more relevant the effect of blood perfusion is.

Table 7.3 reports the radial and longitudinal dimensions of the ablation profiles achieved in the presence of blood perfusion. For comparison, the table also includes the dimensions obtained in the first numerical scenario proposed in this study where blood perfusion was neglected. The results show consistency in the dimensions of the ablation zone between the two numerical scenarios. A more visible difference between the two scenarios occurs only at 30 W for Orientation #2. With this orientation, the longitudinal dimension achieved in the adrenal gland in the presence of blood perfusion is 24% smaller than in its absence. In all the other cases, the differences in the extent of the ablation zones between the two scenarios do not exceed 2 mm both in radial and longitudinal dimensions. In addition, it can also be observed that in the case of blood perfusion, the radial extent of the ablation zone in fat remains below 5 mm.

Table 7.3: Radial and longitudinal extents calculated at 30 W (first line) and at 60 W (second line) in the in vivo numerical study considering the presence of blood perfusion both in the fat tissue (1,626 W m-3 °C-1) and in the adrenal gland (155,163 W m-3 °C-1). For comparison, the dimensions of the ablation zones previously calculated in the numerical scenario where blood perfusion was disabled and already reported in Table 7.2 are reported.

Settings		Blood perfusion								No blood perfusion							
		Orientation # 1				Orientation # 2				Orientation #1				Orientation #2			
		Fat		Adrenal gland		Fat		Adrenal gland		Fat		Adrenal gland		Fat		Adrenal gland	
P (W)	t (s)	R	L	R	L	R	L	R	L	R	L	R	L	R	L	R	L
30	60	4	6	4	8	3	2	5	13	4	6	5	8	4	4	7	17
60	60	5	17	7	16	5	19	8	21	6	18	8	17	6	21	9	22

Overall, the results presented so far show that the role of the fat layer in shaping asymmetric thermal patterns remained almost unchanged independent of the type of background material and the presence of blood perfusion. As seen for the *ex vivo* scenario in Chapter 6, *in vivo* numerical models (perfused and non-perfused) show that a low input power may provide a better control of the increase of temperature in the space surrounding the gland, compared with high power.

Finally, it is worth noting that the numerical findings show no increase in the temperature of the kidney both in the case of non-perfused and perfused scenarios independent of the antenna orientation and of the input power. This result is in agreement with what was already observed in the previous study (§6.2).

7.3.2 Experimental *in vivo* assessment and histology analysis

The findings of the numerical study informed the experimental protocol designed for the *in vivo* study. The low input power (30 W) was selected and applied for 60 s, to spare the surrounding anatomical structures from excessive increase of temperature and to preserve the integrity of part of adrenal functional tissues.

Figure 7.7 shows the shallow ablation zone achieved in the ovine adrenal cortex after the *in vivo* microwave ablation procedure conducted at 30 W for 60 s. The radial and longitudinal dimensions were measured on the plane of maximum exposure of the ablation zone by cutting the adrenal gland along the longitudinal tract of the applicator. The dimensions achieved in the adrenal cortex are approximately 6 mm in the radial dimension and 9 mm in the longitudinal dimension. The extent of the ablation zone measured after the ablation procedure lie within the radial and longitudinal values predicted by the numerical simulations accounting for the two different orientations of the MW applicator. Also, the acute animal test shows a more spherical ablation zone in the target tissue, compared with the *ex vivo* experimental results shown in Figure 6.9. This effect may be linked to two aspects. First, the MW applicator adopted for the *in vivo* study has a triaxial structure which is able to reduce the backward current compared to the coaxial structure (§ 4.5). Second, the presence of the blood together with the effect
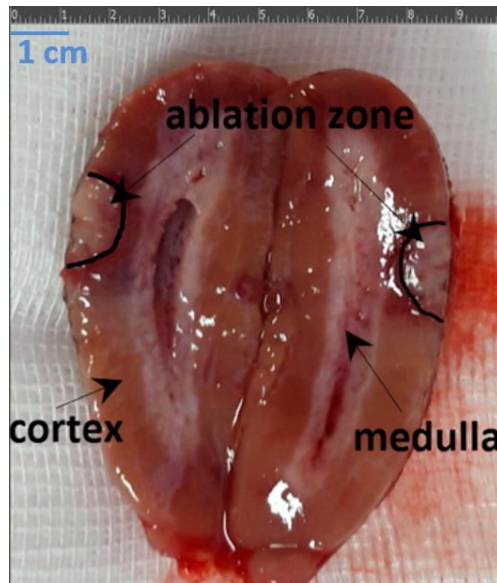
Figure 7.7: Ablation zone obtained in the ovine adrenal gland after MWA procedure executed in vivo at 30 W for a duration of 60 s. The applicator was placed on the external surface of the adrenal cortex beneath the fat layer surrounding the gland. The section of ablation zone was obtained by cutting the sample along the longitudinal tract of the applicator, thus reaching the maximum exposure of the ablation zone. In addition, the normal cortex (outer tissue) and medulla (inner tissue) of the adrenal gland are highlighted.

of the tissue blood perfusion contributes to improve the sphericity of the ablation zones, especially because of the slower and more controllable increase of temperature.

Within 48h of the procedure, a section of tissue including the ablation zone and a margin of the adjacent fat layer were resected and processed for the following histology analysis. All slides acquired from the tissue sample were assessed by a consultant histopathologist. Figure 7.8 shows the cellular morphology of the adrenal tissue and the margin of the adjacent fat. The power level used (30 W) induced a limited tissue damage and coagulative necrosis, as predicted by the numerical simulations. The zone adjacent to the axis of the MW applicator (Zone 1) includes part of the adrenal cortex and a rim of the surrounding fat. This zone shows hyalinisation both of the adrenal tissue and the adjacent fat. Hyalinisation indicates the degradation of the tissue due to heating, after which the tissue becomes translucent (i.e. hyalinised). The hyalinised tissue generally appears pinkish after the H&E staining. The squamous and elongated shapes of the cells in Zone 1 are responsible for the 'ghost effect' mentioned in Chapter 6 (§ 6.3.3). A detail of Zone
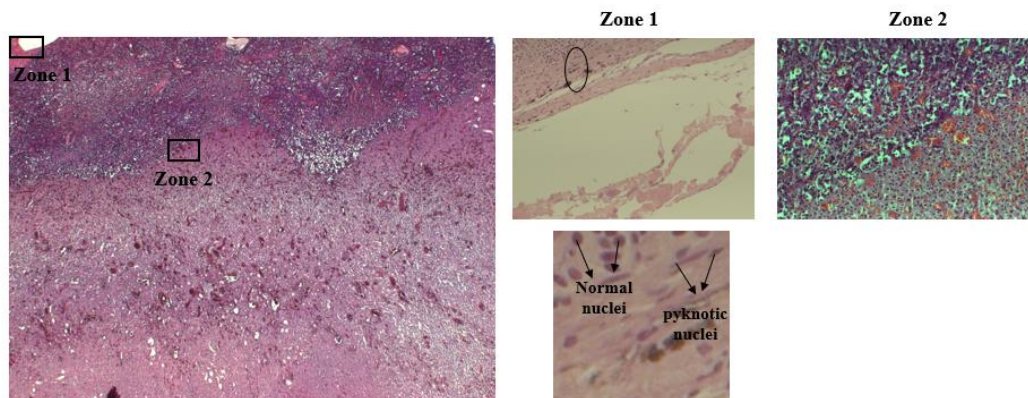
Figure 7.8: Histological section of an ovine adrenal gland treated in vivo with a microwave thermal ablation performed at 30 W for 60 s. Two zones with different histological features are recognised: hylinisation of the cells both in the adrenal tissue and in the adjacent rim of fat layer indicating the cellular apoptosis in the tissue in close contact with the MW applicator (zone 1); cascade inflammatory and blood extravasation caused by the immune system as response to the thermal insult occurring in the whole adrenal cortex up to the non-ablated medulla.

1 shows the difference in shape between normal round-shaped nuclei and the nuclei affected by the thermal insult, i.e. pyknosis nuclei. Pyknosis is the release of the chromatin contained in the cellular nuclei, which condensates in the cellular cytoplasm [261].

The distal zone with respect to the applicator (Zone 2) shows neutrophil infiltration (i.e. immune infiltration) due to the thermal insult. The infiltration of immune cells (such as neutrophil) provides evidence of an acute inflammation reaction and blood extravasation. The immune infiltration delineates the transition zone between the innermost part of the cortex (*reticularis zona*) and the non-ablated medulla. This result agrees with the findings presented in [262] for lower MWA dose tested (i.e. 45 W). The results presented in [262] showed no damage at the distal zone of the tissue with respect to the position of the applicator. The delineating immune infiltration which separates the ablated and non-ablated zones is visible only after the *in vivo* MWA procedure while it is absent after *ex vivo* procedures (§ 6.3). This difference is linked to the immediate reaction of the immune system to the thermal insult typically observed in the *in vivo* scenarios [261], [262], [272]. A further difference in the histological features between *ex vivo* and *in vivo* studies is in the zone of adrenal tissue adjacent to the applicator. Here, the *in vivo* study shows the

cellular hyalinisation and the changes from rounded-shaped cellular nuclei to squamous-shaped. In the case of *ex vivo* study at the same power and time setting, the region proximal to the applicator appears eosinophilic indicating the necrosis of the cellular nuclei (Figure 6.11 (A)). Instead, squamous and elongated cells are visible in the transition zone of the tissue (Figure 6.11 (B)). Such a difference in the histological findings between the *in vivo* and *ex vivo* scenarios confirms that lower peak temperature values are achieved in the *in vivo* study due to the effect of blood perfusion.

7.4 Conclusions

This study investigates the performance of the periadrenal fat layer and its ability to protect the surrounding sensitive anatomical structures during the MWA procedure in an *in vivo* scenario. A range of numerical simulations was completed. First, blood surrounding the entire adrenal model and an initial temperature of 37°C (instead of 25°C) were considered. Then, the tissue blood perfusion rate was added. In support of the numerical simulations, a MWA procedure was conducted *in vivo* on an ovine adrenal gland adopting the 'side firing' approach discussed in the previous chapters. Then, histology analysis was performed on ablated tissue to qualitatively assess both the necrotic coagulation occurring in the ablation zone and the inflammatory responses.

The main findings of the study are:

- Comparable dimensions of the ablation zones were observed in the numerical findings between *ex vivo* and *in vivo* conditions. For the *in vivo* conditions, comparable ablation zones were also achieved both with and without blood perfusion. The study confirms that the geometry of the target influences the growth of the ablation zone along the longitudinal and the radial directions. Compared to the *ex vivo* scenario, a slight improvement in the sphericity of the ablation pattern is observed in the case of the *in vivo* scenario. Due to the relatively short duration of the procedure, blood perfusion has a negligible impact on the ablation zone. The only visible effect is in the peak temperature values reached, which were lower compared with the scenario of null blood perfusion. Finally, the numerical results achieved in

the *in vivo*-mimicking numerical scenario confirm low input power, i.e. 30 W being a more cautious approach to use in the *in vivo* test. Indeed, numerical results show that the temperature in fat remained below 55°C in most of the tissue.

- The *in vivo* study conducted on the ovine animal model shows a spherical and shallow ablation zone in the tissue target. Histology analysis conducted on the tissue after the MWA procedure shows that the greatest degree of changes in the cellular morphology of the tissue is limited to the tissue in proximity to the applicator. The experimental results suggest a low input power approach may maximise the role of the fat layer in sparing surrounded healthy structures from excessive temperature increases. A low power approach may also allow for a shallow ablation zone limited to the target tissue. Finally, such a conservative approach would minimise the side effects that the patient may experience during and following the procedure. For example, lower input power may allow for a better control of the stress induced to the adrenal medulla. The excessive release of catecholamines following the stress of the medulla may induce an increase of the heart activity rate.

This chapter along with Chapter 6 provide a rigorous description of the role of the fat layer surrounding the adrenal gland in creating asymmetric ablation zones both in *ex vivo* and *in vivo* scenarios at 2.45 GHz. This study confirms the ability of the fat layer to lag the increase of the temperature and to shield the surrounding anatomical structures from the excessive heating. In agreement with the results presented in Chapter 6, this study shows that a more cautious approach is provided by low input power. At 30 W, the ablation zone in the adrenal gland appears more spherical and localised in proximity to the applicator. In addition, the fat layer shows better performance in lagging the increase of temperature and maintaining it below 55°C for most of the tissue. However, results show that the radial extent of the ablation zone at 30 W is smaller than some of the target dimensions of adreno-cortical adenomas (i.e. < 20 mm in diameter), when MWA is conducted at 2.45 GHz. Thus, new strategies should be investigated to enlarge the extent of the ablation zone using low input power for relatively short durations. A strategy worthy of exploration involves a high operating frequency within the ISM frequency

range, for example 5.8 GHz. Chapter 8 is devoted to the effects that the increase of the operating frequency to 5.8 GHz has on the extent of the ablation zone in the adrenal tissues and on the ability of the fat layer to lag the temperature increase.

Chapter 8

MWA performed at 5.8 GHz through 'side firing' approach: an exploring study

8.1 Introduction

The previous chapters demonstrated the ability of the fat layer to shield the electromagnetic field and create asymmetric ablation profiles. The MW applicator was excited at 2.45 GHz and two different levels of input power, i.e. 30 W and 60 W, were delivered into the tissue for 60 s. The operating frequency of 2.45 GHz is typically adopted for MWA procedures [17], [82], [150], [152], [271].

Numerical results showed the effects of the 'side firing' approach, taking into account the size and the shape of the tissues, the orientation of the applicator at the interface between fat and adrenal tissues, the type of the surrounding material (i.e. air or blood) and the blood perfusion of the tissues. In particular, the effect of blood perfusion was included in the study presented in Chapter 7 to better represent the *in vivo* conditions. Experimental tests were conducted *ex vivo* (in Chapter 6) and *in vivo* (in Chapter 7) on ovine adrenal models. The temperature values were measured locally both in fat and in adrenal tissues during the MWA procedure. The experimental data confirmed the ability of the fat layer to lag the increase of temperature. Visual inspection and histological analysis, where possible, were used to assess the effects of the thermal insult in the adrenal gland and in the surrounding tissues. Both numerical and experimental results indicate that the 'side firing' approach could enable the selective targeting of the ablation zone in the area of interest. Indeed, the proposed 'side firing' approach is underpinned by the contrast in dielectric properties between the two biological tissues (§ 5.3 and § 6.3) which gives rise to the asymmetric ablation profiles observed in the prior chapters.

In this chapter the 'side firing' ablation approach is investigated at 5.8 GHz. The values of relative permittivity and effective conductivity at 5.8 GHz were reported in Chapter 3 and compared to the same properties at 2.45 GHz. From that comparison, it can be observed that the contrast in effective conductivity between the adrenal cortex and fat is

approximately two-fold higher compared to the contrast at 2.45 GHz. This higher contrast in conductivity obtained at 5.8 GHz presents an opportunity to improve the deposition of the EM energy in the target tissue.

To consider this potential, the chapter investigates:

- The distribution of SAR and temperature in simplified multilayered and 3D models. For each model, a triaxial monopole applicator operating at 5.8 GHz (§ 4.2.1) was placed parallel to the interface between adrenal cortex and fat tissue. Two different orientations of the antenna (Orientation #1, Orientation #2) were considered by reference to the interface between the two tissues;

- The ablation profiles achievable *ex vivo* on porcine adrenal tissues at the interface with fat. The increase of temperature was monitored both in fat and in the adrenal tissues during the MWA procedure;

- The influence of water vaporisation on the distribution of temperatures over the tissue target.

The study reported in this chapter was conducted at UW Institute for Clinical and Translational Research, University of Wisconsin-Madison, US, within a Short-Term Scientific Mission supported by the MyWave COST Action (CA17115 - European network for advancing Electromagnetic hyperthermic medical technologies).

The structure of the chapter is as follows: Section 8.1 describes the numerical models specifying the properties of the adrenal tissues at 5.8 GHz and the setup for the experimental assessment. Section 8.2 shows and discusses the ablation profiles obtained for each numerical geometry, the temperature values over the radial distance from the applicator and with respect to time, and the effect of water vaporisation on the temperatures achieved in the adrenal tissues. Section 8.3 concludes the chapter.

8.2 Methodology

8.2.1 Numerical study

Geometrical models. Figure 8.1 shows the multilayer simplified model and the three-dimensional model adopted in this study to investigate the influence of the geometry on the ablation profiles at 5.8 GHz. The dimensions of the two models and the orientations of the MW applicator with respect to the cortex-fat interface are consistent with those reported in the previous chapter (§ 6.1.1). Table 8.1 lists the dielectric and thermal properties assigned to each layer, representing the adrenal tissues (i.e. medulla and cortex) and the external fat layer. The values of relative permittivity and effective conductivity described in Chapter 3 (§3.3.2) were assigned to the adrenal cortex and medulla. The dielectric properties assigned to the fat tissue and the thermal properties of each tissue were acquired from [245]. The dielectric properties of air ($\varepsilon_r = 1, \sigma = 0$) were assigned as the background material, which are representative of the *ex vivo* conditions of the experimental scenario.

The triaxial monopole applicator optimised to operate at 5.8 GHz and described in Chapter 4 was placed parallel to the interface between the fat and the adrenal cortex both in the simplified and 3D geometry. The widths of the fat layer and the adrenal tissues agree with those reported in the previous studies (§ 6.2). The minimum requirement of
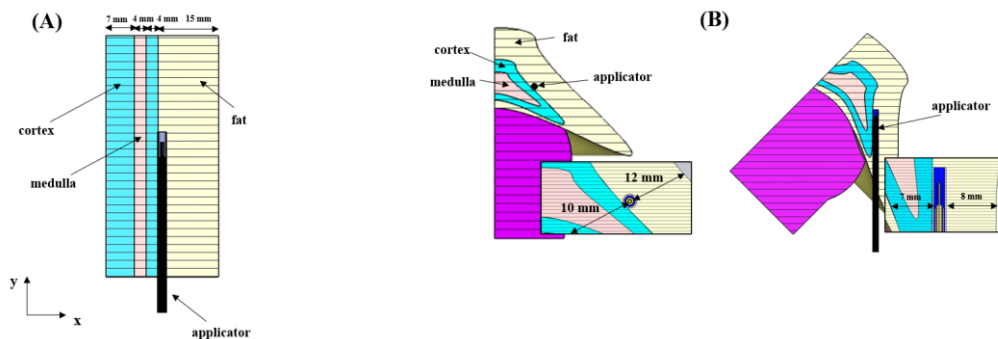
Figure 8.1: Multilayer simplified model (A) and 3D model (B) of the adrenal tissues and the adjacent fat layer. The triaxial MW applicator optimised to operate at 5.8 GHz was placed parallel to the interface between fat and the adrenal cortex. For the 3D model, only the half right side was considered to reduce the computational load. The dimensions of the tissue layers are the same as those described in chapter 6 (§ 6.1.1).

Table 8.1: Tissue dielectric and thermal properties at 25 °C employed in the numerical simulations. Relative permittivity (εr) and effective conductivity (σ (S m-1)) of cortex and medulla at 5.8 GHz refer to the mean values of dielectric data reported in (§ 3.3).

Parameter	Fat	Cortex	Medulla
Relative permittivity, ε_r	8.3	41.2	47.6
Effective conductivity, σ (S m^{-1})	0.5	4.2	5.1
Specific heat capacity, c (kJ m^{-3}K^{-1})	2.3	3.6	3.7
Thermal conductivity, k (W m^{-1}K^{-1})	0.2	0.5	0.5
Density, ρ (kg m^{-3})	911	1025	1025
Frequency (GHz)		5.8	

at least 10 cells per wavelength model was upheld while increasing the operating frequency from 2.45 GHz to 5.8 GHz. A total of 12,004,200 tetrahedral meshing cells ranging between 0.02 mm and 0.3 mm defined the simplified model. For the 3D model, 34,776,336 meshing cells ranging between 0.02 mm and 0.5 mm defined the right half side of the model. It is notable that the number of meshing cells was approximately four times higher than in the case of 2.45 GHz for the planar geometry and five times higher for the right-side cut 3D geometry.

Electromagnetic and thermal simulations. The thermal transient solver included in the CST MWS Suite 2018 was used to compute the distribution of the SAR (4.12) solving the Helmholtz equation (4.11) and the distribution of the temperature solving the BHE (4.13). As first approximation, BHE included the terms indicating the heat transfer due to thermal conduction ($\nabla \cdot (k\nabla T)$) and the heating resulting from the deposition of SAR (ρSAR). The terms indicating the blood perfusion ($m_b \rho \rho_b c_b (T - T_b)$) and the metabolic heat (ρQ) were excluded to better represent the *ex vivo* experimental conditions (§ 4.3).

Next, a second set of numerical simulations were considered which aimed to account for the water losses due to vaporisation. Vaporisation is expected to have a more dominant role in MWA at 5.8 GHz compared with 2.45 GHz, since higher temperatures are reached at 5.8 GHz in shorter times. The model represented by Equation (4.19) was used to modify the BHE. This model describes the variation of the specific heat capacity with temperature. The variation in the heat specific capacity is linked to the loss of the tissue water content when temperatures exceed 70 °C. The model was developed by [145]

161

accounting for the characteristics of liver tissue and the percentage of water content at
the baseline conditions, which is about 80% of the mass of the tissue. The same model
was used in this study for the adrenal tissues, as a water content similar to liver is
expected (70% - 76%) [265]. The model was not applied to the fat tissue which is
characterised by a water content approximately four times lower than the adrenal and
hepatic tissue [265].

The function describing the variation of the water content (4.18) was reproduced in
MATLAB. The values of the modified specific heat capacity were obtained for each
temperature included in the range between 25°C and 300°C. The sequence of values at
the corresponding temperature was loaded in CST MW Studio for both tissues. Then, bi-
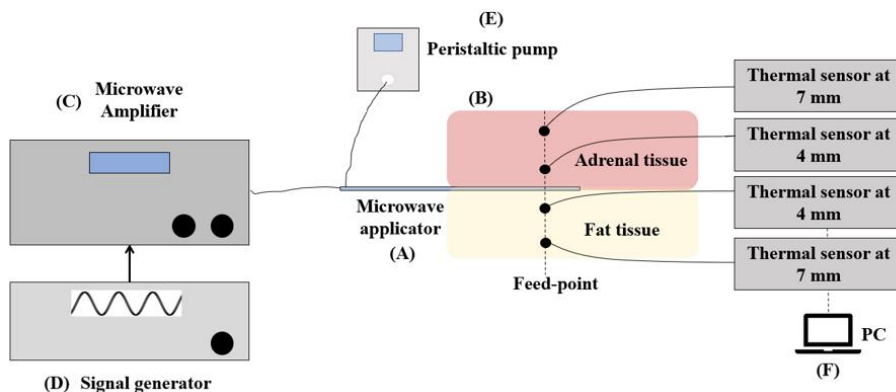
Figure 8.2: Setup adopted for the experimental validation of the computational results (top) and
related schematisation (bottom). The setup includes the microwave applicator (A) powered for 60 s
at the input power provided by the microwave amplifier (C) which amplifies the signal at the
designed operating frequency (D); a peristaltic pump (E) connected to the inflow and outflow tubes
of the refrigerating system integrated in the applicator; four fiber optic sensors connected to a laptop
(F) to acquire values of temperature at 0.1 s time step.

directional numerical simulations were enabled. The bi-directional simulations involve a continuous update of the parameters of the tissue (i.e. heat specific capacity) with the temperature reached at a specific time. Thus, the temperature increment at the next time step was calculated based on the new value of specific heat capacity calculated at the related temperature. The update was performed at a time step of 1 s for the entire duration of the signal excitation.

Two different levels of input power, 30 W and 60 W, were applied for 60 s to the waveguide port defined at the proximal end of the applicator. The vaporisation model was considered only for the simplified geometry of the adrenal gland because of the excessive computational load required for the 3D geometry. The values obtained from each simulation were exported and analysed in MATLAB (R2017a, The MathWorks, Inc., Natick, MA, US).

8.2.2 Experimental *ex vivo* study

The experimental study was conducted at UW Institute for Clinical and Translational Research, University of Wisconsin-Madison, US. Porcine adrenal glands (N = 6) of 26.2 ± 1.0 (length), 15.3 ± 1.0 mm (width), 3.4 ± 1 mm (thickness) were obtained from the local abattoir. *Ex vivo* porcine adrenal glands were used for this study because of the limitation in the availability of ovine samples. However, the values of relative permittivity and effective conductivity of the porcine model are comparable to those of the ovine at 5.8 GHz [192]. Figure 8.2 provides an overview of the experimental setup adopted, along with the schematisation of each component included in the setup. The applicator was positioned on the surface of the adrenal sample and covered by the surrounding fat layer. A signal generator (HP 83620A, 10 MHz – 20 GHz, 15 dBm maximum input power) was used to provide a 10 dBm continuous wave sinusoidal signal at 5.8 GHz. A solid-state microwave amplifier (Milmega, Ametek, AS0860-50, 0.8 – 6.0 GHz, 47 dBm W maximum gain) was then used to amplify the signal to 34 W and 68 W (§ 4.3.1), by selecting the gain at 75% and 82% respectively. The two different gains selected at the amplifier accounted for the power losses along to cable. Thus, the two values for power gain provided the required levels of power (30 W and 60 W) at the

Table 8.2: Summary of the power and time settings and of actual positions of the fibre optic sensors with reference to the feed of the antenna for each MWA experimental procedure. The original positions of the sensors were 4 mm and 7 mm along the radial distance from the axis of the applicator both in the adrenal tissue and in the surrounding fat.

Sample #	Settings		Actual position Sensor 1		Actual position Sensor 2	
	Power (W)	Time (s)	Fat	Adrenal gland	Fat	Adrenal gland
1	30	60	4 mm	5 mm	7 mm	7 mm
2	30	60	4 mm	4 mm	6 mm	6 mm
3	30	60	5 mm	6 mm	8 mm	6 mm
4	60	60	3 mm	4 mm	6 mm	6 mm
5	60	60	4 mm	4 mm	7 mm	6 mm
6	60	60	5 mm	5 mm	8 mm	8 mm

antenna feed. Water at the temperature of 17.2 ± 3.3°C was circulated through the applicator by a peristaltic pump (Cool-tip RF System, Valleylab).

For each experiment, the temperature was monitored using four fibre optic sensors (Neoptix Inc., Québec, CA). The fibre optic sensors were placed at a radial distance of approximately 4 mm and 7 mm from the antenna feed in both the adrenal tissue and in the fat tissue. Such distances were selected in order to consider the increase of the temperature caused by the direct heating in proximity to the antenna (i.e. 4 mm) and the possible effects of the thermal diffusivity at higher radial distances from the feed (i.e. 7 mm) in both tissues. Because of the changes undergone by the sample at high temperatures (e.g. tissue contraction [143], [248]), and the movement of the fiber optic sensors in the tissues, a shift in the starting position of the sensors may occur during the procedure. Table 8.2 lists the actual positions measured at the end of the MWA procedure for all the samples used.

For each combination of power and time setting (30 W – 60 s, 60 W – 60 s), ablation experiments were performed three times on a total of six samples.

8.3 Results

8.3.1 Numerical study

Simplified model. Figure 8.3 shows the distributions of SAR (A) – (B) and temperature (C) – (D) achieved in the simplified model at 30 W and 60 W for 60 s. Both thermal and SAR profiles are depicted in frontal (A) – (C) and coronal (B) – (D) planes. SAR values are normalised to the maximum and expressed in decibels (dB). In the adrenal layers, values of SAR higher than -20 dB extend up to 6 mm radially and 18 mm longitudinally at 30 W, and up to 8 mm and 22 mm at 60 W. In the fat layer, values higher than -20 dB reach 3 mm along the radial direction and 10 mm along the longitudinal direction at 30 W; 4 mm and 14 mm along the corresponding directions at 60 W. Thus, a difference in the absorption of the electromagnetic power between fat and adrenal tissues can be observed. This difference in the absorbed electromagnetic power results in asymmetric ablation profiles delineated by the isothermal contour at 55°C.

Table 8.3 provides radial (R) and longitudinal (L) dimensions of the ablation zone obtained in the adrenal gland and in fat both at 30 W and 60 W. The ablation zones in fat
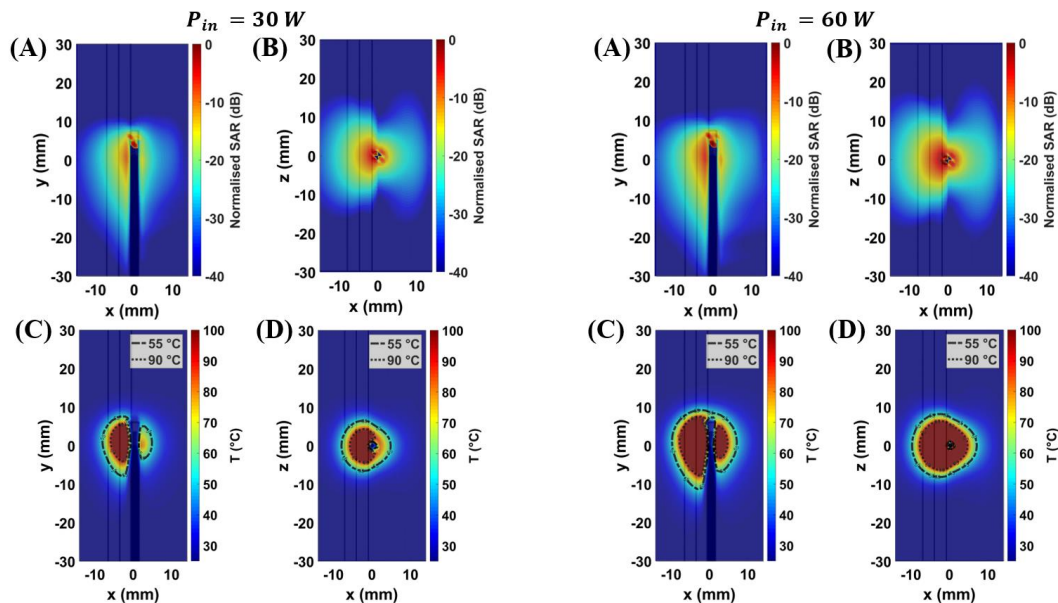
Figure 8.3: Maps of SAR (A) – (B) and of temperature (C) – (D) obtained numerically in the simplified model at 30 W and 60 W, adopting 5.8 GHz as operating frequency. Profiles of SAR and temperature are presented both in the frontal plane (xy-plane) and in the coronal plane (xz-plane) and in the coronal (xz) with reference to the feed of the antenna.

Table 8.3: Radial and longitudinal extents calculated at 30W (first line) and at 60 W (second line) in the simplified geometry and in the 3D model, in the case of 5.8 GHz operating frequency. The radial and the longitudinal dimensions of ablation zones measured experimentally are reported in terms of mean and standard deviation for each power and time setting considered.

Settings		Simplified model		3D model Orientation #1		3D model Orientation #2		Experimental	
		Fat	Adrenal gland	Fat	Adrenal gland	Fat	Adrenal gland	Adrenal gland	
P (W)	t (s)	R L	R L	R L	R L	R L	R L	R	L
30	60	4 8	9 15	5 11	8 11	5 9	9 16	8 ± 2	10 ± 2
60	60	7 15	10 20	7 17	10 15	7 14	10 20	9 ± 2	13 ± 2

are 55% and 47% (30 W) and 30% and 25% (60 W) smaller than in adrenal gland, along the radial and longitudinal directions. The asymmetry is emphasised in the case of low input power, while it is slightly attenuated in the case of high input power, as observed also at 2.45 GHz (§ 6.2.1). Larger ablation zones are achieved in the two tissues compared with those observed at 2.45 GHz (§ 6.2.1). The difference in the extent of the ablation zones between the two studies is linked to the higher values of effective conductivity for adrenal gland (σ_{cortex}= 4.2 S m^{-1}) and the slightly higher effective conductivity for fat (σ_{fat} = 0.5 S m^{-1}) at 5.8 GHz compared with the values at 2.45 GHz (σ_{cortex} = 1.6 S m^{-1}; σ_{fat}= 0.1 S m^{-1}). Furthermore, the higher contrast in effective conductivity (σ_{cortex} - σ_{fat} = 3.7 S m^{-1}) at this higher operating frequency allows for bigger ablation zones in the adrenal gland compared to those achieved at 2.45 GHz (§ 6.2.1), using the same power and time settings.

Three-dimensional model. Figure 8.4 and Figure 8.5 show the distributions of SAR (A) – (B) and temperature (C) – (D) obtained at 30 W – 60 s and 60 W – 60 s, in the 3D model. The figures refer to the two different orientations of the antenna with respect to the interface between adrenal tissue and fat layer. SAR and thermal distributions are provided for the frontal plane (A) – (C) and coronal plane (B) – (D). Both Figure 8.4 (A) – (B) and Figure 8.5 (A) – (B) show SAR values higher than -20 dB are distributed over larger areas of the adrenal tissues compared with fat. As already observed in the previous chapters, the difference in the absorbed electromagnetic power between the two tissues results in asymmetric ablation profiles. The extent of the ablation zones achieved in each
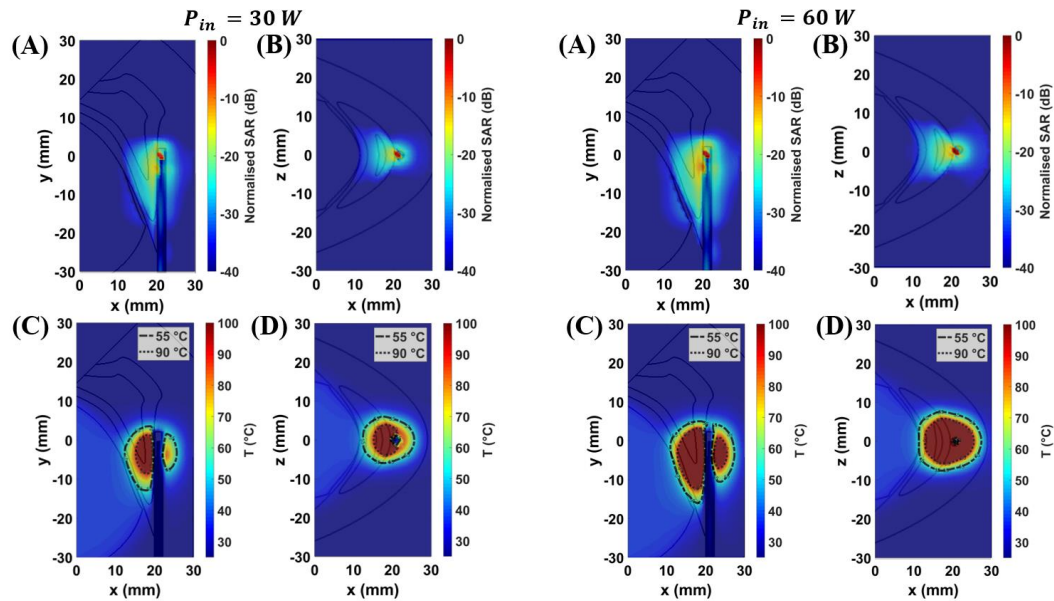
Figure 8.4: Maps of SAR (A: frontal plane (xy-plane)) – (B: coronal plane (xz-plane)) and of temperature (C: frontal plane (xy-plane)) – (D: coronal plane (xz-plane)) obtained in the 3D model at 30 W and 60 W at 5.8 GHz. The applicator is aligned at the interface between fat and adrenal gland orientating the longitudinal axis parallel to the y-axis of the reference system (orientation #2). Frontal plane (xy-plane) and coronal plane (xz-plane) are indicated with reference to the longitudinal axis of the antenna.

tissue and for each setting are reported in Table 8.3, along with the dimensions achieved in the simplified geometry. The influence of the higher effective conductivity of both tissues compared with 2.45 GHz is also visible in the 3D model, resulting in larger ablation zones in both the adrenal and fat tissues, independent on the orientation of the antenna. Specifically, most of the electromagnetic field is absorbed close to the applicator, limiting the propagation of the field through the tissue. This result is linked to the difference in the penetration depth of the electric field which is approximately two-fold lower at 5.8 GHz compared with 2.45 GHz [224]. The rapid increase of temperature in proximity to the applicator enables faster passive heating due to the thermal conduction which contributes to enlarging the ablation zone. However, asymmetric ablation profiles are still visible, particularly in the case of low input power. At 30 W, the radial extent of the ablation zone in fat are 38% and 44% smaller than in the adrenal gland for Orientation #1 and Orientation #2, respectively. At 60 W the ablation zone in fat becomes larger
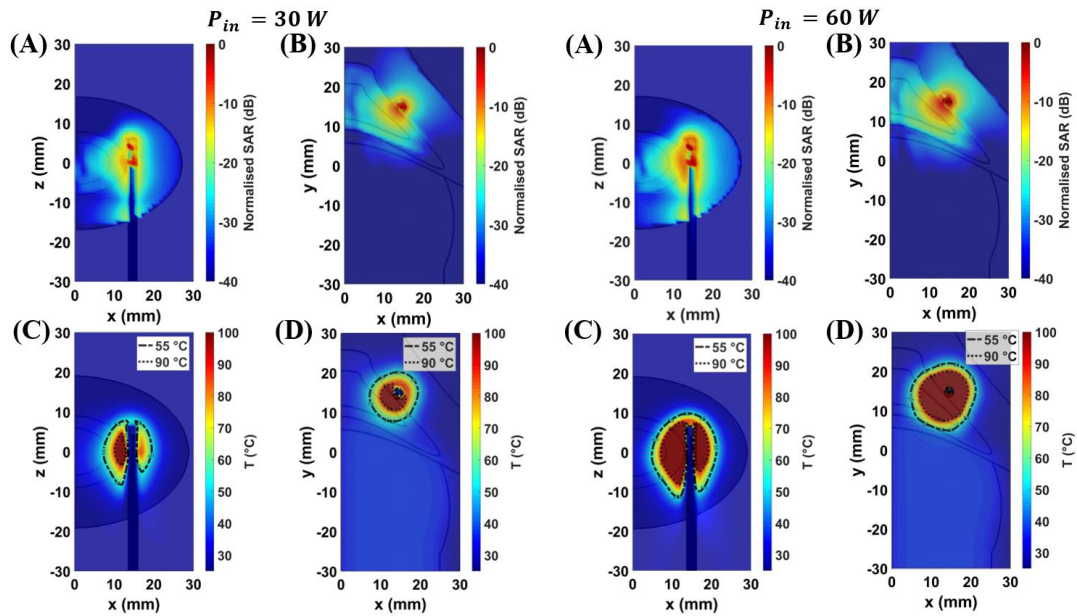
Figure 8.5: Maps of SAR (A: frontal plane (xy-plane)) – (B: coronal plane (xz-plane)) and of temperature (C: frontal plane (xy-plane)) – (D: coronal plane (xz-plane)) obtained in the 3D model at 30 W and 60 W at 5.8 GHz. The applicator is aligned at the interface between fat and adrenal gland orientating the longitudinal axis parallel to the z-axis of the reference system (orientation #1). Frontal plane (xz-plane) and coronal plane (xy-plane) are indicated with reference to the axis of the antenna.

compared with the case of low energy dose, but it is still 30% smaller than in the adrenal gland for both orientations.

Table 8.3 highlights similar dimensions in the ablation zone between the two orientations, especially along the radial direction. The main difference between the two orientations is observed in the longitudinal dimensions which are approximately 25% smaller in the adrenal gland for Orientation #1 compared with Orientation #2. This difference is linked to the difference in the geometrical characteristics of the two tissues, depending on the orientation of the MW applicator, as already observed at 2.45 GHz GHz.

Numerical results show that fat can provide the shielding effect on the ablation zone, at both 2.45 GHz to 5.8 GHz. This effect was observed for both input powers, 30 W and 60 W. As already observed in the previous studies, the setting at low input power allows for a better control in the increase of temperature in both tissues. It is conceivable that low input power in combination with relatively short durations (60 s) helps to mitigate the

effect of the heat transfer due to thermal conduction and yields ablation zones of smaller diameter. This effect is most evident in fat, where the ablation zone remains within 5 mm from the axis of the applicator. It should be noted that adrenal glands are surrounded by sensitive anatomical structures, such as IVC, abdominal aorta, diaphragm and liver. These structures are 10 – 30 mm distant from the external surface of the periadrenal fat capsule, which is approximately 10 – 15 mm in thickness [273]–[275]. Thus, an ablation zone not exceeding 5 mm diameter in fat is desirable to protect all the above-mentioned structures from the risk of thermal damage.

In addition, an improvement in the sphericity of the ablation profile can be noted in the adrenal tissue at 5.8 GHz both at 30 W and 60 W compared with the ablation profiles achieved at 2.45 GHz (§ 6.2.1). The triaxial structure of the MW applicator used in this study partially enhances the ablation profile. The third metallic axis limits the effect of the backward currents flowing along the feedline of the applicator (§ 4.3.1). However, the highest contribution in the sphericity of the ablation zone derives from the higher operating frequency used. As already observed in [134], [135], an increase in the operating frequency requires a radiating element of shorter length.

No substantial differences in the ablation patterns are observed between the simplified model and the 3D model, for both orientations of the antenna and for both input powers (30 W and 60 W) at 5.8 GHz. The similarity in the ablation profiles may be attributed to the higher operating frequency adopted in this study. At 5.8 GHz, the wavelength in the adrenal and fat tissues is 8 mm and 18 mm against 18 mm and 41 mm at 2.45 GHz. Because of the shorter wavelength, at 5.8 GHz the size of the meshing cells decreases by a factor of 10 compared with 2.45 GHz. Thus, the geometry within each cell can be locally assumed as planar. Overall, the 3D geometry has a smaller impact on the growth of the ablation zones compared with 2.45 GHz (§ 6.2.2). For this study, the simplified model was assumed as a good representation of the tissue target. Two aspects led to the adoption of the planar model: (1) the high computational load linked to the complexity of the 3D model and (2) the negligible difference in the results between the two models.

In particular, the multilayered geometry was used for investigating the influence of the water vaporisation on the ablation zone.

Vaporisation phenomena are linked to the high temperatures reached in the adrenal tissue, due to the faster interactions between the electromagnetic field and the tissue at 5.8 GHz. Thus, the water vaporisation is more influential at 5.8 GHz compared with 2.45 GHz (§ 4.3.1) and needs to be considered in the numerical models. These numerical results will be discussed along with the experimental data (§ 8.3.2). The main goal is to understand the role of vaporisation in the increase of temperature and on the achievable dimensions of the ablation zone.

8.3.2 Experimental *ex vivo* assessment of the ablation zone and temperature increments

The experimental assessment aimed to evaluate the effect of the frequency higher than 2.45 GHz on the profile of the ablation zone in the adrenal gland. To this end, a total of six MWA procedures were carried out on six (N = 6) *ex vivo* porcine adrenal glands. Three adrenal glands were used for each setting, i.e. 30 W – 60 s and 60 W – 60 s. Figure 8.6 shows an example of the ablation zone obtained in the adrenal gland. The MW applicator was placed at the interface between the adrenal gland and the external fat layer to apply the 'side-firing' approach. The ablation zone was delineated by visual inspection
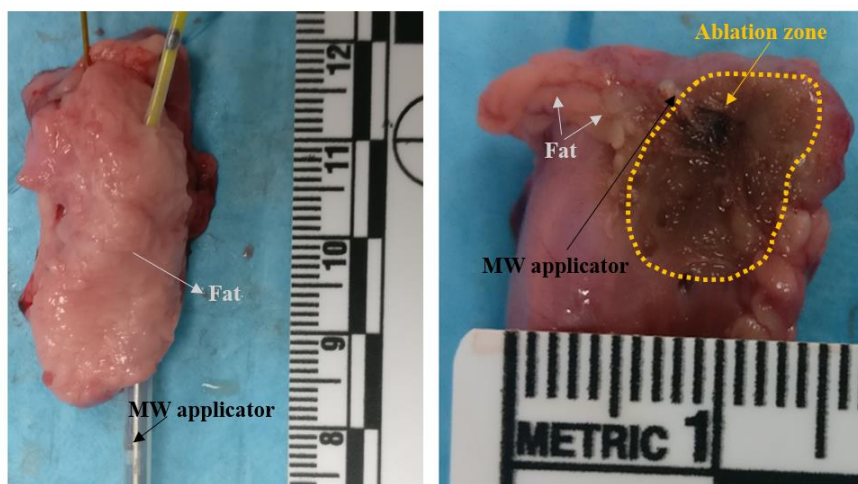
Figure 8.6: Section of the ablation zone obtained ex vivo in a porcine adrenal gland: the triaxial monopole MW applicator (§ 4.2.1) is placed on the surface of the gland and covered by fat, then it is excited at 5.8 GHz. The ablation zone in adrenal gland is marked (not visible in fat).

on the surface of the adrenal cortex. Dark-coloured areas delineated the ablation zones at 5.8 GHz instead of the whitening effect observed in the ablated area at 2.45 GHz (§ 6.2.2). This difference confirms the effect of the higher temperatures occurring in proximity to the applicator in the case of a higher operating frequency [134], [135].

Table 8.3 reports the mean and related standard deviation values of the radial and longitudinal dimensions of the ablation zone. The two dimensions were measured on each adrenal gland at the end of the procedure (60 s). The radial dimensions correlated with the radial values predicted by the numerical simulations in both adrenal models (planar and 3D) and for both input power levels (30 W and 60 W). The highest discrepancy was observed in the longitudinal dimensions. Visibly shorter ablation zones were observed in the experimental assessment compared with the numerical findings. Thus, more spherical ablation zones were found in the experimental test. A similar finding was also observed at 2.45 GHz. This discrepancy can be attributed to multiple factors including the actual shape of the sample, the changes in the structure of the tissue due to high temperatures, and the contraction of the tissue [13], [248], [250], [251].

The experimental assessment helped to support the results of the numerical simulations, however some limitations in this experimental study must be considered. First, the study was conducted on adrenal glands excised from a different animal source (porcine)
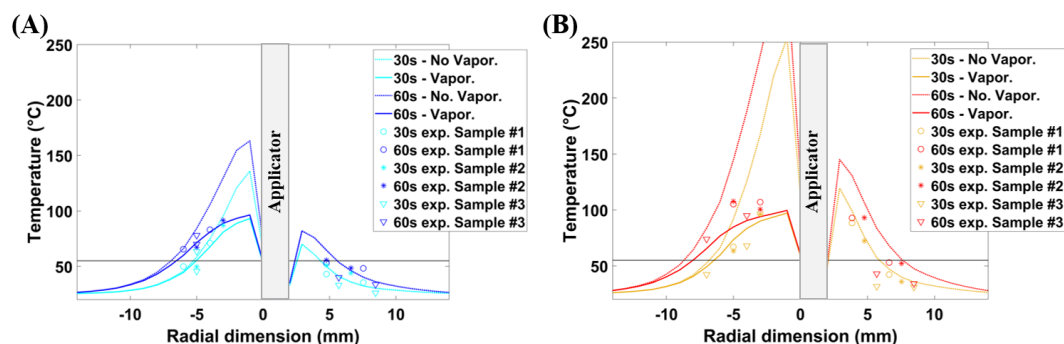
Figure 8.7: Numerical and experimental values of temperature along the radial distance from the MW antenna axis (applicator) both in the fat and adrenal gland at 30 s and 60 s for 30 W (A) and 60 W (B). Numerical values include the temperature obtained from standard BHE (dot lines) and from the modified BHE, accounting for the effect of water vaporisation (solid lines). Horizontal line highlights the temperature threshold at 55 °C.

compared to the experimental study conducted at 2.45 GHz (ovine). Porcine adrenal glands have different dimensions and a different shape compared to the ovine adrenal glands used in the previous studies. Ovine adrenal glands are rounded and thick (similarly to human), while porcine adrenal glands are more elongated and flatter. These factors must be considered when comparing the experimental results with the numerical findings, in terms of the extent of the ablation zone. Finally, a recurrent swelling of the tissue occurred in the porcine adrenal glands that was not observed during the MWA procedures at 2.45 GHz. This effect is likely linked to the high temperatures reached and the consequent increase in pressure developed inside the tissue due to vaporisation [276].

8.3.3   Effect of the water vaporisation on the temperature increase

Figure 8.7 shows the temperature values acquired experimentally in the adrenal gland and fat. The experimental values align well with the actual positions of the thermal sensors in the tissue as reported in Table 8.2. The temperatures refer to two power levels, 30 W (A) and 60 W (B), and to two time-steps, 30 s and 60 s. The curves of temperature derive from two different numerical scenarios: (1) without considering the effect of the vaporisation model, (2) accounting for the vaporisation phenomena (§ 4.2.2). Both experimental and numerical results are expressed as a function of the radial distance from the longitudinal axis of the MW applicator.

Figure 8.8 compares the experimental and numerical temperature increments as a function of time. Again, in one case the effect of water vaporisation was neglected (A) – (C), in the other case the water vaporisation was considered (B) – (D). Numerical and experimental values refer to 30 W (A) – (B) and at 60 W (C) – (D). Two different distances from the antenna feed were considered (4 mm and 7 mm). The distances were chosen in accordance with the starting positions of the thermal sensors. The mean values and standard deviation of the experimental measurements were reported.

Both figures show a good correlation between the experimental and the numerical results, when the effect of vaporisation is considered. The absence of water vaporisation in the numerical simulations results in unrealistically high temperatures in proximity to the MW applicator. At 30 W, the temperature exceeds 120 °C after 30 s (Figure 8.7 (A)). At
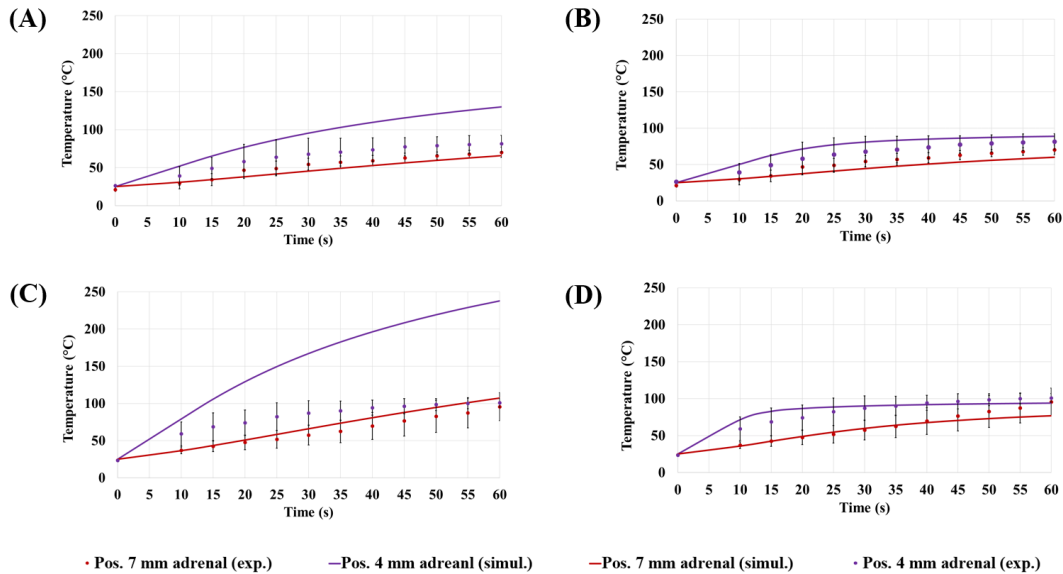
Figure 8.8: Comparison between the numerical results (solid lines) obtained in the case of standard BHE (A) – (C) and implementing the model of water vaporisation (C) – (D). The increments of temperature were considered for two input powers: 30 W (A) – (B) and 60 W (C) – (D). The temperature values distances from the MW applicator are 4 mm and 7 mm. Mean values of temperatures measured over the time through fiber optic sensors were also reported along with the related standard deviation values (markers).

60 W, temperatures higher than 250°C are observed after 30 s (Figure 8.7 (B)). Thus, the numerical model accounting only for the standard BHE is not capable of accurately predicting the increase in temperature observed experimentally. This limitation results in a high discrepancy between the numerical and experimental data (Figure 8.8 (A) – (C)). At 4 mm from the applicator, the measured values differ from the numerical findings by approximately 48°C at 30 W (Figure 8.8 (A)) and 137°C at 60 W (Figure 8.8 (C)). In the case of a higher distance (7 mm) from the applicator, the difference between the numerical and experimental data is within the standard deviation of the experimental data.

Implementing the vaporisation model, the maximum temperature reached is approximately 100°C, which was observed in the case of the highest power and at the closest distance from the applicator (Figure 8.8 (D)). The modified specific heat capacity described by Equation (4.19) accounts for the energy (i.e. heat) required to allow the water phase transition from liquid to vapour. As a consequence, this energy does not

contribute to the increase of temperature in the tissue. It is worth noting that the radial dimensions of the area delimited by isothermal contour at 55°C in the adrenal gland differ less than 0.5 mm between the two numerical scenarios. This small variation is nearly unchanged both at 30 W and 60 W (Figure 8.7).

Overall, the vaporisation model has a negligible impact on the final extent of the ablation zones for the settings considered. Instead, water vaporisation shows a sizable impact on the maximum temperature reached at the end of the MWA procedure. In particular, the closer the distance from the feed of the antenna is, the higher the vaporisation effect will be.

The model of water vaporisation influences not only the maximum temperature achieved, but also the trend of the increase of temperature over time, especially at small distances from the applicator. At 4 mm from the antenna axis and at 30 W, the temperature increases with an approximately linear slope of 4°C s^{-1} for the first 20 s for both numerical models. From 20 s onwards, the temperature in the case of the standard BHE continues increasing steadily at a rate of approximately 3 °C s^{-1} (Figure 8.8 (A)). In the case of modified BHE, temperature elevations slow to a rate of approximately 1 °C s^{-1} for the next 10 s and a slower rate of 0.1 °C s^{-1} from 10 s up to 60 s (Figure 8.8 (B)). At the same distance (4 mm) from the applicator and at 60 W, the approximately linear slope at which the temperature increases is 7 °C s^{-1}. This rate is similar between the two models (i.e. standard BHE and modified BHE) for the first 10 s only. When the vaporisation model is considered, the increment in temperature slows to 3 °C s^{-1} between 10 s and 35 s. Then, such a slope rate becomes much slower (0.08 °C s^{-1}) up to the end of the procedure. It can be also observed that at further distance from the applicator (7 mm), the water vaporisation is less influential due to the lower temperatures reached.

In summary, this study shows that the water vaporisation model has a high impact on the maximum temperature reached at the end of the MWA, especially in proximity to the applicator. The same model also influences the trend of the temperature increase over time. On the other hand, the vaporisation model shows a negligible effect on the extent of the ablation zone, for the settings considered (Figure 8.6). Finally, it is worth noting

that dynamic simulation requires a higher computational load compared to the standard numerical simulations. For this study, standard simulations required approximately 7h against 19h for the dynamic simulations, using CST MWS Suite 2018 on an Intel® Core™ i7@ 4GHz with 16 GB RAM.

8.4 Conclusions

This chapter discusses the effect of a higher operating frequency (5.8 GHz) compared to 2.45 GHz on the ability of the fat layer to shield the electromagnetic energy and create asymmetric adrenal ablation zones. The ablation zones obtained at two different power levels (30 W and 60 W) for 60 s were evaluated numerically in the simplified multilayered model and in the 3D model. An experimental study supported the numerical investigation. The experimental assessment was conducted *ex vivo* on porcine adrenal glands using the same power and time settings (30 W and 60 W).

The results of the study show that:

- The 'side firing' approach is also capable of creating asymmetric ablation zones also at 5.8 GHz, using the same power and time settings as in the previous studies conducted at 2.45 GHz. At 5.8 GHz, no difference is observed in the radial and longitudinal dimensions of the ablation zone between the simplified and 3D models and for both orientations of the antenna. This result is likely due to the shorter wavelength at 5.8 GHz compared to 2.45 GHz. Shorter wavelength implies smaller meshing cells, within which the geometry can be assumed planar. As a result, the influence of the 3D geometry on the final shape and size of the ablation is minimised;

- The higher effective conductivity of the adrenal cortex at 5.8 GHz allows for a faster deposition of the electromagnetic energy in the tissue compared to 2.45 GHz. The faster interaction mechanism between the tissue and the electric field helps to achieve ablation zones able to cover small adreno-cortical adenomas (≤10 mm in diameter). The results suggest use of a low input power level for a more precautionary ablation procedure, as observed also at 2.45 GHz. Indeed, at 30 W the ablation zone in fat is

within 5 mm from the applicator, which is desirable to preserve the sensitive anatomical structures placed in the area surrounding the gland;

- The radial dimensions of the ablation zone measured *ex vivo* on porcine adrenal tissue are in good agreement with the numerical prediction. Conversely, the numerical simulation overestimates the longitudinal dimensions obtained experimentally. A model accounting for the water vaporisation is needed to predict the temperature elevations occurring in the tissue during the ablation, especially when the temperatures exceed 70°C. On the other hand, the vaporisation model has no sizable influence on the prediction of the extent of the ablation zone.

Chapter 9
Conclusions and future work

9.1 Summary and conclusions

Adreno-cortical functional adenomas and bilateral hyperplasia are the leading causes for autonomous release of aldosterone hormone and related hypertension. Early interventions to restore normal levels of blood pressure are necessary to avoid life-threatening events such as ventricular hypertrophy and cerebrovascular ischemic attacks. The front-line treatments for this condition, known as Primary Aldosteronism, are adrenalectomy and hormonal-antagonists pharmacotherapy. However, both techniques have limitations. Adrenalectomy is only a feasible procedure for patients with unilateral abnormalities and normal conditions in the contralateral gland. Pharmacotherapy is administered to patients affected by bilateral hyperplasia or in the case of unilateral recurrency. Depending on the dose, 6% to 50% of patients show poor tolerance to the hormonal therapy, which is generally a long-life treatment [Funder et al., 2008], [Velema et al., 2018], [Yoshida et al., 2021].

The motivation behind this thesis is detailed in Chapter 1, together with the primary contributions of the thesis. The chapter introduces a new microwave ablation approach based on the dielectric characteristics of the adrenal gland. In particular, the dielectric contrast existing between the tissues of the gland and the surrounding fat capsule may be exploited to treat shallow adenomas.

Then, the anatomy of the adrenal gland, the biological mechanism underlying the release of the aldosterone and the regulation of the levels of blood pressure were reviewed in Chapter 2. In the same chapter, the anomalies of the gland responsible for Primary Aldosteronism and the limitations of the gold standard techniques were described. Given the limitations, an extensive review of different alternative treatments was conducted. The performance of these alternative techniques was compared to the conventional treatments in terms of eradicating the functional adenomas, normalisation of the blood pressure and hormonal activity (see Appendix A). MWA was proposed to address the limitations presented by the gold standard techniques; the potential of the MWA versus

the other techniques was highlighted. Finally, the main challenges and contributions of this thesis were described as follows:

1. Ovine adrenal glands are identified as suitable animal model to represent human adrenal tissues in healthy conditions. This assumption is based on two key factors. First, the anatomical characteristics of the ovine adrenal gland approximate better the shape and the size of the human adrenal glands compared with other animal models, e.g. bovine adrenal glands. Then, the measurement and analysis of the dielectric properties show less than 2% difference between *ex vivo* ovine adrenal cortex and *ex vivo* healthy human adrenal cortex. The dielectric characterisation of ovine adrenal glands also provides information on the medulla. Medulla is the innermost tissue of the adrenal gland, hence it is not accessible for measurements on human adrenal samples. The results show slightly higher values in the dielectric properties of the medulla compared with the cortex. This difference in dielectric properties between the two functional tissues was considered in the numerical modelling of the tissues to enable accurate EM and thermal simulations. The values in the dielectric properties of normal adrenal tissues are a reference to compare against the dielectric properties measured *ex vivo* on a range of different diseased human adrenal glands. The comparison shows that the experimental data in the diseased adrenal glands examined in this study lies within the variability range of the dielectric properties of the animal model and the human adrenal gland in normal conditions. Only the dielectric properties measured on one adreno-cortical functional adenoma show was lower than those of normal tissues. This result may depend on the amount of lipidic content resulting from the infiltration of the tumour in the surrounding fat capsule. Nevertheless, this result needs to be investigated in a larger population. The values of dielectric properties both for animal and human samples were shown across the microwave frequency range (500 MHz – 8.5 GHz) and at the single frequency suitable for MWA procedures (i.e. 915 MHz, 2.45 GHz, 5.8 GHz). The results highlight that the effective conductivity of the adrenal tissues increases at least 160% when the operating frequency is increased from 2.45 GHz to 5.8 GHz. This result motivated the study described in Chapter 8 and is summerised below (Point 5).

2. Three different models for the MW applicator were designed and prototyped. The design of the MW applicators was modified accounting for the specific experimental scenario and operating frequency. The first prototype was designed to conduct a proof-of-concept study aiming of investigating and assessing the effects of the 'side firing' approach in an *ex vivo* scenario at 2.45 GHz. Then, this coaxial-based applicator was improved for *in vivo* animal tests. In particular, a triaxial structure was used to reduce the backward current which may induce unintended injuries to the healthy tissues during the MWA procedure. A similar triaxial structure was used to design and prototype a further MW applicator, optimised to work at 5.8 GHz. As expected, the results show that the deposition of SAR varies with the structure of the MW applicator and the operating frequency. At 2.45 GHz, the triaxial-based applicator shows slightly lower values of SAR along the feeding cable compared with the coaxial-based design. At 5.8 GHz the triaxial MWA applicator provides a significant decrease in the SAR values along the feeding cable, thus more spherical SAR profiles compared with 2.45 GHz. Once the performances of each MW applicator were analysed, the workflow for EM and thermal simulations was set. The main factors of influence during MWA procedures were reviewed and evaluated in relation to the levels of input power and time adopted. At 2.45 GHz, the results show that the standard bioheat equation is able to predict the increment of temperature in the tissue model considering the power and time settings used (i.e. 30 W – 60 s and 60 W – 60 s). Conversely, at 5.8 GHz and for the same settings, unrealistic high temperatures are reached using the standard bioheat equation. Reliable temperature values are instead obtained when the bioheat equation is modified to include the water vaporisation model.

3. Different models of the tissue target were developed to test the novel 'side firing' MWA approach at 2.45 GHz.

a. A simple model including fat and muscle was used for a proof-of-concept study. The contrast in the dielectric properties between fat and muscle provided two main results. Fat is capable of shielding the electromagnetic energy and reducing the temperature increase below 55°C for most of the tissue. In addition, the dielectric

179

contrast forces the electromagnetic energy into the tissue target (i.e. muscle) because of the lower wave impedance compared with fat. Thus, fat provides a natural reflector which can be used to effectively direct the electromagnetic field. To support this finding, the dimensions of the ablated areas were compared with those achieved in a reference scenario involving only homogeneous muscle tissue. Ablation zones at least two-fold larger were observed in the interface scenario when compared with the homogeneous scenario. A significant increase in the longitudinal dimension of the ablation zone was observed in the muscle at the interface with fat compared to the homogenous case. This is because part of the EM energy reflected from the fat redistributes in the tissue target along the central axis of the applicator. Similar results were observed for different widths of the fat layer and are independent of the accuracy in the antenna alignment.

b. A simplified multilayered geometry and a 3D geometry were modelled to represent the adrenal structure and the same 'side firing' approach was tested. In correlation with the findings from the proof-of-concept study, the dielectric contrast between the fat capsule and target tissue was also responsible for asymmetric ablation profiles in the adrenal models. However, the geometry and the orientation of the MW applicator influence the shape and the size of the ablation zones. Differences in the distributions of SAR and temperature are observed in the 3D model depending on the orientation of the MW applicator with respect to the interface between the two tissues. Overall, the results show that the more the antenna is aligned to the interface between fat and target tissue, the more the fat is capable of shielding the EM energy and creating asymmetric heating patterns. Additionally, the low input power (30 W) can provide more spherical ablation zones in the tissue target and limit the ablation zone in fat compared with the high input power (60 W). Essentially, similar results are obtained changing the type of background material from air to blood and implementing blood perfusion in order to represent *in vivo* conditions. The small impact of the blood perfusion on the ultimate dimensions of the ablation zones is likely due to the relatively short duration of the procedure (60 s).

4. *Ex vivo* and *in vivo* studies conducted on ovine adrenal models validated the numerical models and findings. Both experimental studies were supported by histological analyses. The analysis conducted on *ex vivo* tissues after MWA procedure showed two key aspects. First, coagulation necrosis in the adrenal tissues was limited to the region in proximity to the applicator even in the case of high input power. The region of the cortex and medulla far from the MW applicator was instead characterised by a normal cellular structure. The second aspect was that the fat layer confirms the ability to protect the abutting artery, as observed in the reported case. The entire structure of the blood vessel appeared intact, while inflammation among adipocytes was observed only in the region of the fat layer in proximity to the applicator. In the *in vivo* study, only the low input power setting (30 W) was adopted. The histological findings in this case showed no coagulation necrosis, only inflammation. This is likely due to the role of perfusion in low power ablations and the effect of the immediate response of the immune system.

The above described multilayered and 3D adrenal models were also used to investigate the effect of MWA at an higher operating frequency, 5.8 GHz. An *ex vivo* experimental study confirmed the computational findings. Conversely to what was observed at 2.45 GHz, in the case of 5.8 GHz there was no substantial impact of the geometrical characteristics of the tissues and orientations of the MW applicator on the distributions of SAR and temperature. In addition, more spherical ablation zones were achievable thanks to the shorter length of the radiating element. Very high temperatures were reached in proximity to the applicator because of the faster mechanism of action at 5.8 GHz compared with 2.45 GHz. As a result, water vaporisation was more impactful on the increase of temperature when MWA is conducted at 5.8 GHz. Thus, a water vaporisation model was necessary to accurately predict the increase in the temperature with the time reducing the unrealistically high temperature values. However, no substantial impact of the water vaporisation was observed in the ultimate extent of the ablation zone. The radial dimensions of the ablation zones in the tissue target were approximately 10 mm at low input power. With the same power and time setting, the radial dimensions achieved in the adrenal tissue at 2.45 GHz were approximately 5 mm.

As a result, MWA procedures conducted at 5.8 GHz and at a low energy dose show the potential to achieving a thermal coverage with dimensions comparable to the average size of adrenal adenomas.

9.2 Future work

In this thesis, the experimental data derived from the measurements of dielectric properties in animal models were used as reference values for the numerical studies. The reliability of the values was evaluated by comparing them with the values measured *ex vivo* on human adrenal tissues. However, only a limited number of human tissues was available for the study. The small number of adrenalectomy procedures performed in the local hospital limited the possibility of reaching a larger population over the period of this doctoral study. This first investigation paves the way for the collection of a larger number of measurements of dielectric properties both on healthy and diseased human tissues. A larger population is required to account for the variability in the dielectric properties depending on the patients' diseases and general health conditions. The variability in the dielectric properties may affect the dielectric contrast between the tissue target and the adjacent fat layer, especially in diseased tissues. Thus, a larger dataset may allow for a sensitivity analysis to evaluate the effects on the ablation profiles in relation to the variation in the dielectric contrast.

The 'side firing' MWA approach was investigated considering a simplified model and a 3D model for adrenal glands. The functional adrenal tissues and the surrounding fat layer were modelled taking into account the realistic average widths of the contiguous layers. The numerical models described in this thesis provide a base for future development of patient-specific models based on diagnostic imaging data (e.g. PET/CT). First, patient-specific models provide a better understanding of the distribution of the electromagnetic energy based on the real clinical scenario (e.g. size and location of the adrenal adenoma), leading to personalised pre-clinical protocols. Then, these models enable the pre-clinical evaluation of the most suitable positioning of the MW applicator at the interface between the tissue target and the fat layer.

In this thesis, the capability of the fat layer to shield the EM energy was studied in relation to two different levels of energy dose. The results show consistency in the capability of the fat layer to create asymmetric ablation profiles and to contain the increase of temperature, thereby protecting the surrounding sensitive structures. Future studies should be devoted to exploring and refining the combinations of power and time settings and different methods of energy deliveries. For example, the efficacy of continuous and pulsed energy methods may be evaluated in terms of impact on microwave ablation growth and shaping of asymmetric heating patterns both in *ex vivo* and *in vivo* scenarios. The effect of the increase of the temperature on the cellular structure of the tissue was evaluated through the histology analysis. In particular, the deformations in the cell membrane or in the shape of cell nuclei, the infiltration of immune inflammation cells and microhaemorrhage due to the extravasation of the blood vessels were qualitatively assessed. However, the evaluation of the functionality of the adrenal tissue following the thermal insult requires further *in vivo* investigations. Immunohistochemical analysis should be combined with the histology analysis to estimate the damage to the functionality of the adrenal gland in the hormones release that was induced by the MWA procedure. For example, the levels of the aldosterone values or the levels of renin activity could be measured immediately after the procedure and during the follow-up periods.

This thesis provides a comprehensive understanding of the role of the fat layer in the shaping of ablation zones in MWA conducted at 2.45 GHz. In addition, the last study of this thesis provides an outlook on the possibility to use 5.8 GHz as operating frequency. The main purpose of this study was to evaluate if the increase in the operating frequency could improve the effectiveness of the 'side firing' approach. This preliminary study highlights positive aspects in using higher operating frequency. For example, the alignment of the MW applicator plays a marginal role in the shaping asymmetric ablation patterns in contrast with the high variability observed at 2.45 GHz. Also, the higher frequency provides a better thermal coverage in the tissue target and enhances the sphericity of the ablation zone. Given the promising results, a comprehensive study should be conducted at 5.8 GHz (as completed for 2.45 GHz) including *ex vivo* and *in vivo* experimental studies on ovine adrenal glands and post-treatment histology analyses.

Bibliography

[1] J. W. Funder, 'Primary Aldosteronism: Present and Future', in *Vitamins and Hormones*, vol. 109, Elsevier, 2019, pp. 285–302.

[2] G. P. Rossi, 'Primary Aldosteronism', *J. Am. Coll. Cardiol.*, vol. 74, no. 22, pp. 2799–2811, 2019.

[3] W. F. Young, 'Primary aldosteronism: renaissance of a syndrome', *Clin. Endocrinol. (Oxf.)*, vol. 66, no. 5, pp. 607–618, 2007.

[4] M. Nishimura *et al.*, 'Cardiovascular complications in patients with primary aldosteronism', *Am. J. Kidney Dis.*, vol. 33, no. 2, pp. 261–266, 1999.

[5] G. P. Rossi *et al.*, 'Excess ldosterone Is Associated With Alterations of Myocardial Texture in Primary Aldosteronism', *Hypertension*, vol. 40, no. 1, pp. 23–27, 2002.

[6] P. Mulatero *et al.*, 'Comparison of Confirmatory Tests for the Diagnosis of Primary Aldosteronism', *J. Clin. Endocrinol. Metab.*, vol. 91, no. 7, pp. 2618–2623, 2006.

[7] P. Milliez *et al.*, 'Evidence for an increased rate of cardiovascular events in patients with primary aldosteronism', *J. Am. Coll. Cardiol.*, vol. 45, no. 8, pp. 1243–1248, 2005.

[8] J. W. Funder *et al.*, 'Case Detection, Diagnosis, and Treatment of Patients with Primary Aldosteronism: An Endocrine Society Clinical Practice Guideline', *J. Clin. Endocrinol. Metab.*, vol. 93, no. 9, pp. 3266–3281, 2008.

[9] S. Karashima *et al.*, 'Comparison of eplerenone and spironolactone for the treatment of primary aldosteronism', *Hypertens. Res.*, vol. 39, no. 3, pp. 133–137, 2016.

[10] G. S. Gazelle, 'Tumor Ablation with Radio-frequency Energy', *Radiology*, vol. 217, no. 3, pp. 633–646, 2000.

[11] C. L. Brace, 'Microwave Tissue Ablation: Biophysics, Technology, and Applications', *Crit. Rev. Biomed. Eng.*, vol. 38, no. 1, pp. 65–78, 2010.

[12] T. P. Ryan, P. F. Turner, and B. Hamilton, 'Interstitial microwave transition from hyperthermia to ablation: Historical perspectives and current trends in thermal therapy', *Int. J. Hyperthermia*, vol. 26, no. 5, pp. 415–433, Aug. 2010.

[13] M. H. H. Tehrani, M. Soltani, F. M. Kashkooli, and K. Raahemifar, 'Use of microwave ablation for thermal treatment of solid tumors with different shapes and sizes—A computational approach', *PLOS ONE*, vol. 15, no. 6, pp. 1–20, 2020.

[14] T. Livraghi, F. Meloni, L. Solbiati, and G. Zanus, 'Complications of Microwave Ablation for Liver Tumors: Results of a Multicenter Study', *Cardiovasc. Intervent. Radiol.*, vol. 35, no. 4, pp. 868–874, 2012.

[15] Y. Liu, Y. Zheng, S. Li, B. Li, Y. Zhang, and Y. Yuan, 'Percutaneous microwave ablation of larger hepatocellular carcinoma', *Clin. Radiol.*, vol. 68, no. 1, pp. 21–26,

2013.[16] J. Yu *et al.*, 'US-guided Percutaneous Microwave Ablation of Renal Cell Carcinoma: Intermediate-term Results', *Radiology*, vol. 263, no. 3, pp. 900–908, 2012.

[17] L. Zheng *et al.*, 'Hypertensive Crisis during Microwave Ablation of Adrenal Neoplasms: A Retrospective Analysis of Predictive Factors', *J. Vasc. Interv. Radiol.*, vol. 30, no. 9, pp. 1343–1350, 2019.

[18] F. J. Wolf, D. E. Dupuy, J. T. Machan, and W. W. Mayo-Smith, 'Adrenal neoplasms: Effectiveness and safety of CT-guided ablation of 23 tumors in 22 patients', *Eur. J. Radiol.*, vol. 81, no. 8, pp. 1717–1723, 2012.

[19] C. Ren, P. Liang, X. Yu, Z. Cheng, Z. Han, and J. Yu, 'Percutaneous microwave ablation of adrenal tumours under ultrasound guidance in 33 patients with 35 tumours: A single-centre experience', *Int. J. Hyperthermia*, vol. 32, no. 5, pp. 517–523, 2016.

[20] G. Ruvio, J. Eaton-Evans, A. Shahzad, and M. O'Halloran, 'Numerical evaluation of microwave thermal ablation to treat small adrenocortical masses', *Int. J. RF Microw. Comput.-Aided Eng.*, vol. 28, no. 3, pp. 1–8, 2018.

[21] H. Fallahi and P. Prakash, 'Antenna Designs for Microwave Tissue Ablation', *Crit. Rev. Biomed. Eng.*, vol. 46, no. 6, pp. 495–521, 2018.

[22] K. Yamakado, 'Image-Guided Ablation of Adrenal Lesions', *Semin. Interv. Radiol.*, vol. 31, no. 02, pp. 149–156, 2014.

[23] J. F. Swietlik *et al.*, 'Microwave Ablation of Adrenal Tumors in Patients With Continuous Intra-Arterial Blood Pressure Monitoring Without Prior Alpha-Adrenergic Blockade: Safety and Efficacy', *Cardiovasc. Intervent. Radiol.*, vol. 43, no. 9, pp. 1384–1391, 2020.

[24] B. Manchec, Y. Koethe, B. Schiro, C. Peña, and R. Gandhi, '"How We Do It" – A Practical Approach to Percutaneous Adrenal Ablation Techniques', *Tech. Vasc. Interv. Radiol.*, vol. 23, no. 2, pp. 1–8, 2020.

[25] J. Sebek, S. Curto, R. Bortel, and P. Prakash, 'Analysis of minimally invasive directional antennas for microwave tissue ablation', *Int. J. Hyperthermia*, vol. 33, no. 1, pp. 51–60, 2017.

[26] J. E. Hall, *Guyton and Hall textbook of medical physiology*, 13th edition. Philadelphia, PA: Elsevier, 2016.

[27] C. E. Fardella, L. Mosso, and C. G. M.-S. Nchez, 'Primary Hyperaldosteronism in Essential Hypertensives: Prevalence, Biochemical Profile, and Molecular Biology', vol. 85, no. 5, pp. 1863–1868, 2000.

[28] G. P. Rossi, 'A comprehensive review of the clinical aspects of primary aldosteronism', *Nat. Rev. Endocrinol.*, vol. 7, no. 8, pp. 485–495, 2011.

[29] O. A. Carretero and S. Oparil, 'Essential Hypertension: Part I: Definition and Etiology', *Circulation*, vol. 101, no. 3, pp. 329–335, 2000.

[30]   A. E. Norlander, M. S. Madhur, and D. G. Harrison, 'The immunology of hypertension', *J. Exp. Med.*, vol. 215, no. 1, pp. 21–33, 2018.

[31]   R. M. Fagugli and C. Taglioni, 'Changes in the Perceived Epidemiology of Primary Hyperaldosteronism', *Int. J. Hypertens.*, vol. 2011, pp. 1–7, 2011.

[32]   A. Moraitis and C. Stratakis, 'Adrenocortical Causes of Hypertension', *Int. J. Hypertens.*, vol. 2011, pp. 1–10, 2011.

[33]   American Diabetes Association, 'Diagnosis and Classification of Diabetes Mellitus', *Diabetes Care*, vol. 33, no. Supplement 1, pp. S62–S69, 2010.

[34]   R. Rossi *et al.*, 'Percutaneous computed tomography-guided ethanol injection in aldosterone-producing adrenocortical adenoma', *Eur. J. Endocrinol.*, vol. 132, no. 3, pp. 302–305, 1995.

[35]   Y. Shigematsu, M. Hamada, and et al., 'Left Ventricular Hypertrophy Precedes Other Target-Organ Damage in Primary Aldosteronism', *Hypertension*, vol. 29, no. 3, pp. 723–727, 1997.

[36]   F. Fallo *et al.*, 'Prevalence and Characteristics of the Metabolic Syndrome in Primary Aldosteronism', *J. Clin. Endocrinol. Metab.*, vol. 91, no. 2, pp. 454–459, 2006.

[37]   M. K. Kwak, J. Y. Lee, B.-J. Kim, S. H. Lee, and J.-M. Koh, 'Effects of Primary Aldosteronism and Different Therapeutic Modalities on Glucose Metabolism', *J. Clin. Med.*, vol. 8, no. 12, pp. 2194–2208, 2019.

[38]   N. M. Kaplan, 'Hypokalemia in the Hypertensive Patient: With Observations on the Incidence of Primary Aldosteronism', *Ann. Intern. Med.*, vol. 66, no. 6, pp. 1079–1090, 1967.

[39]   L. M. Fishman and et al., 'Incidence of Primary Aldosteronism Uncomplicated "Essential" Hypertension', *JAMA Cardiol.*, vol. 205, no. 7, pp. 497–502, 1968.

[40]   A. M. Sinclair, C. G. Isles, I. Brown, G. D. Murray, and J. W. K. Robertson, 'Secondary Hypertension in a Blood Pressure Clinic', pp. 1289–1293.

[41]   D. H. P. Streeten, N. Tomycz, and H. Anderson, 'Reliability of Screening Methods for the Diagnosis of Primary Aldosteronism', pp. 403–413.

[42]   K. Hiramatsu, 'A Screening Test to Identify Aldosterone-Producing Adenoma by Measuring Plasma Renin Activity: Results in Hypertensive Patients', *Arch. Intern. Med.*, vol. 141, no. 12, pp. 1589–1593, 1981, doi: 10.1001/archinte.1981.00340130033011.

[43]   'Blood pressure test', Visit 2018. https://www.mayoclinic.org/tests-procedures/blood-pressure-test/about/pac-20393098

[44]   'Test catalog', Visit 2018. https://www.mayocliniclabs.com/test-catalog/Overview/602352

[45]   M. Stowasser, A. Ahmed, E. Pimenta, P. Taylor, and R. Gordon, 'Factors Affecting the Aldosterone/Renin Ratio', *Horm. Metab. Res.*, vol. 44, no. 03, pp. 170–176, 2012.

[46]   G. P. Rossi *et al.*, 'A Prospective Study of the Prevalence of Primary Aldosteronism in 1,125 Hypertensive Patients', *J. Am. Coll. Cardiol.*, vol. 48, no. 11, pp. 2293–2300, 2006.

[47]   J. W. Funder *et al.*, 'The Management of Primary Aldosteronism: Case Detection, Diagnosis, and Treatment: An Endocrine Society Clinical Practice Guideline', *J. Clin. Endocrinol. Metab.*, vol. 101, no. 5, pp. 1889–1916, 2016.

[48]   Y. Song *et al.*, 'Confirmatory Tests for the Diagnosis of Primary Aldosteronism: A Prospective Diagnostic Accuracy Study', *Hypertension*, vol. 71, no. 1, pp. 118–124, 2018.

[49]   G. Giacchetti, P. Mulatero, F. Mantero, F. Veglio, M. Boscaro, and F. Fallo, 'Primary aldosteronism, a major form of low renin hypertension: from screening to diagnosis', *Trends Endocrinol. Metab.*, vol. 19, no. 3, pp. 104–108, 2008.

[50]   M. Bergstrom *et al.*, 'PET Imaging of Adrenal Cortical Tumors with the 11beta-HydroxylaseTracer 11C-Metomidate', vol. 41, no. 2, pp. 275–282, 2000.

[51]   J. Hennings, Ö. Lindhe, M. Bergström, B. Långström, A. Sundin, and P. Hellman, '[11C]Metomidate Positron Emission Tomography of Adrenocortical Tumors in Correlation with Histopathological Findings', *J. Clin. Endocrinol. Metab.*, vol. 91, no. 4, pp. 1410–1414, 2006.

[52]   T. J. Burton *et al.*, 'Evaluation of the Sensitivity and Specificity of ^{11}C-Metomidate Positron Emission Tomography (PET)-CT for Lateralizing Aldosterone Secretion by Conn's Adenomas', *J. Clin. Endocrinol. Metab.*, vol. 97, no. 1, pp. 100–109, 2012.

[53]   A. S. Powlson, M. Gurnell, and M. J. Brown, 'Nuclear imaging in the diagnosis of primary aldosteronism', *Curr. Opin. Endocrinol. Diabetes Obes.*, vol. 22, no. 3, pp. 150–156, 2015.

[54]   B. Strauch, T. Zelinka, M. Hampf, R. Bernhardt, and J. Widimsky, 'Prevalence of primary hyperaldosteronism in moderate to severe hypertension in the Central Europe region', *J. Hum. Hypertens.*, vol. 17, no. 5, pp. 349–352, 2003.

[55]   P. Mulatero *et al.*, 'Increased Diagnosis of Primary Aldosteronism, Including Surgically Correctable Forms, in Centers from Five Continents', *J. Clin. Endocrinol. Metab.*, vol. 89, no. 3, pp. 1045–1050, 2004.

[56]   K.-C. Loh, E. S. Koay, M.-C. Khaw, S. C. Emmanuel, and W. F. Young, 'Prevalence of Primary Aldosteronism among Asian Hypertensive Patients in Singapore', *Antihypertens. Ther.*, vol. 85, no. 2854–2859, p. 6, 2000.

[57]   C. Nakama *et al.*, 'The influence of aging on the diagnosis of primary aldosteronism', *Hypertens. Res.*, vol. 37, no. 12, pp. 1062–1067, 2014.

[58]   A. H. Ahmed *et al.*, 'Seated Saline Suppression Testing For The Diagnosis Of Primary Aldosteronism: A Preliminary Study', *J. Clin. Endocrinol. Metab.*, vol. 99, no. 8, pp. 2745–2753, 2014.

[59]   L. Mosso *et al.*, 'Primary Aldosteronism and Hypertensive Disease', *Hypertension*, vol. 42, no. 2, pp. 161–165, 2003.

[60]   G. P. Rossi, 'Primary aldosteronism: A needle in a haystack or a yellow cab on fifth avenue?', *Curr. Hypertens. Rep.*, vol. 6, no. 1, pp. 1–4, 2004.

[61]   S. Savard, L. Amar, P.-F. Plouin, and O. Steichen, 'Cardiovascular Complications Associated With Primary Aldosteronism: A Controlled Cross-Sectional Study', *Hypertension*, vol. 62, no. 2, pp. 331–336, 2013.

[62]   H. Wachtel and D. L. Fraker, 'Therapeutic Outcomes with Surgical and Medical Management of Primary Aldosteronism', *Curr. Cardiol. Rep.*, vol. 23, no. 7, pp. 89–98, 2021.

[63]   G. E. Umpierrez *et al.*, 'Primary Aldosteronism in Diabetic Subjects With Resistant Hypertension', *Diabetes Care*, vol. 30, no. 7, pp. 1699–1703, 2007.

[64]   A. Di Murro *et al.*, 'Renin-angiotensin-aldosterone system in patients with sleep apnoea: prevalence of primary aldosteronism', *J. Renin Angiotensin Aldosterone Syst.*, vol. 11, no. 3, pp. 165–172, 2010.

[65]   J. Burrello *et al.*, 'Diagnostic accuracy of aldosterone and renin measurement by chemiluminescent immunoassay and radioimmunoassay in primary aldosteronism', *J. Hypertens.*, vol. 34, no. 5, pp. 920–927, 2016.

[66]   A. A. Gumbs and M. Gagner, 'Laparoscopic adrenalectomy', *Best Pract. Res. Clin. Endocrinol. Metab.*, vol. 20, no. 3, pp. 483–499, 2006.

[67]   J. B. Byrd, A. F. Turcu, and R. J. Auchus, 'Primary Aldosteronism: Practical Approach to Diagnosis and Management', *Circulation*, vol. 138, no. 8, pp. 823–835, 2018.

[68]   T. Ishikawa *et al.*, 'Laparoscopic adrenalectomy for benign adrenal tumors', *Biomed. Pharmacother.*, vol. 54, Supplement 1, pp. 183–186, 2000.

[69]   K. L. Anderson *et al.*, 'Each procedure matters: threshold for surgeon volume to minimize complications and decrease cost associated with adrenalectomy', *Surgery*, vol. 163, no. 1, pp. 157–164, 2018.

[70]   T. C. Pang *et al.*, 'Outcome of laparoscopic adrenalectomy for hyperaldosteronism', *ANZ J. Surg.*, vol. 77, no. 9, pp. 768–773, 2007.

[71]   O. Steichen, F. Zinzindohoué, P.-F. Plouin, and L. Amar, 'Outcomes of adrenalectomy in patients with unilateral primary aldosteronism: review', *Horm. Metab. Res.*, vol. 44, no. 3, pp. 221–227, 2012.

[72]   S.-F. Chen *et al.*, 'Clinical outcomes in patients undergoing laparoscopic adrenalectomy for unilateral aldosterone producing adenoma: partial versus total adrenalectomy', *J. Endourol.*, vol. 28, no. 9, pp. 1103–1106, 2014.

[73]   D. A. Heinrich *et al.*, 'Adrenal insufficiency after unilateral adrenalectomy in primary aldosteronism: long-term outcome and clinical impact', *J. Clin. Endocrinol. Metab.*, vol. 104, no. 11, pp. 5658–5664, 2019.

[74]   R. T. Strebel, M. Müntener, and T. Sulser, 'Intraoperative complications of laparoscopic adrenalectomy', *World J. Urol.*, vol. 26, no. 6, pp. 555–560, 2008.

[75]   J. C. Carr and J. R. Howe, 'Laparoscopic Adrenalectomy', in *Chassin's Operative Strategy in General Surgery*, C. E. H. Scott-Conner, Ed. New York, NY: Springer New York, 2014, pp. 1075–1080.

[76]   A. Vaidya, C. D. Malchoff, and R. J. Auchus, 'An Individualized Approach to The Evaluation and Management of Primary Aldosteronism', *Endocr. Pract.*, vol. 23, no. 6, pp. 680–689, 2017.

[77]   L. Amar, A. Lorthioir, M. Azizi, and P.-F. Plouin, 'Progress in primary aldosteronism: mineralocorticoid antagonist treatment for aldosterone-producing adenoma', *Eur. J. Endocrinol.*, vol. 172, no. 3, pp. 125–129, 2015.

[78]   S.-J. Galati, S. M. Hopkins, K. C. Cheesman, R. A. Zhuk, and A. C. Levine, 'Primary aldosteronism: emerging trends', *Trends Endocrinol. Metab.*, vol. 24, no. 9, pp. 421–430, 2013.

[79]   M. Yamamoto *et al.*, 'Comparison of effects of aldosterone receptor antagonists spironolactone and eplerenone on cardiovascular outcomes and safety in patients with acute decompensated heart failure', *Heart Vessels*, vol. 34, no. 2, pp. 279–289, 2019.

[80]   M. Ahmed and et al., 'Principles of and Advances in Percutaneous Ablation', *Radiology*, vol. 258, no. 2, pp. 351–369, 2011.

[81]   M. G. Lubner, C. L. Brace, J. L. Hinshaw, and F. T. Lee, 'Microwave Tumor Ablation: Mechanism of Action, Clinical Results, and Devices', *J. Vasc. Interv. Radiol.*, vol. 21, no. 8, pp. S192–S203, 2010.

[82]   L. Sidoff and D. E. Dupuy, 'Clinical experiences with microwave thermal ablation of lung malignancies', *Int. J. Hyperthermia*, vol. 33, no. 1, pp. 25–33, 2017.

[83]   M. A. Roubidoux, W. Yang, and R. J. Stafford, 'Image-Guided Ablation in Breast Cancer Treatment', *Tech. Vasc. Interv. Radiol.*, vol. 17, no. 1, pp. 49–54, 2014.

[84]   K. Yamakado *et al.*, 'Adrenal Metastasis From Hepatocellular Carcinoma: Radiofrequency Ablation Combined With Adrenal Arterial Chemoembolization in Six Patients', *Am. J. Roentgenol.*, vol. 192, no. 6, pp. 300–305, 2009.

[85]   G. M. Lee *et al.*, 'Successful radiofrequency ablation strategies for benign thyroid nodules', *Endocrine*, vol. 64, no. 2, pp. 316–321, 2019.

[86]   A. Singal, J. R. Ballard, E. N. Rudie, E. N. K. Cressman, and P. A. Iaizzo, 'A Review of Therapeutic Ablation Modalities', *J. Med. Devices*, vol. 10, no. 4, pp. 801–812, 2016.

[87]   G. D. Dodd *et al.*, 'Minimally Invasive Treatment of Malignant Hepatic Tumors: At the Threshold of a Major Breakthrough', *RadioGraphics*, vol. 20, no. 1, pp. 9–27, 2000.

[88]   T. Livraghi and et al., 'Hepatocellular carcinoma and cirrhosis in 746 patients: long-term results of percutaneous ethanol injection', *Radiology*, vol. 197, no. 1, pp. 101–108, 1995.

[89]   T. W. I. Clark and M. C. Soulen, 'Chemical Ablation of Hepatocellular Carcinoma', *J. Vasc. Interv. Radiol.*, vol. 13, no. 9, pp. 245–252, 2002.

[90]   J. M. Monchik, G. Donatini, J. Iannuccilli, and D. E. Dupuy, 'Radiofrequency Ablation and Percutaneous Ethanol Injection Treatment for Recurrent Local and Distant Well-Differentiated Thyroid Carcinoma':, *Ann. Surg.*, vol. 244, no. 2, pp. 296–304, 2006.

[91]   P. Chevallier *et al.*, 'Treatment of hepatocellular carcinomas by thermal ablation and hepatic transarterial chemoembolization', *Diagn. Interv. Imaging*, vol. 96, no. 6, pp. 637–646, 2015.

[92]   N. Galanakis, E. Kehagias, N. Matthaiou, D. Samonakis, and D. Tsetis, 'Transcatheter arterial chemoembolization combined with radiofrequency or microwave ablation for hepatocellular carcinoma: a review', *Hepatic Oncol.*, vol. 5, no. 2, pp. 1–10, 2018.

[93]   E. S. Alexander, R. Mick, G. J. Nadolski, J. I. Mondschein, S. W. Stavropoulos, and M. C. Soulen, 'Combined chemoembolization and thermal ablation for the treatment of metastases to the liver', *Abdom. Radiol.*, vol. 43, no. 10, pp. 2859–2867, 2018.

[94]   Z. Xu, H. Xie, L. Zhou, X. Chen, and S. Zheng, 'The Combination Strategy of Transarterial Chemoembolization and Radiofrequency Ablation or Microwave Ablation against Hepatocellular Carcinoma', *Anal. Cell. Pathol.*, vol. 2019, pp. 1–7, 2019.

[95]   H.-L. Liang *et al.*, 'Small Functional Adrenal Cortical Adenoma: Treatment with CT-guided Percutaneous Acetic Acid Injection—Report of Three Cases', *Radiology*, vol. 213, no. 2, pp. 612–615, Nov. 1999, doi: 10.1148/radiology.213.2.r99nv10612.

[96]   S. Minowada, T. Fujimura, N. Takahashi, H. Kishi, K. Hasuo, and M. Minami, 'Computed Tomography-Guided Percutaneous Acetic Acid Injection Therapy for Functioning Adrenocortical Adenoma', *J. Clin. Endocrinol. Metab.*, vol. 88, no. 12, pp. 5814–5817, 2003.

[97]   I. Chang, I. Mikityansky, D. Wray-Cahen, W. F. Pritchard, J. W. Karanian, and B. J. Wood, 'Effects of Perfusion on Radiofrequency Ablation in Swine Kidneys', *Radiology*, vol. 231, no. 2, pp. 500–505, 2004.

[98]   Y.-Y. Xiao, J.-L. Tian, J.-K. Li, L. Yang, and J.-S. Zhang, 'CT-Guided Percutaneous Chemical Ablation of Adrenal Neoplasms', *Am. J. Roentgenol.*, vol. 190, no. 1, pp. 105–110, Jan. 2008, doi: 10.2214/AJR.07.2145.

[99]   M. Nakajo *et al.*, 'Scintigraphic Assessment of Therapeutic Success in Aldosteronomas Treated by Transcatheter Arterial', *J. Nucl. Med.*, vol. 38, no. 2, pp. 237–241, 1997.

[100] H. Hokotate, H. Inoue, Y. Baba, S. Tsuchimochi, and M. Nakajo, 'Aldosteronomas: Experience with Superselective Adrenal Arterial Embolization in 33 Cases', *Radiology*, vol. 227, no. 2, pp. 401–406, 2003.

[101] J. G. Baust, K. K. Snyder, K. L. Santucci, A. T. Robilotto, R. G. Van Buskirk, and J. M. Baust, 'Cryoablation: physical and molecular basis with putative immunological consequences', *Int. J. Hyperthermia*, vol. 36, no. 1, pp. 10–16, 2019.

[102] H. Wang, P. J. Littrup, Y. Duan, Y. Zhang, H. Feng, and Z. Nie, 'Thoracic Masses Treated with Percutaneous Cryotherapy: Initial Experience with More than 200 Procedures', *Radiology*, vol. 235, no. 1, pp. 289–298, 2005.

[103] J. L. Hinshaw, L. Sampson, F. T. Lee, P. F. Laeseke, and C. L. Brace, 'Does Selective Intubation Increase Ablation Zone Size during Pulmonary Cryoablation?', *J. Vasc. Interv. Radiol.*, vol. 19, no. 10, pp. 1497–1501, 2008.

[104] Y.-F. Fu and et al., 'Computed tomography-guided cryoablation for functional adrenal aldosteronoma', *Minim. Invasive Ther. Allied Technol.*, vol. 30, no. 3, pp. 169–173, 2019.

[105] R. Munver and R. E. Sosa, 'Cryosurgery of the Adrenal Gland', *Technol. Cancer Res. Treat.*, vol. 3, no. 2, pp. 181–185, 2004.

[106] J. L. Hinshaw, M. G. Lubner, T. J. Ziemlewicz, F. T. Lee, and C. L. Brace, 'Percutaneous Tumor Ablation Tools: Microwave, Radiofrequency, or Cryoablation—What Should You Use and Why?', *RadioGraphics*, vol. 34, no. 5, pp. 1344–1362, 2014.

[107] M. C. Jansen *et al.*, 'Cryoablation induces greater inflammatory and coagulative responses than radiofrequency ablation or laser induced thermotherapy in a rat liver model', *Surgery*, vol. 147, no. 5, pp. 686–695, 2010.

[108] S. N. Goldberg, 'Radiofrequency tumor ablation: principles and techniques', *Eur. J. Ultrasound*, vol. 13, no. 2, pp. 129–147, 2001.

[109] C. Brace, 'Thermal Tumor Ablation in Clinical Use', *IEEE Pulse*, vol. 2, no. 5, pp. 28–38, 2011.

[110] D. Haemmerich, 'Biophysics of Radiofrequency Ablation', *Crit. Rev. Biomed. Eng.*, vol. 38, no. 1, pp. 53–63, 2010.

[111] E. J. Berjano, 'Theoretical modeling for radiofrequencyablation: state-of-the-art and challenges for the future', *Biomed. Eng. OnLine*, vol. 5, no. 1, p. 24, 2006.

[112] M. Ahmed, Z. Liu, S. Humphries, and S. N. Goldberg, 'Computer modeling of the combined effects of perfusion, electrical conductivity, and thermal conductivity on tissue heating patterns in radiofrequency tumor ablation', *Int. J. Hyperthermia*, vol. 24, no. 7, pp. 577–588, 2008.

[113] S. N. Goldberg, M. C. Stein, G. S. Gazelle, R. G. Sheiman, K. MDr, and M. E. Clouse, 'Percutaneous Radiofrequency Tissue Ablation: Optimization of Pulsed-Radiofrequency Technique to Increase Coagulation necrosis', vol. 10, no. 7, p. 10, 1999.

[114] T. Fukushima *et al.*, 'Randomized Controlled Trial Comparing the Efficacy of Impedance Control and Temperature Control of Radiofrequency Interstitial Thermal Ablation for Treating Small Hepatocellular Carcinoma', *Oncology*, vol. 89, no. 1, pp. 47–52, 2015.

[115] D. J. Schutt and D. Haemmerich, 'Effects of variation in perfusion rates and of perfusion models in computational models of radio frequency tumor ablation: RF ablation perfusion model', *Med. Phys.*, vol. 35, no. 8, pp. 3462–3470, 2008.

[116] D. Haemmerich, L. Chachati, A. S. Wright, D. M. Mahvi, F. T. Lee, and J. G. Webster, 'Hepatic radiofrequency ablation with internally cooled probes: effect of coolant temperature on lesion size', *IEEE Trans. Biomed. Eng.*, vol. 50, no. 4, pp. 493–500, 2003.

[117] R. Lencioni *et al.*, 'Radio-frequency thermal ablation of liver metastases with a cooled-tip electrode needle: results of a pilot clinical trial', *Eur. Radiol.*, vol. 8, no. 7, pp. 1205–1211, 1998.

[118] M. Trujillo, J. Bon, M. José Rivera, F. Burdío, and E. Berjano, 'Computer modelling of an impedance-controlled pulsing protocol for RF tumour ablation with a cooled electrode', *Int. J. Hyperthermia*, vol. 32, no. 8, pp. 931–939, 2016.

[119] L. Solbiati *et al.*, 'Percutaneous US-guided radio-frequency tissue ablation of liver metastases: treatment and follow-up in 16 patients', *Radiology*, vol. 202, no. 1, pp. 195–203, 1997.

[120] T. Livraghi *et al.*, 'Sustained complete response and complications rates after radiofrequency ablation of very early hepatocellular carcinoma in cirrhosis: Is resection still the treatment of choice?', *Hepatology*, vol. 47, no. 1, pp. 82–89, 2007.

[121] G. Francica *et al.*, 'Radiofrequency and microwave ablation of subcapsular hepatocellular carcinoma accessed by direct puncture: Safety and efficacy', *Eur. J. Radiol.*, vol. 85, no. 4, pp. 739–743, 2016.

[122] T. A. Protretzke *et al.*, 'Microwave versus radiofrequency ablation treatment for hepatocellular carcinoma: a comparison of efficacy at a single center', *J. Vasc. Interv. Radiol.*, vol. 27, no. 5, pp. 631–638, 2016.

[123] L. Solbiati, M. Ahmed, L. Cova, T. Ierace, M. Brioschi, and S. N. Goldberg, 'Small Liver Colorectal Metastases Treated with Percutaneous Radiofrequency Ablation: Local Response Rate and Long-term Survival with Up to 10-year Follow-up', *Radiology*, vol. 265, no. 3, pp. 958–968, 2012.

[124] J. Faddoul *et al.*, 'Radiofrequency ablation of spinal osteoid osteoma: a prospective study', *J. Neurosurg. Spine*, vol. 26, no. 3, pp. 313–318, 2017.

[125] J. S. Lewin *et al.*, 'Phase II Clinical Trial of Interactive MR Imaging–guided Interstitial Radiofrequency Thermal Ablation of Primary Kidney Tumors: Initial Experience', *Radiology*, vol. 232, no. 3, pp. 835–845, 2004.

[126] M. Mendiratta-Lala *et al.*, 'Efficacy of Radiofrequency Ablation in the Treatment of Small Functional Adrenal Neoplasms', *Radiology*, vol. 258, no. 1, pp. 308–316, 2011.

[127] S. Y. Liu *et al.*, 'Radiofrequency ablation compared with laparoscopic adrenalectomy for aldosterone-producing adenoma', *Br. J. Surg.*, vol. 103, no. 11, pp. 1476–1486, 2016.

[128] R. Yang, L. Xu, H. Lian, W. Gan, and H. Guo, 'Retroperitoneoscopic-Guided Cool-Tip Radiofrequency Ablation of Adrenocortical Aldosteronoma', *J. Endourol.*, vol. 28, no. 10, pp. 1208–1214, 2014.

[129] A. Sarwar *et al.*, 'Clinical Outcomes following Percutaneous Radiofrequency Ablation of Unilateral Aldosterone-Producing Adenoma: Comparison with Adrenalectomy', *J. Vasc. Interv. Radiol.*, vol. 27, no. 7, pp. 961–967, 2016.

[130] D. Szejnfeld *et al.*, 'Radiofrequency Ablation of Functioning Adrenal Adenomas: Preliminary Clinical and Laboratory Findings', *J. Vasc. Interv. Radiol.*, vol. 26, no. 10, pp. 1459–1464, 2015.

[131] M.-H. Yang, Y.-S. Tyan, Y.-H. Huang, S.-C. Wang, and S.-L. Chen, 'Comparison of radiofrequency ablation versus laparoscopic adrenalectomy for benign aldosterone-producing adenoma', *Radiol. Med. (Torino)*, vol. 121, no. 10, pp. 811–819, 2016.

[132] D. Haemmerich and F. T. Lee, 'Multiple applicator approaches for radiofrequency and microwave ablation', *Int. J. Hyperthermia*, vol. 21, no. 2, pp. 93–106, 2005.

[133] C. L. Brace, 'Radiofrequency and Microwave Ablation of the Liver, Lung, Kidney, and Bone: What Are the Differences?', *Curr. Probl. Diagn. Radiol.*, vol. 38, no. 3, pp. 135–143, 2009.

[134] J. F. Sawicki, J. D. Shea, N. Behdad, and S. C. Hagness, 'The impact of frequency on the performance of microwave ablation', *Int. J. Hyperthermia*, vol. 33, no. 1, pp. 61–68, 2017.

[135] H. Fallahi, D. Clausing, A. Shahzad, M. O'Halloran, M. C. Dennedy, and P. Prakash, 'Microwave antennas for thermal ablation of benign adrenal adenomas', *Biomed. Phys. Eng. Express*, vol. 5, no. 2, p. 025044, 2019.

[136] J. Chiang, P. Wang, and C. L. Brace, 'Computational modelling of microwave tumour ablations', *Int. J. Hyperthermia*, vol. 29, no. 4, pp. 308–317, 2013.

[137] Y. Wang, Y. Sun, L. Feng, Y. Gao, X. Ni, and P. Liang, 'Internally cooled antenna for microwave ablation: Results in ex vivo and in vivo porcine livers', *Eur. J. Radiol.*, vol. 67, no. 2, pp. 357–361, 2008.

[138] M. Bedoya, A. M. del Rio, J. Chiang, and C. L. Brace, 'Microwave ablation energy delivery: Influence of power pulsing on ablation results in an *ex vivo* and *in vivo* liver model: Microwave ablation energy delivery', *Med. Phys.*, vol. 41, no. 12, p. 123301, 2014.

[139] A. U. Hines-Peralta *et al.*, 'Microwave Ablation: Results with a 2.45-GHz Applicator in ex Vivo Bovine and in Vivo Porcine Liver', *Radiology*, vol. 239, no. 1, pp. 94–102, 2006.

[140] M. G. Lubner, J. L. Hinshaw, A. Andreano, L. Sampson, F. T. Lee, and C. L. Brace, 'High-powered Microwave Ablation with a Small-gauge, Gas-cooled Antenna: Initial Ex Vivo and In Vivo Results', *J. Vasc. Interv. Radiol.*, vol. 23, no. 3, pp. 405–411, 2012.

[141] M. Cavagnaro, C. Amabile, S. Cassarino, N. Tosoratti, R. Pinto, and V. Lopresto, 'Influence of the target tissue size on the shape of *ex vivo* microwave ablation zones', *Int. J. Hyperthermia*, vol. 31, no. 1, pp. 48–57, 2015.

[142] M. Cavagnaro, R. Pinto, and V. Lopresto, 'Numerical models to evaluate the temperature increase induced by *ex vivo* microwave thermal ablation', *Phys. Med. Biol.*, vol. 60, no. 8, pp. 3287–3311, 2015.

[143] Z. Ji and C. L. Brace, 'Expanded modeling of temperature-dependent dielectric properties for microwave thermal ablation', *Phys. Med. Biol.*, vol. 56, no. 16, pp. 5249–5264, 2011.

[144] V. Lopresto, R. Pinto, G. A. Lovisolo, and M. Cavagnaro, 'Changes in the dielectric properties of ex vivo bovine liver during microwave thermal ablation at 2.45 GHz', *Phys. Med. Biol.*, vol. 57, no. 8, pp. 2309–2327, 2012.

[145] D. Yang, M. C. Converse, D. M. Mahvi, and J. G. Webster, 'Expanding the Bioheat Equation to Include Tissue Internal Water Evaporation During Heating', *IEEE Trans. Biomed. Eng.*, vol. 54, no. 8, pp. 1382–1388, 2007.

[146] G. Deshazer, D. Merck, M. Hagmann, D. E. Dupuy, and P. Prakash, 'Physical modeling of microwave ablation zone clinical margin variance: Modeling of microwave ablation zone clinical margin variance', *Med. Phys.*, vol. 43, no. 4, pp. 1764–1776, 2016.

[147] C. M. Sommer *et al.*, 'Effect of Tissue Perfusion on Microwave Ablation: Experimental in Vivo Study in Porcine Kidneys', *J. Vasc. Interv. Radiol.*, vol. 22, no. 12, pp. 1751–1757, 2011.

[148] X. He *et al.*, 'Investigation of the thermal and tissue injury behaviour in microwave thermal therapy using a porcine kidney model', *Int. J. Hyperthermia*, vol. 20, no. 6, pp. 567–593, 2004.

[149] L. S. Poulou, 'Percutaneous microwave ablation vs radiofrequency ablation in the treatment of hepatocellular carcinoma', *World J. Hepatol.*, vol. 7, no. 8, p. 1054, 2015.

[150] M. Solbiati *et al.*, 'A novel software platform for volumetric assessment of ablation completeness', *Int. J. Hyperthermia*, vol. 36, no. 1, pp. 336–342, 2019.

[151] W. Zhou *et al.*, 'Comparison of Ablation Zones among Different Tissues Using 2450-MHz Cooled-Shaft Microwave Antenna: Results in Ex Vivo Porcine Models', *PLoS ONE*, vol. 8, no. 8, pp. 1–7, 2013.

[152]   M. E. Klapperich *et al.*, 'Effect of Tumor Complexity and Technique on Efficacy and Complications after Percutaneous Microwave Ablation of Stage T1a Renal Cell Carcinoma: A Single-Center, Retrospective Study', *Radiology*, vol. 284, no. 1, pp. 272–280, 2017.

[153]   T. J. Vogl *et al.*, 'High-frequency versus low-frequency microwave ablation in malignant liver tumours: evaluation of local tumour control and survival', *Int. J. Hyperthermia*, vol. 32, no. 8, pp. 868–875, 2016.

[154]   M. Kostrzewa *et al.*, 'Microwave Ablation of Osteoid Osteomas Using Dynamic MR Imaging for Early Treatment Assessment: Preliminary Experience', *J. Vasc. Interv. Radiol.*, vol. 25, no. 1, pp. 106–111, 2014.

[155]   C. Prud'homme, J.-P. Nueffer, M. Runge, J. Dubut, B. Kastler, and S. Aubry, 'Prospective pilot study of CT-guided microwave ablation in the treatment of osteoid osteomas', *Skeletal Radiol.*, vol. 46, no. 3, pp. 315–323, 2017.

[156]   T. J. Vogl *et al.*, 'Microwave ablation of pancreatic tumors', *Minim. Invasive Ther. Allied Technol.*, vol. 27, no. 1, pp. 33–40, 2018.

[157]   F. D'Amico *et al.*, *Microwave Thermal Ablation in an Unusual Case of Malignant and Locally Advanced Rare Tumor of Pancreas in ASA IV Old Male Patient and Literature Review*, vol. 2018. 2018, pp. 1–7.

[158]   X.-J. Cao, Z.-L. Zhao, Y. Wei, L.-L. Peng, Y. Li, and M.-A. Yu, 'Efficacy and safety of microwave ablation treatment for secondary hyperparathyroidism: systematic review and meta-analysis', *Int. J. Hyperthermia*, vol. 37, no. 1, pp. 316–323, 2020.

[159]   L. Zhuo *et al.*, 'US-guided Microwave Ablation of Hyperplastic Parathyroid Glands: Safety and Efficacy in Patients with End-Stage Renal Disease—A Pilot Study', *Radiology*, vol. 282, no. 2, pp. 576–584, 2017.

[160]   Y. Wang, P. Liang, X. Yu, Z. Cheng, J. Yu, and J. Dong, 'Ultrasound-guided percutaneous microwave ablation of adrenal metastasis: Preliminary results', *Int. J. Hyperthermia*, vol. 25, no. 6, pp. 455–461, 2009.

[161]   A. H. Ahmed, R. D. Gordon, N. Sukor, E. Pimenta, and M. Stowasser, 'Quality of Life in Patients with Bilateral Primary Aldosteronism before and during Treatment with Spironolactone and/or Amiloride, Including a Comparison with Our Previously Published Results in Those with Unilateral Disease Treated Surgically', *J. Clin. Endocrinol. Metab.*, vol. 96, no. 9, pp. 2904–2911, 2011.

[162]   C. Catena *et al.*, 'Long-Term Cardiac Effects of Adrenalectomy or Mineralocorticoid Antagonists in Patients With Primary Aldosteronism', *Hypertension*, vol. 50, no. 5, pp. 911–918, 2007.

[163]   G. P. Rossi *et al.*, 'Vascular Remodeling and Duration of Hypertension Predict Outcome of Adrenalectomy in Primary Aldosteronism Patients', *Hypertension*, vol. 51, no. 5, pp. 1366–1371, 2008.

[164] M. Murashima, S. O. Trerotola, D. L. Fraker, D. Han, R. R. Townsend, and D. L. Cohen, 'Adrenal Venous Sampling for Primary Aldosteronism and Clinical Outcomes After Unilateral Adrenalectomy: A Single-Center Experience', *J. Clin. Hypertens.*, vol. 11, no. 6, pp. 316–323, 2009.

[165] J. Waldmann *et al.*, 'Outcome of Surgery for Primary Hyperaldosteronism', *World J. Surg.*, vol. 35, no. 11, pp. 2422–2427, 2011.

[166] N. Sukor, R. D. Gordon, Y. K. Ku, M. Jones, and M. Stowasser, 'Role of Unilateral Adrenalectomy in Bilateral Primary Aldosteronism: A 22-Year Single Center Experience', *J. Clin. Endocrinol. Metab.*, vol. 94, no. 7, pp. 2437–2445, 2009.

[167] N. Sukor, C. Kogovsek, R. D. Gordon, D. Robson, and M. Stowasser, 'Improved Quality of Life, Blood Pressure, and Biochemical Status Following Laparoscopic Adrenalectomy for Unilateral Primary Aldosteronism', *J. Clin. Endocrinol. Metab.*, vol. 95, no. 3, pp. 1360–1364, 2010.

[168] E. Letavernier, S. Peyrard, L. Amar, F. Zinzindohoue, B. Fiquet, and P.-F. Plouin, 'Blood pressure outcome of adrenalectomy in patients with primary hyperaldosteronism with or without unilateral adenoma', *J. Hypertens.*, vol. 26, no. 9, pp. 1816–1823, 2008.

[169] A. M. Ierardi *et al.*, 'Outcomes following minimally invasive imagine-guided percutaneous ablation of adrenal glands', *Gland Surg.*, vol. 9, no. 3, pp. 859–866, 2020.

[170] K.-W. Liang, Y. Jahangiri, T.-F. Tsao, Y.-S. Tyan, and H.-H. Huang, 'Effectiveness of Thermal Ablation for Aldosterone-Producing Adrenal Adenoma: A Systematic Review and Meta-Analysis of Clinical and Biochemical Parameters', *J. Vasc. Interv. Radiol.*, vol. 30, no. 9, pp. 1335-1342.e1, 2019.

[171] D. H. Abbott and I. M. Bird, 'Nonhuman primates as models for human adrenal androgen production: Function and dysfunction', *Rev. Endocr. Metab. Disord.*, vol. 10, no. 1, pp. 33–42, Mar. 2009, doi: 10.1007/s11154-008-9099-8.

[172] L. O. Lerman *et al.*, 'Animal Models of Hypertension: A Scientific Statement From the American Heart Association', *Hypertension*, vol. 73, no. 6, 2019.

[173] P. C. Qian *et al.*, 'Transvascular Pacing of Aorticorenal Ganglia Provides a Testable Procedural Endpoint for Renal Artery Denervation', *JACC Cardiovasc. Interv.*, vol. 12, no. 12, pp. 1109–1120, 2019.

[174] C. N. May and J. A. Bednarik, 'Regional Hemodynamic and Endocrine Effects of Aldosterone and Cortisol in Conscious Sheep: Comparison With the Effects of Corticotropin', *Hypertension*, vol. 26, no. 2, pp. 294–300, 1995.

[175] S. C. Velaphi, K. Despain, T. Roy, and C. R. Rosenfeld, 'The Renin-Angiotensin System in Conscious Newborn Sheep: Metabolic Clearance Rate and Activity', *Pediatr. Res.*, vol. 61, no. 6, pp. 681–686, 2007.

[176] S. A. S. Tait, J. F. Tait, and J. P. Coghlan, 'The discovery, isolation and identification of aldosterone: reflections on emerging regulation and function', *Mol. Cell. Endocrinol.*, vol. 217, no. 1–2, pp. 1–21, 2004.

[177] P. M. Kistler *et al.*, 'Atrial electrical and structural abnormalities in an ovine model of chronic blood pressure elevation after prenatal corticosteroid exposure: implications for development of atrial fibrillation', *Eur. Heart J.*, vol. 27, no. 24, pp. 3045–3056, 2006.

[178] M. T. Rademaker, C. J. Charles, M. G. Nicholls, and A. M. Richards, 'Interactions of Enhanced Urocortin 2 and Mineralocorticoid Receptor Antagonism in Experimental Heart Failure', *Circ. Heart Fail.*, vol. 6, no. 4, pp. 825–832, 2013.

[179] A. J. Forhead, F. B. Pipkin, and A. L. Fowden, 'Effect of cortisol on blood pressure and the renin—angiotensin system in fetal sheep during late gestation', *J. Physiol.*, vol. 526, no. 1, pp. 167–176, 2000.

[180] R. K. Lingam *et al.*, 'CT of Primary Hyperaldosteronism (Conn's Syndrome): The Value of Measuring the Adrenal Gland', *Am. J. Roentgenol.*, vol. 181, no. 3, pp. 843–849, 2003.

[181] J. D. Barreiro-Vázquez, A. Barreiro-Lois, and M. Miranda, 'Ultrasonography of Normal Adrenal Glands in Adult Holstein–Friesian Cows: A Pilot Study', *Animals*, vol. 10, no. 7, p. 1171, 2020.

[182] A. La Gioia *et al.*, 'Open-Ended Coaxial Probe Technique for Dielectric Measurement of Biological Tissues: Challenges and Common Practices', *Diagnostics*, vol. 8, no. 2, p. 40, 2018.

[183] C. Gabriel, 'Compilation of the Dielectric Properties of Body Tissues at RF and Microwave Frequencies.', Defense Technical Information Center, Fort Belvoir, VA, 1996.

[184] H. P. Kok *et al.*, 'Heating technology for malignant tumors: a review', *Int. J. Hyperthermia*, vol. 37, no. 1, pp. 711–741, 2020.

[185] M. Lazebnik *et al.*, 'A large-scale study of the ultrawideband microwave dielectric properties of normal breast tissue obtained from reduction surgeries', *Phys. Med. Biol.*, vol. 52, no. 10, pp. 2637–2656, 2007.

[186] L. Abdilla, C. Sammut, and L. Z. Mangion, 'Dielectric properties of muscle and liver from 500 MHz–40 GHz', *Electromagn. Biol. Med.*, vol. 32, no. 2, pp. 244–252, 2013.

[187] P. M. Meaney, T. Zhou, D. Goodwin, A. Golnabi, E. A. Attardo, and K. D. Paulsen, 'Bone Dielectric Property Variation as a Function of Mineralization at Microwave Frequencies', *Int. J. Biomed. Imaging*, vol. 2012, pp. 1–9, 2012.

[188] A. P. O'Rourke *et al.*, 'Dielectric properties of human normal, malignant and cirrhotic liver tissue: *in vivo* and *ex vivo* measurements from 0.5 to 20 GHz using a precision open-ended coaxial probe', *Phys. Med. Biol.*, vol. 52, no. 15, pp. 4707–4719, 2007.

[189] A. Martellosio *et al.*, 'Dielectric Properties Characterization From 0.5 to 50 GHz of Breast Cancer Tissues', *IEEE Trans. Microw. Theory Tech.*, vol. 65, no. 3, pp. 998–1011, 2017.

[190] V. Lopresto, R. Pinto, L. Farina, and M. Cavagnaro, 'Microwave thermal ablation: Effects of tissue properties variations on predictive models for treatment planning', *Med. Eng. Phys.*, vol. 46, pp. 63–70, 2017.

[191] H. Fallahi, J. Sebek, and P. Prakash, 'Broadband Dielectric Properties of *Ex Vivo* Bovine Liver Tissue Characterized at Ablative Temperatures', *IEEE Trans. Biomed. Eng.*, vol. 68, no. 1, pp. 90–98, 2021.

[192] A. Peyman and C. Gabriel, 'Dielectric properties of porcine glands, gonads and body fluids', *Phys. Med. Biol.*, vol. 57, no. 19, pp. 339–344, 2012.

[193] A. Shahzad, D. Clausing, P. Prakash, M. C. Dennedy, and M. O'Halloran, 'Broadband dielectric properties of adrenal gland for accurate anatomical modelling in medical applications', in *2017 International Conference on Electromagnetics in Advanced Applications (ICEAA)*, Verona, Italy, 2017, pp. 1465–1468.

[194] A. J. Conley, M. A. Kaminski, S. A. Dubowsky, A. Jablonka-Shariff, D. A. Redmer, and L. P. Reynolds, 'Immunohistochemical Localization of 301-Hydroxysteroid Dehydrogenase and P450 17a-Hydroxylase during Follicular and Luteal Development in Pigs, Sheep, and Cows'', *Biol. Reprod.*, vol. 52, pp. 1081–1094, 1995.

[195] Keysight Technologies, 'Basics of Measuring the Dielectric Properties of Materials'. 2017.

[196] K. Raghavan *et al.*, 'Electrical Conductivity and Permittivity of Murine Myocardium', *IEEE Trans. Biomed. Eng.*, vol. 56, no. 8, pp. 2044–2053, 2009.

[197] S. Curto, M. Taj-Eldin, D. Fairchild, and P. Prakash, 'Microwave ablation at 915 MHz vs 2.45 GHz: A theoretical and experimental investigation', *Med. Phys.*, vol. 42, no. 11, pp. 6152–6161, 2015.

[198] A. L. Gioia, E. Porter, and M. O'Halloran, 'Examination of the sensing radius of open-ended coaxial probes in dielectric measurements of biological tissues', in *2017 IEEE International Symposium on Antennas and Propagation & USNC/URSI National Radio Science Meeting*, San Diego, CA, USA, 2017, pp. 215–216.

[199] P. M. Meaney, A. P. Gregory, J. Seppala, and T. Lahtinen, 'Open-Ended Coaxial Dielectric Probe Effective Penetration Depth Determination', *IEEE Trans. Microw. Theory Tech.*, pp. 1–9, 2016.

[200] C. Gabriel and A. Peyman, 'Dielectric measurement: error analysis and assessment of uncertainty', *Phys. Med. Biol.*, vol. 51, no. 23, pp. 6033–6046, 2006.

[201] P. De Langhe, K. Blomme, L. Martens, and D. De Zutter, 'Measurement of low-permittivity materials based on a spectral-domain analysis for the open-ended coaxial probe', *IEEE Trans. Instrum. Meas.*, vol. 42, no. 5, pp. 879–886, 1993.

[202]   M. Lazebnik, M. C. Converse, J. H. Booske, and S. C. Hagness, 'Ultrawideband temperature-dependent dielectric properties of animal liver tissue in the microwave frequency range', *Phys. Med. Biol.*, vol. 51, no. 7, pp. 1941–1955, 2006.

[203]   C. L. Brace, 'Temperature-dependent dielectric properties of liver tissue measured during thermal ablation: Toward an improved numerical model', in *2008 30th Annual International Conference of the IEEE Engineering in Medicine and Biology Society*, Vancouver, BC, Aug. 2008, pp. 230–233.

[204]   A. Peyman, C. Gabriel, and E. H. Grant, 'Complex permittivity of sodium chloride solutions at microwave frequencies', *Bioelectromagnetics*, vol. 28, no. 4, pp. 264–274, 2007.

[205]   A. Stogryn, 'Equations for Calculating the Dielectric Constant of Saline Water', *IEEE Trans. Microw. Theory Tech.*, vol. 19, no. 8, pp. 733–736, 1971.

[206]   R. Buchner, G. T. Hefter, and P. M. May, 'Dielectric Relaxation of Aqueous NaCl Solutions', *J. Phys. Chem. A*, vol. 103, no. 1, pp. 1–9, 1999.

[207]   B. N. Taylor and C. E. Kuyatt, 'Guidelines for Evaluating and Expressing the Uncertainty of NIST Measurement Results'. US Department of Commerce, Technology Administration, National Institute of Standards and Technology: Gaithersburg, MD, USA, 1994.

[208]   S. Salahuddin, E. Porter, F. Krewer, and M. O' Halloran, 'Optimised analytical models of the dielectric properties of biological tissue', *Med. Eng. Phys.*, vol. 43, pp. 103–111, 2017.

[209]   M. Lazebnik, M. Okoniewski, J. H. Booske, and S. C. Hagness, 'Highly Accurate Debye Models for Normal and Malignant Breast Tissue Dielectric Properties at Microwave Frequencies', *IEEE Microw. Wirel. Compon. Lett.*, vol. 17, no. 12, pp. 822–824, 2007.

[210]   H. P. Schwan and K. R. Foster, 'RF-field interactions with biological systems: Electrical properties and biophysical mechanisms', *Proc. IEEE*, vol. 68, no. 1, pp. 104–113, 1980.

[211]   R. Irastorza, M. Mayosky, J. Grigera, and F. Vericat, 'Dielectric properties of natural and demineralized collagen bone matrix', *IEEE Trans. Dielectr. Electr. Insul.*, vol. 18, no. 1, pp. 320–328, 2011.

[212]   J. J. Park, B. K. Park, and C. K. Kim, 'Adrenal imaging for adenoma characterization: imaging features, diagnostic accuracies and differential diagnoses', *Br. J. Radiol.*, vol. 89, no. 1062, pp. 1018–1031, 2016.

[213]   A. K. Lam, 'Update on Adrenal Tumours in 2017 World Health Organization (WHO) of Endocrine Tumours', *Endocr. Pathol.*, vol. 28, no. 3, pp. 213–227, Sep. 2017, doi: 10.1007/s12022-017-9484-5.

[214]   G. W. Boland, M. J. Lee, G. S. Gazelle, E. F. Halpern, M. M. McNicholas, and P. R. Mueller, 'Characterization of adrenal masses using unenhanced CT: an analysis of the CT literature.', p. 4, 1998.

[215] M. Taffel, S. Haji-Momenian, P. Nikolaidis, and F. H. Miller, 'Adrenal Imaging: A Comprehensive Review', *Radiol. Clin. North Am.*, vol. 50, no. 2, pp. 219–243, 2012.

[216] L. Yip *et al.*, 'The Adrenal Mass: Correlation of Histopathology with Imaging', *Ann. Surg. Oncol.*, vol. 17, no. 3, pp. 846–852, 2010.

[217] L. M. Gruber *et al.*, 'Not all adrenal incidentalomas require biochemical testing to exclude pheochromocytoma: Mayo clinic experience and a meta- analysis', *Gland Surg.*, vol. 9, no. 2, pp. 362–371, 2020.

[218] J. M. Seo, B. K. Park, S. Y. Park, and C. K. Kim, 'Characterization of Lipid-Poor Adrenal Adenoma: Chemical-Shift MRI and Washout CT', *Am. J. Roentgenol.*, vol. 202, no. 5, pp. 1043–1050, 2014.

[219] C. S. Peña, G. W. L. Boland, P. F. Hahn, M. J. Lee, and P. R. Mueller, 'Characterization of Indeterminate (Lipid-poor) Adrenal Masses: Use of Washout Characteristics at Contrast-enhanced CT', *Radiology*, vol. 217, no. 3, pp. 798–802, 2000.

[220] M. G. Elbanan *et al.*, 'Adrenal cortical adenoma: current update, imaging features, atypical findings, and mimics', *Abdom. Radiol.*, vol. 45, no. 4, pp. 905–916, 2020.

[221] V. Lopresto, R. Pinto, L. Farina, and M. Cavagnaro, 'Treatment planning in microwave thermal ablation: clinical gaps and recent research advances', *Int. J. Hyperthermia*, vol. 33, no. 1, pp. 83–100, 2017.

[222] P. Prakash, 'Theoretical Modeling for Hepatic Microwave Ablation', *Open Biomed. Eng. J.*, vol. 4, p. 12, 2010.

[223] V. Lopresto, R. Pinto, R. Lodato, G. A. Lovisolo, and M. Cavagnaro, 'Design and realisation of tissue-equivalent dielectric simulators for dosimetric studies on microwave antennas for interstitial ablation', *Phys. Med.*, vol. 28, no. 3, pp. 245–253, 2012.

[224] J. C. Lin, *Electromagnetic Fields in Biological Systems*. Boca Raton, FL: CRC Press, 2012.

[225] C. A. Balanis, *Antenna theory: analysis and design*, 3rd ed. Hoboken, NJ: John Wiley, 2005.

[226] F. S. Barnes and B. Greenebaum, *Biological and Medical Aspects of Electromagnetic Fields*, 3rd ed. Boca Raton, FL: Taylor and Francis Group LLC, 2007.

[227] J. C. Lin, P. Bernardi, S. Pisa, M. Cavagnaro, and E. Piuzzi, 'Antennas for Medical Therapy and Diagnostics', in *Modern Antenna Handbook*, Hoboken, NJ: John Wiley & Sons, 2008, pp. 1377–1428.

[228] C. Furse, C. H. Durney, and D. A. Christensen, *Basic introduction to bioelectromagnetics*, 2nd ed. Boca Raton, FL: CRC Press, 2009.

[229] C. Rossmann and D. Haemmerich, 'Review of Temperature Dependence of Thermal Properties, Dielectric Properties, and Perfusion of Biological Tissues at Hyperthermic and Ablation Temperatures', *Crit. Rev. Biomed. Eng.*, vol. 42, no. 6, pp. 467–492, 2014.

[230] H. H. Pennes, 'Analysis of Tissue and Arterid Blood Temperatures', *J. Appl. Physiol.*, vol. 1, no. 2, pp. 93–122, 1948.

[231] G. Deshazer, P. Prakash, D. Merck, and D. Haemmerich, 'Experimental measurement of microwave ablation heating pattern and comparison to computer simulations', *Int. J. Hyperthermia*, vol. 33, no. 1, pp. 74–82, 2017.

[232] M. Clemens and T. Weil, 'Discrete Electromagnetism with the Finite Integration Technique', *Prog. Electromagn. Res.*, vol. 32, pp. 65–87, 2001.

[233] CST-Computer Simulation Technology, 'Workflow & Solver Overview'. 2010.

[234] T. L. Bergman and A. S. Lavine, *Fundamentals of heat and mass transfer*, 8th ed. Hoboken, NJ: John Wiley & Sons, 2017.

[235] K. A. Simo *et al.*, 'Microwave ablation using 915-MHz and 2.45-GHz systems: what are the differences?', *HPB*, vol. 15, no. 12, pp. 991–996, 2013.

[236] S. Pisa, M. Cavagnaro, P. Bernardi, and J. C. Lin, 'A 915-MHz antenna for microwave thermal ablation treatment: physical design, computer modeling and experimental measurement', *IEEE Trans. Biomed. Eng.*, vol. 48, no. 5, pp. 599–601, 2001.

[237] M. Cavagnaro, C. Amabile, P. Bernardi, S. Pisa, and N. Tosoratti, 'A Minimally Invasive Antenna for Microwave Ablation Therapies: Design, Performances, and Experimental Assessment', *IEEE Trans. Biomed. Eng.*, vol. 58, no. 4, pp. 949–959, 2011.

[238] P. Prakash, G. Deng, M. C. Converse, J. G. Webster, D. M. Mahvi, and M. C. Ferris, 'Design optimization of a robust sleeve antenna for hepatic microwave ablation', *Phys. Med. Biol.*, vol. 53, no. 4, pp. 1057–1069, 2008.

[239] C. L. Brace, P. F. Laeseke, D. W. van der Weide, and F. T. Lee, 'Microwave ablation with a triaxial antenna: results in ex vivo bovine liver', *IEEE Trans. Microw. Theory Tech.*, vol. 53, no. 1, pp. 215–220, 2005.

[240] I. Longo, G. B. Gentili, M. Cerretelli, and N. Tosoratti, 'A coaxial antenna with miniaturized choke for minimally invasive interstitial heating', *IEEE Trans. Biomed. Eng.*, vol. 50, no. 1, pp. 82–88, 2003.

[241] P. Wang and C. L. Brace, 'Tissue Dielectric Measurement Using an Interstitial Dipole Antenna', *IEEE Trans. Biomed. Eng.*, vol. 59, no. 1, pp. 115–121, 2012.

[242] 'MICROWAVE & RF CABLE Semi-Rigid, hand-formable & flexible microwave cable'. Carlisle Interconnect Technologies, 2017.

[243] T. P. Ryan and C. L. Brace, 'Interstitial microwave treatment for cancer: historical basis and current techniques in antenna design and performance', *Int. J. Hyperthermia*, vol. 33, no. 1, pp. 3–14, 2017.

[244] S. J. S. Ruiter, W. J. Heerink, and K. P. de Jong, 'Liver microwave ablation: a systematic review of various FDA-approved systems', *Eur. Radiol.*, vol. 29, no. 8, pp. 4026–4035, 2019.

[245] P. A. Hasgall *et al.*, 'IT'IS Database for thermal and electromagnetic parameters of biological tissues'. Version .0 2018. [Online]. Available: https://itis.swiss/virtual-population/tissue-properties/database/

[246] National Centre for Replacement Refinement & Reduction of animals in Research, 'The 3Rs'. https://nc3rs.org.uk/the-3rs

[247] B. T. McWilliams, E. E. Schnell, S. Curto, T. M. Fahrbach, and P. Prakash, 'A Directional Interstitial Antenna for Microwave Tissue Ablation: Theoretical and Experimental Investigation', *IEEE Trans. Biomed. Eng.*, vol. 62, no. 9, pp. 2144–2150, 2015.

[248] L. Farina *et al.*, 'Characterisation of tissue shrinkage during microwave thermal ablation', *Int. J. Hyperthermia*, vol. 30, no. 7, pp. 419–428, 2014.

[249] L. Farina, Y. Nissenbaum, M. Cavagnaro, and S. N. Goldberg, 'Tissue shrinkage in microwave thermal ablation: comparison of three commercial devices', *Int. J. Hyperthermia*, vol. 34, no. 4, pp. 382–391, 2018.

[250] C. S. Park, C. Liu, S. K. Hall, and S. J. Payne, 'A thermoelastic deformation model of tissue contraction during thermal ablation', *Int. J. Hyperthermia*, vol. 34, no. 3, pp. 221–228, 2018.

[251] D. Liu and C. L. Brace, 'Numerical simulation of microwave ablation incorporating tissue contraction based on thermal dose', *Phys. Med. Biol.*, vol. 62, no. 6, pp. 2070–2086, 2017.

[252] S. N. Goldberg, G. S. Gazelle, and P. R. Mueller, 'Thermal Ablation Therapy for Focal Malignancy: A Unified Approach to Underlying Principles, Techniques, and Diagnostic Imaging Guidance', *Am. J. Roentgenol.*, vol. 174, no. 2, pp. 323–331, 2000.

[253] M. Mendiratta-Lala, A. Avram, A. F. Turcu, and N. R. Dunnick, 'Adrenal Imaging', *Endocrinol. Metab. Clin. North Am.*, vol. 46, no. 3, pp. 741–759, 2017.

[254] C. J. McCarthy, S. McDermott, and M. A. Blake, 'Adrenal Imaging: Magnetic Resonance Imaging and Computed Tomography', in *Frontiers of Hormone Research*, vol. 45, M. Buchfelder and F. Guaraldi, Eds. S. Karger AG, 2016, pp. 55–69.

[255] B. C. Allen and I. R. Francis, 'Adrenal Imaging and Intervention', *Radiol. Clin. North Am.*, vol. 53, no. 5, pp. 1021–1035, 2015.

[256] K. S. Suvarna, C. Layton, and J. D. Bancroft, *Bancroft's Theory and Practice of Histological Techniques*, 7th ed. Elsevier, 2013. doi: 10.1016/C2015-0-00143-5.

[257] D. J. Cook and P. J. Warren, *Cellular Pathology: an introduction to techniques and applications*, 3rd ed., vol. 64. Chatham, Kent, UK: Scion, 2015.

[258] J. Sebek, N. Albin, R. Bortel, B. Natarajan, and P. Prakash, 'Sensitivity of microwave ablation models to tissue biophysical properties: A first step toward probabilistic modeling and treatment planning: Sensitivity of microwave ablation models to tissue properties', *Med. Phys.*, vol. 43, no. 5, pp. 2649–2661, 2016.

[259] A. Bottiglieri *et al.*, 'Dielectric Characterization of Ex Vivo Ovine and Human Adrenal Glands for Microwave Thermal Ablation Applications', *IEEE J. Electromagn. RF Microw. Med. Biol.*, vol. 5, no. 3, pp. 254–261, 2021.

[260] M. W. Dewhirst, B. L. Viglianti, M. Lora-Michiels, M. Hanson, and P. J. Hoopes, 'Basic principles of thermal dosimetry and thermal thresholds for tissue damage from hyperthermia', *Int. J. Hyperthermia*, vol. 19, no. 3, pp. 267–294, 2003.

[261] J. Dong *et al.*, 'Dynamic imaging and pathological changes in pig liver after MR-guided microwave ablation', *BMC Cancer*, vol. 18, no. 1, pp. 397–408, 2018.

[262] P. T. Donlon *et al.*, 'Using microwave thermal ablation to develop a subtotal, cortical-sparing approach to the management of primary aldosteronism', *Int. J. Hyperthermia*, vol. 36, no. 1, pp. 904–913, 2019.

[263] A. L. Mescher, *Junqueira's basic histology: text and atlas*, 13th ed. McGraw-Hill, 2013.

[264] J. Chiang *et al.*, 'Effects of Microwave Ablation on Arterial and Venous Vasculature after Treatment of Hepatocellular Carcinoma', *Radiology*, vol. 281, no. 2, pp. 617–624, 2016.

[265] R. L. Mcintosh and V. Anderson, 'A comprehensive tissue properties database provided for the thermal assessment of a human at rest', *Biophys. Rev. Lett.*, vol. 5, no. 3, pp. 129–151, 2010.

[266] Z. Liu, M. Ahmed, A. Sabir, S. Humphries, and S. N. Goldberg, 'Computer modeling of the effect of perfusion on heating patterns in radiofrequency tumor ablation', *Int. J. Hyperthermia*, vol. 23, no. 1, pp. 49–58, 2007.

[267] Y. J. Liu, A. K. Qiao, Q. Nan, and X. Y. Yang, 'Thermal characteristics of microwave ablation in the vicinity of an arterial bifurcation', *Int. J. Hyperthermia*, vol. 22, no. 6, pp. 491–506, 2006.

[268] D. T. Tompkinsn *et al.*, 'Temperature-dependent versus constant-rate blood perfusion modelling in ferromagnetic thermoseed hyperthermia: results with a model of the human prostate', *Int. J. Hyperthermia*, vol. 10, no. 4, pp. 517–536, 1994.

[269] W. T. Joines, 'Frequency-Dependent Absorption of Electromagnetic Energy in Biological Tissue', *IEEE Trans. Biomed. Eng.*, vol. 31, no. 1, pp. 17–20, 1984.

[270] W. Franco, A. Kothare, S. J. Ronan, R. C. Grekin, and T. H. McCalmont, 'Hyperthermic injury to adipocyte cells by selective heating of subcutaneous fat with a novel radiofrequency device: Feasibility studies', *Lasers Surg. Med.*, vol. 42, no. 5, pp. 361–370, 2010.

[271] G. A. Carberry *et al.*, 'Pulmonary Microwave Ablation Near the Heart: Antenna Positioning Can Mitigate Cardiac Complications in a Porcine Model', *Radiology*, vol. 282, no. 3, pp. 892–902, 2017.

[272] N. Bhardwaj, A. D. Strickland, F. Ahmad, L. Atanesyan, K. West, and D. M. Lloyd, 'A comparative histological evaluation of the ablations produced by microwave, cryotherapy and radiofrequency in the liver', *Pathology (Phila.)*, vol. 41, no. 2, pp. 168–172, 2009.

[273] K. L. Moore, A. F. Dalley, and A. M. R. Agur, *Clinically Oriented Anatomy*, 8th ed. Philadelphia, PA: Wolters Kluwer, 2018.

[274] S. S. Pearlstein, J. H. Kuo, J. A. Chabot, and J. A. Lee, 'Periadrenal Volume is a Better Predictor of Prolonged Operative Time in Laparoscopic Retroperitoneal Adrenalectomy than BMI', *World J. Surg.*, vol. 44, no. 2, pp. 578–584, 2020.

[275] O. Agcaoglu, D. A. Sahin, A. Siperstein, and E. Berber, 'Selection algorithm for posterior versus lateral approach in laparoscopic adrenalectomy', *Surgery*, vol. 151, no. 5, pp. 731–735, 2012.

[276] D. T. Nguyen, M. Zipse, R. T. Borne, L. Zheng, W. S. Tzou, and W. H. Sauer, 'Use of Tissue Electric and Ultrasound Characteristics to Predict and Prevent Steam-Generated Cavitation During High-Power Radiofrequency Ablation', *JACC Clin. Electrophysiol.*, vol. 4, no. 4, pp. 491–500, 2018.

Appendix A

Performances of ablation procedures and gold standard techniques in the management of PA

This review compares the performances of both gold standard therapeutic techniques (LA and MRAs pharmacotherapy) and emerging approaches (i.e. ablation therapies) for the treatment of PA. As extensively discussed in Chapter 2, emerging ablation therapies are recently investigated for the treatment of PA to overcome the limitations presented by the gold standard techniques.

The main purpose of this apperndix is to have an overview of the most recent results in terms of performances of the ablation techniques compared with the gold standard techniques. Also, the results gathered from different studies help to observe if ablation techniques may have advantages upon the traditional techniques in the management of hypertension caused by unilateral adenoma or bilateral hyperplasia.

A.1 Methodology

The studies were selected based on the following criteria:

a) Type of diagnosis (APA and/or BIH);

b) Type of treatment, "emerging" (RFA, MWA, cryoablation or chemical ablation/chemo-embolisation), or "gold standard" (adrenalectomy, or mineralocorticoid antagonists);

c) Report of pre- and post-treatment clinical (i.e. SBP and DBP) or biochemical parameters (i.e. PRA, PAC, ARR, bK).

Only clinical studies targeting PA are considered. Publications dedicated to animal studies, review articles, studies reporting only malignant adrenal tumours, such as pheochromocytoma or metastasis, were not included.

A total of 21 studies were selected. For a better comparison, the studies were categorised in two different groups (Group 1 and Group 2) in accordance with the treatment approach

adopted. Group 1 aggregates in total 12 studies related to the therapeutic techniques currently used in the clinical practice (LA: 10 studies, MRAs-based treatment: 2 studies). Group 2 includes in total 9 studies that investigate the performances of ablation techniques (RFA: 6 studies, cryoablation: 1 study, MWA: 1 study, transcatheter chemoembolisation: 1 study).

Table A.1 lists the available characteristics of the studies including the author's name, PA subtype (i.e. APA or BIH), number of patients, mean duration of the follow-up, size of the lesion, treatment technique and related outcomes. The outcomes are evaluated based on the values of blood pressure and biochemical parameters. Three studies [129], [131], [162] were reported two times. In these studies, two different cohorts of patients were treated using two different clinical approaches. In particular, in [162] two groups of patients were treated separately by LA and MRAs. Both in [131] and [129], one group of patients was treated via CT-guided RFA, whereas LA was adopted for the other group of patients.

Mean and standard deviation of clinical and/or biochemical parameters measured before and after a specific treatment were reported for each study. Paired t-tests were conducted to determine the change in the mean values of the clinical and/or biochemical parameters for the sample of patients. Two-tailed P values < 0.05 was considered statistically significant. The post-treatment change for blood pressure (SBP and DBP) and biochemical parameters (PAC, PRA, ARR, bK) are reported in the following section for each study reviewed.

Finally, the percentage of patients reporting the resolution of the hypertension and the percentage of those showing improvements from the hypertension were extracted from the studies of Group 1 and Group 2.

A.2 Results

Figures (Fig A.1 – A.6) show mean, standard deviation values and the calculated post-treatment change in the clinical and biochemical parameters measured before and after the specific treatment.

The values of blood pressure were reported in 20 out 21 studies included in this review

Table A.1: Summary of the main characteristics of the studies included in the review: study name, PA subtype, number of patients, mean time to follow-up (in months), maximum size of the adenoma (in cm) and type of the treatment. The availability (A) or not-availability (NA) of the outcomes of both clinical (BP) and biochemical parameters (PAC, PRA, ARR, bK) is reported for each study. APA: aldosterone-producing adenoma, ARR: aldosterone-to-renin ratio (ng dL^{-1} ng^{-1} mL h); BIH: bilateral idiopathic hyperplasia, bK (mmol L^{-1}): blood potassium concentration, SBP: systolic blood pressure (mmHg), DBP: diastolic blood pressure, CA: cryoablation, CT: computer tomography, LA: laparoscopic adrenalectomy, MRA: mineralocorticoids antagonists, MWA: microwave ablation, PRA: plasma renin activity (ng mL^{-1} h^{-1}), RFA: radiofrequency ablation, PAC: plasma aldosterone concentration (ng dL^{-1}), TACE: transcatheter arterial chemo-embolisation.

Study [Ref.]	PA subtype	Patients #	Mean Follow-up (months)	Max. size lesion (cm)	Treatment Technique	Reported Outcomes				
						SBP/ DBP	PAC	PRA	ARR	bK
Group 1: LA or MRAs-based treatments										
[161]	BIH	21	6.0	NA	MRA	A	A	A	A	A
[162]	APA	24	76.8	NA	LA	A	A	A	NA	NA
[162]	APA	30	76.8	NA	MRA	A	A	A	NA	NA
[168]	APA	109	9.0	NA	LA	A	NA	NA	NA	A
[163]	APA	50	32.8	1.8	LA	A	A	A	A	A
[164]	APA	56	9.4	NA	LA	A	NA	NA	NA	A
[165]	APA	54	49.0	3.0	LA	A	NA	NA	NA	A
[72]	APA	47	12.0	3.0	LA	A	A	NA	A	A
[131]	APA	13	3.0	2.5	LA	A	A	NA	NA	A
[129]	APA	32	11.5	4.0	LA	A	NA	NA	NA	A
[166]	BIH	40	56.4	NA	LA	A	A	A	A	A
[167]	APA	22	6.0	2.5	LA	A	A	A	A	A
Group 2: Ablation techniques										
[99]	APA	10	19.1	1.9	TACE	A	A	NA	NA	NA
[126]	APA	10	41.4	3.2	CT-guided RFA	A	A	A	NA	A
[127]	APA	36	74.4	2.5	CT-guided RFA	A	A	NA	A	A
[131]	APA	7	3.0	2.5	CT-guided RFA	A	A	NA	NA	A
[129]	APA	12	11.5	4.0	CT-guided RFA	A	NA	NA	NA	A
[130]	APA	9	3.0	3.0	CT-guided RFA	A	A	A	A	A
[128]	APA	12	49.2	3.0	Scope RFA	A	NA	NA	A	NA
[104]	APA	11	12.0	5.0	CT-guided CA	A	A	A	NA	A
[19]	APA	3	24.0	5.0	CT-guided MWA	NA	A	A	NA	A
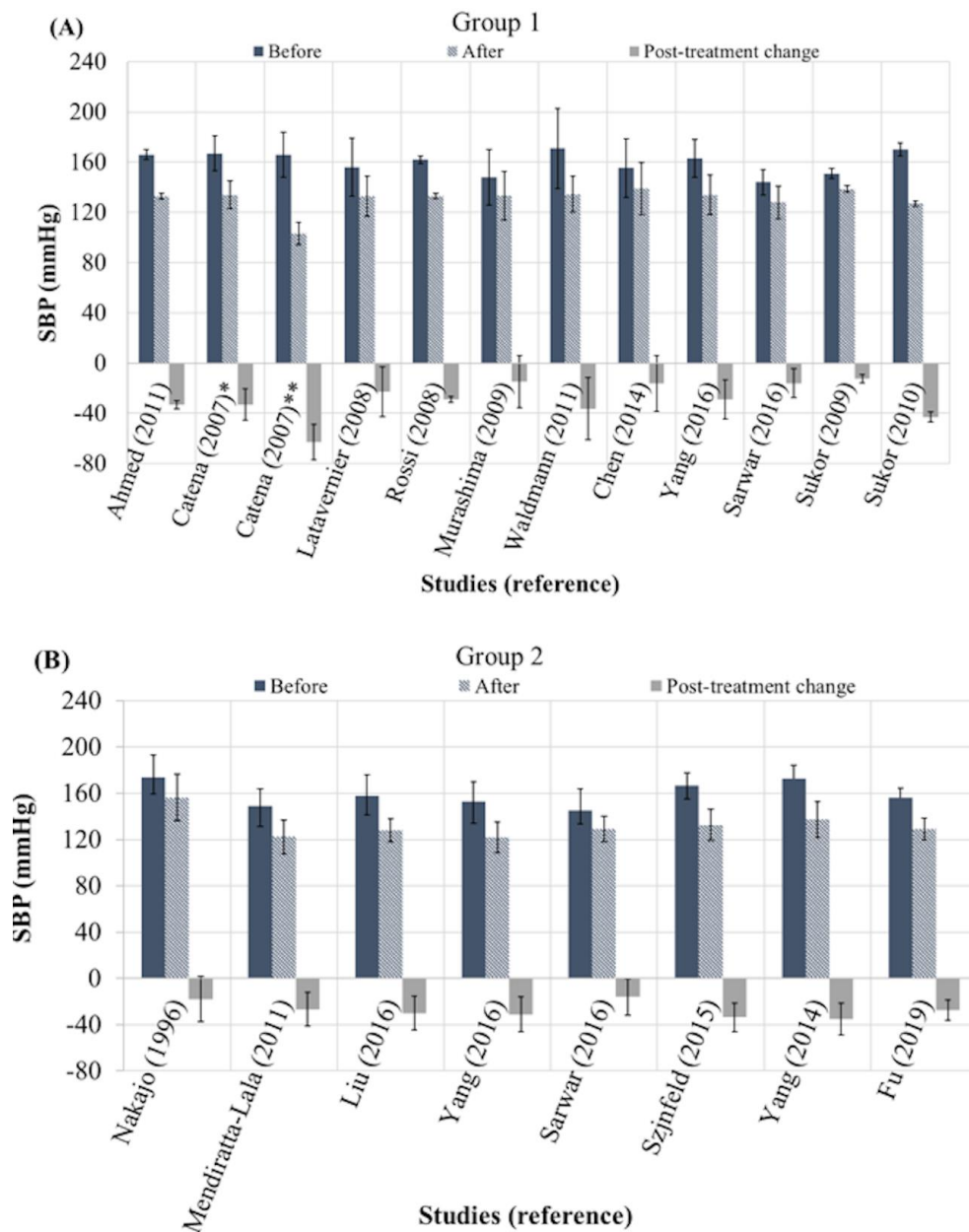
Figure A.1: Mean and standard deviations values of SBP data reported in 11 studies before and after LA or MRAs administration and related effect size (A); Mean and standard deviations values of SBP data reported in 8 studies before and after the ablation treatments and related effect size (A). SBP: systolic blood pressure, LA: laparoscopic adrenalectomy, MRA: mineralcorticoid antagonists.

(Group 1: 12 studies, Group 2: 8 studies). Only [19] presented a lack in the blood pressure values, thus it was excluded from the comparison in terms of clinical parameters. Figures A.1 – A.2 show mean and standard deviation values of systolic blood pressure (A) and
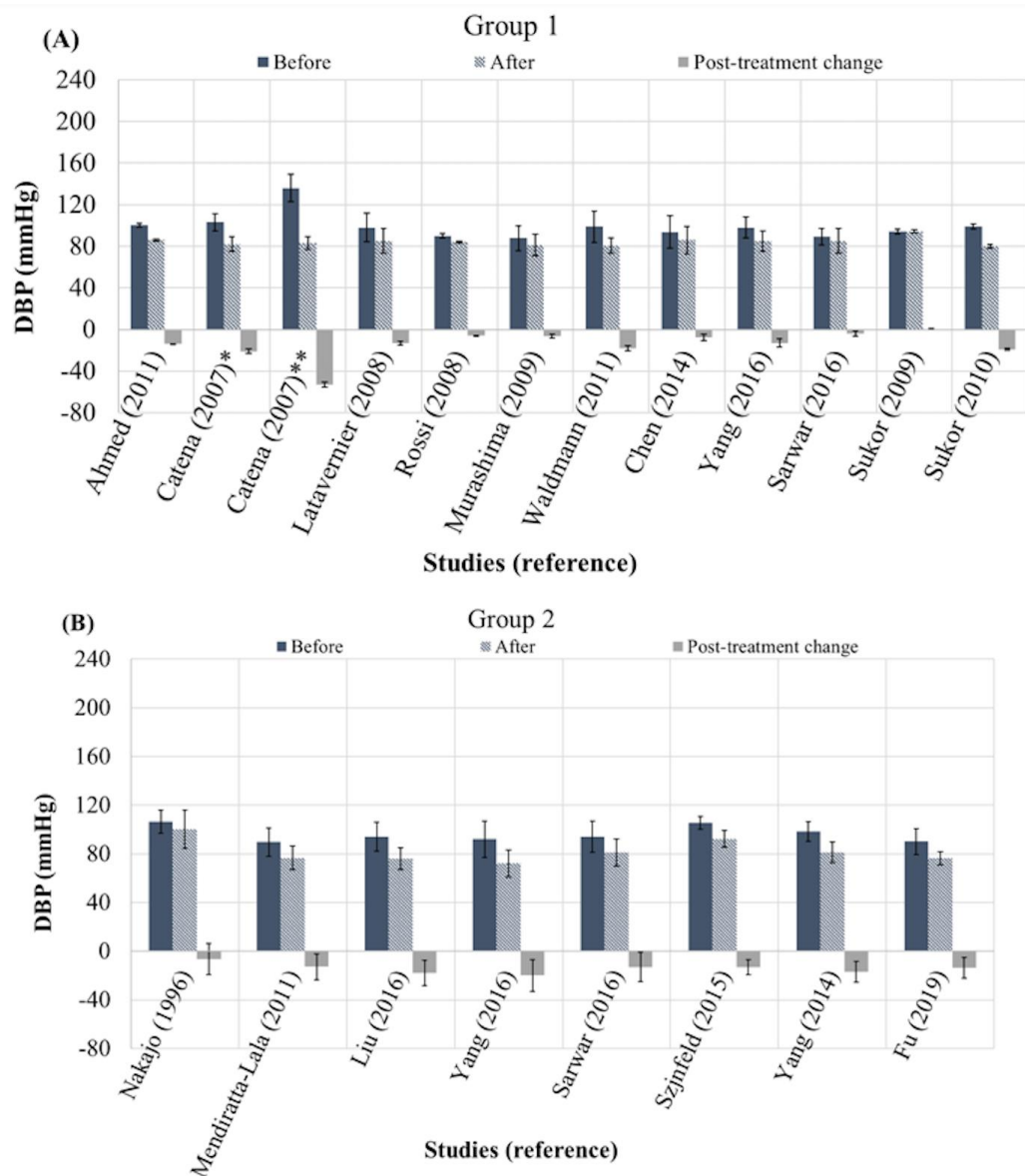
Figure A.2: Mean and standard deviations values of DBP (mmHg) data reported in 11 studies before and after LA or MRAs administration and related effect size (B); Mean and standard deviations values of DBP data reported in 8 studies before and after the ablation treatments and related effect size (A). DBP: diastolic blood pressure, LA: laparoscopic adrenalectomy, MRA: mineralocorticoid antagonists.

diastolic blood pressure (B) before and after the treatment. In particular, Figure A.1 and Figure A.2 show the clinical values (SBP and DBP) related to Group 1 and Group 2, respectively. The averages calculated across the pre-treatment SBP and DBP values are respectively 159.9 ± 14.5 mmHg and 98.9 ± 8.7 mmHg for Group 1, and 159.3 ± 14.8

mmHg and 96.2 ± 10.6 mmHg for Group 2. The average values of SBP and DBP post-treatment are respectively 130.8 ± 10.7 and 84.4 ± 6.9 mmHg for Group 1, whereas 132.1 ± 2.0 mmHg (SBP) and 82.0 ± 9.7 mmHg (DBP) for the Group 2. The overall post-treatment changes reported in SBP and DPB are -29.1 ± 14.4 mmHg and -14.6 ± 13.8 mmHg for the Group 1 -27.2 ± 7.0 mmHg (SBP) and -14.3 ± 4.2 mmHg (DBP) for the Group 2.
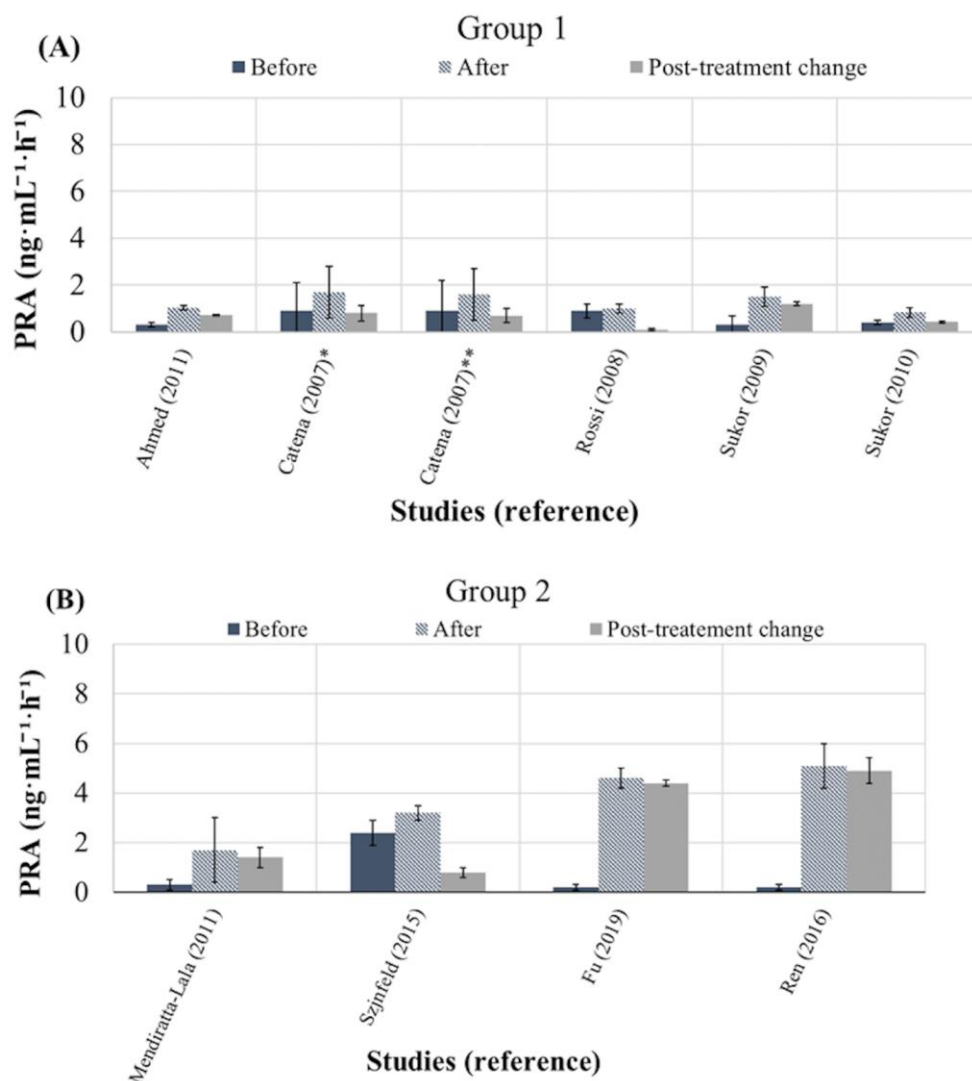

Figure A.3: Mean and standard deviations values of PRA (ng·mL-1·h-1) data reported in 5 studies before and after LA or MRAs administration and related effect size (A); Mean and standard deviations values of PRA data reported in 4 studies before and after the ablation treatments and related effect size (B). PRA: plasma renin activity, LA: laparoscopic adrenalectomy, MRA: mineralocorticoid antagonists.

The available mean and standard deviation values related to the biochemical parameters (i.e. PRA, PAC, ARR and bK) measured before and after the treatment are reported in Figure A.3 – A.6. Figure A.3, Figure A.4, Figure A.5, show the parameters describing the regulation of the renin-angiotensin system. In particular, the pre-treatment and post-treatment levels of renin suppression indicated by PRA ($ng \cdot mL^{-1} \cdot h^{-1}$) are shown in Figure A.3. The values corresponding to 6 studies for the Group 1 and 4 studies for the Group 2 are presented. The average PRA pre-treatment values are 0.6 ± 0.6 $ng \cdot mL^{-1} \cdot h^{-1}$ for Group 1 and 0.8 ± 0.2 $ng \cdot mL^{-1} \cdot h^{-1}$ for Group 2; while the average PRA post-treatment values are 1.3 ± 0.5 $ng \cdot mL^{-1} \cdot h^{-1}$ for Group 1 and 3.7 ± 0.7 $ng \cdot mL^{-1} \cdot h^{-1}$ for Group 2. The
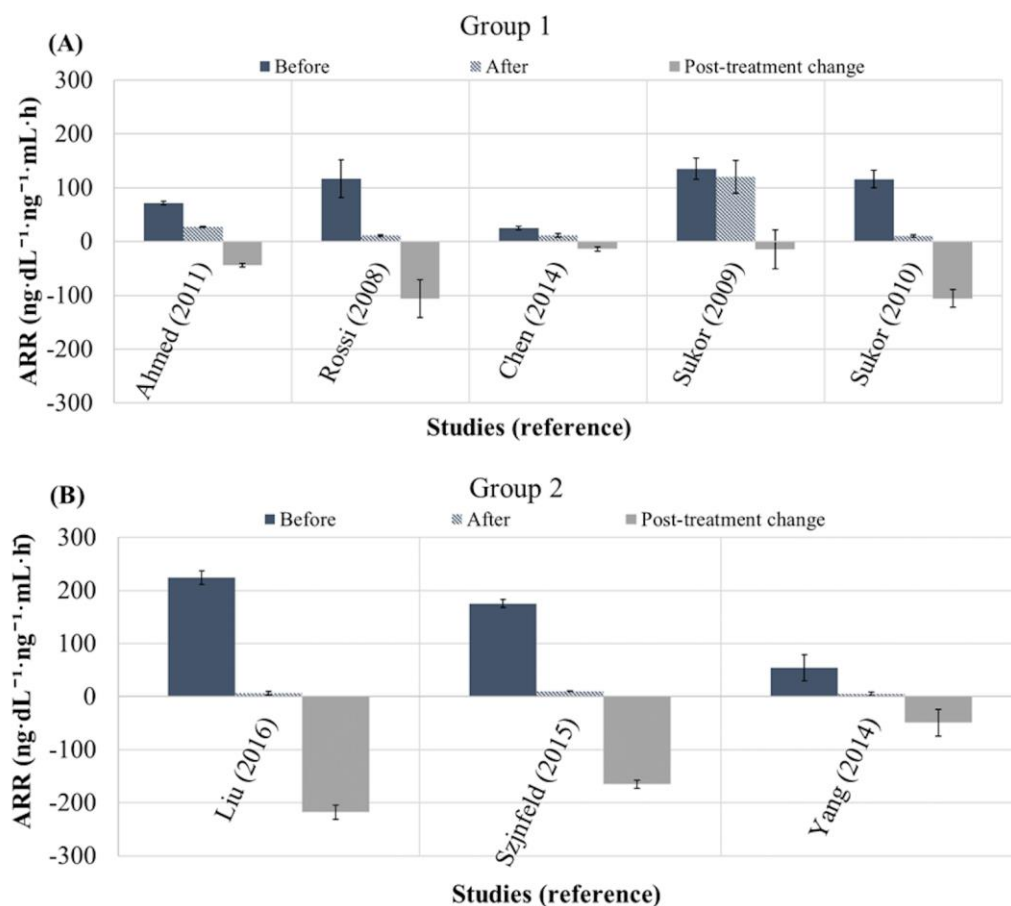
Figure A.4: Mean and standard deviations values of ARR (ng·dL-1·ng-1·mL·h) data reported in 5 studies before and after LA or MRAs administration and related effect size (A); mean and standard deviations values of ARR data reported in 3 studies before and after the ablation treatments and related effect size (B). ARR: aldosterone-to-renin ratio, LA: laparoscopic adrenalectomy, MRA: mineralocorticoid antagonists.
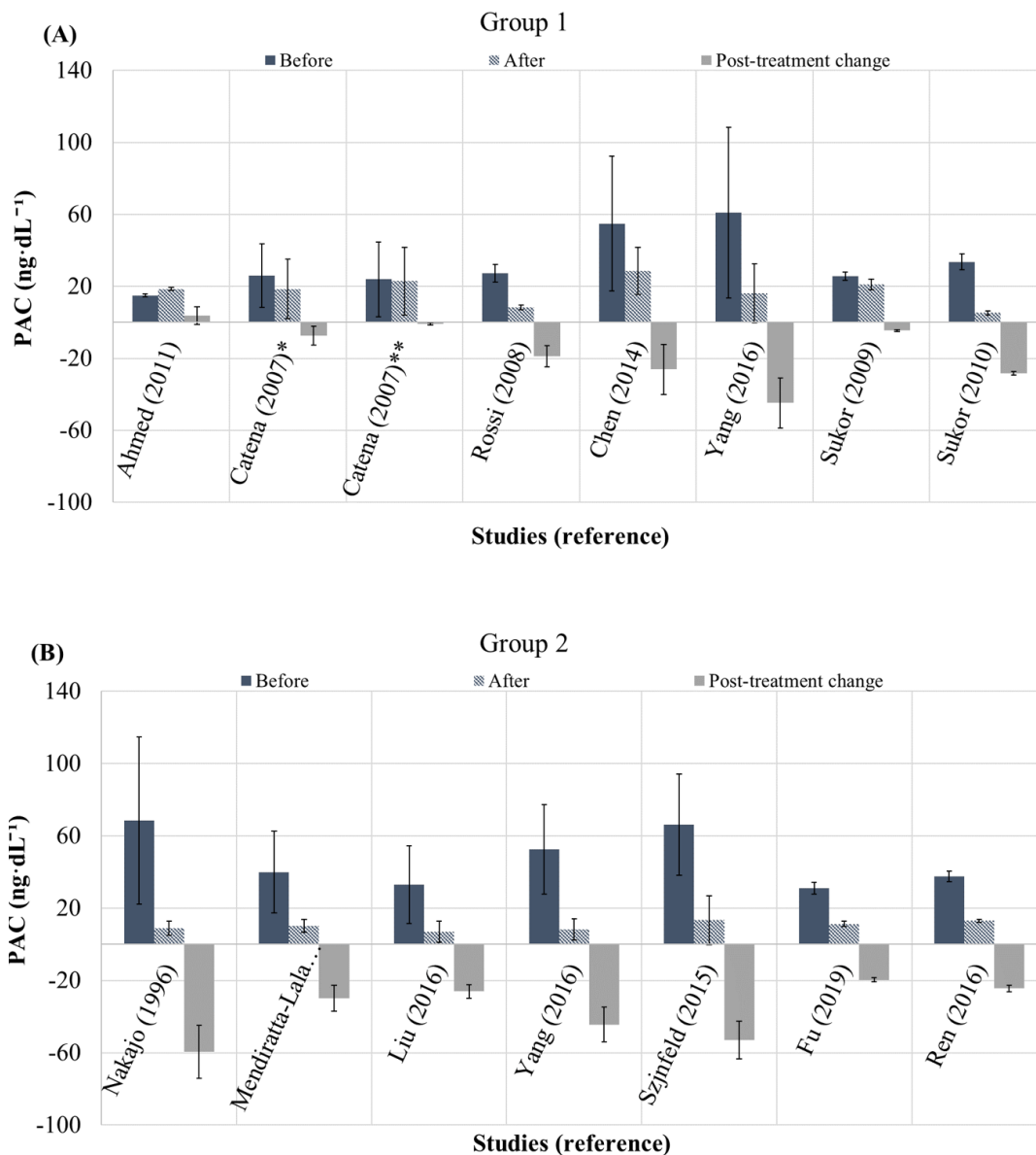
Figure A.5: Mean and standard deviations values of PAC (ng·dL-1) data reported in 7 studies before and after LA or MRAs administration and related effect size (A); Mean and standard deviations values of PAC data reported in 7 studies before and after the ablation treatments and related effect size (B). PAC: plasma aldosterone concentration, LA: laparoscopic adrenalectomy, MRA: mineralocorticoid antagonists.

overall post-treatment changes show an average increase in PRA levels of 0.7 ± 0.4 and 2.9 ± 2.1 ng·mL^{-1}·h^{-1} for the Group 1 and Group 2, respectively. In Figure A.4, the pre-treatment and post-treatment values of PAC (ng·dL^{-1}) are reported from 14 studies: 7 studies for Group 1 and 7 studies for Group 2. The average pre-treatment values are 33.4

± 16.9 ng·dL^{-1} for Group 1 and 43.4 ± 17.2 ng·dL^{-1} for Group 2; while post-treatment values are 17.4 ± 8.8 ng·dL^{-1} for Group 1 and 10.5 ± 5.2 ng·dL^{-1} for Group 2. Post-treatment changes showed overall decreases in the levels of the aldosterone hormone in the blood stream (PAC) of 15.9 ± 16.6 ng·dL^{-1} for the Group 1 and 36.7 ± 15.5 ng·dL^{-1} for the Group 2.

The values of the parameter ARR indicating both the degree of renin suppression and the amount of the aldosterone hormone released from the adrenal glands are reported in Figure A.5. The average ARR values calculated over 5 studies of the Group 1 and 3 studies of the Group 2 are: 151.8 ± 15.2 ng·dL^{-1}·ng^{-1}·mL·h^{-1} and 93.0 ± 15.6 ng·dL^{-1}·ng^{-}
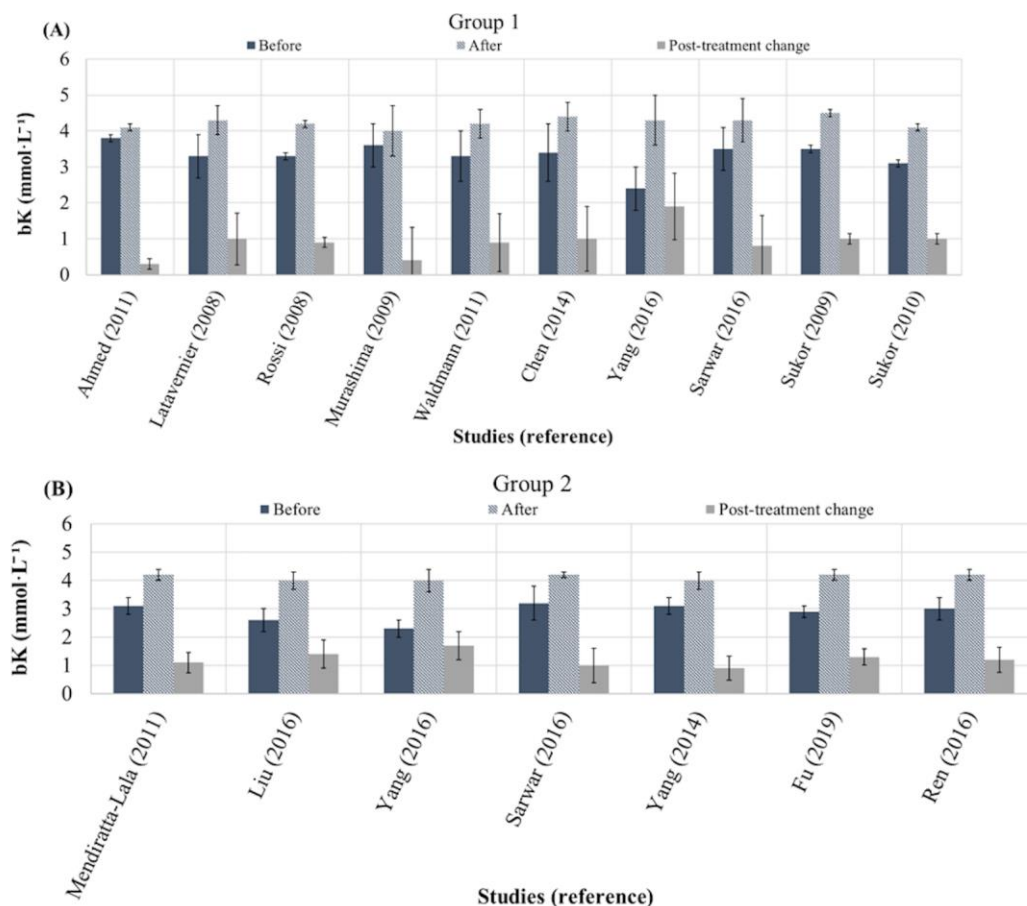

Figure A.6: Mean and standard deviations values of bK (mmol·L-1) data reported in 10 studies before and after LA or MRAs administration and related effect size (A); mean and standard deviations values of bK data reported in 7 studies before and after the ablation treatments and related effect size (B). bK: blood potassium concentration, LA: laparoscopic adrenalectomy, MRA: mineralocorticoid antagonists.

$^{1} \cdot mL \cdot h^{-1}$ (pre-treatment); and 14.0 ± 2.4 ng$\cdot$dL$^{-1} \cdot$ng$^{-1} \cdot$mL$\cdot$h^{-1} and 36.2 ± 7.7 ng$\cdot$dL$^{-1} \cdot$ng$^{-1} \cdot$mL$\cdot$h^{-1} (post-treatment). For both groups of studies the overall post-treatment changes in ARR parameter decrease of 56.8 ± 46.4 ng$\cdot$dL$^{-1} \cdot$ng$^{-1} \cdot$mL$\cdot$h^{-1} and 144 ± 86.6 ng$\cdot$dL$^{-1} \cdot$ng$^{-1} \cdot$mL$\cdot$h^{-1} for the Group 1 and the Group 2, respectively.

Finally, the mean and standard deviation values of the blood potassium concentration (bK) before and after the treatment are shown in Figure A.6 for the 10 studies included in Group 1 and the 7 studies included in Group 2. The average pre-treatment values calculated across the studies are 3.3 ± 0.4 mmol$\cdot$L^{-1} for Group 1 and 2.9 ± 0.4 mmol$\cdot$L^{-1} for Group 2. The post-treatment values are 4.2 ± 0.4 mmol$\cdot$L^{-1} for Group 1 and 4.1 ± 0.2 mmol$\cdot$L^{-1} for Group 2. A recover from the hypokalaemia is indicated by the increases in the levels of potassium concentration in the blood of 0.9 ± 0.5 mmol$\cdot$L^{-1} (Group 1) and 1.2 ± 0.3 mmol$\cdot$L^{-1} (Group 2).

The incidences of the resolution and of the improvement of the hypertension are reported in Table A.2 for all the studies. The definition of resolution is based on the elimination of hypertension without any adjuvant hypertensive medications; improvement is defined in the cases of ameliorated hypertension (not elimination) and decrease of the antihypertensive medications. The overall incidence of the resolution of the hypertension is 39.8% for the studies of the Group 1 and 51.2% for the studies of the Group 2, whereas the overall improvement of the hypertension accounts for an incidence of 45.7% (Group 1) and 36.0% (Group 2).

The studies gathered in this review revealed promising results in the normalisation and/or improvement of the clinical and biochemical parameters by using ablation techniques. It can be noticed (Table A.1) that the studies based on the ablation techniques targeted unilateral functional adenomas of 3.3 ± 1.1 cm in diameter.

Comparable results were obtained in the clinical parameters (SBP and DBP) between studies of Group 1 and Group 2, considering follow-up durations of 32.9 ± 31.1 months for the Group 1 and 26.4 ± 22.7 months for the Group 2. The studies of Group 1 (Figure A.1 (A), Figure A.2 (A)) showed no significant difference after the treatment in DBP values reported in 2 over 12 studies. Small post-treatment changes in DBP values of -4.0

$\pm$ 10.2 mmHg (*P-value* = 0.12) and -0.4 $\pm$ 1.9 mmHg (*P-value* = 0.35) were observed in [129] and [166], respectively (Figure A.2(A)). For the remaining 10 studies significative improvements are observed (*P-value* < 0.0001) both for the SBP and DBP parameter. In

Table A.2: Incidence (%) of the resolution of the hypertension and prevalence (%) of the hypertension improvements both for the studies of the Group 1 (LA or MRAs-pharmacotherapy), Group 2 (ablation-based studies).

Group 1			
Study name	**Treatment type**	**Complete resolution (%)**	**Improvement (%)**
[161]	MRAs	NA	NA
[162]	MRAs	37	63
[162]	LA	42	58
[168]	LA	39	38
[163]	LA	29	53
[164]	LA	21	70
[165]	LA	37	37
[72]	LA	0	64
[131]	LA	94	NA
[129]	LA	38	40
[166]	LA	15	20
[167]	LA	86	14
Overall		39.8	45.7
Group 2			
[99]	TACE	50	20
[126]	RFA	20	70
[127]	RFA	36	19
[131]	RFA	29	71
[129]	RFA	17	75
[130]	RFA	NA	NA
[128]	RFA	58	33
[104]	CA	100	0
[19]	MWA	100	0
Overall		51.2	36.0

Group 2, all the studies based on the adoption of RFA and on the cryoablation technique showed significant decreases (*P-value* < 0.001) both in SBP and DBP values after the treatment (Figure A.1(B)−A.2(B)) [13], [104], [126] −[130]. The data reported in [Nakajo et al. 1996] showed no statistically significant difference in the SBP (*P-value* = 0.051) and DBP (*P-value* = 0.29) values before and after the chemo-embolisation treatment. Given the values of the clinical parameters after the treatment, the complete resolution of the hypertension without any adjuvant anti-hypertensive therapy was observed in 51.2% of patients who underwent ablation treatments, whereas the gold standard techniques showed the resolution of the hypertension in 36.0% of patients. However, these results should be interpreted with caution, because of the limited number of studies (N = 9) adopting ablation techniques.

This survey investigated also the normalisation of the biochemical parameters (PRA, PAC, ARR, bK) both after laparoscopic adrenalectomy (LA) or the administration of MRAs (Figure A.3 (A) – A.6 (A)) and after ablation procedures (Figure A.3 (B) – A.6 (B)).

The overall increases in the level of the renin activity (PRA) indicated the normalisation of the renin-angiotensin system after the treatment. Significant increases (*P-value* < 0.0001) in the PRA parameter were observed in the results both of the Group 1 (Figure A.3(A)) and Group 2 (Figure A.3(B)). Only in one study included of the Group 1 [163] showed no significative improvement (*P-value* = 0.06) in PRA values.

Overall, ablation techniques showed better performances in the normalisation of values of PAC (Figure A.4(B)), compared to LA- and MRAs- based treatments (Figure A.4(A)). In particular, statistically significative decreases (*P-value* < 0.0001) in PAC levels were obtained in all of the studies included in Group 2. Instead, no significative decreases in the release of the aldosterone hormone were observed after the treatment based on LA or MRAs in both the cohorts of patients included in [162] (*P-value* > 0.14).

Both for ARR (Figure A.5(A) – (B)) and bK (Figure A.6 (A) – (B)) parameters statistically significant decreases (*P-value* < 0.05) were obtained in the studies included in Group 1 and in Group 2. It must be mentioned that ARR parameter is linked both to

the concentration of aldosterone (PAC) and to the renin activity (PRA), thus the decrease of ARR parameter not necessarily indicates both the reduction of the aldosterone (PAC) release and the increase of the renin activity (PRA). Thus, the performances of a specific treatment should be evaluated not only in terms of ARR values, but PRA and PAC levels should be also evaluated separately. For example, in [161], a significant decrease (*P-value* < 0.0001) in ARR was found. This result was mainly affected by the significant increase of the renin-activity indicated by PRA levels, while levels of PAC were found persistently high after the treatment. In [163], the significative decrease in the mean value of ARR is linked to the normalisation of the mean value of PAC. However, no significant improvement observed in PRA levels indicated the persistent suppression of the renin activity. In these cases, further investigations are required as the persistent suppression of the plasma renin activity even after the treatment, may be not related to PA but to other causes such as ant-inflammatory drugs, renal dysfunction, advancing ages [45].

In the patients showing hypokalaemia as consequence of the PA, the concentration of potassium (bK) in the blood is monitored together with the other biochemical parameters. The significative increases in the levels of potassium (*P-value* < 0.0001) showed after the specific treatment both in the Group 1 and in the Group 2 indicated the reactivation in the absorption of potassium, thus the recover from hypokalaemia.

Overall, the ablation techniques included in Group 2 showed performances in terms of normalisation of clinical and biochemical parameters comparable to those of the gold standard techniques, included in Group 1. In addition, ablation techniques showed shorter duration of operation, faster recovery, lower analgesic requirement and shorter hospital stay compared to LA. Most of the studies reviewed in this work adopted RFA for a novel approach to PA treatment. In addition, a prospective study on 20 patients affected by adreno-cortical adenomas investigating a radiofrequency endoscopic ablation solution is currently in progress (St Bartholomew's Hospital, UK). Further studies should be conducted to enable a better understanding of the outcomes in terms of resolution or improvement of hypertension, normalisation of biochemical parameters, complications during the procedure and side effects experienced from the patient. Because of the

proximity of the adrenal glands to sensitive structures such as blood vessels, nerves and diaphragm, a more comprehensive investigation aimed to evaluate the performances of the ablation techniques to spare the surrounding structures is required. In addition, all the reviewed studies gathered in this work showed results related to the complete elimination of the adreno-cortical adenomas and normalisation of biochemical and/or clinical parameters. However, no histology analysis was provided to quantitatively establish whether the healthy functional tissues composing the adrenal gland was preserved.

A.3 Conclusion

In this analysis, studies using ablation techniques and gold-standard techniques for the treatment of PA were reviewed. The results of each selected study were gathered and presented in order to compare the performances of the ablation techniques against the laparoscopic adrenalectomy and pharmacotherapy.

The study showed:

- Comparable performances between ablation and traditional techniques (LA or MRAs) in terms of resolution or improvements of hypertension. According to the aggregated studies included in this review, about 89% of the patients treated via ablation and about 88% of the patients treated through LA or MRAs-based pharmacotherapy showed resolution or improvement from hypertension;

- Promising performances of the ablation techniques also in terms of normalisation of the aldosterone levels (PAC) and renin activity (PRA) compared to the traditional techniques. With respect to the pre-treatment values, an overall increase of more than 20% in PRA values and a decrease of 35% in the PAC and ARR values were observed after the ablation treatment.

- The complete resolution of the hypertension in the case of MWA was observed after 24 months follow-up. Successful results were obtained also for adenomas adjacent to critical structures. In these cases, it was possible to complete the procedure without damaging the sensitive structures through the injection of saline solution into the peritoneal cavity to achieve a separation larger than 0.5 cm. Although promising

results were reported in the only study exploiting MWA to treat functional adenomas, a lack in the data regarding the pre-treatment and post-treatment values of SBP and DBP was observed. Thus, further investigations are required to evaluate the reliability of the performances of MWA in the resolution of hypertension linked to functional adrenal adenomas.

Appendix B

Influence of the temperature dependent dielectric properties on the asymmetrical ablation patterns

B.1 Introduction

During MWA procedures, temperatures can easily exceed 100 °C in the tissue, particularly in proximity to the feed of the MW applicator [145]. Because of this increment of temperature, structural changes and water loss occur in the tissue. In turn, the changes in the water content affect the dielectric properties of the tissue.

A number of studies was dedicated to characterise the changes in the dielectric properties of the biological tissue when the temperature increases. In most of these studies, temperatures below 70°C were considered. Linear or quadratic functions were used to model the temperature dependence of the dielectric properties [183], [202]. However, these models may be not adequate to represent the changes in the dielectric characteristics when severe temperature increases occur.

Two studies, [143] and [144], considered temperatures above 70 °C. In these studies, the changes in relative permittivity and effective conductivity of liver tissue were measured during MWA procedures conducted at 2.45 GHz. Both studies showed a decrease in the values of dielectric properties with the increment of temperature modelled by a sigmoid function. The function shows a rapid drop in the values of relative permittivity and effective conductivity between 60°C and 100°C. At these temperatures, phenomena such as protein denaturation and water vaporisation occur.

In [142] a comprehensive study evaluated the effects of both models described in [143] and [144] on the increment of temperature during a MWA procedure. The study revealed that the results obtained using temperature-dependent models (dynamic models) for the dielectric properties diverge from those obtained using static dielectric properties (standard BHE) when temperatures exceed 55 – 60°C. For durations below 60 s no

significant differences in the temperature were observed between the standard BHE and the dynamic models. Given the results presented in [142] and the relatively short ablation durations (60 s) adopted in this thesis, no differences in using dynamic or static (standard BHE) dielectric property models should be expected.

This appendix shows the results of numerical simulations conducted at 2.45 GHz implementing dynamic models of relative permittivity and effective conductivity. The results are compared with those obtained from the static models adopted in the body of this thesis. The extent of the predicted ablation zones both in the fat and adrenal tissues are discussed.

B.2 Methodology

The multilayered tissue model described in Chapter 6 (Figure 6.1) was adopted in this work to conduct EM and thermal simulations. The numerical simulations were completed using CST MW Studio software. EM and thermal boundary conditions as well as the size of the mesh cells adopted in this study were consistent with those described in Chapter 4 (§ 4.4).

$$\varepsilon_r(T) = a_3 \left\{ 1 - \frac{1}{1 + exp[a_1(a_2 - T)]} \right\} + 1 \qquad \text{(B.1)}$$

$$\sigma(T) = b_3 \left\{ 1 - \frac{1}{1 + exp[b_1(b_2 - T)]} \right\} \qquad \text{(B.2)}$$

In this study, the sigmoid functions developed by [143] for *ex vivo* bovine liver were assumed valid for the adrenal tissues, both medulla and cortex. This assumption was made given the similar water content (75.7% in the adrenal gland vs 72.2% in liver)

Table B.1: Coefficients of the sigmoidal functions describing the dependence of the relative permittivity (ε_r) and the effective conductivity (σ) on the temperature, both for cortex and medulla.

Tissue	Relative permittivity			Effective conductivity		
	a_1	a_2	a_3	b_1	b_2	b_3
Cortex	0.0764	82.271	44.76	0.0697	85.375	0.61
Medulla	0.0764	82.271	51.76	0.0697	85.375	0.817
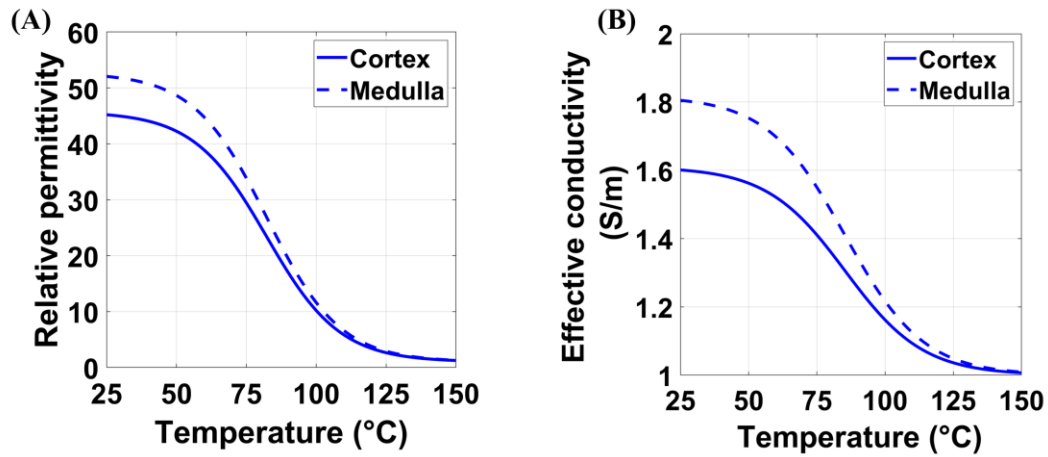
Figure B.1: Values of relative permittivity (A) and effective conductivity (B) for cortex and medulla over the temperature according to the model described in [143]. Relative permittivity and effective conductivity measured at 25°C both in cortex and medulla and reported in Chapter 3 (Tables 3.4–3.5) are considering as starting values of the sigmoidal functions. The values of dielectric properties decrease as the temperature increases. The values decrease with linear slope occurs when the temperature exceeds 55°C but remains below 100°C. While, such drop is slower water before to reach 55°C and after 100°C.

[265], and the comparable values of relative permittivity and effective conductivity at 2.45 GHz measured at 25°C [143], (Tables 3.4 –3.5). On the other hand, the sigmoid models were not considered valid for fat due to the lower water content of the tissue compared with liver (20.0% vs 72.2% in liver) [265]. Additionally, the baseline dielectric properties of fat at 25°C are noticeably lower than liver [183]. Thus, static dielectric properties were considered for the fat tissue during the EM and thermal simulations.

Equations B.1 and B.2 describe the temperature-dependent dielectric properties of medulla and cortex based on the model reported in [143]. The corresponding coefficients are listed in Table B.1. It can be noted that the coefficients a_3 and b_3 are different from the values used in [143] ($a_3 = 44.3$, $b_3 = 1.8$). The coefficients a_3 and b_3 were modified both for the cortex and medulla in order to have consistency in the models at the initial conditions. Indeed, the values of the relative permittivity and effective conductivity at 25°C for both functional tissues are consistent with the values reported in Chapter 3 (Tables 3.4 – 3.5) at 2.45 GHz.

Those functions were implemented in MATLAB (R2017a, The MathWorks, Inc., Natick, MA, US) and temperatures between 25°C and 150°C were used as input variables [143]. Figure B.1 depicts the sigmoid functions of relative permittivity (A) and electrical conductivity (B) both for cortex and medulla.

The values of the dielectric properties calculated by Equations B.1 and B.2 for the temperatures between 25°C and 150°C were imported in CST MW Studio software. Then, bi-directional numerical simulations were completed. In the bi-directional numerical simulations conducted for this study, the dielectric properties of the adrenal tissues were updated every second for the entire duration of the signal excitation. Power and time settings consistent with those used in the other chapters of the thesis were used in this study: 30 W and 60 W delivered for 60 s.

B.3 Results

Figure B.2 shows the maps of SAR (A) – (B) and temperature (C) – (D) at 30 W and 60 W input powers. SAR values normalised to the maximum and expressed in decibel (dB)
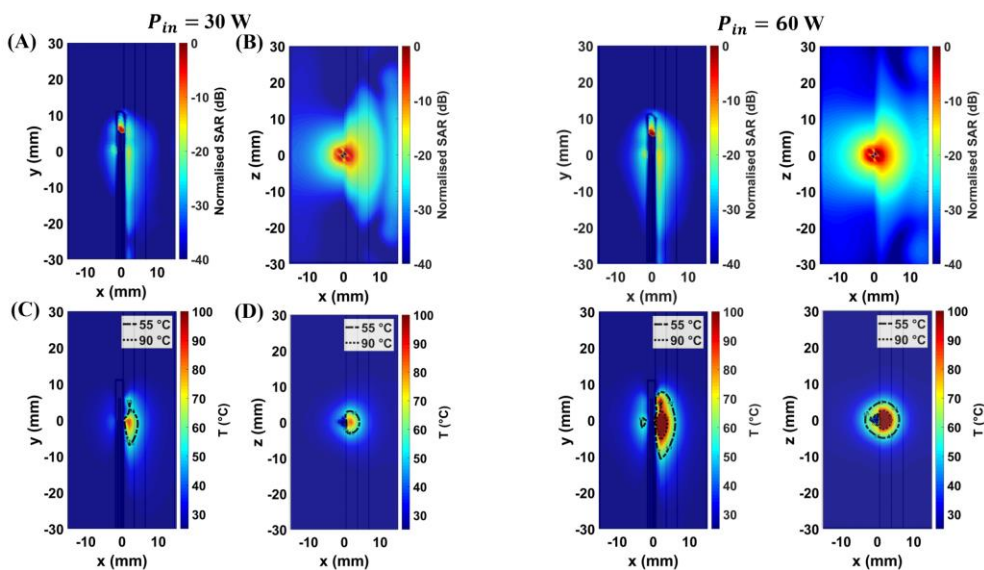
Figure B.2: Maps of SAR (A) – (B) and of temperature (C) – (D) obtained numerically in the simplified multi-layered model at 30 W and 60 W, considering temperature-dependent dielectric properties for adrenal tissues. Profiles of SAR and temperature are presented both in the frontal plane (xy-plane) and in the coronal plane (xz-plane) with reference to the feed of the antenna.

and thermal values at 60 s are depicted in the frontal (A) – (C) and coronal (B) – (D) planes.

This study shows asymmetrical SAR profiles, consistent with the results discussed in Chapter 6 (Figure 6.6 (A) – (B)). In the adrenal gland, values of SAR higher than -20 dB extend up to 3 mm (at 30 W) and 5 mm (at 60 W) radially from the axis of the applicator. In the fat tissue, values of SAR higher than -20 dB are absent in the case of 30 W and extend no farther than 2 mm from the longitudinal axis of the applicator at 60 W. These results agree with the values obtained in the case of standard BHE (§6.2.1). More visible differences in the distribution of SAR can be observed along the longitudinal dimension in the adrenal gland. This study shows that values higher than -20 dB in the longitudinal dimensions reach 3 mm at 30 W and 14 mm at 60 W. In the case of standard BHE (Figure 6.6 (A)), those values of SAR extend up to 10 mm at 30 W and to 22 mm at 60 W. A reduction of 70% at 30 W and 36% at 60 W in the longitudinal profile of SAR is obtained in the case of dynamic models compared with the standard BHE.

Asymmetrical thermal profiles are also obtained in the case of the dynamic models. Overall, the thermal profiles are comparable with those achieved using the standard BHE (Figure 6.6 (C) – (D)). In agreement with the SAR maps, a larger difference between the two numerical conditions is visible in the longitudinal dimension of the ablation zone. For a direct comparison, Table B.3 lists the radial and longitudinal dimensions of the ablation zone in the fat and adrenal tissues achieved both in the case of the dynamic model and the standard BHE. No difference in the extent of the ablation zone in fat is

Table B.2: Radial and longitudinal extents calculated at 30 W (first line) and at 60 W (second line) using temperature-dependent dielectric properties (dynamic model) and standard BHE (Chapter 6) in the simplified geometry including fat and adrenal tissue.

Settings		Temperature-dependent dielectric properties (Dynamic model)				Fixed dielectric properties (Standard BHE)			
		Fat		Adrenal gland		Fat		Adrenal gland	
P (W)	t (s)	R	L	R	L	R	L	R	L
30	60	0	0	5	10	0	0	7	19
60	60	2	2	7	19	2	2	9	27

visible between the two numerical conditions. In both cases, the ablation zone is absent at 30 W and negligible at 60 W. In the adrenal gland, the radial extent of the ablation zone achieved in the case of dynamic models is approximately 2 mm smaller than the extent achieved in the case of standard BHE. With reference to the longitudinal dimension, the difference between two numerical scenarios is more visible. In particular, the dynamic model provides ablation zones approximately 47% (30 W) and 30% (60 W) shorter compared with the standard BHE. When dynamic models are adopted, the discrepancy in the longitudinal dimension between numerical and experimental results (Chapter 6) is reduced. These differences are 29% at 30W and 19% at 60W in the case of dynamic models; whereas they are 36% at 30W and 69% at 60W in the case of standard BHE. It is worth noting that the extent of the area delineated by the isothermal at 90°C appears visibly smaller in the case of the dynamic model compared with the case of standard BHE (Figure 6.6). Specifically, this area is absent at 30 W, while at 60 W it is 33 % and 56% smaller in the radial and longitudinal dimensions, respectively.

The study included in this appendix showed that the decrease in the dielectric properties of the adrenal tissues with the increase of the temperature has little influence if any on the ability of the fat layer to shield the electromagnetic energy, at the operating conditions used. On the other hand, some differences between the standard BHE and the dynamic model were observed.

A slightly smaller radial extent of the ablation zone was obtained in the case of the dynamic models compared with the standard BHE. A more visible discrepancy between the two models was observed in the longitudinal extent of the ablation zone in the adrenal gland. Overall, shorter and more spherical ablation zones were achieved in the case of the dynamic model compared with the standard BHE. This effect is linked to the lower values of SAR reached at the feed point of the applicator due to the decrease of the tissue electrical conductivity. Thus, a different redistribution of the electromagnetic power occurs in the tissue.

Lower peak temperatures are achieved compared to the standard BHE as can be inferred from the shrinkage of the isothermal contour at 90°C. The smaller thermal gradient

between the tissue close to the applicator and the peripheral areas also contributes to reduce the extent of the ablation zones compared with the standard BHE.

Finally, it is worth noticing that dynamic simulations conducted only in the simplified model required a higher computational load compared to the standard BHE. The EM and thermal simulations were completed on an Intel® Core™ i7@ 4GHz with 16 GB RAM. The simulations using standard BHE required approximately 7h against 17h for the dynamic simulations, both conducted in the simplified model using CST MWS Suite 2018. This information should be taken into account based on the objective of the numerical simulations.

To summarise, both the models confirmed the asymmetric heating patterns due to the shielding effect of the fat layer. The study highlighted that standard BHE overestimates the ablation zone in terms of longitudinal dimensions compared with the dynamic model. However, the study using dynamic models presents limitations which are the lack of the temperature-dependent model suitable for the fat tissue and the high computational costs even for a simplified model. Hence, the results confirmed the reliability of the assumption adopted throughout this thesis, according to which static dielectric properties (standard BHE) were assigned to the adrenal tissues.

B.4 Conclusions

In this study temperature-dependent dielectric models developed in [143] were used to evaluate the influence of the decrease in dielectric properties of the adrenal tissues on the asymmetric ablation patterns.

The study showed that:

- For MWA procedures conducted at 60 s, the changes in dielectric properties due to the increase of temperature do not compromise the ability of the fat layer to shield the EM energy. Thus, the standard BHE is a reliable assumption if the objective of the numerical simulations is to evaluate the role of the fat layer in creating asymmetric heating patterns;

- The temperature-dependent dielectric models have instead a more visible influence on the longitudinal extent of the ablation zone and peak temperature values reached in proximity of the feed of the applicator. As a result, dynamic models are required when the numerical simulations are devoted to accurately evaluate the thermal coverage of the tissue target.